Search for invisible decays of the Higgs boson produced in vector-boson fusion in final states with jets and large missing transverse energy with the ATLAS detector

Dissertation zur Erlangung des Doktorgrades
an der Fakultät für Mathematik, Informatik und
Naturwissenschaften Fachbereich Physik
der Universität Hamburg

vorgelegt von

Vincent Kitali

aus Hameln, Deutschland

Hamburg, 2019

Gutachter der Dissertation	Prof. Dr. Peter Schleper Dr. Krisztian Peters
Gutachter der Disputation	Prof. Dr. Peter Schleper Dr. Krisztian Peters Prof. Dr. Sven-Olaf Moch Prof. Dr. Kerstin Tackmann Prof. Dr. Johannes Haller
Datum der Disputation	23.01.2020
Vorsitzender des Prüfungsausschusses	Prof. Dr. Sven-Olaf Moch
Vorsitzender des Promotionsausschusses	Prof. Dr. Günter Sigl
Leiter des Fachbereichs Physik	Prof. Dr. Wolfgang Hansen
Dekan der Fakultät für Mathematik, Informatik und Naturwissenschaften	Prof. Dr. Heinrich Graener

Abstract

The Standard Model of particle physics is a very successful theory, but it leaves some open questions. Especially the topic of dark matter is a very active field of research and the discovery of dark matter candidates might be accessible to modern collider experiments. Answering open questions of the Standard Model is one of the greater goals of this work.

The dark matter candidates might interact with the recently discovered Higgs boson and would appear invisible to a particle detector. This motivates a search for invisible decays of the Higgs boson produced in vector-boson fusion. The search is looking for a pair of well-separated, highly energetic jets and missing transverse energy in the final state. The analysis uses 36.1 fb^{-1} of proton–proton collision data recorded at a centre-of-mass energy of 13 TeV in 2015 and 2016 with the ATLAS experiment at the LHC. The main backgrounds are leptonically decaying vector bosons. These backgrounds are constrained in dedicated data control regions.

The multijet background is small, since it can only result from mismeasurements of the jet transverse momentum, but it is challenging to quantify. The jet response is a measure for the mismeasurement of jet transverse momenta. To study how well it is simulated in areas of extreme mismeasurements the non-Gaussian tails of these distributions are quantified in a comparison between data and simulation. This is achieved by modelling the Gaussian core with fits. In order to see the effect in data the momentum balance of jet pairs is considered by using an extrapolation to pure dijet events. The effort is undertaken with a new jet definition, particle flow jets, as well as topocluster jets. For both of them simulation and data are in good agreement. This leads to systematic uncertainties small enough to have a negligible impact on the analysis.

The systematic uncertainty resulting from the jet energy resolution is one of the main limitations to the sensitivity of the search. This is addressed with the global sequential calibration (GSC), a simulation-driven method that removes the dependencies of jet momenta on a selection of detector variables in order to improve the jet resolution. The calibration leads to a jet resolution improvement of up to 20%. The GSC is fully derived for particle flow jets for the first time, allowing performance comparisons between different kinds of jet reconstruction algorithms.

The search is able to derive a new observed (expected) limit on the Higgs to invisible branching fraction of 0.37 (0.28) at 95% confidence level. The results are also interpreted considering a Higgs portal model, treating the invisible decay products as dark matter candidates. The resulting limits on the cross-section for the DM candidate to interact with an atomic nucleus is between 10^{-46} cm^2 and 10^{-42} cm^2 at 90% confidence level depending on the DM mass and spin.

Zusammenfassung

Das Standardmodell der Teilchenphysik ist eine äußerst erfolgreiche Theorie, die aber ein paar Fragen unbeantwortet lässt. Insbesondere das Thema der Dunklen Materie ist ein aktives Forschungsfeld und die Entdeckung von Kandidaten für Dunkle Materie könnte sich in Reichweite moderner Teilchenbeschleuniger befinden. Das Beantworten von offenen Fragen des Standardmodells ist eines der übergeordneten Ziele dieser Arbeit.

Die Kandidaten für Dunkle Materie könnten mit dem kürzlich entdeckten Higgs-Boson interagieren und würden für Teilchendetektoren unsichtbar wirken. Das motiviert die Suche nach unsichtbaren Zerfällen des Higgs-Bosons, welches in der Fusion von Vektorbosonen produziert wird. Die Analyse sucht nach einem Paar von stark separierten, hochenergetischen Jets und fehlender Transversalenergie im Endzustand. Die Suche nutzt 36.1 fb^{-1} Daten von Proton–Proton-Kollisionen, die zwischen 2015 und 2016 mit dem ATLAS Experiment am LHC aufgezeichnet wurden. Die Hauptuntergründe sind leptonisch zerfallende Vektorbosonen. Diese Untergründe werden in zugehörigen Kontrollregionen in Daten begrenzt.

Der Multijetuntergrund ist klein, da er nur aus Fehlmessungen des Transversalimpulses von Jets resultiert, aber er ist schwierig zu quantifizieren. Die Jetantwort ist ein Maß für den Grad der Fehlmessung von Transversalimpulsen von Jets. Um herauszufinden, wie gut die Jetantwort in Bereichen extremer Fehlmessung simuliert ist, werden nicht-gaußsche Verteilungsenden in einem Vergleich zwischen Daten und Simulation quantifiziert. Dies wird bewerkstelligt, indem die gaußschen Kerne mit Fits modelliert werden. Um den Effekt in Daten zu untersuchen, wird die Impulsbalance von Jetpaaren durch eine Extrapolation zu reinen Zwei-Jet-Ereignissen in Betracht gezogen. Das Verfahren wird sowohl auf eine neue Jetdefinition, die sogenannten Teilchenstromjets, als auch auf Topogruppenjets angewendet. In beiden Fällen stimmt die Simulation gut mit Daten überein. Dies führt zu systematischen Unsicherheiten, die klein genug sind, um einen vernachlässigbaren Einfluss auf die Analyse zu haben.

Die systematische Unsicherheit, die aus der Jetenergieauflösung resultiert, ist eine der Haupteinschränkungen für die Sensitivität der Suche. Das wird addressiert mit der globalen, sequentiellen Kalibration (GSC), einer simulationsbasierten Methode, die Abhängigkeiten des Jetimpulses von Detektorobservablen entfernt, um die Jetauflösung zu verbessern. Die Kalibration führt zu einer Verbesserung der Jetauflösung von 20%. Dabei wird die GSC erstmalig für Teilchenstromjets hergeleitet, was den Leistungsvergleich mit anderen Jetrekonstruktionsalgorithmen erlaubt.

Die Suche ist dazu in der Lage, ein neues beobachtetes (erwartetes) Limit auf das Verzweigungsverhältnis für den unsichtbaren Higgszerfall von 0.37 (0.28) bei einem Vertrauensniveau von 95% zu setzen. Die Resultate werden im Rahmen eines Higgs-Portal-Modells interprätiert, wobei die unsichtbaren Zerfallsprodukte als Kandidaten für dunkle Materie behandelt werden. Daraus resultieren Limits auf die Wirkungsquerschnitte für die Wechselwirkung zwischen Kandidaten für dunkle Materie und Atomkernen, die in Abhängigkeit von Masse und Spin der dunklen Materie bei einem Vertrauensniveau von 90% zwischen 10^{-46} cm^2 und 10^{-42} cm^2 liegen.

Contents

List of Figures

List of Tables

Chapter 1

Introduction

This is a time unlike any other in particle physics. The community is in the process of closing the successful chapter called Standard Model of particle physics (SM). The original motivation for the creation of the SM was the search for a fundamental model of nature in the form of a theory of fields. These fundamental fields are quantized into particles and are the central concept of this quantum field theory. The SM stood true to that original motivation during its ascension to a theory only falling short of incorporating a theory of gravity.

The SM is the unification of the electroweak (EWK) field theory and quantum chromodynamics (QCD). The former has the interesting property of a symmetry that is broken by the Higgs mechanism, which is explained in one of the chapters of this work. The latter is the theory of quarks, gluons and the strongest interaction known to this day. The nature of QCD and the strong interaction leads to the fact that particles like quarks and gluons cannot be detected in isolation. Instead, they become confined in a cascade of particle interactions called jets when they are produced in collider experiments.

One such collider, the Large Hadron Collider (LHC), which is based at CERN, is the source of most of the experimental data presented in this work. There are four main experiments collecting data at the LHC: Two multi-purpose detectors ATLAS and CMS as well as the specialized detectors ALICE and LHCb.

One of the main goals behind the operation of the four collaborations is to test the last properties of the SM. The breaking of the EWK symmetry is one such phenomenon, which can be explained by the Brout–Englert–Higgs mechanism [1]. The mechanism predicts a scalar particle called the Higgs boson, which was indeed found in 2012 [2, 3]. However, this is only one of the many phenomena the LHC helped us understand and many precision measurements have increased the understanding of the Standard Model [4, 5].

Furthermore, the experiments set out to look for physics beyond the Standard Model (BSM) because many phenomena cannot be explained with the current form of the quantum field theory. One of the most interesting questions is the nature of dark matter (DM). Astrophysical observations of the rotation curves of galaxies [6], galaxy clustering [7] and the cosmic microwave background (CMB) [8] among other experiments [9, 10] suggest that there is a kind of matter that is not visible with the current methods of detection. However, it is quite possible that DM can be produced at the LHC. The search for DM gained a huge boost from the discovery of the Higgs boson because it could interact with DM particles and in fact might be the only known particle that does so [11].

To the detectors ATLAS and CMS DM would not be detectable, but it is known that energy and momenta are conserved in the collision events. Therefore, DM would appear as missing transverse energy ($E_{\mathrm{T}}^{\mathrm{miss}}$) in the detector. This makes the search for DM at the LHC very challenging, since it requires experimentalists to reproduce every detectable object in the event with high accuracy in order to describe what is undetectable.

One such analysis is the search for invisible decays of the Higgs boson produced in vector-boson fusion with the ATLAS detector [12]. The analysis is discussed in detail in this work. In short, it uses the jets that come into existence as a byproduct of the Higgs boson production to identify the events in that DM would appear as invisible particles and therefore as $E_{\mathrm{T}}^{\mathrm{miss}}$. To ensure maximal effectiveness in the analysis a good understanding of the jet reconstruction is needed. This is important for most searches in ATLAS but this one in particular has the challenging task of analysing extreme kinematic phase spaces with high jet momenta and large spatial separation of the jets.

In Chapter 2 of this work the theoretical groundwork is set. This includes a description of the Standard Model with a focus on Higgs boson physics, jets and high energy particle collisions. A second focus are extensions of the SM that can incorporate particle dark matter from Higgs portal [13] models to Supersymmetry [14]. Chapter 3 is an overview of the experimental methods necessary for this thesis. It begins with the operation of the LHC and a description of the ATLAS detector. It also includes the discussion of the relevant physics objects, missing transverse momentum and the simulation of collision events. The calibration of jets in the ATLAS detector is detailed in Chapter 4. Here, the greatest focus is on the global sequential calibration (GSC), a method, which improves the jet energy resolution.

The search of invisible decays of the Higgs boson with the ATLAS detector is described in Chapter 5. It offers insight into the methods used for the study published in 2018 [12]. The multijet background estimate of the search is especially challenging. It requires a good understanding of the mismeasurement of jets. A study that seeks to test how well this is modelled in simulation is presented in Chapter 6. Finally, Chapter 7 is a summary of the most important lessons of this work and a discussion of the impact on other analyses and our understanding of nature.

1.1 Author's contribution

The studies presented in this work were undertaken on behalf of ATLAS, a collaboration consisting of about 3000 members all around the globe. The success of the experiment is achieved via the efforts of every single member contributing to the detector operation, analyses, simulation, software development, calibration and many other tasks. Each study had direct input from many other people and the part the author played in it is highlighted below.

To optimize the precision of jet measurements many improvements are constantly studied. One of them is the introduction of a new jet collection called particle flow (PFlow) jets, which are meant to replace the currently used topocluster (Topo) jets. The author was the first one to derive the global sequential calibration, a method to improve the jet energy resolution, for the new jet collection on a level equivalent to topocluster jets. That work made it possible to compare both types of jets on an equal footing and is important for many analyses in the collaboration.

For the search for invisible decays of the Higgs boson, the author worked on the multijet

background. In particular he studied the accuracy of the simulation of non-Gaussian tails in jet response distributions. These distributions are used to quantify how often an event with jets in the final state has enough $E_{\mathrm{T}}^{\mathrm{miss}}$ to appear like an invisible decay of a Higgs boson. The study required the development of new software and methods, which lead to the most precise results.

The author also compared how the choice of jet collection between particle flow and topocluster jets affects the search for invisible decays of the Higgs boson. For that he investigated many analysis variables and studied the signal region selection with special care for the $E_{\mathrm{T}}^{\mathrm{miss}}$ requirements and the third jet veto. The impact on the multijet background estimation and the above mentioned study was examined as well.

Chapter 2

Theoretical introduction

For the theoretical foundation of the following chapters two larger topics are relevant: The Standard Model (SM) is the basis of modern particle physics. It is presented in broad strokes in Section 2.1. Physics beyond the SM in the form of dark matter (DM) is discussed in Section 2.2.

In the following natural units are used: $\hbar = c = \varepsilon_0 = 1$.

2.1 The Standard Model of particle physics

2.1.1 Introduction to the Standard Model

The SM is a theory that describes fundamental laws of nature through the interaction of elementary, point-like particles and underlying symmetries [15, 16, 17]. It is a quantum field theory that treats the particles as quantized excitations of fundamental fields. The theory is characterized by its symmetry groups, its particle content and by the SM Lagrangian that formalizes the interactions.

The particle content of the SM is shown in Figure 2.1. The particles can be divided into fermions, which form matter, and bosons, which mediate three fundamental interactions. These are the strong interaction with gluons as the corresponding bosons, the weak interaction with W and Z bosons as well as the electromagnetic interaction with the photon (γ). Gravity, the fourth fundamental interaction of physics, is not described by the SM. The Higgs boson is not directly linked to an interaction but rather to the electroweak (EWK) symmetry breaking.

Each fundamental particle is assigned a set of quantum numbers that inform about their possible interactions. Most importantly there are the charges under the symmetry groups and the spin. The latter also formalizes the difference between fermions and bosons, which have half integer spin and integer spin, respectively. The charges under the symmetry groups are discussed in the respective sections.

Another interesting property of the SM are the three generations of fermions. In the left column in Figure 2.1 the up quark (u), down quark (d), electron (e) and electron neutrino (ν_e) are listed. The second and third column consist of variations of these particles that vary by their mass, but all other properties are qualitatively the same. Only the lightest generation constitutes ordinary matter because the heavier elementary particles decay within a fraction of a second. Neutrinos are an exception of this, which is beyond the scope of this work.

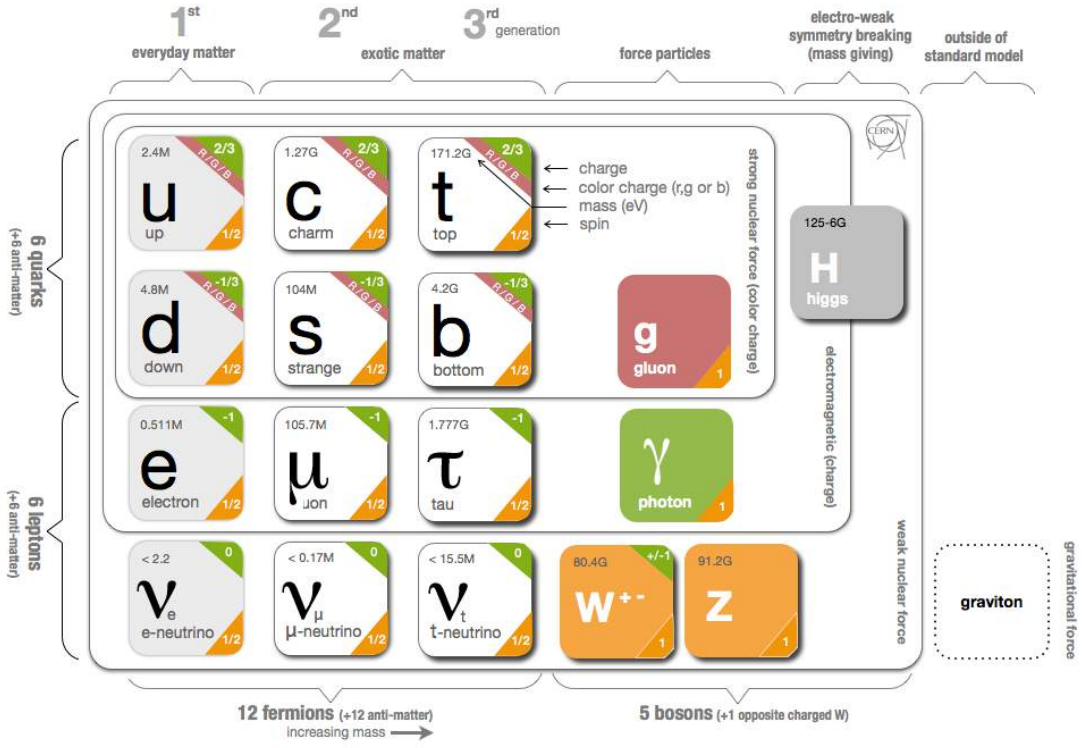

Figure 2.1: Elementary particles of the Standard Model. The neutrinos are ordered in association with the corresponding charged leptons and not by their own mass. The graviton is hypothesized and not discovered [18].

The SM Lagrangian is constructed to be invariant under local symmetry transformations following the gauge symmetry group:

$$SU(3)_C \otimes SU(2)_L \otimes U(1)_Y, \tag{2.1}$$

where U is a unitary group and SU is a special unitary group. Particles charged under $SU(3)_C$ are colour charged. The charges for $SU(2)_L$ and $U(1)_Y$ are the weak isospin and the hypercharge, respectively. However, the $SU(2)_L \otimes U(1)_Y$ symmetry is broken and the weak isospin as well as electromagnetic charge guide the interactions.

The Lagrangian can be divided into multiple parts:

$$\mathscr{L}_{\text{SM}} = \mathscr{L}_{\text{EWK}} + \mathscr{L}_{\text{Higgs}} + \mathscr{L}_{\text{QCD}} + \mathscr{L}_{\text{Yukawa}}. \tag{2.2}$$

$\mathscr{L}_{\text{EWK}}$ is the electroweak Lagrangian. It is invariant under $SU(2)_L \otimes U(1)_Y$ and it is further discussed in Section 2.1.2. The process of EWK symmetry breaking described by the Brout–Englert–Higgs mechanism is presented in Section 2.1.3. Here, the Yukawa term $\mathscr{L}_{\text{Yukawa}}$ is introduced as well. This also give rise to the Higgs interactions described by $\mathscr{L}_{\text{Higgs}}$. The term $\mathscr{L}_{\text{QCD}}$ is the topic of Section 2.1.4. Finally, Section 2.1.5 covers the entire Lagrangian in a larger context and summarizes the key aspects of the SM. As preparation for later chapters the most important concepts of relativistic collisions are shown in Section 2.1.6. The production and decay modes of the Higgs boson get their own section in Section 2.1.7. Finally, some of the questions left open by the SM are listed in Section 2.1.8 to guide into later sections of this chapter.

2.1.2 Electroweak interaction

Historically, the electromagnetic interaction and the weak interaction were considered separate until a more fundamental symmetry was discovered. It is therefore useful to discuss the theory of electromagnetic interactions, quantum electrodynamics (QED), and the theory of the weak interactions individually before considering the full $SU(2)_L \otimes U(1)_Y$ symmetry.

Quantum electrodynamics

The mathematical description of the SM starts with the Dirac equation [19]:

$$(i\gamma^\mu \partial_\mu - m)\psi(x) = 0. \tag{2.3}$$

It describes a free fermion field $\psi(x)$ of mass m in a generic coordinate system x. The gamma matrices are denoted by γ^μ, the index μ and all other greek letter indices in this chapter run from 0 to 3. Summation over repeat indices is implied here and in the following. The corresponding Lagrangian is:

$$\mathscr{L}_{\text{Dirac}} = \bar{\psi}(x)(i\gamma^\mu \partial_\mu - m)\psi(x), \tag{2.4}$$

where $\bar{\psi}(x) = \psi^\dagger \gamma^0$. In order to make this Lagrangian invariant under local transformations of the group $U(1)$, it has to be invariant under the transformation:

$$\psi(x) \to \psi'(x) = e^{i\alpha(x)}\psi(x), \tag{2.5}$$

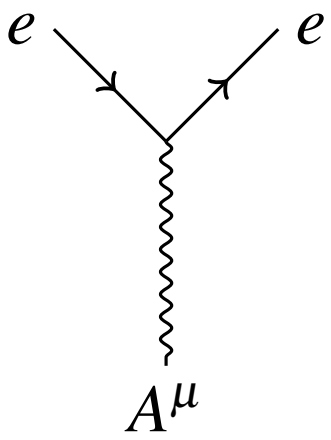

Figure 2.2: The vertex of QED. All Feynman diagrams of the theory can be constructed as combinations of vertices.

where $\alpha(x)$ is a space-time dependent phase. To ensure invariance ∂_μ has to be changed as follows:

$$\partial_\mu \rightarrow D_\mu = \partial_\mu + ieA_\mu(x), \tag{2.6}$$

where e is the electric charge and $A_\mu(x)$ is a bosonic field. Under local phase transformations it transforms as follows:

$$A_\mu(x) \rightarrow A'_\mu(x) = A_\mu(x) - \frac{1}{e}\partial_\mu \alpha(x). \tag{2.7}$$

Any term that is invariant under the local phase transformation can be added to the Lagrangian without hurting the invariance of the original Lagrangian. By adding $-1/4[F_{\mu\nu}F^{\mu\nu}] = -1/4[(\partial_\mu A_\nu(x) - \partial_\nu A_\mu(x))(\partial^\mu A^\nu(x) - \partial^\nu A^\mu(x))]$ to $\mathscr{L}_{\text{Dirac}}$ the following equation is obtained:

$$\begin{aligned}\mathscr{L}_{\text{QED}} &= \bar{\psi}(x)(i\gamma^\mu D_\mu - m)\psi(x) - \frac{1}{4}F_{\mu\nu}F^{\mu\nu} \\ &= \bar{\psi}(x)(i\gamma^\mu \partial_\mu - m)\psi(x) - e\bar{\psi}(x)\gamma^\mu A_\mu(x)\psi(x) - \frac{1}{4}F_{\mu\nu}F^{\mu\nu}.\end{aligned} \tag{2.8}$$

This is the Lagrangian describing QED. Now $\mathscr{L}_{\text{Dirac}}$ is the kinetic term of a free fermion, which can be any fermion that is electromagnetically charged. The kinetic term of a free boson, the photon, is $\frac{1}{4}F_{\mu\nu}F^{\mu\nu}$. The middle term $e\bar{\psi}(x)\gamma^\mu A_\mu(x)\psi(x)$ describes their interaction. Finally, according to Noether's theorem [20] the current $j_\nu = \partial_\mu F^{\mu\nu}/2$ is conserved as a result of the symmetry.

The Lagrangian can be used to derive the Maxwell equations and classical electrodynamics. It can also be used to derive the Feynman rules. They are the basis of drawing Feynman diagrams like the example in Figure 2.2. They also serve to calculate scattering angles, lifetimes and other measurable quantities from first principles. Most importantly they are used to derive cross-sections, which is a measure for the probability of a process to occur.

At the core of the Feynman rules is the vertex, an example of which can be found in Figure 2.2. Depicted is the vertex of QED, which corresponds to the term $e\bar{\psi}(x)\gamma^\mu A_\mu(x)\psi(x)$ in the Lagrangian in Eq. 2.8.

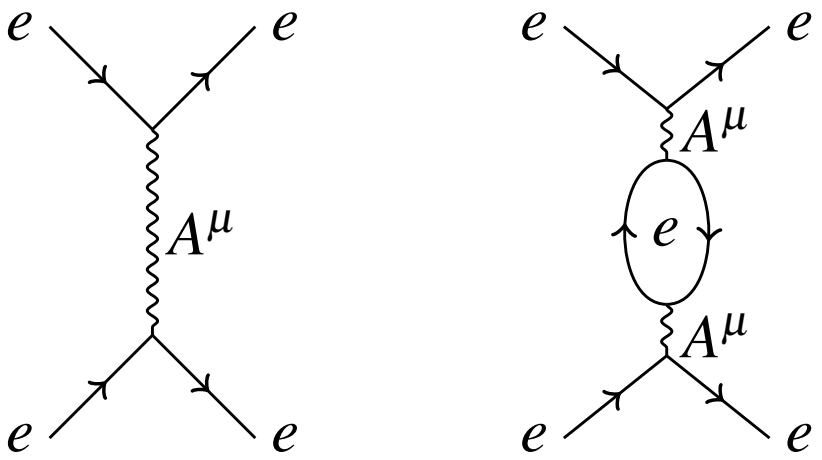

Figure 2.3: Diagrams for electron-electron scattering also called Møller scattering. Left: leading-order diagram. Right: next-to-next-to-leading-order (one loop) diagram.

Combining multiple vertices by connecting the outgoing particle lines can be used for the construction of diagrams of any level of complexity and can describe any process in the theory. The left of Figure 2.3 for example combines two vertices to describes electron–electron scattering and allows the calculation of one contribution to the rate this interaction takes place at. To determine the exact rate all possible diagrams with the same final and initial state have to be considered. Further contributions can be constructed by adding loops like it is done on the right of Figure 2.3 for example. In addition to the so-called one-loop diagrams in Figure 2.3 there are even higher order diagrams with multiple loops. There are also multiple possible diagrams at a given order of loops and the number of possible diagrams increases with the number of loops.

In QED diagrams contribute less and less to the final result with an increasing amount of vertices. For each pair of vertices in the diagram another factor that is proportional to the fine structure constant α_{QED} is multiplied. The fine structure constant is measured as $\alpha_{\text{QED}} = e^2/4\pi \simeq 1/137$ [21], which means that a calculation up to two or three vertices is often sufficient to deliver results of the same precision as experiments. The strength of the QED coupling is given by the coupling constant $g_{\text{QED}} = \sqrt{4\pi\alpha_{\text{QED}}}$. As long as $g_{\text{QED}} < 1$, diagrams with more than a certain number of vertices can be neglected in approximate calculations, which is the case.

Diagrams with a minimal amount of vertices for the considered process are called leading-order (LO) diagrams. With one additional vertex they become next-to-leading-order (NLO). This logic is continued for next-to-next-to-leading-order (NNLO) and so on (N3LO, ...). Conclusions about processes can be drawn perturbatively by considering only the simplest diagrams [22].

Weak interaction

The weak interaction is not too dissimilar from QED, but there are some key differences. Again there are vertices that couple the bosons to fermions as shown in Figure 2.4. However, this time there are three bosons W^1, W^2 and W^3. This leads to multiple different vertices including

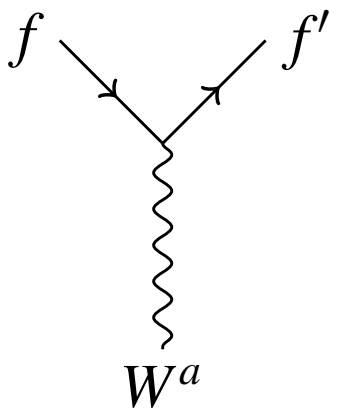

Figure 2.4: Vertex of the weak interaction. W^a boson coupling to the fermions f and f'. The index a can be 1, 2 or 3. Note that f and f' may be different fermions.

couplings between the bosons.

The weak bosons are also massive in contrast to the massless photon. This has an effect on the effective coupling, which is given by the Fermi coupling constant in Eq. 2.9 in the limit where the momentum transfer between particles is small compared to the W boson mass m_W.

$$G_F = \frac{\sqrt{2}}{8}\frac{g^2_{\text{weak}}}{m^2_W}, \tag{2.9}$$

where g_{weak} is the weak coupling constant. The weak fine structure constant is $\alpha_{\text{weak}} = g^2_{\text{weak}}/4\pi = 1/29.5$ [21].

2.1.3 Electroweak unification and symmetry breaking

The EWK symmetry $SU(2)_L \otimes U(1)_Y$ demands the consideration of the fermionic fields separated into left-handed doublets and right-handed singlets as shown by:

$$\begin{aligned} \chi_{i,L} &= \begin{pmatrix} f'_i \\ f_i \end{pmatrix}_L \rightarrow \begin{pmatrix} \nu_e \\ e \end{pmatrix}_L, \begin{pmatrix} \nu_\mu \\ \mu \end{pmatrix}_L, \begin{pmatrix} \nu_\tau \\ \tau \end{pmatrix}_L, \begin{pmatrix} u \\ d \end{pmatrix}_L, \begin{pmatrix} c \\ s \end{pmatrix}_L, \begin{pmatrix} t \\ b \end{pmatrix}_L \\ f_{i,R} &= e_R, \mu_R, \tau_R, u_R, d_R, c_R, s_R, t_R, b_R. \end{aligned} \tag{2.10}$$

Note that there are no right-handed neutrinos [23]. The EWK Lagrangian is then invariant under the symmetry $SU(2)_L \otimes U(1)_Y$ and takes the following form:

$$\mathscr{L}_{\text{EWK}} = \sum_j (\bar{\chi}_{j,L} i D^\mu \gamma_\mu \chi_{j,L} + \bar{f}_{j,R} i D^\mu \gamma_\mu f_{j,R}) - \frac{1}{4} B_{\mu\nu} B^{\mu\nu} - \frac{1}{4} W^a_{\mu\nu} W^{\mu\nu}_a, \tag{2.11}$$

where the last two terms are the kinetic terms for the gauge bosons. The field B^μ is the gauge field of the $U(1)_Y$ symmetry group and the W bosons correspond to the $SU(2)_L$ symmetry. The index a runs from 1 to 3 and summation is implied. Both the covariant derivative D and the

gauge fields are constructed such that the invariance is respected, which leads to:

$$\begin{aligned} W^a_{\mu\nu} &= \partial_\mu W^a_\nu - \partial_\nu W^a_\mu + g_{\mathrm{W}} \varepsilon^{abc} W^b_\mu W^c_\nu \\ B_{\mu\nu} &= \partial_\mu B_\nu - \partial_\nu B_\mu \\ D_\mu &= \partial_\mu - \frac{1}{2} g_{\mathrm{B}} Y B_\mu + \frac{1}{2} g_{\mathrm{W}} \sigma^a W^a_\mu, \end{aligned} \tag{2.12}$$

where g_{B} and g_{W} are the coupling constants of the interactions with the B boson and the W bosons, respectively. At this point these are massless boson fields. The Levi-Civita symbol is ε^{abc} with $\varepsilon^{123} = 1$ and σ^a are the Pauli matrices. The indices $b = 1,2,3$ and $c = 1,2,3$ like a are summed over. The weak hypercharge is denoted by Y.

The bosons in Equation 2.12 cannot be the physical bosons because two weak bosons are measured to be charged. The physicals bosons come into existence through the mixing of the B and W bosons and are the ones that are actually measured in experiments. They are constructed as follows:

$$\begin{aligned} W^\pm_\mu &= \frac{1}{\sqrt{2}} (W^1_\mu \mp W^2_\mu) \\ A_\mu &= \sin\theta_{\mathrm{W}} W^3_\mu + \cos\theta_{\mathrm{W}} B_\mu \\ Z_\mu &= \cos\theta_{\mathrm{W}} W^3_\mu - \sin\theta_{\mathrm{W}} B_\mu, \end{aligned} \tag{2.13}$$

where θ_{W} is the Weinberg angle given by $\sin\theta_{\mathrm{W}} = g_{\mathrm{B}} / \sqrt{g^2_{\mathrm{B}} + g^2_{\mathrm{W}}}$. The mixing of W^3 and B is simply a freedom of the theory and θ_{W} could take any angular value.

In the Lagrangian in Eq. 2.11 there are no mass terms, which are terms of the form $m^2\chi^2$, where χ is some field and m is its mass. However, charged fermions and weak bosons were measured to be massive. This can be rectified by adding a complex scalar field ϕ with the potential $V(\phi)$:

$$\mathscr{L}_{\mathrm{Higgs}} = D_\mu \phi^\dagger D^\mu \phi - V(\phi) = D_\mu \phi^\dagger D^\mu \phi - \mu^2 \phi^\dagger \phi - h(\phi^\dagger \phi)^2, \tag{2.14}$$

where the parameters are chosen to be $\mu^2 < 0$ and $h > 0$ in order to get a non-trivial vacuum expectation value v. Both are free parameters that can only be determined by measurements. The potential has a local maximum at $\phi = 0$ and a ring of degenerate global minima at $e^{i\theta}\sqrt{-\mu^2/2h}$. For the vacuum to be stable the system has to pick a ground state:

$$v = e^{i(\theta=0)} \sqrt{\frac{-\mu^2}{2h}} = \sqrt{\frac{-\mu^2}{2h}}, \tag{2.15}$$

where the phase θ is arbitrarily chosen to be 0. Afterwards the $SU(2)_L \otimes U(1)_Y$ symmetry is broken into a $U(1)_{\mathrm{QED}}$ symmetry, which also leads to the name "spontaneous symmetry breaking". This is illustrated in Figure 2.5.

The spontaneous symmetry breaking introduces another physical boson, the Higgs boson, and in the new form of the Lagrangian the W and Z bosons now have mass terms, leading to the masses given by:

$$\begin{aligned} m_Z \cos\theta_{\mathrm{W}} = m_W &= \frac{1}{2} v g_{\mathrm{W}} \\ m_H &= \sqrt{2h} v, \end{aligned} \tag{2.16}$$

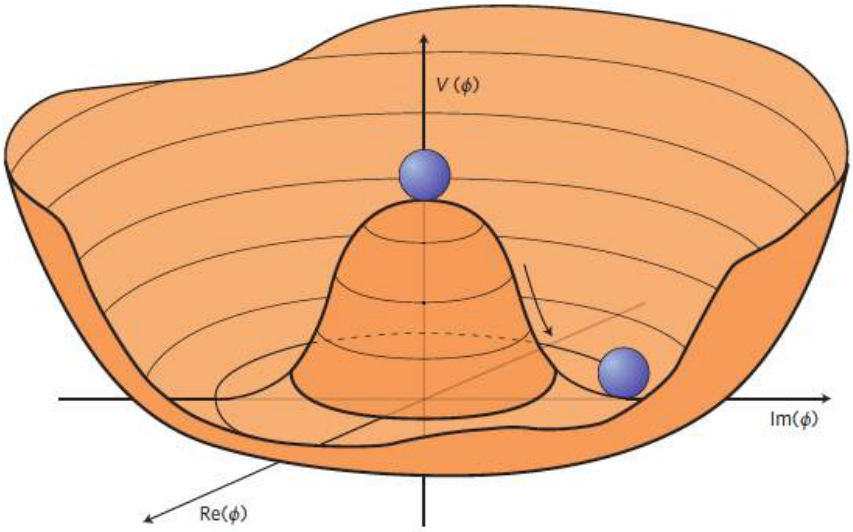

Figure 2.5: The complex quartic Higgs potential or "Mexican hat potential". The ground state is arbitrarily chosen. Therefore the symmetry is broken spontaneously [24].

where m_H is the mass of the Higgs boson. In addition, the fermions acquire mass terms. The process of particles acquiring masses via spontaneous symmetry breaking is also called Brout–Englert–Higgs mechanism. In addition, the complex scalar field $\phi(x)$ can be written as:

$$\phi(x) = \frac{1}{\sqrt{2}} \begin{pmatrix} 0 \\ v + H(x) \end{pmatrix}, \tag{2.17}$$

where $H(x)$ is the physical, scalar Higgs boson field. Again an additional phase is chosen to be vanishing. Without the Brout–Englert–Higgs mechanism a Lagrangian term of the form $\mathscr{L}_m = -m\bar{\psi}\psi$ would break the gauge symmetry. However, after spontaneous symmetry breaking the Lagrangian acquires the term:

$$\mathscr{L}_{\text{Yukawa}} = \frac{1}{\sqrt{2}}(v+H)\sum_i c_i \bar{f}_i f_i = (1+\frac{H}{v})\sum_i m_i \bar{f}_i f_i, \tag{2.18}$$

where f_i are all fermion fields excluding neutrinos and c_i are some arbitrary parameters, which can be measured by determining the fermion masses m_i. From this it also follows that the Higgs boson couples to all massive fermions. Together with the couplings between weak bosons and the Higgs bosons this leads to:

$$\mathscr{L}_{\text{HV}} = m_W^2 W_\mu^\dagger W^\mu \left(1 + \frac{2}{v}H + \frac{H^2}{v^2}\right) + \frac{1}{2} m_Z^2 Z_\mu Z^\mu \left(1 + \frac{2}{v}H + \frac{H^2}{v^2}\right). \tag{2.19}$$

In all cases the Higgs coupling is proportional to the mass or the squared mass of the particle in question. This rule may even extend to particles that are not discovered yet. This part of the SM Lagrangian also determines the kinds of couplings between the Higgs boson and the vector bosons $W^\pm$ and Z. The two types of vertices are shown in Figure 2.6 with V standing for either of the three vector bosons.

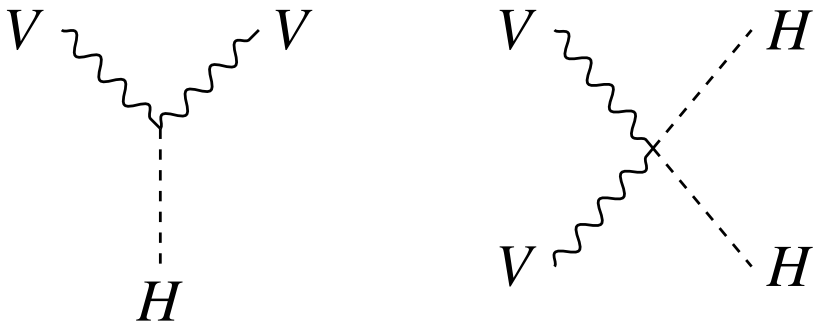

Figure 2.6: Vertices for the interaction between vector (W and Z) bosons and the Higgs boson.

Through measurements of the weak boson masses and couplings the free parameters of the Higgs sector are fixed [21]:

$$\begin{aligned} v &= 246 \text{ GeV} \\ \sin^2(\theta_W) &= 0.2223. \end{aligned} \tag{2.20}$$

2.1.4 Quantum chromodynamics

The final sector of the SM is quantum chromodynamics (QCD). Its $SU(3)_C$ symmetry leads to a Lagrangian of the following form:

$$\begin{aligned} \mathscr{L}_{\text{QCD}} &= -\frac{1}{4} G^{a\mu\nu} G^a_{\mu\nu} + i\bar{\psi}\gamma_\mu D^\mu \psi \\ G^a_{\mu\nu} &= \partial_\mu G^a_\nu - \partial_\nu G^a_\mu - g_S f^{abc} G^b_\mu G^c_\nu \\ D^\mu &= \partial^\mu + i g_S T^a G^{a\mu} \end{aligned} \tag{2.21}$$

Here, G^a_μ are eight massless bosonic fields corresponding to the gluons. The generators of the symmetry group are the Gell-Mann matrices T^a and f_{abc} are the $SU(3)$ structure constants with $T_a T_b - T_b T_a = i f_{abc} T_c$. The symbol g_S is the strong coupling constant, which is measured to be $g_S(m_Z) = 4\pi\sqrt{\alpha_s(m_Z)}$, $\alpha_s(m_Z) = 0.1182(12)$ at the Z boson mass scale [21]. Notably $g_S > 1$.

The Lagrangian contains the terms:

$$\begin{aligned} &-g_S \bar{\psi} T^a \gamma_\mu G^{\mu a} \psi \\ &g_S f_{abc} (\partial^\mu G^{a\nu}) G^b_\mu G^c_\nu \\ &g_S^2 f_{abc} f_{ade} G^{b\mu} G^{c\nu} G^d_\mu G^e_\nu. \end{aligned} \tag{2.22}$$

The first one is the standard vertex of QCD, describing the coupling of a gluon to two colour-charged fermions. Using quarks as the example this is depicted in Figure 2.7. The second two terms describe gluon self-coupling, which is shown in Figure 2.8. The gluons carry colour charges themselves and are massless.

There are three types of colour charges: red, green and blue. Quarks always carry one of these charges, while anti-quarks can have anti-red, anti-green or anti-blue. Gluons carry a colour

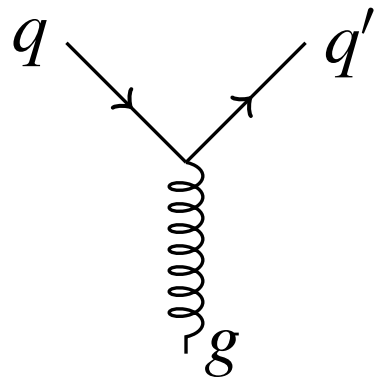

Figure 2.7: Standard QCD vertex describing quark-gluon couplings.

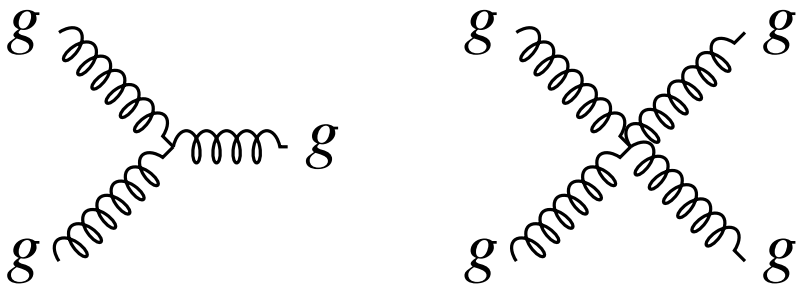

Figure 2.8: Least complex examples of gluon self-coupling with the three- (left) and four-gluon vertex (right).

charge pair like (red,anti-green) for example. No colour-charged particle was ever detected in isolation, which is explained by the phenomenon called confinement.

At large distances the effective potential between two colour charged particles takes the form:

$$V(\mathbf{r}) \propto r. \tag{2.23}$$

Therefore, a larger separation of quarks requires ever larger amounts of energy. It is thus most energetically stable for all colour-charged particles to form colour-neutral bound states [25]. Bound states of colour-charged particles fall under the generic term hadron. Examples include mesons, which are combinations of a quark and an antiquark with opposite colour charge, and baryons, which are three-quark combinations with the quarks having all three colour charges between them.

As result a free colour-charged particle is not a stable state. However, a colour-neutral bound state can be stable. Therefore, free quarks and gluons inexorably form hadrons with other particles. This process is called hadronization. It is a series of QCD interactions that combine the standard QCD vertex in Figure 2.7 and gluon self-couplings in Figure 2.8 until a stable configuration is reached. An example is illustrated in Figure 2.9 in which two quarks are pair-produced, which triggers a series of interactions. In collider experiments this shower of strong interactions is detected as a "collimated spray of hadrons" called a jet. Jets are further discussed in Section 3.3.2.

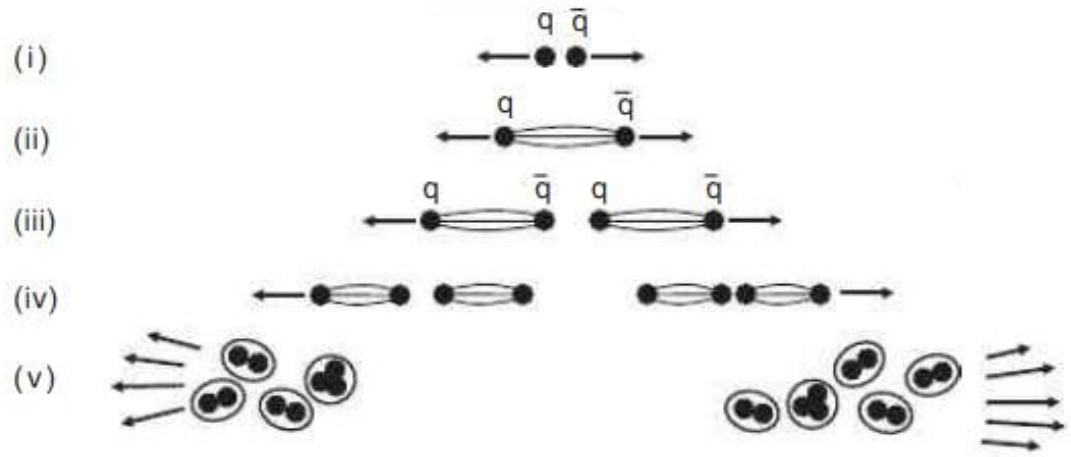

Figure 2.9: Qualitative illustration of hadronization: Two quarks are pair-produced (i). The spacial separation increases, leading to a highly energetic potential (ii). The potential energy is enough to form another quark pair (iii). This process is repeated (iv). The multitude of thus created quarks is bound into colour-neutral bound states (v) [25].

Even after being bound into a hadron the interactions between colour-charged particles do not cease. Calling a meson a two-quark bound state and a baryon a three-quark bound state is only a simplification, which describes the two or three valence quarks. These quarks are bound by gluon interactions that can give rise to low energetic quark-antiquark pairs, which are called sea quarks. Together the valence quarks, sea quarks and gluons are called the partons of the hadron.

2.1.5 Summary of the Standard Model

The SM can be summarized with the Lagrangian in a compact form:

$$\mathscr{L}_{\mathrm{SM}} = -\frac{1}{4}F_{\mu\nu}F^{\mu\nu} + i\bar{\psi}\gamma_\mu D^\mu \psi + |D_\mu \phi|^2 - V(\phi) + (\psi_i Y_{ij} \psi_j \phi + h.c.), \tag{2.24}$$

where $h.c.$ describes the hermitian conjugate and Y_{ij} is a matrix containing the Yukawa coupling strengths. Each of the four terms breaks down as:

$$-\frac{1}{4}F_{\mu\nu}F^{\mu\nu} = -\frac{1}{4}G_{\mu\nu}G^{\mu\nu} - \frac{1}{4}W^a_{\mu\nu}W^{a\mu\nu} - \frac{1}{4}B_{\mu\nu}B^{\mu\nu}. \tag{2.25}$$

These are the kinetic terms of the bosons. After spontaneous symmetry breaking one of the vector bosons $W_{\mu\nu}$ mixes with $B_{\mu\nu}$ to form the photon and the Z boson. The fermion-boson interaction is given by:

$$\begin{aligned} i\bar{\psi}\gamma_\mu D^\mu \psi = \bar{\psi}_{L_i}\gamma_\mu (i\partial^\mu - g_{\mathrm{S}} T G^\mu - g_{\mathrm{W}}\frac{\sigma}{2}M_{\mathrm{CKM}}W^\mu - g_{\mathrm{B}}\frac{Y}{2}B^\mu)\psi_{L_i} \\ + \bar{\psi}_{R_i}\gamma_\mu (i\partial^\mu - g_{\mathrm{S}} T G^\mu - g_{\mathrm{B}}\frac{Y}{2}B^\mu)\psi_{L_i}, \end{aligned} \tag{2.26}$$

where M_{CKM} is the Cabibbo-Kobayashi-Maskawa (CKM) matrix, which describes the flavour-changing weak interaction of quarks [26]. Note that the W^μ bosons do not interact with right-handed particles. The coupling of the Higgs bosons to the vector bosons together with the Higgs potential $V(\phi)$ is described by:

$$|D_\mu \phi|^2 - V(\phi) = |(i\partial_\mu - g_{\mathrm{W}}\frac{\sigma}{2}W_\mu - g_{\mathrm{B}}\frac{Y}{2}B_\mu)\phi|^2 - \mu^2\phi^\dagger\phi - h(\phi^\dagger\phi)^2. \tag{2.27}$$

After spontaneous symmetry breaking this leads to mass terms for the vector bosons and couplings between the Higgs and the vector bosons. The spontaneous symmetry breaking also allows fermion mass terms via the Yukawa coupling:

$$\psi_i Y_{ij} \psi_j \phi + h.c. = \bar{d}_i Y_{ij} d_j \phi + \bar{u}_i Y_{ij} u_j \phi + \bar{e}_i Y_{ij} e_j \phi + h.c., \tag{2.28}$$

where d_j, u_j, e_j are all the down-type quarks, up-type quarks and charged leptons, respectively. This also means that the Higgs boson couples to each fermion and the coupling strength is proportional to its mass.

2.1.6 Relativistic kinematics and particle collisions

The strongest tests of the SM are conducted in high energy physics (HEP) with relativistic collisions. A few definitions are important when discussing this field.

The data used in this work were recorded using proton-proton (pp) collisions. Protons are baryons with a complex substructure, which binds the three valence quarks (up, up and down) with strong interactions. These inner hadron interactions happen at such a low energy scale that they are inaccessible for the perturbative Feynman calculus. Instead the partons are described phenomenologically with parton distribution functions (PDFs). They are the probability distributions of a parton carrying a given momentum fraction of the hadron's total momentum.

They are necessary for the description of hadron-hadron interactions because at high energies the relevant interaction takes place between partons.

Furthermore, the underlying event (UE) is defined. The term refers to all the interactions in the event that are not the primary, hard parton-parton interaction. This includes interactions of the remnants of the colliding hadrons. Many of these interactions are soft and therefore cannot be calculated perturbatively. The simulation of the UE is challenging as a result.

As mentioned above, the behaviour of particles is quite different at higher energy scales. In HEP the scale is expressed via the centre-of-mass energy ($\sqrt{s}$), which is the total energy of the system in the centre-of-mass frame. That is the reference frame in which all particle momenta vectorially add up to zero.

Further, there is a distinction between the initial and final state. The former describes the particles before the collision. Trivially, these are two protons but more informatively the term refers the partons taking part in the interaction. The final state are all particles that are produced as a result of the collision. Derived from that are the terms initial state radiation (ISR) and final state radiation (FSR). They refer to particles (most likely gluons) radiating off other particles before or after the scattering event.

The SM also allows a particle to decay as long as its mass is larger than the combined masses of the decay products. The decay also has to be in accordance with all conservation laws. Thus, the lightest particles that has a conserved quantum number is stable. An example of this is the electron, the lightest particle with an electromagnetic charge of -1. Particles generally decay faster, the more possible final state particles the decay has and the larger the mass difference between the particle and its decay products is.

A final consideration is that processes can only take place if they are kinematically allowed. In other words, they have to respect energy, momentum and angular momentum conservation. That is why high centre-of-mass energies are needed to produce especially massive particles.

There is, however, the possibility to produce a particle "off-shell", which means that it comes into existence as an intermediate state without conforming to classical equations of motion. This heavy particle will decay quickly, producing a final state that is kinematically allowed. Such processes are suppressed.

2.1.7 The Higgs boson in the context of hadron collisions

The following chapters discuss data that were recorded in pp collisions at a centre-of-mass energy of $\sqrt{s} = 13$ TeV. That is enough energy to produce Higgs bosons. The prevalence of their production mechanisms depends on the collision energy. Thus, the production modes and possible decay products are discussed in this specific context here.

Higgs boson production modes

The Higgs boson couples to all[1)] massive SM particles via direct vertices and to all other SM particles via one-loop diagrams. The coupling strengths vary strongly and because of the hadron

[1)] It is currently unknown, whether neutrinos take part in the Yukawa coupling or acquire their masses via another mechanism [27]. The answer to this question is irrelevant to the discussion of Higgs boson production and decay at the LHC, because the coupling would be incredibly small.

collision setup the initial state particles are partons of the colliding protons. As a result only four dominant production modes are considered here:

- Gluon–gluon Fusion (ggF): Via a fermion loop (typically a heavy quark) the gluon pair couples to the Higgs boson as shown on the right of Figure 2.10. Due to the abundance of gluon–gluon interactions, this is the dominant production mode at $\sqrt{s} = 13$ TeV.
- Vector-boson fusion (VBF): The production can happen via W and Z bosons because of their strong couplings with the Higgs boson. The final state of this process contains two quark jets in addition to the Higgs boson decay products. This is illustrated on the left of Figure 2.10. This particular mode is of central importance to Chapter 5.
- Production in association with a vector boson (Higgsstrahlung, VH): As depicted on the right of Figure 2.11 a vector boson radiates a Higgs boson in a process that is similar to bremsstrahlung in QED.
- Production in association with heavy quarks ($b\bar{b}H, t\bar{t}H, tH$): The Higgs boson couples to any quark, but the coupling to top and bottom quarks is the strongest as a result of their large masses. In addition to the diagram on the left of Figure 2.13 there are also modes with only one quark in the final state. The production mode offers the strongest experimental tests of the Yukawa coupling.

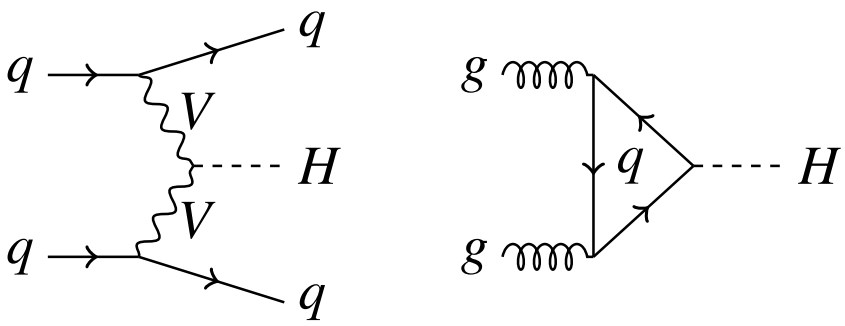

Figure 2.10: Example diagrams of VBF (left) and ggF (right) Higgs boson production.

The cross-sections of various Higgs boson production modes in dependence of the Higgs boson mass and the centre-of-mass energy in pp collisions are depicted in Figure 2.12. Of course it is now known that the Higgs boson mass is $m_H = 125$ GeV [28] and the production cross sections are therefore fixed.

Higgs boson decay modes

The average lifetime of a Higgs boson is only $\tau = 1.56 \times 10^{-22}$ s [29]. As a result the boson can only be detected by its decay products in collider experiments. The probability for a particle to decay into one particular set of decay products is expressed through the branching ratio (BR). Here, it is defined via the example of Higgs boson decays:

$$B(H \to X_j) = \frac{\Gamma(H \to X_j)}{\sum_i \Gamma(H \to X_i)}, \tag{2.29}$$

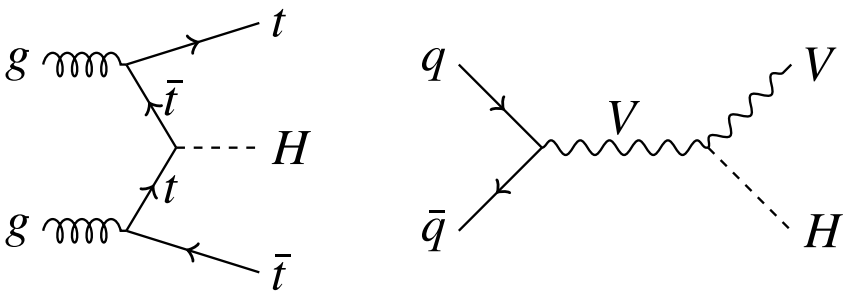

Figure 2.11: Example diagrams of Higgs boson production in association with a top quark pair (left) and a vector boson (right).

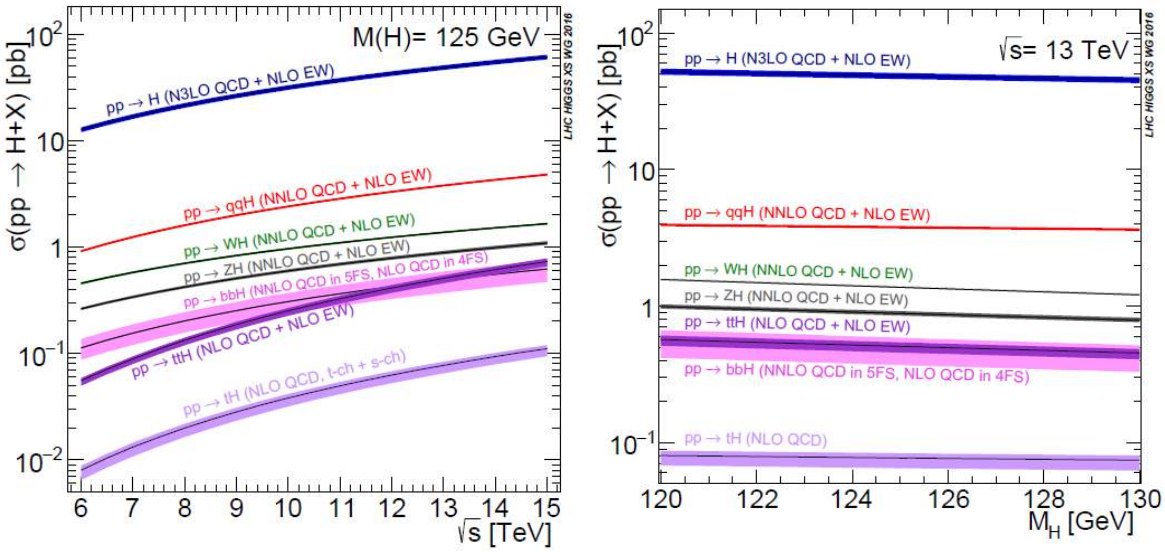

Figure 2.12: The most common Higgs boson production modes in dependence of the centre-of-mass energy (left) and the Higgs boson mass (right). The denomination $pp \to H$ is ggF, $pp \to qqH$ is VBF, $pp \to ZH/WH$ are Higgsstrahlung and $pp \to bbH/ttH/tH$ are production in association with one or two heavy quarks [28].

where X_i is any possible final state of a Higgs boson decay and $B(...)$ is the BR. $\Gamma(...)$ is the decay width. The total decay width is the inverse of the lifetime. For the reconstruction of the Higgs boson it is important to discuss the most likely decay modes:

- $H \to b\bar{b}$: As expected from the strong coupling with the heavy quark, this is a dominant decay mode. The even heavier top is excluded as a decay product because particles can only decay into lighter ones due to energy conservation.
- $H \to VV$: A vector boson pair is heavier than the Higgs, but the decay is possible with an off-shell vector boson. The decay products can be identified with their parent vector boson via their invariant mass.
- $H \to gg$: This is simply the reverse of the ggF production mode. It is shown in Figure 2.13. The process is indistinguishable from many QCD processes that produce gluons.
- $H \to \gamma\gamma$ and $H \to ZZ^* \to 4l$: Again, the Z^* is an off-shell boson. These two decay channels are worth mentioning because the final state is relatively easy to reconstruct. The processes were crucial in the discovery of the Higgs boson despite their low BRs.
- $H \to$ BSM: The Higgs boson couples to most massive SM particles. Should any undiscovered particle also be massive, there is a good possibility for a Yukawa-like coupling to the Higgs boson, making it a possible decay product. The known decay channels can impose a constraint on this possibility because all BRs have to add up to 1 as is apparent from Eq. 2.29.

Some of the dominant decay channels are shown in Figure 2.13.

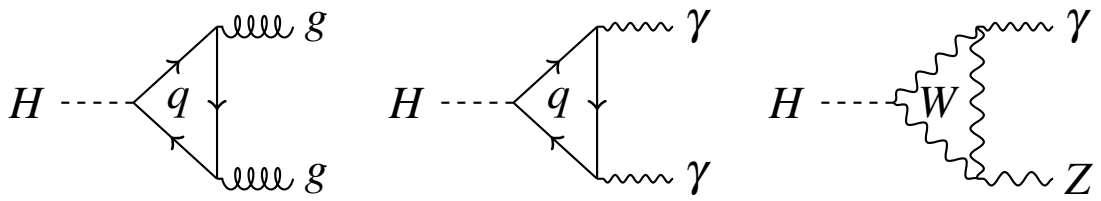

Figure 2.13: Example diagrams of Higgs boson decays into two gluons (left), two photons (middle) as well as a Z boson and a photon (right).

The predicted BRs of the dominant Higgs boson decay products are shown in Figure 2.14 as a function of the Higgs boson mass. Measuring these values is an important test to find out whether the scalar particle that was discovered in 2012 [2] is actually the Higgs boson as predicted by the SM.

2.1.8 Questions left open by the standard model

The predictions of the SM have come true in countless experiments. After the discovery of the Higgs boson [2, 3] one of the last sectors of the SM Lagrangian was confirmed and also

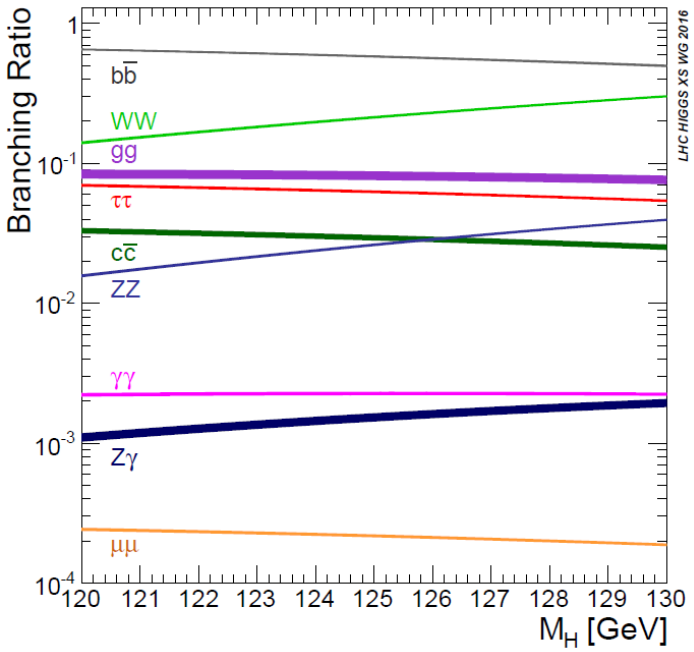

Figure 2.14: BRs of the dominant Higgs boson decay modes in dependence of the Higgs boson mass [28].

the Higgs couplings to the heaviest fermions are being verified one by one [30]. Still, there are open questions that cannot be answered by the SM and some of them are presented in this section. However, there are already multiple beyond the Standard Model (BSM) models that offer potential explanations for phenomena without one. It is the task of current and future experiments to test their predictions.

Neutrinos

Neutrinos do not take part in the Yukawa couplings in the same way the other fermions do [31]. However, they can oscillate, meaning that they switch between different flavours. This necessitates that the neutrinos do not have the same masses, from which it can be concluded that at least two of the three have a non-vanishing mass. Furthermore, neutrino oscillation is not a SM process. Either way new theories are needed to explain, what makes neutrinos so different from other SM particles [32].

Grand unification

The weak and electromagnetic interaction were found to be part of the more fundamental EWK interaction. This manifests at an energy scale that is significantly above m_W. Also the coupling constants of the three SM interactions are dependent on the energy scale as illustrated in Figure 2.15. With some modification to the model they might even coincide at very high energies. It is not a huge leap to think of an even more fundamental symmetry that is the basis of the low energy limit that is called the Standard Model. Such a model is called a grand unified theory (GUT) [33].

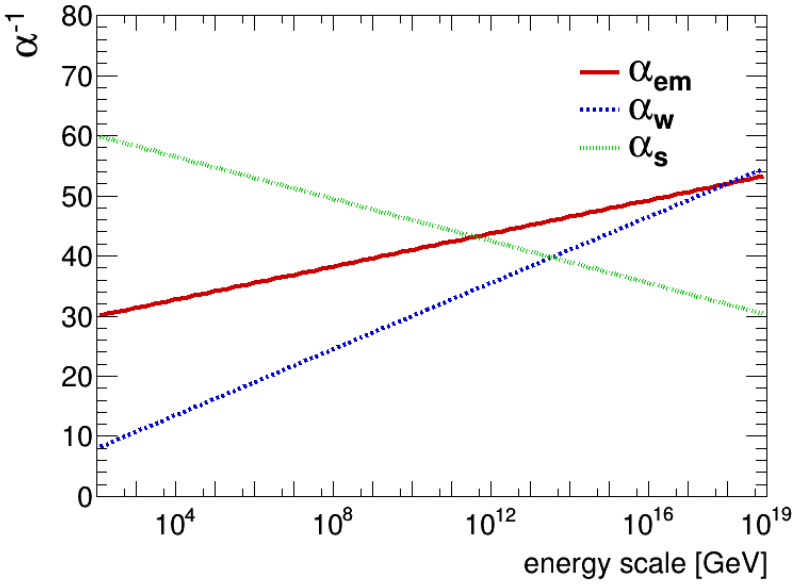

Figure 2.15: Energy dependent behaviour of the SM coupling constants. They each converge pairwise, but with some underlying fundamental symmetry they might all coincide at the GUT scale.

Gravity

With general relativity (GR) there is a working theory of gravity. There is, however, no quantum theory of gravity and therefore the SM and GR are completely independent of each other. The thought of a fundamental theory incorporating gravity as a fourth interaction is compelling. It is even possible that there is an even grander unification, a theory of everything, which potentially manifests at the Planck scale (10^{19} GeV).

Naturalness

Naturalness is often demanded of a theory. It is the requirement that the parameters of a theory do not differ by orders of magnitude, meaning that their ratios are of order one. This is not given when comparing the weak scale (100 GeV) of the Higgs boson and vector boson masses to the Planck scale (10^{19}) of gravity. This is also called the hierarchy problem.

Furthermore, the Higgs boson mass itself is subject to loop corrections like the one in Figure 2.16. Notably, the corrections from fermion and boson loops have different signs. These corrections can be large and differ greatly given the huge mass scale differences of SM particles and especially when considering the potential coupling to yet undiscovered particles. Despite this the Higgs boson mass "works out" to be on the order of the weak scale [34].

Matter-antimatter asymmetry

To each particle in the SM there is a corresponding anti-particle, which differs only by the sign of the electromagnetic charge and charge-like quantum numbers. Exceptions are particles like the photon, Z and Higgs boson, which are their own anti-particles. Thus, for each process

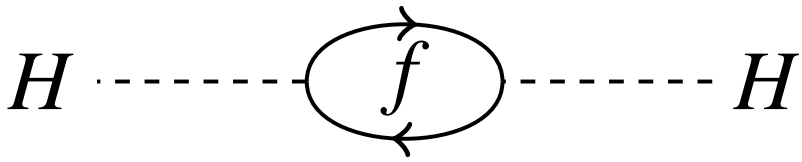

Figure 2.16: Loop correction to the Higgs boson mass resulting from the coupling with a fermion.

involving particles there is a mirrored process involving anti-particles. Assuming a symmetry between matter and antimatter (CP symmetry), both processes necessarily happen at the same rate. Therefore, any process that would have produced matter in the early universe would have necessarily produced antimatter of the same amount. Any conversion from matter to antimatter would be reverted equally in the thermal equilibrium of the early universe.

However, astrophysical observations show that there is way more matter than antimatter in the unviverse today and the CP symmetry must be broken somehow [35]. Indeed experiments with K mesons show such a CP violation, which is caused by a phase in the CKM matrix [36]. This, however, does not account for the matter abundance observed and a BSM process is needed to explain the rest [33].

Connected to this is the strong CP problem. Despite the fact that CP violating terms can be added to the QCD sector of the SM Lagrangian without violating the invariance under any of the SM symmetry groups, no CP violation has been observed in the context of strong interactions [37]. There might be a BSM mechanism that preserves the CP symmetry specifically in the QCD sector.

To solve the strong CP problem Peccei and Quinn proposed a so-called Θ-term as an extension of the QCD Lagrangian [38]. This gives rise to a new field that dynamically breaks the CP symmetry. The field can be quantized into a particle, the axion.

Energy content of the universe

Astrophysical observations are consistent with an accelerated expansion of the universe [39], which hints at a new type of unknown energy, dark energy, that causes this acceleration. Furthermore, there is evidence for an as of yet undetectable type of matter, which was named dark matter. In fact the SM seems to only account for $4.860 \pm 0.073\%$ of the energy content of the universe [40].

Dark matter is discussed in more detail in the next section.

2.2 Dark matter

The phenomenon of DM is essential for understanding the universe. Discoveries that grant greater insight into its nature might just be around the corner. In the following the topic is presented from the first proposal over necessary DM properties to current experiments that hope to make a DM discovery.

The discussion starts in Section 2.2.1 where astrophysical phenomena hinting at DM are presented. In Section 2.2.2 particle candidates that could constitute dark matter are discussed.

The genesis of DM in the early universe and how it informs the search for DM today is the topic of Section 2.2.3. Section 2.2.4 compares the three different DM search approaches: direct detection, indirect detection and collider experiments. A selection of BSM models and how they may incorporate particle DM are discussed in Section 2.2.5. In Section 2.2.6 a few alternative theories that try to explain some of the aforementioned phenomena without predicting particle DM are mentioned.

2.2.1 Evidence for the existence of dark matter

The search for DM looks back at a 85-year-long history of accumulating observations that support a particle dark matter hypothesis. It began with Zwicky determining the velocities of eight galaxies within the Coma Cluster and using the virial theorem to calculate its mass [41]. Later that method was extended to more clusters with a higher number of galaxies [42]. The virial theorem follows from Newton's theory of gravity and can be expressed as the relation between the average kinetic energy $< T >$ and the average potential energy $< U >$ of a system in equilibrium such as the Coma Cluster [43]:

$$< T >= \frac{1}{2} < U > . \tag{2.30}$$

From that Zwicky determined the total mass M of the cluster as:

$$M = \frac{3R}{G} < v_{||}^2 >, \tag{2.31}$$

where R is the radius of the cluster, G is the gravitational constant and $< v_{||} >$ is the average velocity of the galaxies in the cluster parallel to the line of sight as determined by the redshift. Zwicky concluded that the total mass of the system was 400 times larger than it appeared from the sum of visible objects in the cluster.

In 1970 Rubin et al. measured the rotation speed of objects inside galaxies as a function of their distance to the galactic core also using their redshift [44]. The distribution of the velocity depending on the radius from the galaxy centre is referred to as a rotation curve with an example shown in Figure 2.17. Here, the observed velocity (V_c) is rising steadily contrary to the prediction resulting from observable matter. A possible explanation of this discrepancy is the existence of a large amount of unobservable "dark" matter that even extends into the galactic halo.

From GR it is established that clusters of galaxies or other massive objects can bend space-time and thus the light travelling through it, which leads to a lensing effect. The magnitude of this effect is a measure of the mass of such an object. Taylor et al. for example used this to determine the mass of the galaxy cluster Abell 1689 [9] and found a good agreement with mass measurements using an approach similar to Zwicky above. This is a remarkable result, since two entirely different methods were used to measure the same quantity.

The Planck mission [8] was able to measure the cosmic microwave background (CMB) and its miniscule anisotropies with great precision. The CMB is electromagnetic radiation that came into existence about 380.000 years after the Big Bang at the time of recombination, when the universe became cool enough for electrons and protons to form neutral hydrogen, allowing electromagnetic radiation to travel the cosmos freely (see also Ref. [46] for more details). The

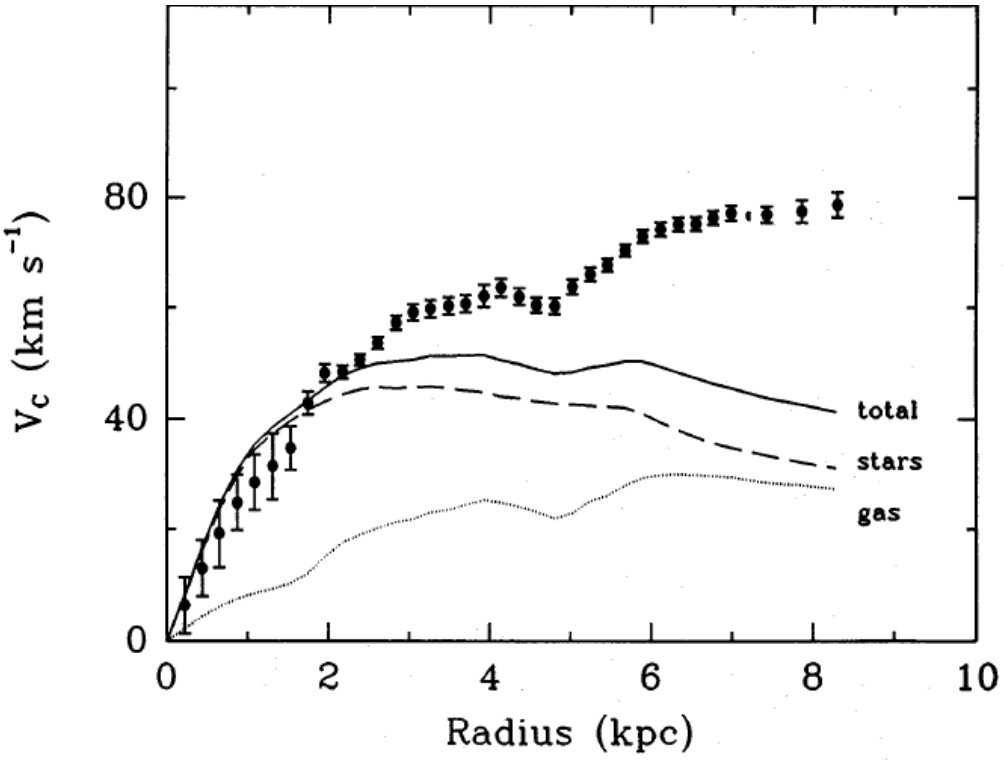

Figure 2.17: Observed rotation curve of the galaxy NGC 1560 (dots). Predicted rotation curves of the gas (dotted line), stars (dashed line) and total observable matter (solid line) within the galaxy. First measured by Rubin et al. [45].

radiation has since cooled down to 2.7 K and is a measure of the content of the early universe and via extrapolation the current one.

The data collected with the Planck mission are interpreted using the Lambda cold dark matter (ΛCDM) model, which describes the evolution of the cosmos assuming the existence of dark matter among other properties [8]. The model predicts the shape of the power spectrum of the CMB with the fraction of DM as one of the free parameters. The power spectrum as measured by the Planck mission is depicted in Figure 2.18 together with a fit based on the ΛCDM model. From the fit parameters the DM fraction of the energy content of the observable universe was calculated to be $25.89 \pm 0.41\%$ [40]. According to the same experiment visible matter accounts for $4.860 \pm 0.073\%$ of the energy content of the universe with the remaining $69.11 \pm 0.62\%$ being dark energy [40]. This is another observation studying a phenomenon completely separate from galaxy rotation curves, gravitational lensing and galaxy cluster dynamics that supports the DM hypothesis.

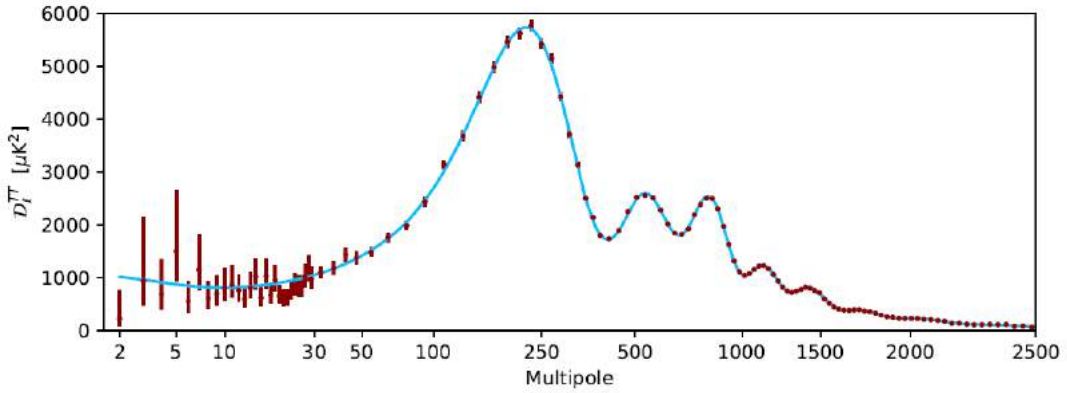

Figure 2.18: Angular power spectrum of the temperature anisotropies of the CMB. The quantity D_l^{TT} is the logarithmic interval of multipoles from the dipole (Multipole 2) to higher orders. The data collected with the Planck mission (red dots) are fitted with the ΛCDM model (solid blue line) [8].

Cold, warm and hot dark matter

Dark Matter is characterized into cold, warm and hot. The designations correspond to the velocity and thus the weight of the candidate particles. Cold dark matter (CDM) is the slowest and consists of the most massive particles. All of these CDM candidates are at least as heavy as $\mathcal{O}(100)$ GeV. Hot dark matter on the other hand describes very light particles with neutrinos being the most well-known candidates with masses below 1 eV. At the intermediate scale of keV to GeV warm dark matter is situated.

The distinction is meaningful because CDM with its low velocities causes tighter clustering, which affects astronomical observations. This is especially important for the formation of galaxies in the early universe. The ΛCDM-model, which is used to explain the anisotropies of the CMB spectrum in experiments like the Planck mission [8], assumes that DM is primarily cold. Since the model describes the observation very well, CDM is currently favoured to be the largest contributor to the DM content of the universe.

2.2.2 Dark matter candidates

As the nature of DM is still an open question, there are a multitude of theoretical predictions about how this new form of matter would behave. There are possibly multiple forms of DM that sum up to the measured DM density.

Looking at the SM first, the only particles that interact so weakly with other matter to appear dark to current methods of detection are neutrinos. However, the study of CMB anisotropies suggests that neutrinos can only account for a small part of the DM abundance [47]. Their close relatives sterile neutrinos result from a small modification to the SM that allows right-handed neutrinos. That is not a huge leap to make, since all other fermions show both kinds of chirality. The range of possible sterile neutrino masses is a staggering 15 orders of magnitude from eV to EeV. Should the mass turn out to be in the keV range, sterile neutrinos are suitable DM candidates [48].

Another possible contribution to the DM spectrum are massive compact halo objects (MACHOs), which can be black holes, planets, white dwarves and other celestial objects with negligible luminosity. The abundance of MACHOs was studied by looking for microlensing effects, which yielded only a few MACHO candidates [49]. Therefore, baryonic DM can only be a small contribution to the DM in the universe and does not account for the observed DM density [50].

Weakly interacting massive particles (WIMPs) are among the most promising candidates for DM. The term describes many different new particles that are predicted by BSM models [50]. The requirements for a BSM particle to be a WIMP are that its mass is around the weak scale (100 GeV) or larger, it interacts with SM particles with a strength similar to the weak interaction and it was produced with a great abundance shortly after the Big Bang. Due to their high mass WIMPs constitute CDM.

From cosmological considerations the WIMP mass can be estimated to yield a WIMP abundance consistent with the observed DM density. Coincidentally, this predicts a WIMP mass of the order of the weak boson masses and an annihilation cross-section similar to a typical electroweak cross-section [51]. This coincidence is often referred to as the WIMP miracle.

The axion mentioned in Section 2.1.8 is another compelling dark matter candidate, because its existence would offer an explanation for two BSM phenomena at the same time. Whether the particle is suitable as an explanation for the DM phenomenon, depends on its mass being sufficiently small [38].

In the following sections only WIMPs are discussed because they are the most important DM candidates for the studies in the chapters below.

2.2.3 Dark matter in the early universe

The abundance of DM in the universe today can serve as a clue for its nature and its interactions. Assuming there are interaction mechanisms between SM and DM particles, they would have been a frequent occurrence in the hot, early universe. In the time shortly after the Big Bang the universe was hot enough and by extension particles were energetic enough to pair-produce heavier particles like WIMPs. Conversely heavier particles can also decay or produce lighter SM particles in annihilation processes. If both types of particles — SM and WIMP — exist in a large enough density, these reactions constantly occurs back and forth. For the reaction rate Γ it follows:

$$\Gamma = n\sigma v, \tag{2.32}$$

where n is the number density of the particles, σ is the cross-section of the interaction and v is the relative velocity of the interacting particles [50]. The state in which the two states of matter can produce each other back and forth is called thermal equilibrium. However, the universe is also expanding, which decreases the number density and thus the interaction rate. At the same time the universe is cooling down, making the production of ever more massive particles impossible. At some point the thermal equilibrium ended in an event that is called the freeze-out.

At freeze-out both pair-production and annihilation do not occur, which means that the co-moving density of WIMPs remains constant from that point forward. This process is illustrated in Figure 2.19. The graph depicts a measure of the abundance of particles over time as determined via the Boltzmann equation [50]. The figure shows that at some point the abundance of WIMPs breaks off from the thermal equilibrium and remains constant at the so-called relic density. Furthermore, the value of the relic density decreases with an increasing annihilation cross-section times relative velocity $< \sigma v >$. In other words, the less likely it is for a particle to annihilate the more of it is left long term.

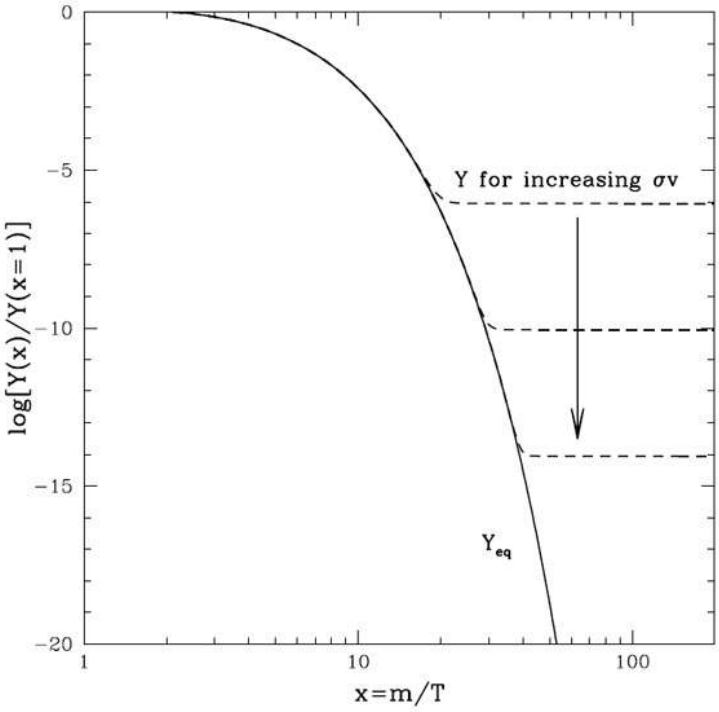

Figure 2.19: WIMP abundance as a function of time in the early universe. The quantity $Y(x)/Y(x=1)$ is proportional to the WIMP abundance, where $Y(x) = n/s$, n is the WIMP density and s is the entropy density. The variable x is defined as $x = m/T$ with m being the WIMP mass and T being the temperature [50].

This conclusion informs future searches for WIMPs. From the astrophysical observations above there is a good understanding of the abundance of WIMPs today. That puts a constraint on the cross-sections and therefore the parameters of any model that is tested with a WIMP search.

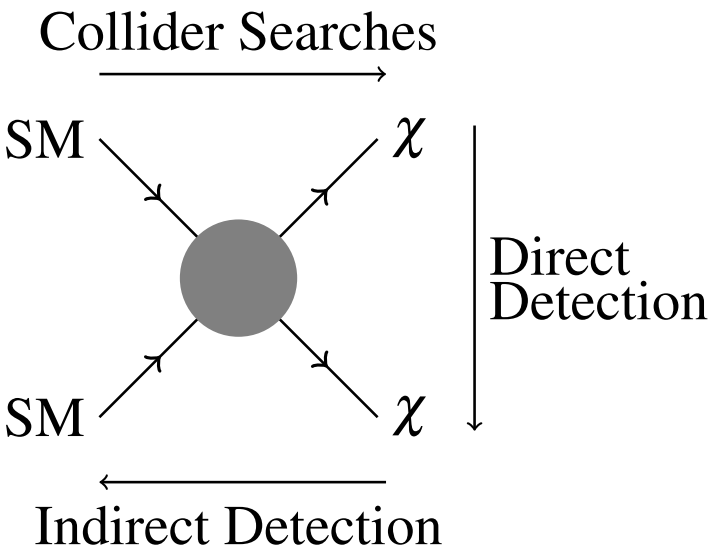

Figure 2.20: Illustration of the three basic methods of DM searches: direct detection, indirection detection and collider experiments. The particle χ is a DM candidate. No assumption is made about the nature of the interaction at this stage.

2.2.4 Dark matter searches

The experimental searches for DM can be divided into three categories, which are illustrated in Figure 2.20. There are collider searches [52], which try to produce DM particles by colliding SM particles. One such analysis is presented in Chapter 5. Direct detection experiments attempt to measure the recoil of DM particles against SM particles that are part of the detector medium [53]. Finally, indirect detection is based on DM particles from cosmic sources producing SM particles that can then be detected [47, 54].

In general, the challenge is that DM itself cannot be detected and couplings to the SM need to be exploited. Even direct detection methods measure recoiling SM particles.

Collider searches

Potential couplings between DM and SM particles are necessarily small. This leads to two problems: the produced DM particles are not expected to interact with the detector material and are therefore invisible. Also the DM production is expected to have a low rate. The first problem is circumvented by demanding additional SM particles in the final state. The event topology of the SM particles can be evidence for the presence of DM in this case. The second problem can be addressed with high collision rates. If enough events are recorded, a statistically significant amount of DM events could be among them. The DM particles could also be very massive, which means that large energies are needed to produce them. Both high collision rates and high energies are in effect at the LHC, which housed several DM searches already [55, 56, 57]. Because of the WIMP miracle, there is a good argument for a discovery at current colliders being in the near future.

Because there are many competing BSM models featuring DM as is discussed in Sec-

tion 2.2.5, these searches are kept as general as possible. Often an analysis is looking for a SM particle or its decay products in the final state together with missing transverse energy ($E_{\mathrm{T}}^{\mathrm{miss}}$). Large $E_{\mathrm{T}}^{\mathrm{miss}}$ is the expected signature of invisible particles because momentum balance leads to all final state particle momenta adding up to 0 in the plane transverse to the beam axis. The event property $E_{\mathrm{T}}^{\mathrm{miss}}$ is therefore the negative vectorial sum of all visible particle momenta. If such a signature appears in excess of the SM backgrounds, this can be seen as evidence for new physics.

Typically, the results of a search are interpreted in the context of a so-called simplified model. In that case only the free parameters relevant for an interaction are considered for the interpretation. Other features of a non-simplified BSM are ignored. Parameters that are constrained by such an analysis can for example be the WIMP mass or the cross-section for the DM candidate to interact with an SM particle. The constraints can then be used to make statements about non-simplified models that share these parameters.

An example of this is to search for DM as a mediator. As shown in Figure 2.21 this would entail SM particles both in the initial and in the final state. However, the existence of the BSM mediator changes the invariant mass spectrum of the final state particles and creates a resonance. The approach is applicable even if the BSM particle is too heavy to be produced. There have been several searches for mediator DM already. Some of their results are summarized in Ref. [55].

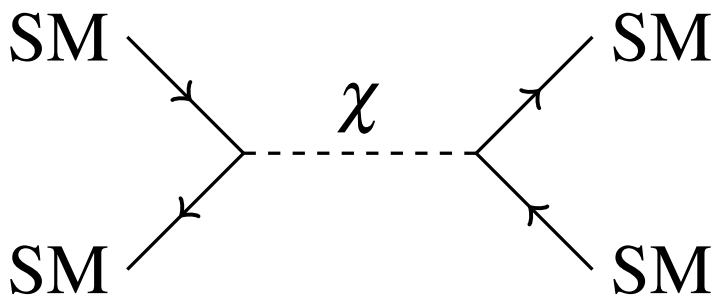

Figure 2.21: Example diagram with a DM candidate χ as a mediator for the scattering of SM particles.

Direct detection

In the case of direct detection the DM particles are actually supposed to interact with the detector medium. The underlying interaction is the scattering of the DM particle against an atomic nucleus. Because DM has no electromagnetic charge, there would be no noticeable interaction with the electrons of the atom in the case of DM particles that are on the mass scale of the nucleus and therefore way more massive than the electrons. By measuring the recoil energy of the atomic nucleus the mass of the DM candidate can be inferred.

A typical experimental setup contains a large detector medium with examples including high purity germanium crystals or liquid xenon. The large detector size is a consequence of the expected low rate of interactions and the active media are chosen to ensure a large interaction

cross section by using large atomic nuclei. Examples for such experiments are XENON1T [58], which uses a 1.3 t xenon medium, and CDEX-10 [59], a germanium detector.

The recoil energy is mostly transferred into heat. A small part of the recoil energy causes the excitation of the atom, which then causes an electron or photon signal depending on the active medium. The often faint signal on the order of keV is then either detected with photomultipliers or by measuring temperature and charge of the medium [53]. Because the signal is so small and interactions between DM and SM particles are expected to be rare, background is a large problem. Examples for background sources are cosmic muons and radioactive isotopes in the vicinity of the detector. This is mitigated by building detectors underground and shielding them with special materials.

The main challenges lie in detecting low DM masses and interactions with small cross-sections. The latter can be addressed by using even larger detectors, at which point the cost of such an experiment becomes a limiting factor. DM candidates with low masses cause smaller recoils. To still be sensitive in that realm new techniques are needed.

The DM halo of the galaxy is expected to not rotate with it, which causes the solar system to have a velocity relative to the halo. Due to the rotation around the sun the earth periodically moves against and with the movement of the solar system. In high-rate experiments this leads to an annual modulation of the DM signal. This is exploited for the signal prediction in direct detection experiments.

Past experiments impose constraints on a potential discovery of DM particles. A selection of exclusion limits from direct detection experiments are shown in Figure 2.22.

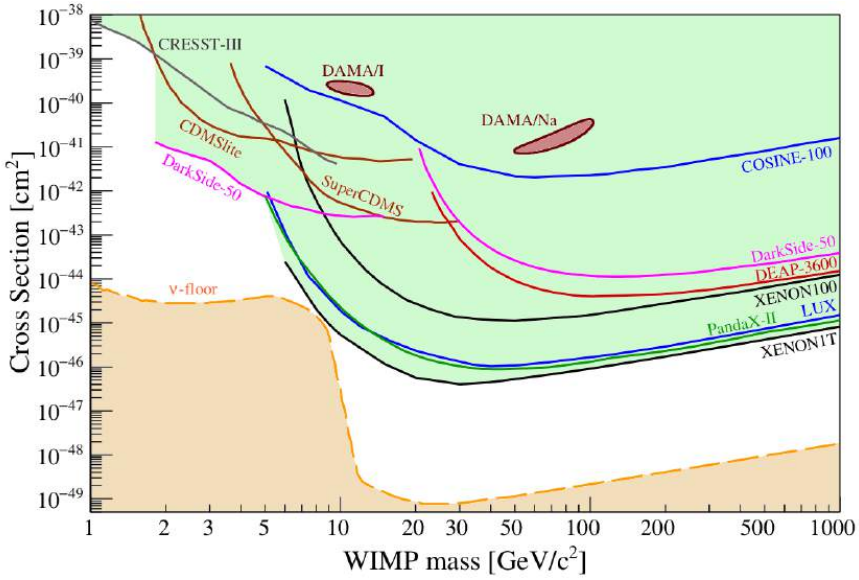

Figure 2.22: Spin-independent DM 90% exclusion limits imposed by a selection of direct detection experiments. The neutrino floor (ν-floor) is a result of the irreducible background from neutrino-nucleus scattering [53].

The so-called neutrino floor is limiting the direct detection of DM particles. The scattering of highly energetic solar neutrinos against atomic nuclei is an irreducible background. Therefore, the region of the WIMP-mass-cross-section phase space functions as a WIMP discovery limit [53].

Indirect detection

Indirect detection methods aim to reconstruct SM particles that were produced in DM pair annihilation. In some cases the SM particles that are measured by the experiment are not the ones produced in DM annihilation but were produced in additional SM interactions after the annihilation process. The searches are directed at regions where the DM density is expected to be especially high. This is in areas with a high gravitational pull like the core of the milky way galaxy or the centre of the sun. The DM particles also have to be slow enough to allow for annihilation processes, which is given in the same regions.

There is a large variety of measurements in different energy ranges and considering different SM particles. The most important prerequisite on the SM final state particle is its stability [54]. There are for example gamma ray telescopes like MAGIC [60] and H.E.S.S. [61]. In addition, neutrino experiments like IceCube [62] are sensitive to DM annihilation as well. The aforementioned Planck mission [8] to observe the CMB is an example of DM detection in the microwave spectrum.

Results from indirect detection neutrino experiments are shown in Figure 2.23. For indirect detection the limits are given in terms of the DM annihilation cross-section σ times the relative velocity of DM particles v_{rel}. This quantity is proportional to the number of annihilations in a given volume.

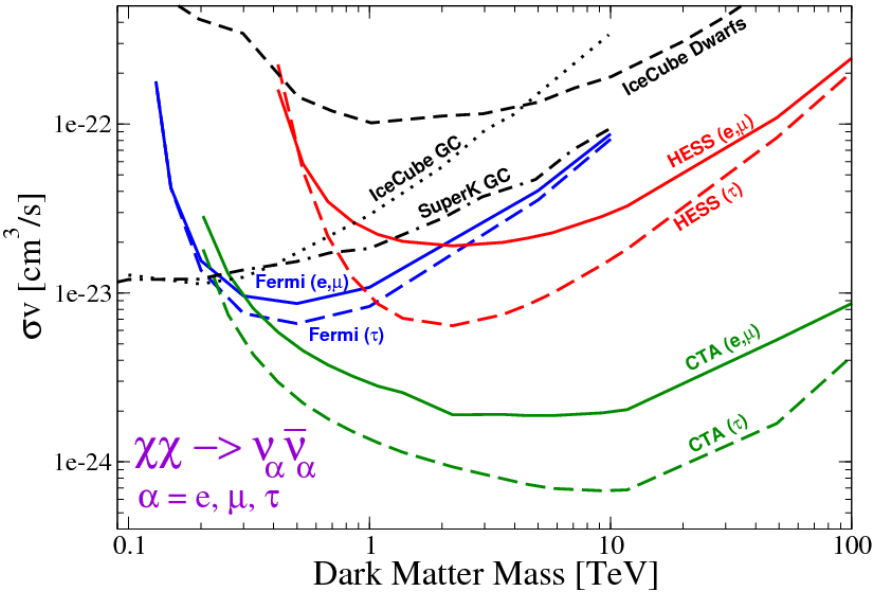

Figure 2.23: DM 90% exclusion limits imposed by a selection of indirect detection neutrino experiments. The dark matter mass is a WIMP mass and $< \sigma v_{\text{rel}} >$ is DM annihilation cross-section times the relative velocity of DM particles [63].

2.2.5 BSM models in the context of dark matter

To address the shortcomings of the SM many BSM models have emerged. A multitude of them predicts particles with the necessary properties to be a DM candidate. Discussing all models

that predict particle DM is beyond the scope of this work. However, some of the most promising ones are presented here.

Higgs portal models

As shown in Section 2.1.3 the Higgs boson couples to most massive SM particles. This rule could be universal enough to extend to physics beyond the SM. If there is some hidden sector containing massive particles from a new model, the Higgs boson might be the only particle to couple to them. This scenario is the motivation for Higgs portal models. The fact that other SM particles do not couple to the new sector is the explanation for its hidden nature. However, the Higgs boson interactions still make it experimentally accessible.

A Higgs portal can be introduced by modifying the SM Lagrangian, given in Eq. 2.24, by:

$$\mathscr{L} = \mathscr{L}_{\mathrm{SM}} - \frac{1}{2}\partial_\mu \chi \partial^\mu \chi - \frac{1}{2} m_\chi^2 \chi^2 - c_\chi |\phi(x)|^2 \chi^2, \tag{2.33}$$

where χ is a field in the hidden sector, m_χ is its mass, c_χ the coupling constant to the hidden sector and $\phi(x)$ is the SM Higgs doublet as introduced in Eq. 2.17 [64]. This is just one possibility under the assumption that the DM candidate is a Majorana fermion. The other possibilities are a scalar or vector nature of the particle, which changes the Lagrangian [65].

The DM candidates in this model come from the lightest particles in the hidden sector. Because they do not couple to the SM sector, they cannot decay into lighter SM particles and are stable. For the same reason they are invisible. These particles might also be massive and thus be WIMPs. Such a model is very predictive because the Higgs boson-dark sector coupling c_χ is fixed for a given WIMP mass m_χ if it is supposed to account for the entire DM abundance [64].

One specific scenario predicts the existence of a second particle that is similar to the Higgs boson. Both of these Higgs boson fields mix with some mixing angle ξ. This leads to a suppression of the SM couplings to H_1 by a factor of $\cos(\xi)$ and a suppression of the H_2 couplings by $\sin(\xi)$. Therefore, only one of the Higgs bosons is identified with the SM Higgs boson discovered in 2012. Its couplings to SM particles receives a small correction, which can be measured. The other Higgs boson presumably has a higher mass, which might explain, why it was not discovered yet together with its small couplings to SM particles [11]. The hidden sector could in principle contain many particles, but for the interpretation of searches it is generally sufficient to only assume one for the sake of simplicity.

The concept of Higgs portal models can be generalized to some undiscovered scalar field as the only link between a hidden sector and the SM. This heavy scalar mediator can be a heavy Higgs boson, but it does not have to be. Therefore, experiments interpreted in the light of a Higgs portal model always have the option to probe other mediator masses.

Supersymmetry

In contrast to the Higgs portal models, which are simplified, Supersymmetry (SUSY) is a complex model that addresses many of the shortcomings of the SM. The prediction of DM candidates is just one of its features. The fact that it addresses many open questions is one of the reasons for its popularity. However, with the complexity come many free parameters that hurt the falsifiability of the model.

At the core of the SUSY model is the addition of a spacetime symmetry, supersymmetry, to the SM Lagrangian. The symmetry relates fermions to bosons with a transformation that changes the spin of a particle. This has the effect of more than doubling the amount of existing elementary particles by adding a fermionic partner for every boson and a bosonic partner for every fermion. They are commonly known as superpartners. As per the common convention the names of the partners of fermions are constructed by adding an "s" (selectron, squark, ...) and the partners of bosons end on "ino" (photino, higgsino, ...). These additional particles are a convenient solution to the hierarchy problem discussed in Section 2.1.8 because fermions and bosons can exactly cancel out the loop corrections to the Higgs boson mass.

However, this also introduces a problem. Superpartners are supposed to be exact duplicates except for the spin of the particle. This includes mirrored masses and quantum numbers. Such particles would have been discovered already. Many of them have an electromagnetic charge or a colour charge, making them very easy to detect. The problem is circumvented by introducing a symmetry breaking mechanism that causes the superpartners to exist at a higher mass scale.

There are multiple ways to construct a model with a supersymmetry of the kind described above. To ensure the predictive strength of the model some assumptions need to be made. Choosing this to be the smallest extension of the SM leads to the minimal supersymmetric Standard Model (MSSM). It predicts an extended Higgs sector, containing two Higgs doublets with an electromagnetically charged and neutral Higgs boson each. The superpartners of the neutral bosons (B, neutral W and both neutral Higgs bosons) can mix, forming four neutralinos. Similarly the superpartners of the charged bosons mix into four charginos, two each with positive and negative charge.

The MSSM further introduces a new conserved, multiplicative quantum number called R-parity. SM particles and the extended Higgs bosons have an R-parity of $+1$, while their superpartners have an R-parity of -1. It was introduced to ensure lepton and baryon number conservation and thus the stability of the proton. It has the consequence that the lightest supersymmetric particle (LSP) is stable and supersymmetric particles can only be produced in even numbers. If the LSP is neutral like one of the neutralinos for example, it is an excellent DM candidate [34].

Two Higgs doublet model

The two Higgs doublet model (2HDM) is only a small extension of the SM. Like supersymmetry it predicts an extended Higgs sector with two doublets. In that sense SUSY is one example of a 2HDM. Even without an additional symmetry and a variety of superpartners it is possible to construct DM scenarios.

The two Higgs doublets give rise to five physical Higgs boson fields after electroweak symmetry breaking. Two are neutral scalar bosons, one of which might be the discovered SM Higgs. Two are charged Higgs bosons and one is a neutral pseudoscalar [66].

In one scenario the second Higgs doublet transforms under a parity transformation as:

$$H_2 \rightarrow -H_2. \tag{2.34}$$

As a consequence only H_1 has a vacuum expectation value, couples to fermions and causes electroweak symmetry breaking. The other doublet gives rise to a stable particle, which would contribute to the DM relic density. Depending on the values of the free parameters of the model it could even account for the entire relic density [67].

Another scenario is called the lepton-specific 2HDM. In it one of the Higgs doublets couples only to quarks and the other only to leptons. In addition, there is a scalar singlet with a mass eigenstate that is a DM candidate. The DM mass is predicted to be in the range 7-10 GeV and can be constrained by indirect detection experiments [68].

A third scenario is 2HDM with a pseudoscalar. This model adds a pseudoscalar field P to the extended Higgs sector. This changes the electroweak symmetry breaking and leads to six fields: two neutral Higgs bosons h and H, two charged Higgs bosons H^+ and H^- and two pseudoscalars (a and A). In addition, a DM candidate χ is added. Here, h is the 125 GeV Higgs boson discovered at the LHC.

The phenomenology of the model depends on the masses of its particles. As long as $m_h > 2m_a$ is true, the Higgs boson can decay into a pair of a bosons. If $m_a > 2m_\chi$ is also given, the Higgs boson can decay into 4χ. That also means that the BR for the Higgs boson to decay invisibly is larger than what is predicted by the SM. An excess could potentially be measured at the LHC. A similar situation is given when $m_h - 2m_\chi > m_a > m_h/2$ is given, which means that only the decay $h \to a\chi\chi \to 4\chi$ is allowed. In the case of $m_h - 2m_\chi > m_a$ the decay $h \to 4\chi$ is still possible but suppressed [69].

Interactions between the Higgs boson and DM in the context of collider searches

Knowing that multiple BSM models predict couplings between the Higgs boson and DM, it is well-motivated to consider directing the efforts of collider searches in that direction. Often this is done by looking for invisibly decaying Higgs bosons. The searches can then be categorized by the Higgs production mechanism, which determines the possible final states of the process. The invisible decay product can give rise to $E_{\mathrm{T}}^{\mathrm{miss}}$ by recoiling against other produced particles. Therefore, $E_{\mathrm{T}}^{\mathrm{miss}}$ is typically demanded of a DM signature in a collider search. Like the other chapters of this work the discussion is limited to proton–proton collisions:

- Gluon–gluon Fusion (ggF): Despite being the dominant production mode at $\sqrt{s} = 13$ TeV, this is not the most sensitive channel for the search for invisible decays of the Higgs boson. This is due to the fact that the signal is hard to distinguish from multijet events. The channel is further discussed in Chapter 5.

- Vector-boson fusion (VBF): This is the most sensitive channel and the main topic of Chapter 5. As can be seen on the left of Figure 2.10, there are at least two quark jets in addition to the Higgs boson decay products in the final state of the process. These jets are typically highly energetic and well-separated, which is exploited in the analysis.

- Production in association with a vector boson (Higgsstrahlung, VH): The process can be identified by reconstructing the decay products of the vector boson. The process is depicted in Figure 2.11 and an example of such a search can be found in Ref. [70].

- Production in association with DM candidates: In this case the Higgs boson is identified via its visible decay products, which can be $b\bar{b}$ or $\gamma\gamma$ for example.

2.2.6 Alternatives to the dark matter hypothesis

It is reasonable to look for alternatives to the particle DM hypothesis. To understand many of these approaches, it is helpful to gain some perspective on the models predicting particle

DM. All of these assume that GR is the correct model of gravity. However, the observations consistent with the DM hypothesis can also be seen as contradictions to GR. The inability of GR to explain the shape of galaxy rotation curves, CMB anisotropies and other phenomena without a new particle could be seen as a reason to replace or append the theory. As such there are many alternative models already.

On example is modified newtonian dynamics (MOND). The model is based on the idea that gravitational attraction has a dependence on acceleration. This is an explanation for the observed rotation curves discussed in Section 2.2.1. The concept could also be extended to dwarf spheroidal galaxies and superclusters [71]. The model is somewhat disfavoured after the discovery of DM less galaxies [72]. From the point of view of modified gravity the modification should be similar everywhere in the universe. However, with particle DM it is entirely possible that anisotropies in the early universe lead to regions that are poor in particle DM now.

The observation of the collisions of two clusters of galaxies, one of which is known as the bullet cluster, is even more damning for the model. By studying the clusters both in the X-ray spectrum and via gravitational lensing, two types of matter were observed to be separated. The weakly interacting DM halo, which was only detected gravitationally, was barely slowed down by the collision and thus moves ahead of the electromagnetically detectable part of the cluster. This phenomenon cannot be explained by MOND, where the gravitational effect cannot be decoupled from visible matter [73].

Another proposal is the introduction of matter with negative masses. This would cause gravitational repulsion and thus accelerate the expansion of the universe, as long as negative masses are continuously created. As such negative masses have the potential to explain the dark energy phenomenology. It was also shown that this kind of matter can flatten galaxy rotation curves and would accumulate in galactic halos. It is thus an explanation of both dark phenomena at the same time [74]. The problem here is that the negative mass proposal also allows the spontaneous creation of pairs of particles with masses of both signs from a vacuum state. This clearly does not happen in our universe and would need to be circumvented by modifying the model.

Both of these proposals fall under the umbrella of modified gravity models. They can be tested by measuring the red-shifts of distant galaxies and looking for deviations from the GR field equations [75].

In general, particle DM is more successful in creating predictions that are consistent with all current experimental observations than modified gravity models. Therefore, alternative models are not considered in the following chapters.

Chapter 3

Experimental methods

The Large Hadron Collider (LHC) was built to probe the interactions of elementary particles at the highest possible energies [76]. This makes it possible to research the smallest accessible scales and to produce new massive particles. In particle physics there are two general areas of innovation: the energy frontier and the intensity frontier. The LHC advances the energy frontier, which pushes for particle collisions at ever higher energies.

The particle collisions are recorded with four main detectors. One of these is the ATLAS detector, which recorded the data for the studies presented in Chapter 4, Chapter 5 and Chapter 6. The main goals of the experiments at the time of approval were the discovery of the Higgs boson[1)] and possible evidence of physics beyond the Standard Model.

In Section 3.1 a brief introduction into the operation of the LHC is given. ATLAS is discussed in greater detail in Section 3.2 where the different parts of the detector are introduced. In Section 3.3 the reconstruction and definition of physics objects is presented with a special focus on jets and missing transverse energy ($E_{\mathrm{T}}^{\mathrm{miss}}$). Finally, Section 3.4 is the presentation of the use of Monte Carlo (MC) simulation in predicting particle collision events measured with the ATLAS detector.

3.1 The LHC

As the most powerful particle accelerator in the world the LHC is an enormous international project. The accelerator complex uses existing infrastructure at the European council for nuclear research (CERN[2)]) near Geneva. The circular collider is built into the existing tunnel that was used by the Large Electron–Positron Collider (LEP) and has a circumference of 26.7 km [76].

The accelerator is designed to provide particles for collisions at centre-of-mass energies of up to 14 TeV (The physics of particle collisions and the definition of the term centre-of-mass energy are presented in Section 2.1.6.). These particle collisions occur at four main detectors, with which the particle interactions are measured and recorded:

- ATLAS (a toroidal LHC apparatus): As one of the two multi-purpose detectors ATLAS is built to reconstruct a large array of final states of particle collisions even when parti-

[1)] This was achieved in 2012 both at ATLAS [2] and at CMS [3].

[2)] The acronym originated in French and stands for conseil européen pour la recherche nucléaire [77].

cle interactions happen at the highest intensity. Its individual strengths are explained in Section [78].

- CMS (compact muon solenoid): The other multi-purpose detector includes a powerful solenoid magnet in order to build a very accurate muon detection system [79].
- ALICE (a large ion collider experiment): The goal of this experiment is to study heavy-ion collisions at high densities of strongly interacting matter. The key subdetector here is a powerful time projection chamber [80].
- LHCb (LHC beauty): The detector focusses on the reconstruction of events containing B-meson decays with excellent proper time resolution in order to study CP violation among other phenomena. Most of its instrumentation is concentrated in the forward direction where B-hadrons are expected to be found [81].

The LHC is designed for three types of collisions: proton–proton (pp), proton–lead (p-Pb) and lead–lead (Pb-Pb). Proton–proton collisions are the most common and are in fact the only kind of collisions that are discussed further in the following chapters. Protons are produced by ionising hydrogen atoms, before the hadrons are accelerated by the linear accelerator LINAC 2 and fed into the rest of the complex. Lead ions are created by heating and vaporising a piece of lead before the ionization in an electric field. The ions are then accelerated with LINAC 3. The purpose of colliding heavy ions is to study hot dense matter and other subjects especially at ALICE.

The particles are accelerated in bunches, which makes their injection easier and allows a high concentration of particles when beams collide. However, this high particle density also leads to multiple collisions happening nearly at the same time, which complicates the measurement of specific events. This effect is called pile-up (see Section 3.3.2 for more details).

Figure 3.1 is not only a depiction of the LHC accelerator complex but also a window into the history of CERN. To reach centre-of-mass energies of up to 14 TeV, hadrons have to be accelerated in multiple stages. Before entering the largest ring with its 26.7 km circumference, the particles go through a series of pre-accelerators, most of which were independent colliders in the past themselves. In the order from low to high energies the list is: The proton synchrotron booster (BOOSTER), the proton synchrotron (PS) and the super proton synchrotron (SPS).

The protons then enter the LHC ring at an energy of 450 GeV and thus practically at the speed of light.[3)] Here, further acceleration is accomplished through a series of changing electric fields referred to as radiofrequency cavities. These alternate their direction at such a frequency that the particles are always boosted forward. The near light speed travel is necessary because two proton beams are injected in opposite directions in the form of bunches. Only if the particles travel at nearly constant speed during their acceleration to ever higher energies, can they receive energy from electric fields of constant size on multiple revolutions around the ring.

The LHC ring is not perfectly round but rather consists of eight straight sections and eight arcs. The charged particles are kept on their curved trajectory with powerful superconducting magnets, which are cooled to below 2 K to deliver 8 T fields. They are one of the limiting factors

[3)] At 450 GeV protons start their acceleration in the LHC ring at $0.999997826c$, where c is the speed of light. Once they reach 6.5 TeV their speed increases to $0.999999990c$. Therefore, there is no significant velocity increase for the purpose of the operation of the machine.

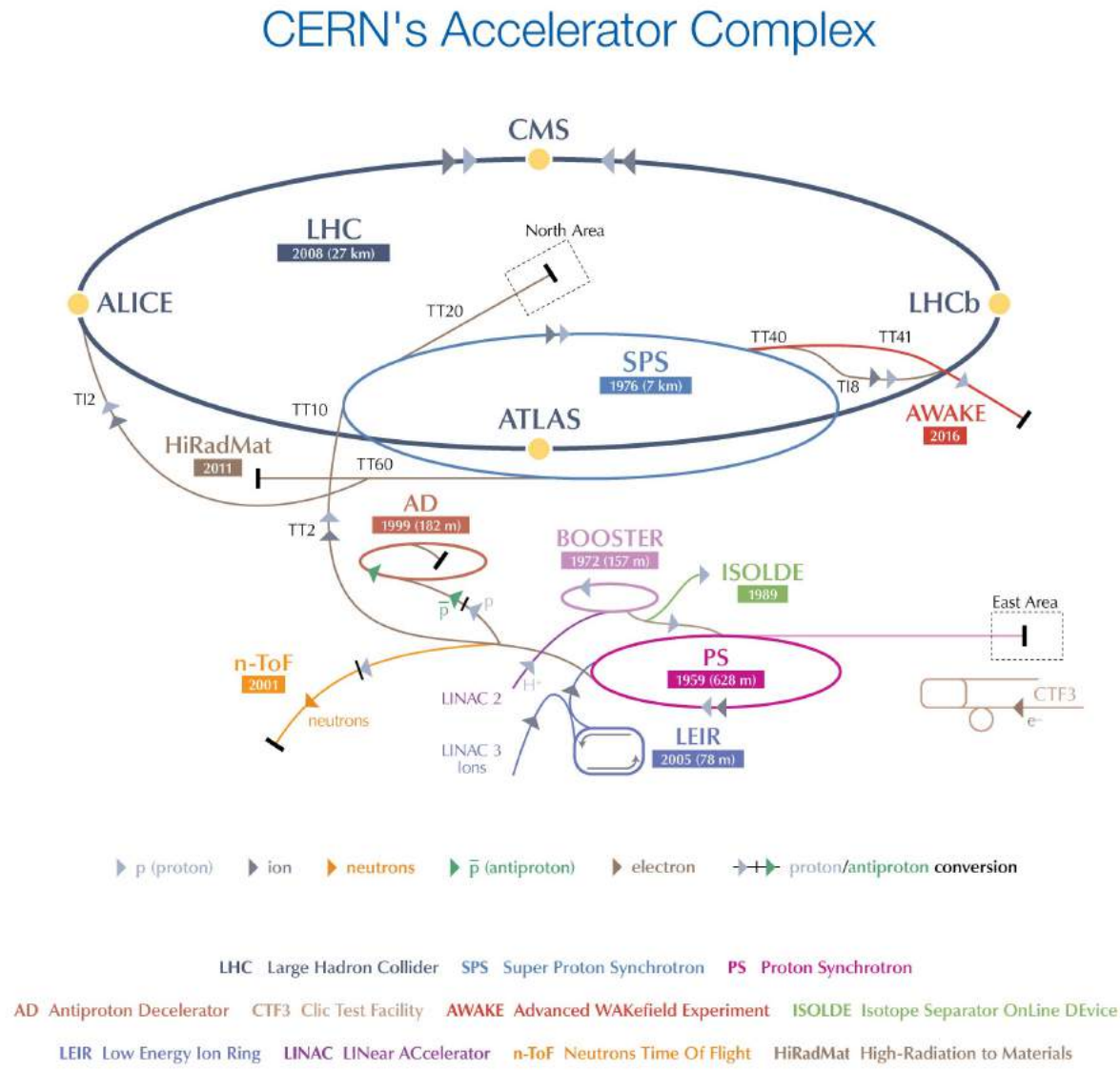

Figure 3.1: CERN's accelerator complex as it was in 2013. Since then CTF3 was partially converted into CLEAR [82]. Shown is the accelerator chain for protons (LINAC 2 → BOOSTER → PS → SPS → LHC) and lead (LINAC 3 → LEIR → PS → SPS → LHC) among other experiments and facilities. On the LHC ring the position of the four main experiments (ATLAS, CMS, ALICE and LHCb) is shown albeit not to scale [83].

for reaching higher centre-of-mass energies in the LEP tunnel. The proton bunches travel inside a vacuum to avoid the beams from degrading as a result of collisions with air molecules. In order to shield the detectors from cosmic radiation the entire complex is about 100 m below earth's surface.

3.1.1 Luminosity

One of the most important properties of a particle accelerator is the amount of luminosity it can deliver. Generally the goal is to cause as many particle collisions as possible in order to produce large datasets and keep the statistical uncertainties of analyses low. Also some processes occur very rarely, which makes it unlikely that they exist in smaller datasets. However, the amount of particle interactions N also depends on the cross-section σ of a particular process, which cannot be improved by optimising the experiment. Further, there is a distinction between the instantaneous luminosity $\mathscr{L}$ defined in Eq. 3.1 and the integrated luminosity L (just luminosity from now on) defined in Eq. 3.2:

$$\dot{N} = \mathscr{L}\sigma, \tag{3.1}$$

$$N = L\sigma = \int_0^T \mathscr{L}(t)\sigma \mathrm{d}t, \tag{3.2}$$

where $\dot{N}$ is the event rate or the number of expected events N per unit time. The time parameter is t and T is the length of operation. Of course the luminosity can be increased trivially by running the experiment over a longer time period T. However, it is also desirable to get as much data as possible in a short amount of time. The key is to optimize the instantaneous luminosity, for which it is important to look at its dependencies on accelerator properties in:

$$\mathscr{L} = \frac{N_b^2 n_b f_{\mathrm{rev}} \gamma}{4\pi\varepsilon_n \beta^*} F, \tag{3.3}$$

where N_b is the number of particles per bunch, n_b is the number of bunches per particle beam, f_{rev} is the revolution frequency around the accelerator ring and $\gamma = 1/\sqrt{1 - v^2/c^2}$ is the Lorentz factor, which is defined via the particle velocity v and the speed of light c (see for example Ref. [33] for an introduction into relativistic kinematics). The numerator of the expression can be simplified as the crossing frequency times the number of particles in one beam times the number of particles in the other beam. The denominator is the beam overlap, where ε_n is the beam emittance and β^* is the cross-sectional size of the proton bunches. Finally, F is the reduction factor due to the beam crossing angle. A more detailed explanation of the concept of luminosity and further complications in its calculation can be found in Ref. [84]. Increasing the instantaneous luminosity comes at the cost of higher pile-up, which makes it harder to reconstruct events. This is addressed in Section 3.3.2.

In the following chapters, data recorded with the ATLAS detector in 2015, 2016 and 2017 are analysed. The integrated luminosity that was collected during that time period is depicted in Figure 3.2. The collection of data during 2016 and 2017 is shown separately in Figure 3.3 because the various projects discussed later are using different datasets. During the operation of the LHC machine not all of the data are necessarily recorded by the detectors because of the data acquisition inefficiency and the ramp up of parts of the detector after stable beams are reached. Furthermore, not all data are good for physics analysis, since parts of the detector can

be affected by various malfunctions for short periods of time. The periods of data taking at the highest quality are noted on the good runs list (GRL) discussed in Section 5.4.1.

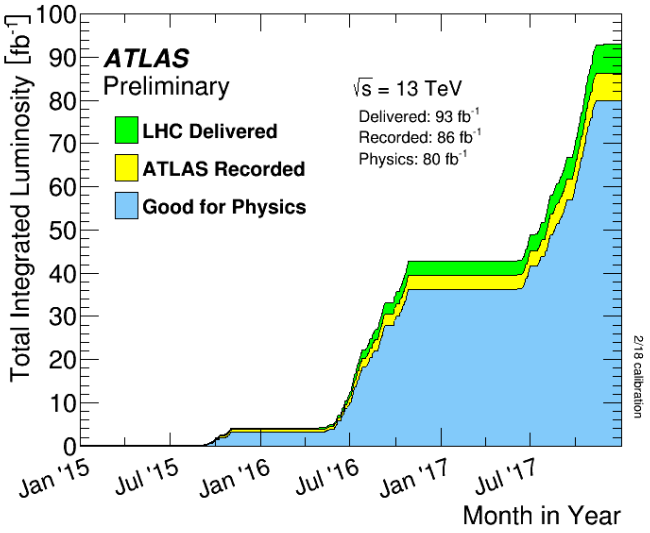

Figure 3.2: Total integrated luminosity per month in the years from 2015 to 2017. The amount of data delivered to ATLAS (green), recorded by ATLAS (yellow) and good for physics (blue) are shown in comparison [85].

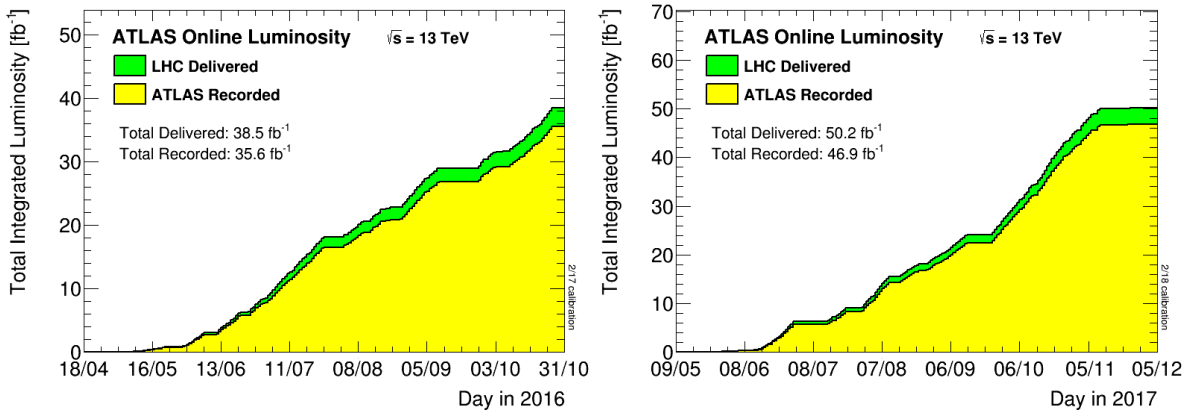

Figure 3.3: Total integrated luminosity per day in the years 2016 (left) and 2017 (right). The amount of data delivered to ATLAS (green) and recorded by ATLAS (yellow) are shown in comparison [85].

Actually measuring the luminosity is a non-trivial task, which gives rise to a systematic uncertainty, which is relevant to all analyses. The problem is reduced to measuring the average number of interactions per bunch crossing μ, which is determined with so-called van der Meer scans. These measure the reaction rate of the proton beams as a function of the beam displacement along x- and y-axis. Furthermore, the beam profile is measured with the beam-gas imaging method, in which the proton beam hits the nuclei of a residual gas. The proton-nucleus interaction is measured and via integration over the beam profile the luminosity is calibrated [86].

The μ measurement depends on the particular method of detection and kind of detector and is always lower than the true μ. By using multiple detector types the true μ is approached and the systematic uncertainty is determined [87].

3.1.2 Important parameters of the LHC

The LHC started operation in 2009. Aside from short periods during the winter the accelerator ran until 2013. Afterwards data taking was interrupted for two years in a time known as the long shutdown in order to perform several upgrades. The time before the long shutdown is referred to as Run 1 and the time afterwards up until the next shutdown starting in 2018 is known as Run 2. The most crucial properties of the LHC are listed here. They are the design properties taken from Ref. [76]. Many parameters changed during the upgrade between Run 1 and Run 2, which is pointed out below if applicable. The following facts only concern pp collisions because they are the subject of later chapters:

- Centre of mass energy ($\sqrt{s}$): After the initial ramp up in 2009 the main physics programme began in 2010 at 7 TeV. In 2012 the centre-of-mass energy was increased to 8 TeV. Starting with Run 2 in 2015 the LHC ran at 13 TeV until the 2nd long shutdown beginning at the end of 2018. The design centre-of-mass energy of 14 TeV is planned to be reached in 2021 after the shutdown.

- Instantaneous luminosity ($\mathscr{L}$): In Run 1 the peak instantaneous luminosity was 8×10^{33} cm^{-2}s^{-1}. The design luminosity of 10^{34} cm^{-2}s^{-1} was reached and even exceeded in Run 2. For 2026 after further upgrades the so-called high luminosity LHC is planned to reach between 5×10^{34} cm^{-2}s^{-1} and 7×10^{34} cm^{-2}s^{-1} in order to deliver a total integrated luminosity of 3000 fb^{-1} [88].

- Number of particles per bunch (N_b): There are 1.15×10^{11} protons per bunch. This number decreases after each injection due to beam losses and collisions, until the beam is dumped eventually. To reach higher luminosities N_b is increased each year.

- Number of bunches in each beam (n_b): Each beam contains 2808 proton bunches. Another parameter that is changed to achieve higher luminosities.

- Proton-proton cross-section: The total cross-section for pp collision depends on the centre-of-mass energy. It is 96.07 mb at 8 TeV [89] and 110.6 mb at 13 TeV [90]. This leads to less then 30 particle collisions per bunch crossing.

- Revolution frequency (f_{rev}): This is simply given by the circumference of the LHC ring (26.7 km) and the velocity of the particle beams, which is the speed of light. Therefore, $f_{\text{rev}} = 11.2$ kHz.

- Bunch spacing: The time between two bunch crossings inside a detector was 50 ns in Run 1 and 25 ns in Run 2. This is the equivalent of bunch crossing rates of 20 and 40 MHz, respectively.

- Magnets: The 1232 superconducting dipole magnets in the tunnel operate at 1.9 K creating 8 T magnetic fields. They are used to keep the proton beams on their circular track or change the beam separation to cause collisions.

The LHC computing grid

The experiments at the LHC collect a tremendous amount of data every day of operation. Each event amounts to about 1.6 MB and a rate of 40 MHz leads to data being produced at 60 TB/s. Not all data are recorded. With some preselection, which is addressed in Section 3.2.5, 40 MHz are effectively lowered to 1 kHz [91]. In addition, the data have to be stored for 15 years. To combat all this the worldwide LHC computing grid (WLCG) [92] was introduced. As of 2019 it consists of more than 170 sites in 42 countries that are used to distribute, process and store data around the world. The sites are arranged into three tiers each with different tasks and responsibilities.

3.2 The ATLAS detector

ATLAS is a general purpose detector. That means that it aims to reconstruct a great variety of particle interactions of collision events that occur at the interaction point it encompasses. It can therefore measure pp as well as heavy ion collisions and reconstruct a large number of physics objects that are produced in the events. The detector consists of three larger systems, which are covered in detail in the following sections: The inner detector (ID), the calorimetry and the muon system.

All of these systems are built around the beryllium beam pipe, forming a cylindrical shape as depicted in Figure 3.4. The cylindrical shape is a logical choice. The detector should be as symmetrical as possible in order to have comparable measurements for particles travelling in different directions. Between subdetectors there is room for magnets and infrastructure like read-out cables and cooling. The magnets cause bent tracks of charged particles for better momentum resolution and particle identification. The inner detector is surrounded by a solenoid magnet and three toroid magnets are part of the muon system. With a length of 44 m and a height of 25 m ATLAS is the largest detector at the LHC.

3.2.1 ATLAS geometry

In order to describe relativistic particle interactions in a detector with cylindrical symmetries it is necessary to define several parameters and a suitable coordinate system. The ATLAS detector has a forward-backward symmetry centred on the nominal interaction point. The toroid magnets in the muon system dictate an eightfold symmetry in the azimuthal direction. Furthermore, there is a distinction between barrel and end-caps. The subdetectors in the barrel region cover the centre of the detector, while the end-caps detect particles that travel in the forward or backward direction (for simplicity this is just called the forward direction because of the symmetry).

The ATLAS coordinate system is defined by the coordinates (x,y,z), (r,θ,ϕ) and (r,η,ϕ). The z-axis is the centre of the beam pipe and thus the centre of the cylindrical symmetry of the detector. Its positive direction points counter-clockwise around the LHC ring in the right-handed coordinate system. The x-y plane is the plane perpendicular to the beam pipe with the x-axis pointing towards the centre of the LHC. The radius is r, which is the distance to the centre of the beam pipe. The azimuthal angle in the x-y plane is ϕ with the x-axis coinciding with $\phi = 0$. Similarly the polar angle θ is defined in the x-z plane with the z-axis coinciding with

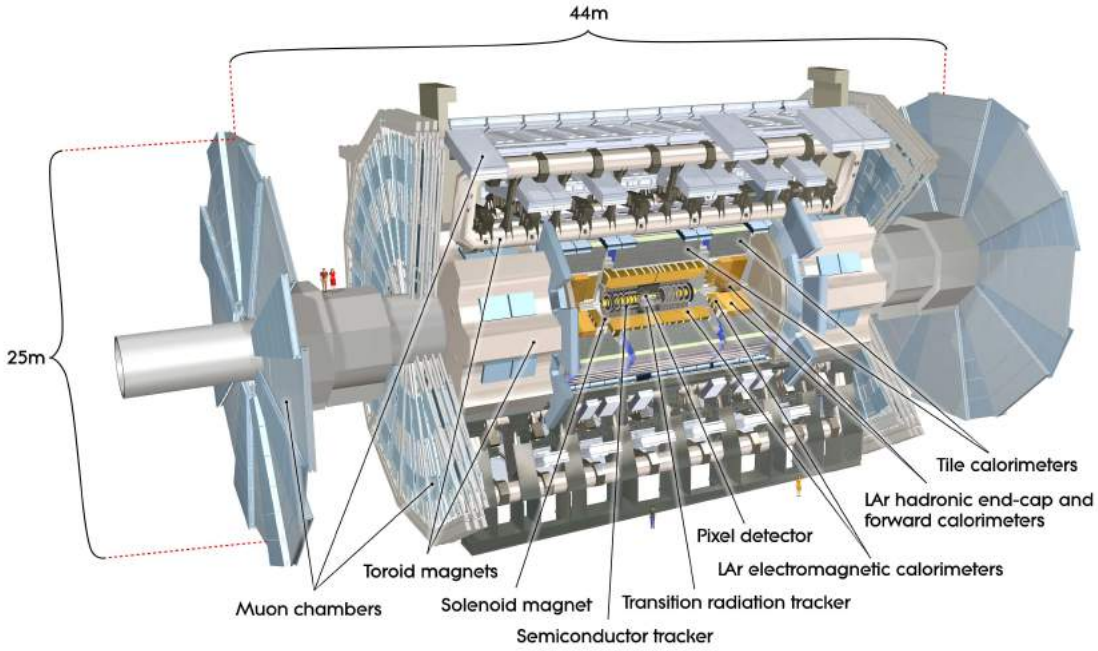

Figure 3.4: Schematic of the ATLAS detector. Shown are the inner detector (pixel detector, semiconductor tracker and transition radiation tracker), calorimetry (liquid argon (LAr) electromagnetic calorimeters, LAr hadronic end-cap and forward calorimeters as well as the tile calorimeters) and the muon system (muon chambers). The solenoid and toroid magnets are shown surrounding the inner detector and muon system. Not depicted is the insertable B-layer, which is part of the inner detector and closest to the beam pipe [78].

$\theta = 0$. The polar angle θ is not Lorentz invariant, but the pseudo-rapidity $\eta = -\ln(\tan(\theta/2))$ is, which is why the latter is used more commonly.

The distance between two objects is often given by $\Delta R = \sqrt{\Delta\eta^2 + \Delta\phi^2}$. In addition, the rapidity $y = 1/2 \times \ln[(E + p_z)/(E - p_z)]$ is introduced. The energy of a particle is E and p_z is its momentum along the z-axis. The rapidity is the boost of a massive particle along the z-axis. If the momentum of a particles is much larger than its mass, rapidity and pseudo-rapidity are approximately the same.

The x-y plane is also called the transverse plane and the transverse momentum is therefore defined as $p_{\mathrm{T}} = \sqrt{p_x^2 + p_y^2}$. Because protons are composite particles and the hard interaction in each collision event mostly occurs between the proton constituents quarks and gluons, the z-component of the momentum of the incoming particles is unknown. However, the momentum in the transverse direction must be negligible and is conserved in the collision. If particles that are invisible to the detector are produced in a collision, the negative vectorial sum of all transverse momenta of reconstructed final state particles, the so-called missing transverse momentum $\vec{p}_{\mathrm{T}}^{\,\mathrm{miss}}$, does not add up to 0. Its absolute value is the missing transverse energy $E_{\mathrm{T}}^{\mathrm{miss}} = \sqrt{(p_x^{\mathrm{miss}})^2 + (p_y^{\mathrm{miss}})^2}$.

3.2.2 Inner detector

In Figure 3.5 the ID is shown as a cut-away view. This innermost subdetector of ATLAS is built to reconstruct the trajectories (also called tracks) of charged particles and contribute to particle identification. From the inside to the outside it consists of the pixel detector, the semiconductor tracker (SCT) and the transition radiation tracker (TRT).

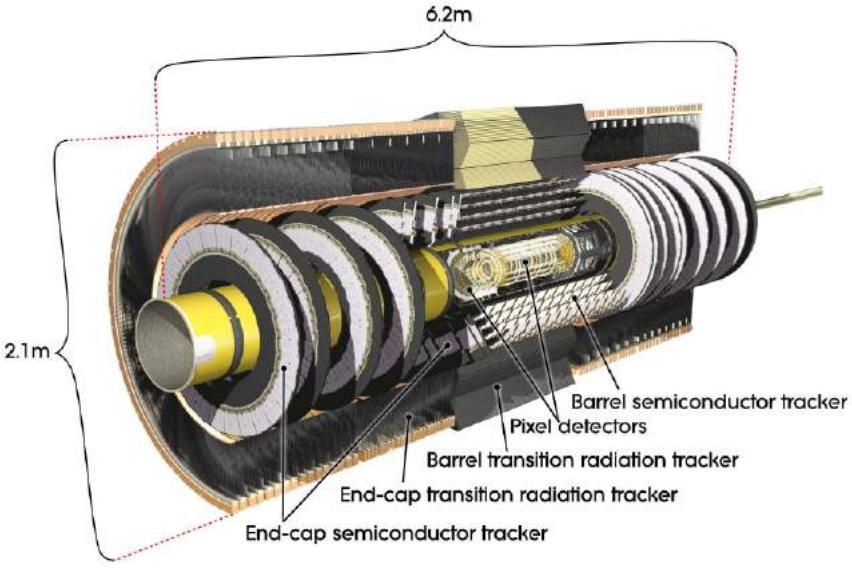

Figure 3.5: Schematic of the ATLAS inner detector (ID). The subsystems of the ID are shown [78].

The ID is inside a 2 T magnetic field produced by a solenoid around the subdetector. As a result the tracks of charged particles that traverse the ID are bent allowing a momentum

measurement. Because a large number of particles are hitting the ID each collision at a rate of 40 MHz, the ID does not only need a high granularity to discern between all of these particles but also needs to be protected from harm through radiation.

Pixel detector

The pixel detector is a series of four silicon layers consisting of discrete semiconducting pixels, which enable the spatial resolution of tracks and the precise measurement of vertices. The precision tracking detector provides measurements at a pseudo-rapidity $|\eta| < 2.5$. The four layers are, insertable B-layer (IBL), B-layer, Layer 1 and Layer 2. In addition, three disks cover the high-$|\eta|$ direction of the pixel detector in each of the two end-caps. With the multi-layered approach every track crosses at least three pixels for better spatial resolution. Together with the smallest pixel size in r-$\phi \times z$ being 50×400 μm^2 this leads to the following accuracies: in the barrel 10 μm in the r-ϕ plane and 115 μm in the z-direction, in the disks 10 μm in the $r-\phi$ plane and 115 μm in the r-direction [78].

The IBL was added to the detector during the first long shutdown before Run 2. The sub-detector improves the measurement of the vertex of the hard interaction and the vertices of the decay of long-lived particles like b quarks. A vertex is a space point where a specific interaction took place. Since the innermost layer of the pixel detector, the B-layer, is deteriorating over time from radiation damage, it became necessary to restore the efficiency of identifying b quarks. Furthermore, the LHC has reached higher instantaneous luminosities than the initially planned 10^{34} cm^{-2}s^{-1} and will even further exceed these records in the so-called High-Luminosity LHC. The IBL is able to compensate for readout inefficiencies because of the high luminosities.

Before the installation of the IBL the beam pipe was located at the radius 29 mm $< r <$ 36 mm. In order to allow space for the IBL its size was decreased to 25 mm $< r <$ 29 mm. The IBL itself is only 40 mm in diameter [93]. In total, about 80.4×10^6 readout channels provide the high granularity of the pixel detector.

Semiconductor tracker

With four double layers of semiconducting silicon microstrip sensors the SCT is able to measure tracks at eight space points. In each pair one layer is oriented radially with the other at an angle of 40 mrad for a stereo measurement. With a total of 15912 sensors and 6.3×10^6 readout channels the SCT also reaches very high accuracies: in the barrel 17 μm in the r-ϕ plane and 580 μm in the z-direction, in the disks 17 μm in the r-ϕ plane and 580 μm in the r-direction [78]. The good ϕ resolution of the SCT also improves the transverse momentum measurement. Spatially the SCT covers the region 299 mm $< r <$ 514 mm and $|\eta| < 2.5$. The 2×9 end-cap disks are located at 275 mm $< r <$ 560 mm.

Transition radiation tracker

The TRT is built around the SCT extending between 554 mm $< r <$ 1082 mm in the barrel and 617 mm $< r <$ 1106 mm in the end-cap over $|\eta| < 2.0$. In the barrel it consists of 52 544 polyimide drift tubes called straws, which are 4 mm wide, 144 cm long and are stabilized by carbon fibres. They are orientated parallel to the beam pipe and therefore provide only

information about the r-ϕ plane where the accuracy amounts to 130 μm for each straw. In the end-cap the orientation is radially with 37 cm long straws.

Each straw is filled with a gas mixture made up of Xe (70%), CO_2 (27%) and O_2 (3%). The straws operate by charged particles ionising the gas mixture or photons being absorbed. The intensity of this transition radiation is mass dependent. Thus electrons, which are light compared to other charged particles, emit significantly more light, which enables their identification. With 52 544 straws in the barrel and 122 880 in each end-cap the straw density is high leading to an average 46 hits per track [78].

3.2.3 Calorimetry

The ATLAS calorimeter [78] is designed to determine the energies and momenta of particles. It is also crucial for the reconstruction of jets. It is divided into two main parts, the electromagnetic calorimetry and the hadronic calorimeters. Furthermore, there are barrel, end-cap and forward calorimeters for each of the two. The entire calorimeter system is contained in three cryostats, two of which are for the end-caps and one is for the barrel. The calorimetry surrounds the ID and is surrounded by the muon system. A schematic is shown in Figure 3.6.

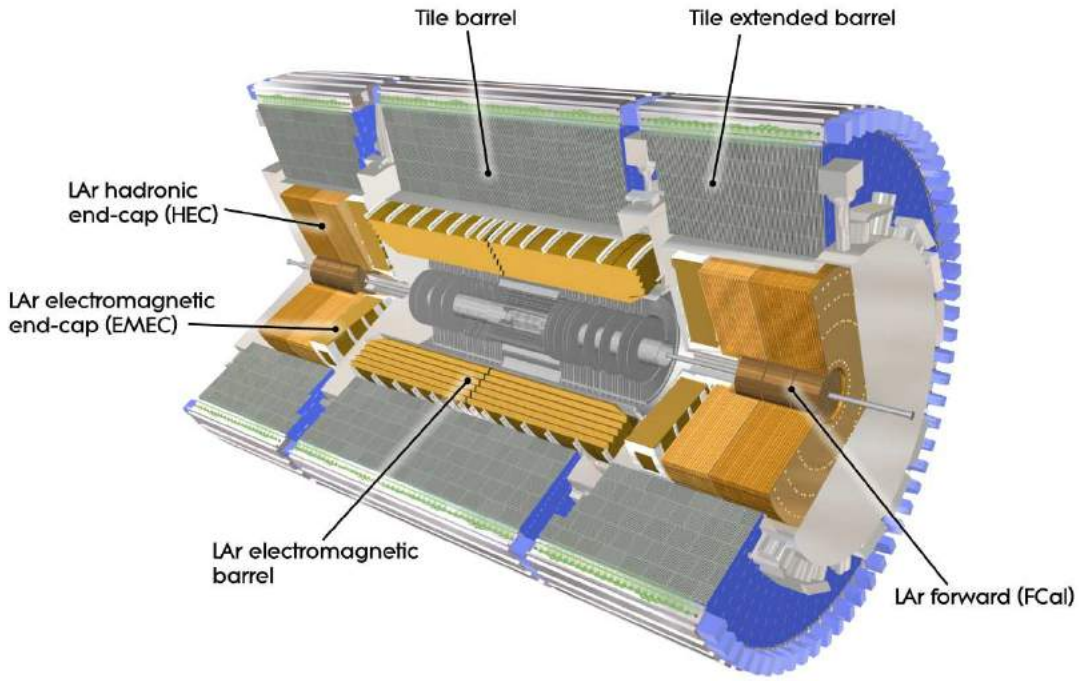

Figure 3.6: Schematic of the ATLAS calorimetry [78].

The calorimetry is constructed to contain electron, photon and jet energies before the particles reach the muon system. Muons and neutrinos are the only Standard Model (SM) particles that pass the system mostly uninhibited. It uses a sampling technique, which means that only a part of the particle energy is measured, from which the full energy is extrapolated. The linearity of this partial energy measurement was tested with test beam experiments [78].

Electromagnetic calorimeter

The electromagnetic calorimetry is subdivided into the barrel and the electromagnetic end-cap (EMEC). Both barrel and end-cap are liquid-argon detectors with lead as the absorber material and the noble gas cooled to 88.5 K as the active material. The copper electrodes and absorbers in barrel and EMEC have an accordion geometry, which has the advantage of providing full coverage in the ϕ direction without any cracks.

The purpose of this part of the detector is the identification of light electromagnetic particles (electrons and photons). Because of the short radiation length of the absorber material, the charged particles cause showers inside the liquid-argon gaps ionising the active material. The gap is under the influence of a high-voltage electric field, which leads to drift electrons that are registered at the copper electrodes.

The radiation length X_0 is an important measure to characterize calorimeters. A particle inside a calorimeter loses energy proportional to $\exp(-x/X_0)$ after a distance x from the point of entry into the material. The radiation length is a property of the absorbing material. Ideally, it is small to fully contain the particle energy within a compact calorimeter. In terms of the radiation length the electromagnetic calorimetry measures 22 X_0 in the barrel and 24 X_0 in the end-caps.

In the barrel region and part of the end-caps ($0 < |\eta| < 2.5$) there are three active layers in depth. From the relative position of photon clusters in the first and second layer the momentum direction in η can be determined. The number of active layers decreases to two in the overlap region between barrel and end-cap ($2.5 < |\eta| < 3.2$).

The three layers are called the strips, the middle and back sections (also EM1, EM2 and EM3). The strips have a fine segmentation to measure the momentum direction of incoming particles. The middle section is the main area for the purpose of energy absorption with a size of 16 radiation lengths. The back section only measures two radiation lengths and collects most of the residual energy of electromagnetic particles. The accordion geometry and different layers are illustrated in Figure 3.7.

The same technology is used in the two wheels that form the EMEC. They cover the $1.375 < |\eta| < 3.2$ region where they overlap with the barrel for $|\eta| < 2.5$. A liquid-argon presampler between barrel and end-cap improves the measurement further.

Hadronic calorimeter

For the measurement of jets two types of technologies are used. In the barrel region there is the tile calorimeter, which has doped polystyrene scintillators as the active medium and steel as the absorber. The hadronic end-cap calorimeter (HEC) and forward calorimeter (FCal) are liquid-argon calorimeters similar to the electromagnetic calorimetry.

The tile calorimeter is further subdivided into a barrel and two extended barrels, one in the $+z$ and one in the $-z$ direction. Each of them is made up of three layers just like the forward calorimeters. The hadronic end-cap on the other hand has four layers. The barrel hadronic calorimeter consists of 64 modules for each of these three sections.

Hadrons cause showers (jets), which themselves deposit their energy in the calorimeter. The signal light from the scintillator tiles is collected at their edges and propagated with wavelength-shifting fibres that lead to readout photomultipliers. The geometry is designed for seamless coverage in the ϕ-direction. For the gap between barrel and extended barrel steel-scintillators

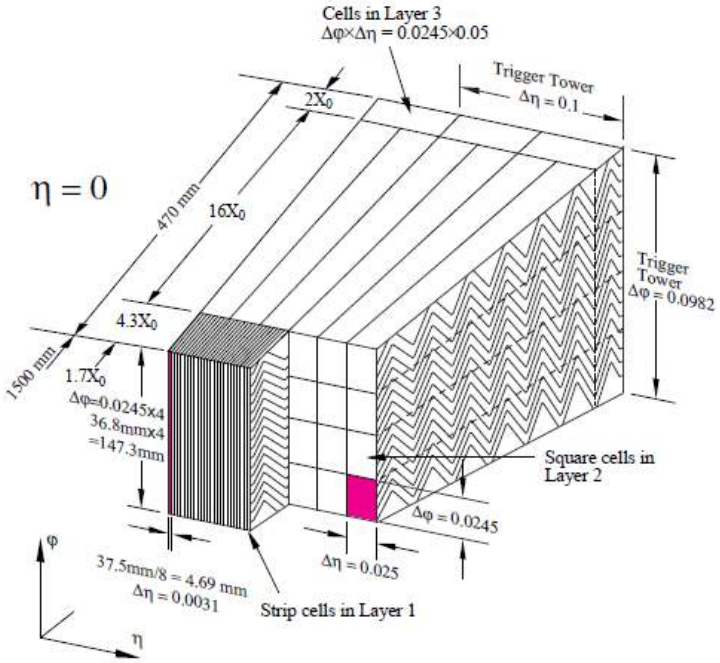

Figure 3.7: Schematic of part of the ATLAS barrel electromagnetic calorimetry [78].

are used. They recover some of the energy loss in a region with compact space. As a calibration system caesium is hydraulically displaced between the tiles, allowing a measurement of disparities in the response. The scintillator setup together with fibers and readout are depicted in Figure 3.8.

Radiation is damaging to the tile calorimeter. Irradiation tests predict up to 10% loss of efficiency after 10 years of LHC operation. As a protective measure the tiles are encased in plastic sleeves, which also improve the scintillation light yield. In the forward direction more radiation resistant technologies are used. The HEC is a liquid-argon/copper sampling calorimeter similar to the electromagnetic calorimetry but lacking the accordion structure. Due to using a similar technology it shares the cryostat with the EMEC.

The FCals cover the $3.1 < |\eta| < 4.9$ range. They consist of three different layers. The first one - FCal1 - is another electromagnetic calorimeter with liquid-argon as the active material and copper as the absorber. Here, the copper takes the form of rods next to liquid-argon tubes inside a copper matrix. FCal2 and FCal3 are hadronic calorimeters with tungsten as the absorber, which reduces the spread of jets and therefore contains the energy for an optimal measurement.

3.2.4 Muon spectrometer

Muons are mostly uninhibited by the calorimeter and can therefore be measured in the outermost region of the detector. The measurement is based on reconstructing tracks of the charged particles that are bent in the longitudinal direction in magnetic fields caused by one large superconducting air-core toroid magnet in the barrel (up to 0.5 T) and two smaller ones in the end-cap (up to 1 T). Each toroid consists of eight coils with the end-cap toroids twisted at a 22.5% angle for optimal field overlap. Each coil is embedded in its own cryostat. The magnetic fields are

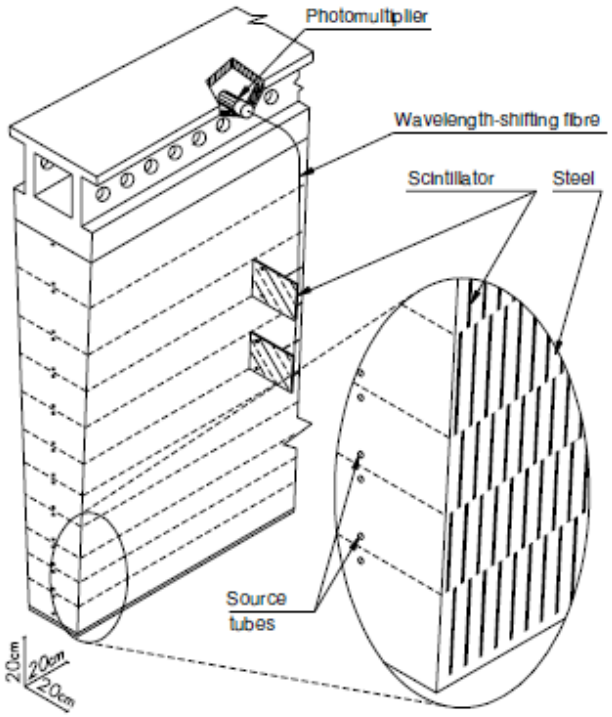

Figure 3.8: Schematic of part of the ATLAS barrel hadronic tile calorimetry [78].

mostly perpendicular to the muon trajectories. Both barrel and end-cap region are subdivided into three layers each. The end-caps form large wheels in the r-ϕ plane. A schematic of the ATLAS muon system is depicted in Figure 3.9.

The actual tracking measurement is undertaken with monitored drift tubes (MDTs) in the barrel and cathode strip chambers (CSCs) in the innermost layer at $2.0 < |\eta| < 2.7$. The MDTs are isolated and pressurized at 3 bar. They have a high accuracy in the 3 GeV range for the energy measurement. The CSCs are multiwire proportional chambers, which are able to withstand the higher rate that is observed in the high-$|\eta|$ region.

The muon spectrometer has its own trigger system (Triggers are discussed in more detail in Section 3.2.5.) in the region $|\eta| < 2.4$. It uses resistive plate chambers (RPCs) in the barrel and thin gap chambers (TGCs) in the end-caps. The three cylindrical RPC layers are located above and below their MDT counterparts. They are a gas mixture (mostly $C_2H_2F_4$) in an 4.9 kV/mm electric field made by electrode-plates. The TGCs are layered in nine segments between the MDTs of the end-cap. A gas mixture (mostly CO_2) fills The multi-wire proportional chambers. Characteristically, the distance between wire and cathode (1.4 mm) is smaller than the distance between wire and wire (1.8 mm) leading to the descriptor “thin”. The technologies of RPCs and TGCs are chosen in order to be fast enough for trigger decisions during the high rate data taking.

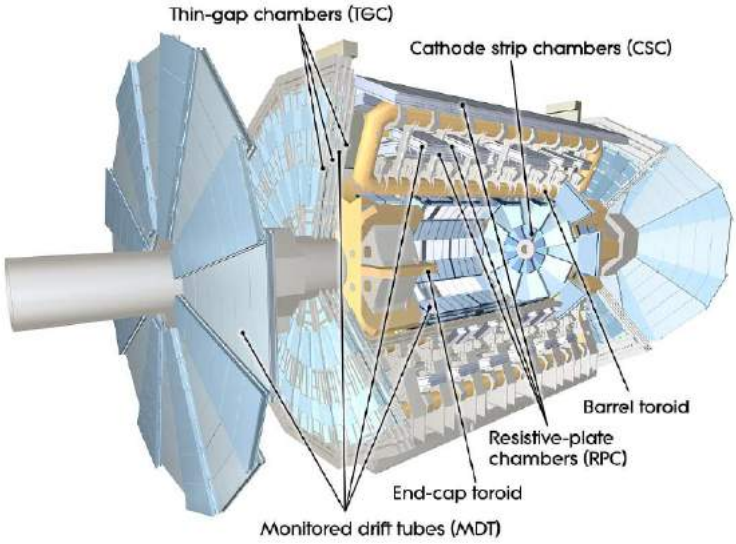

Figure 3.9: Schematic of the ATLAS muon system [78].

3.2.5 Trigger system

As mentioned in Section 3.1.2 the ATLAS detector continuously records large amounts of data. To make data storage and evaluation possible this has to be reduced. However, it is also very important to not discard events that are interesting for analyses. This is where the trigger system comes into play by applying a preselection parallel to the data taking process. Triggers look for large energy deposits or tracks from muons, electrons, photons and jets to identify interesting events. They also select events with large $E_{\mathrm{T}}^{\mathrm{miss}}$. In many cases the criterion for a trigger to select a certain event is that the trigger variable (such as $E_{\mathrm{T}}^{\mathrm{miss}}$ or the electron p_{T}) is above a certain value called the trigger threshold.

The trigger process works in two steps. First, the hardware-based level 1 (L1) trigger provides a fast selection and identifies areas in the $\eta - \phi$ plane as regions of interest (RoI). Afterwards, the mostly software-based high level trigger (HLT) does the final trigger selection, which is based on stricter criteria than the L1 decision. Because the HLT only investigates the previously identified RoIs, which is only an average of 2% of the detector, it can do so with higher accuracy than the L1 while still being sufficiently fast. In this way the L1 trigger reduces the bunch crossing rate to 100 kHz with a decision time of 2.5 μs and the HLT reduces that further down to approximately 1 kHz taking about 200 ms for each decision [94].

Figure 3.10 shows a schematic of the ATLAS trigger and data acquisition (TDAQ) system. The data acquisition system is what buffers the event data coming in from the subdetector hardware and L1 triggers before passing them on for further processing.

The ATLAS trigger system underwent a number of changes during the first long shutdown before Run 2. Before the long shutdown the triggering was done with an L1 trigger, a level 2 (L2) trigger and the event filter. The L2 trigger and the event filter were then merged into one HLT.

There is a variety of triggers available to analysis teams to choose from in the so-called trigger menu. It contains triggers that preselect events containing a muon with large transverse momentum, events with large $E_{\mathrm{T}}^{\mathrm{miss}}$ and many other signatures that could be interesting

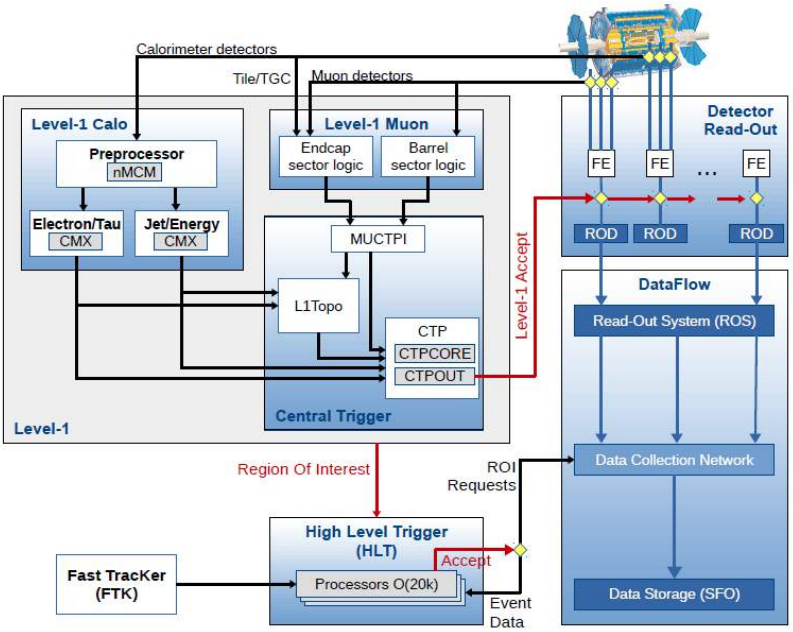

Figure 3.10: Schematic of the ATLAS trigger and data acquisition system. Both L1 and HLT are shown on the left and the data acquisition is shown on the right [94].

for analyses. The trigger menu changes from year to year in order to deal with the changing instantaneous luminosity.

The triggers are constrained by how much data space is available for the storage of new data. Therefore, triggers are not supposed to surpass certain trigger rates. If the selection criteria of a trigger are loose enough for it to surpass this rate a so-called prescale is applied. With a prescale a fraction of the events are randomly discarded and the so recorded dataset has to be scaled up in order to be used. For example a trigger with a prescale of three records only one third of the events satisfying its selection criteria and the events in the corresponding datasets have to be multiplied by a factor of three (An example of how this is done in an analysis is discussed in Section 5.4.2.).

Trigger turn-on curves

The trigger variable as measured at trigger level has a lower resolution than the reconstructed variable that enters the dataset. As a result not all events with the trigger variable above the trigger threshold pass the trigger. The efficiency ε of a trigger T, which is a measure of how many events with a certain value of the trigger variable pass the trigger, takes the form of an error function. This definition and a parametrization is expressed in Eq. 3.4 for a binned distribution of the trigger variable:

$$\varepsilon(T,i) = \frac{number\ of\ events\ in\ bin\ i\ passing\ T}{number\ of\ events\ in\ bin\ i} = \frac{a}{2}\cdot\left[1+\mathrm{erf}(\frac{x_i-b}{\sqrt{2}c})\right], \tag{3.4}$$

where x_i is the value of the trigger variable in bin i. The free parameters a, b and c can be used to model a particular trigger efficiency with a fit. This function is also called the turn-on curve.

In the limit $x_i \to \infty$ it follows that $\varepsilon(T, x_i \to \infty)$ is constant and equal to a. Ideally a equals 1, but there are exceptions.

The turn-on curve for a trigger is measured using a reference trigger. A reference trigger is a trigger with either a looser or orthogonal requirement. Orthogonal means that the probability of events passing the reference trigger correlates very little with the probability of an event passing the trigger under study. In the case of $E_{\mathrm{T}}^{\mathrm{miss}}$ triggers a muon trigger is well suited, since $E_{\mathrm{T}}^{\mathrm{miss}}$ triggers rely on calorimeter information, which is mostly unaffected by muons. The muons are therefore invisible for the purpose of studying the trigger and the $E_{\mathrm{T}}^{\mathrm{miss}}$ definition is changed accordingly.

Figure 3.11 shows four example turn-on curves for illustration.

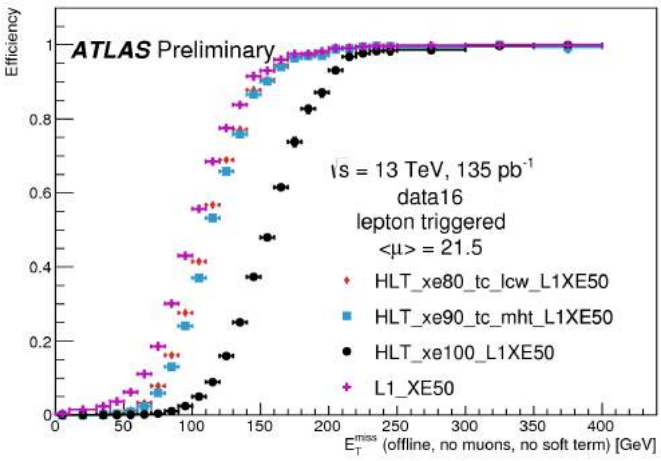

Figure 3.11: Example $E_{\mathrm{T}}^{\mathrm{miss}}$ trigger turn-on curves. The offline $E_{\mathrm{T}}^{\mathrm{miss}}$ was constructed with jets, electrons and photons with no contribution from muons and the track soft term (see Section 3.3.4 for a more general definition of $E_{\mathrm{T}}^{\mathrm{miss}}$ in ATLAS). The events were selected with single lepton triggers [95].

3.3 Reconstruction of physics objects

The ATLAS detector is designed to reconstruct a variety of physics objects by identifying their unique signatures. In general, this is done by identifying patterns in the digitized electronic signals that are recorded by the subdetectors. Particles that are invisible to the detector such as neutrinos or potentially new weakly interacting particles are not reconstructed but contribute to the missing transverse momentum of the event. Below the identification and reconstruction of tracks, vertices, jets, electron, photons, muons and missing transverse energy are discussed. ATLAS is also able to reconstruct heavier particles that are not on this list through their decay products.

3.3.1 Tracks and vertices

Generally, tracks are identified and reconstructed with the inner detector. The exceptions are muon tracks, which are recorded with both the muon spectrometer and the inner detector. The actual measurement of a track is a series of hits in the IBL, pixel detector, SCT and TRT. A hit is an electronic signal caused by a traversing particle at a particular space point. Because of the magnetic field that permeates the ID, the tracks of charged particles are bent, which is crucial for the p_{T} measurement.

The reconstruction of a track is a multistep process. First, the hits are converted into points in the three dimensional coordinate system of the detector. With three space points in either the pixel detector or three in the SCT a so-called seed is defined as the starting point for the tracks. Then, under the assumption of a helical trajectory, the Kalman filter algorithm [96] assigns other hits to the hypothesized track. Often a track also has holes, which are space points where a hit is expected given the trajectory determined from the other hits but no hit is found. Furthermore, there can also be shared hits, which are associated with multiple tracks. Tracks are also identified by starting with hits in the TRT and back-tracking to the innermost subdetectors.

Sometimes a signal is mistaken as a track, in which case it is called a fake track. A set of quality criteria (at least nine hits, no holes in the pixel detector, track $p_{\mathrm{T}} > 400$ MeV) are used to lessen the amount of fake tracks in the final dataset [97].

There is also a categorization into primary tracks, which originate from the hard proton–proton interaction, and secondary tracks, which originate from decaying long-lived particles. The location where a proton–proton interaction takes place is called a primary vertex, the location of a particle decay is a secondary vertex. To discern between the two is important for the reconstruction of the event topology and identification of long-lived particles such as b quarks.

Another important step in reconstructing the correct event topology is finding the right vertex to each track and particle. To do so all primary vertices are reconstructed by using an iterative algorithm [98]. The primary vertex is seeded by fitting to tracks that originate from a certain z position on the beam line, further vertices are added for the tracks that are displaced from the primary vertex. The resolution of this measurement improves with the number of tracks that can be associated with the vertex and ranges between 2 mm and 30 μm.

The quality of a track can partially be quantified with the longitudinal and transverse impact parameters z_0 and d_0. The distance of the track from the primary vertex in the z direction is z_0 and d_0 is defined as the distance between primary vertex and track in the transverse plane. The transverse impact parameter divided by its uncertainty ($|d_0|/\sigma(d_0)$) is the d_0 significance. These three properties of a track are used as primary vertex consistency criteria as is done in Section 5.4.3. Analyses can use different criteria depending on the requirements of the search.

3.3.2 Jets

Hadron collisions can produce colour charged particles and because hadrons are composites of such particles this occurs at a high rate. Since gluons and quarks are both subject to confinement, their production immediately leads to the process of hadronization, which triggers a cascade of reactions and emerging particles, which are measured as jets (see Section 2.1.4 for the discussion of confinement and hadronization from a theoretical point of view.).

Jets are generally defined as a "collimated spray of hadrons" [99]. Their reconstruction is non-trivial because the goal is to identify the properties of the one parton that initiates the jet,

which can never be measured directly. Instead, energy deposits in the calorimeter are identified and a pattern recognition algorithm is employed to group all the deposits consistent with being produced due to the hadronization of the initial parton. There are multiple reconstruction algorithms for jets and the most important ones used in ATLAS are discussed below. After the reconstruction the jet has to go through the process of jet calibration, which is the subject of Chapter 4. During calibration the jet four momentum is corrected for detector effects, pile-up and biases in the reconstruction.

When predicting the number of final state jets (jet multiplicity) of a process under study, initial state radiation (ISR) and final state radiation (FSR) have to be taken into account. The two processes are illustrated in Figure 3.12. In both cases one of the colour charged particles that takes part in the hard interaction emits another colour charged particle that causes an additional jet.

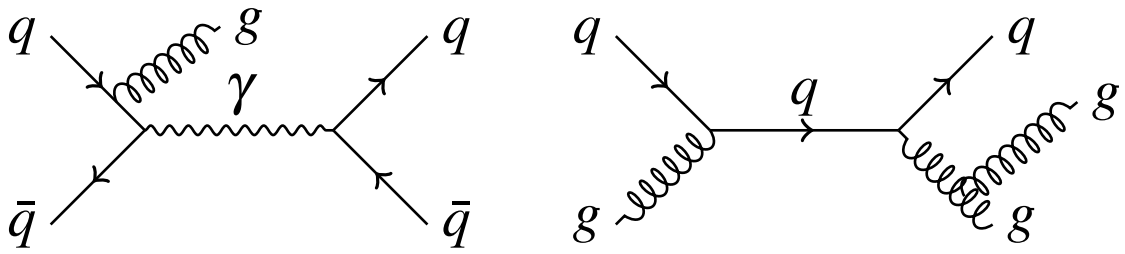

Figure 3.12: Example diagrams containing either initial (left) or final (right) state radiation. The diagrams show quark-quark and quark-gluon scattering, respectively.

Jet reconstruction

Jet reconstruction is based on a method called clustering and begins by identifying calorimeter cells with large cell signal significance $\zeta_{\text{cell}}^{\text{EM}}$, which is defined as:

$$\zeta_{\text{cell}}^{\text{EM}} = \frac{E_{\text{cell}}^{\text{EM}}}{\sigma_{\text{cell}}^{\text{EM}}}, \tag{3.5}$$

where $E_{\text{cell}}^{\text{EM}}$ is the energy excess over the noise threshold that is deposited in the cell or, in other words, the cell signal. The quantity $\sigma_{\text{cell}}^{\text{EM}}$ is the standard deviation of the expected noise in the cell. The calorimeters record a lot of noise both from pile-up and regular detector noise. Therefore, interesting cell signals are those with large deposited energy compared with the noise. The cell noise is measured separately from the regular data taking in the absence of a signal.

The first step of clustering is to seed what is later called a topological cluster (topocluster) with cells in which $\zeta_{\text{cell}}^{\text{EM}} > 4$. Then all cells with $\zeta_{\text{cell}}^{\text{EM}} > 0$ that are adjacent within the same calorimeter layer or have overlap in the η-ϕ plane and are in neighbouring layers, are added to these proto-clusters. If a neighbouring cell also fulfils $\zeta_{\text{cell}}^{\text{EM}} > 2$, its neighbours are added as well. This process is repeated until no suitable neighbours are found. Proto-clusters with different seeds often merge as part of this process. The procedure is illustrated in Figure 3.13.

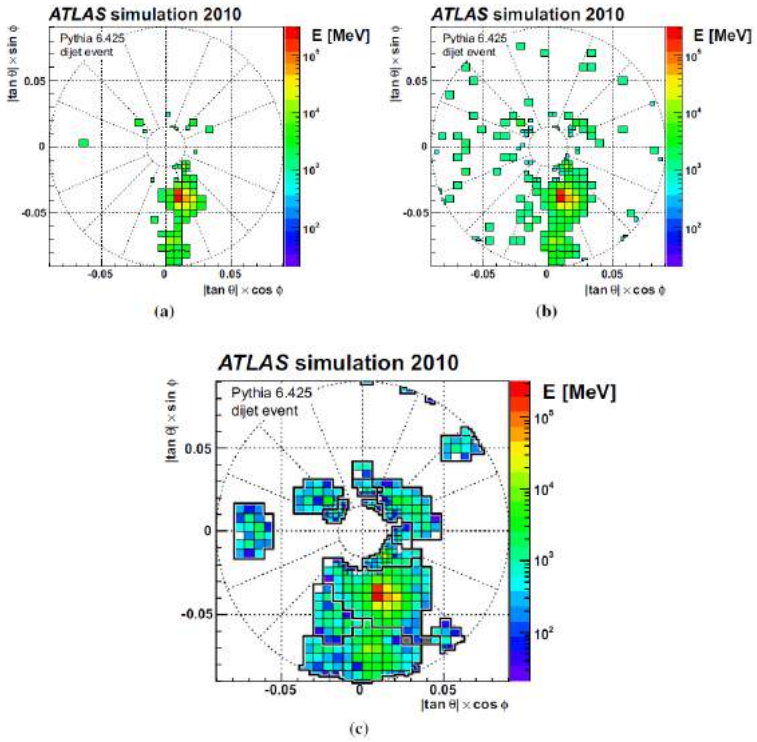

Figure 3.13: Steps of topological clustering: all cells with $\zeta_{\text{cell}}^{\text{EM}} > 4$ that seed the topoclusters (a), cells with $\zeta_{\text{cell}}^{\text{EM}} > 2$ that grow the topoclusters (b), final topoclusters (c). The illustration was generated with simulated dijet events and cell signals in the first layer of the forward calorimeter (FCal0) [100].

The so-determined topoclusters are the input of the anti-k_t algorithm [101]. This algorithm reconstructs jets in an iterative process based on the distances d_{ij} between the entities i and j. These entities can either be particles identified from topoclusters or pseudojets. The latter are combinations of two or more particles. In addition the algorithm defines the distance between i and the beam line as d_{iB}. If the distance d_{ij} between the two entities is smaller than the distance to the beam line d_{iB}, i and j are merged into one entity. If the distance d_{iB} is smaller, i is called a jet and removed from the process. This is repeated with the remaining entities until none are left. The definition of d_{ij} and d_{iB} distinguishes this algorithm from other jet reconstruction algorithms:

$$d_{ij} = \min(p_{\mathrm{T},i}^{-2}, p_{\mathrm{T},j}^{-2}) \frac{\Delta_{ij}^2}{R^2}, \tag{3.6}$$

$$d_{iB} = p_{\mathrm{T},i}^{-2}, \tag{3.7}$$

where $\Delta_{ij}^2 = \Delta y^2 + \Delta\phi^2 = (y_i - y_j)^2 + (\phi_i - \phi_j)^2$ and R is the distance parameter. It can take different values depending on the experiment. Usually in ATLAS it is set to $R = 0.4$. As a result jets reconstructed with the anti-k_t algorithm take the shape of cones with the size $R = 0.4$. In the case of overlap between jets there are deviations from the cone form. The algorithm is constructed in a way that low-p_{T} particles cluster around high-p_{T} particles, before they cluster amongst themselves. This is all but ensured by weighting the distance with the minimum of the two transverse momenta. In practice the algorithm is run with the `FastJet` [102] program. Only jets with $p_{\mathrm{T}} > 20$ GeV and $|\eta| < 4.5$ are used.

Jet collections

Using topoclusters as the input of the anti-k_t algorithm is just the general case, which has a number of variations. Different reconstruction methods have their outputs collected in different jet collections. The most important ones are discussed here.

The calorimeter has a certain response, which leads to the fact that energies recorded with it are not necessarily measured at the correct scale. Getting the right scale requires calibration. The topoclusters described above are initially calibrated at the electromagnetic (EM) scale, which is the correct scale for photons and electrons. Hence, the thus reconstructed jets get the name EM topocluster jets or EMTopo jets for short.

There are multiple ways to calibrate jets to the correct energy scale. The calibration of EM scale jets for example is discussed in detail in Chapter 4. Another possibility is the local hadronic cell weighting (LCW) of topoclusters [100]. The calibration attempts to account for the signal loss resulting from discrete topocluster thresholds and energy losses in uninstrumented or inactive material. The LCW starts with the topocluster formation. Since topoclusters can overlap, some cells record energy from two of them. A geometrical weight $w_{\mathrm{cell}}^{\mathrm{geo}}$ is used to divide the signal in the cell between the different clusters.

The severity of the influence of detector effects on the measurement depends on whether an energy deposit is caused by hadronic or electromagnetic particles. This is accounted for with the weight $w_{\mathrm{cell}}^{\mathrm{cal}}$, which is applied to every cell signal independently. It is defined as:

$$w_{\mathrm{cell}}^{\mathrm{cal}} = \mathscr{P}_{\mathrm{clus}}^{\mathrm{EM}} \cdot w_{\mathrm{cell}}^{\mathrm{em-cal}} + (1 - \mathscr{P}_{\mathrm{clus}}^{\mathrm{EM}}) \cdot w_{\mathrm{cell}}^{\mathrm{had-cal}}, \tag{3.8}$$

where $\mathscr{P}_{\mathrm{clus}}^{\mathrm{EM}}$ is the probability for a given topocluster to have electromagnetic origins and conversely $(1 - \mathscr{P}_{\mathrm{clus}}^{\mathrm{EM}})$ is the probability for the hadronic case. The likely origin is determined from

the depth and the cell signal density of the topocluster. The weights $w_{\text{cell}}^{\text{em}-\text{cal}}$ and $w_{\text{cell}}^{\text{had}-\text{cal}}$ correspond to the electromagnetic and hadronic calibration. Determining their value is a multistep process, which both reweights the entire cluster and local cells. The complete local hadronic cell weighting scheme is summarized in Figure 3.14.

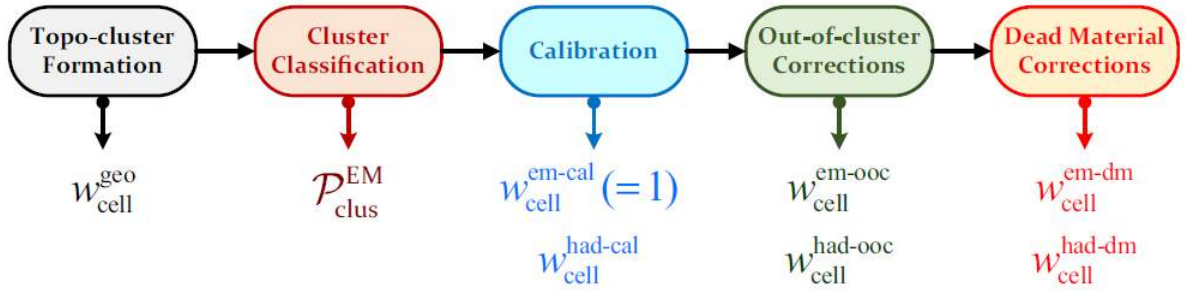

Figure 3.14: Summary of the steps in the local hadronic cell weighting. The value $w_{\text{cell}}^{\text{geo}}$ is the geometrical weight, $\mathcal{P}_{\text{clus}}^{\text{EM}}$ is the probability for a given cluster to be electromagnetic, $w_{\text{cell}}^{\text{em}-\text{cal}}$ and $w_{\text{cell}}^{\text{had}-\text{cal}}$ are weights that reweight the clusters cell by cell to the correct energy scale. The values $w_{\text{cell}}^{\text{em}-\text{ooc}}$ and $w_{\text{cell}}^{\text{had}-\text{ooc}}$ are the out-of-cluster correction factors, and $w_{\text{cell}}^{\text{em}-\text{dm}}$ and $w_{\text{cell}}^{\text{had}-\text{dm}}$ correct for energy losses in uninstrumented regions [100].

In the out-of-cluster correction the energy loss resulting from incorrect assignment of cells to topoclusters is estimated using single-particle simulations. The out-of-cluster correction factors $w_{\text{cell}}^{\text{em}-\text{ooc}}$ and $w_{\text{cell}}^{\text{had}-\text{ooc}}$ correct for this effect. Finally, the dead-material corrections assign a reweighting based on the signal loss due to jets depositing energy in uninstrumented regions of the detector. Like the out-of-cluster corrections this effect is estimated with single-particle simulations.

A third and final possible input to the jet reconstruction algorithms such as anti-k_t are particle flow (PFlow) jets. Particle flow jets use ID tracks in addition to the exact same EM scale topoclusters that are discussed above. The use of ID tracks makes EM scale particle flow jets fundamentally different from EM scale topocluster jets and LCW jets. The purpose is to modify topoclusters by subtracting the energy of particle tracks they contain. The rough outline of how topocluster and tracking information is used to obtain the input for the jet algorithm is shown in Figure 3.15. It is important to note that most tracks associated with a jet are charged pions [104]. As a result the charged pion energy scale and mass is assumed in the following.

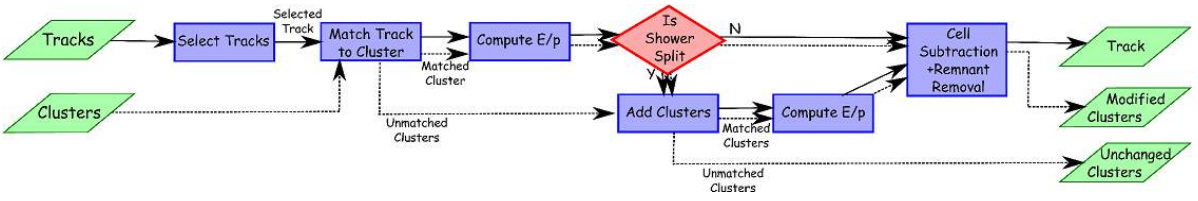

Figure 3.15: Flow chart illustrating the reconstruction of particle flow jets from tracks and topoclusters. The solid arrows describe the flow of tracking information. The dashed arrows describe the flow of topocluster information [103].

Before tracks can be selected and matched to topoclusters several cases have to be taken into account: The simplest one is that a particle deposits all of its energy in a single topocluster.

However, it can also be the case that one particle contributes to multiple clusters or that multiple particles contribute to a single cluster. Unsurprisingly, the particles that contribute to multiple topoclusters tend to be high-p_{T}.

The steps of the particle flow algorithm as named in Figure 3.15 are explained below:

- Select Tracks: a number of quality criteria are demanded of the tracks that are considered for the jet reconstruction. They are required to have $0.5 < p_{\mathrm{T}} < 40$ GeV, $|\eta| < 2.5$ and at least nine hits in pixel detector and SCT without any holes. Furthermore, they may not be matched to electrons or muons because the jet reconstruction algorithm is solely concerned with the subtraction of hadronic showers.

- Match Track to Cluster: the selected tracks are matched to the closest topoclusters with the smallest distance in $\Delta R'$ as long as $\Delta R' < 1.64$. The distance parameter $\Delta R'$ is defined as:

$$\Delta R' = \sqrt{\left(\frac{\Delta\phi}{\sigma_\phi}\right)^2 + \left(\frac{\Delta\eta}{\sigma_\eta}\right)^2}, \tag{3.9}$$

  where σ_ϕ and σ_η are the angular widths of the topocluster defined as one standard deviation from its centre. By using $\Delta R'$ as opposed to ΔR, cases in which a topocluster is wider as a result of containing multiple particles are accounted for.

- Compute E/p: this step has the purpose of determining the average energy of a track with momentum p. This is done with single-particle simulations covering different regions of p_{T} and $|\eta|$ to account for detector effects. Furthermore, the layer with the largest energy density of a topocluster is used as a starting point for the energy subtraction in the core of the topocluster to avoid possible irregularities at the margins.

- Is Shower Split: The discriminating variable for this question is the significance ($S(E^{\mathrm{clus}})$) of the difference between the energy that is expected for the shower and the energy deposited in the matched topocluster. It is defined as:

$$S(E^{\mathrm{clus}}) = \frac{E^{\mathrm{clus}} - < E_{\mathrm{dep}} >}{\sigma(E_{\mathrm{dep}})}, \tag{3.10}$$

  where E^{clus} is the energy of the matched topocluster, $< E_{\mathrm{dep}} >$ is the average energy deposited by the shower given its momentum and $\sigma(E_{\mathrm{dep}})$ is its spread. If $S(E^{\mathrm{clus}}) < -1$ the shower is considered to be part of multiple topoclusters and the split shower recovery procedure is run.

- Cell Subtraction: a p_{T} and η dependent profile of the shower shape is parametrized using the expectation from MC simulations. Starting with the cell with the highest energy density, cells are removed one after the other until they collectively account for $< E_{\mathrm{dep}} >$ of the shower. The subtraction is sequenced in concentric rings around the highest density cell.

- Remnant Removal: the remaining topocluster cells are examined. If the total energy deposited in them is less than $1.5\sigma(E_{dep})$, it is assumed that this is caused by fluctuations and they are removed. Otherwise the remnants of the topocluster are kept under the assumption that other particles caused it.

Finally, as an input to the anti-k_t algorithm the particle flow jet collection delivers a set of shower tracks, topocluster remnants and unmatched topoclusters without significant overlap between the ID and calorimeter information. The performance of the relatively new particle flow algorithm compared with other jet collections is discussed in Section 4.3.2.

There is also the possibility of using the particle flow algorithm together with LCW topoclusters, which could yield better results due to the jet reconstruction profiting from both corrections. This, however, requires further development [103].

Other jet reconstruction algorithms

Not only are multiple jet collections in use as possible inputs of the anti-k_t algorithm with distance parameter $R = 0.4$, there are also multiple examples of algorithms with their own advantages and disadvantages.

- Large-R jets: These use the anti-k_t algorithm with distance parameter $R = 1.0$. As a result they are more likely to pick up pile-up in the huge cone radius. By identifying smaller ($R = 0.2$) sub-jets a so-called grooming procedure is employed to remove everything that is not a hard jet. The fact that these jets often contain many smaller sub-jets is intended because they are used to capture all hadronic decay products of heavy particles. The input topoclusters are usually LCW jets [105].

- Small-R jets: These are defined as jets reconstructed with distance parameter $R \leq 0.6$ in contrast to large-R jets. The reason for the use of small-R jets is to avoid pile-up effects. The most commonly used distance parameter in ATLAS is $R = 0.4$, but analyses with large pile-up sensitivity may use even smaller values [106].

- Variable-R jets: Aimed at highly energetic heavy decaying particles variable-R jets can be used as an alternative to large-R jets. Their distance parameter is variable and proportional to $1/p_{\mathrm{T}}$. The dependence of R on p_{T} is determined from empirical observations about the behaviour of the angular separation of jets in dependence of p_{T} [107].

Jet cleaning

There are multiple phenomena that can cause signatures similar to jets without corresponding to colour charged particles produced in the hard interaction. There is for example non-collision background from cosmic rays or protons that are lost from the proton bunch. There is also potential noise in the calorimeter. If these phenomena cause signals that are reconstructed as a jet, they are called fake jets as opposed to good jets that are actual hadronic showers caused by proton–proton scattering.

With a series of selection cuts on certain variables a high jet quality is ensured. These variables are especially suitable for discriminating between good and fake jets. Examples for discriminating variables are the fraction of energy deposited in the hadronic end-cap or the

maximum energy fraction in one calorimeter layer. The tighter these quality criteria are, the more fake jets are successfully rejected but at the same time more good jets are lost. Different analyses might favour a higher good-jet efficiency or a better fake-jet rejection. Therefore, two jet quality working points are provided: loose and tight also referred to as JetCleanLoose and JetCleanTight [108].

Common objects producing jets

Jets often result from decays of heavy particles. Dedicated strategies are employed to accurately reconstruct the original particle:

- Bottom quarks: B-hadrons have a long lifetime and as a result travel a few millimetres before they decay. This causes a displaced secondary vertex with large impact parameter d_0. The B-hadrons are identified in the process of b-tagging. It relies on the ID for tracking and secondary vertex identification. With multivariate-based algorithms such as MV2c10 jets are identified as b jets using this information [109].
- τ leptons: The heaviest lepton can decay hadronically in which case it produces jets, which can be reconstructed with the methods presented above. To discern them from regular gluon and light-quark jets boosted decision trees are used to optimize the discriminating cuts [110].
- Top quarks: Because they decay instantly, top quarks are reconstructed from their decay products such as b-quarks and leptons [111].

Pile-up

Since the proton beams collide with each other in bunches of 1.15×10^{11} hadrons, there are typically multiple proton–proton collisions in one event. The phenomenon of multiple inelastic pp collisions happening within the same bunch is called in-time pile-up. Because there are only 25 ns between two bunch crossings and the read-out of detector signals takes some amount of time, signals from neighbouring bunch crossings can potentially be measured in the current event, which is called out-of-time pile-up.

Pile-up is a problem for the reconstruction of particle interactions because it makes it more difficult to reconstruct the primary vertex of the hard interaction, and therefore it becomes harder to measure the angular direction of particle tracks. The number of interactions per bunch crossing follow a poisson distribution with the mean μ, a measure for the total pile-up. The amount of in-time pile-up is often given as the number of primary vertices in an event N_{PV}.

The correct identification of primary vertices is an on-going effort described for example in Ref. [112]. It is especially important for the jet reconstruction to discern hard scatter from pile-up jets. In Run 1 the separation between pile-up and hard scatter jets was done using the jet vertex fraction (JVF) as a discriminating variable [113]. The JVF is defined as:

$$\mathrm{JVF}(\mathrm{jet}_i, \mathrm{PV}_j) = \frac{\sum_k p_{\mathrm{T}}(\mathrm{track}_k^{\mathrm{jet}_i}, \mathrm{PV}_j)}{\sum_l \sum_n p_{\mathrm{T}}(\mathrm{track}_l^{\mathrm{jet}_i}, \mathrm{PV}_n)}, \tag{3.11}$$

where JVF is defined for each jet i relative to a primary vertex j. The index k is running over all tracks with $p_{\mathrm{T}} > 500$ MeV that originate from the primary vertex j and can be matched to

the jet i. The index n accounts for all primary vertices in the event and l is running over tracks associated with primary vertex n and jet i. The higher the JVF score of a jet, the more likely it is to be a hard scatter jet. There are three recommended JVF cut alternatives at 0.0, 0.25 and 0.5. The three options are provided to weigh reconstruction efficiency against background rejection depending on the analysis [113].

With this method the efficiency of selecting a hard scatter jet depends on the number of primary vertices in the event N_{PV}. Since the beginning of Run 2 this issue is addressed by employing a multivariate technique using the jet vertex tagger (JVT) [114, 115]. To do so two new variables are defined. The first one is corrJVF, which is a variant of the JVF but corrected for the N_{PV} dependence:

$$\mathrm{corrJVF}^{i} = \frac{\sum_k p_{\mathrm{T}}(\mathrm{track}_k^{\mathrm{jet}_i}, \mathrm{PV}_0)}{\sum_l p_{\mathrm{T}}(\mathrm{track}_l^{\mathrm{jet}_i}, \mathrm{PV}_0) + \frac{\sum_{n\geq 1}\sum_l p_{\mathrm{T}}(\mathrm{track}_l^{\mathrm{jet}_i}, \mathrm{PV}_n)}{0.01 \cdot n_{\mathrm{trk}}^{\mathrm{PU}}}}, \tag{3.12}$$

where PV_0 is the first primary vertex, $n_{\mathrm{trk}}^{\mathrm{PU}}$ is the number of pile-up tracks and 0.01 is a scaling factor determined from the slope of the average scalar sum p_{T} of all pile-up tracks ($< p_{\mathrm{T}}^{\mathrm{PU}} >$) as a function of $n_{\mathrm{trk}}^{\mathrm{PU}}$. In addition, the ratio $R_{p_{\mathrm{T}}}$ of the scalar p_{T} sum of all tracks that originate from the first primary vertex while being associated with the jet and the jet transverse momentum is defined as:

$$R_{p_{\mathrm{T}}}^{i} = \frac{\sum_k p_{\mathrm{T}}(\mathrm{track}_k^{\mathrm{jet}_i}, \mathrm{PV}_0)}{p_{\mathrm{T}}^{\mathrm{jet}_i}}. \tag{3.13}$$

Afterwards the JVT is derived as a combination of the two variables and it is optimized to distinguish pile-up from hard scatter jets. Jets with a high JVT score are most likely to be hard scatter jets similar to the JVF criterion above. The jets that are separated with the JVF or JVT already underwent the calibration described in Chapter 4.

The JVT can only be applied to jets within the ID acceptance ($|\eta| < 2.5$) due to the use of tracking information. In the future the forward JVT (fJVT) technique promises to shore up this weakness by exploiting correlations between central and forward jets [116].

3.3.3 Other physics objects

Electrons and photons

The reconstruction of electrons[4)] and photons is linked because both of them deposit almost all of their energy in the electromagnetic calorimeter and very little in the hadronic calorimeter. When interacting with the detector material, electrons can radiate some of their energy through bremsstrahlung, which creates photons. The photons on the other hand can undergo electron pair production. These two mechanisms can cause a cascade of electromagnetic particles, which is not as wide and particle-rich as the jets resulting from hadronization.

For central electrons ($|\eta| < 2.47$) the reconstruction works by matching ID tracks to clusters in the electromagnetic calorimeter [117]. If a cluster cannot be matched to a track, it is considered a photon candidate. The clusters are seeded in windows of 3×5 towers. A tower is a segment of a grid in the $\eta \times \phi$ direction with a size of $\Delta\eta \times \Delta\phi = 0.025 \times 0.025$. The

[4)] The word "electron" is used interchangeably for electrons and positrons in this work.

track reconstruction is based on the conversion of hits in the ID into three dimensional space points, before matching them to the expected patterns of bent trajectories. After track matching the window size is increased to 3×7 and 5×5 in the barrel and end-cap, respectively. Over the course of the reconstruction the matching requirements become stricter to discern electrons from converted photons. Among other requirements additional TRT hits are demanded.

Electrons are separated from fake electrons by fulfilling a set of identification criteria, which are constructed to deliver an efficiency of 95%, 90% and 80%, respectively. They are referred to as loose, medium and tight working points [118]. The tighter working points have the better background rejection compared to the higher reconstruction efficiency looser working points offer. The selection efficiency is measured by studying the well-understood $Z \to ee$ and $J/\psi \to ee$ processes [119, 120]. Fake electrons can be misidentified pions, jets or other charged particles.

Furthermore, three isolation requirements help many analyses in gaining a better background rejection. For the first requirement the energy that is deposited in the electromagnetic calorimeter within $\Delta R = 0.2$ around the electron candidate is the discriminating variable. The other two concern the shower shape and the activity of other tracks in the vicinity of the matched track within $\Delta R = \min(0.2, 10\ \text{GeV}/E_\text{T})$, where E_T is the transverse energy of the electron.

Both electrons and photons follow the same calibration scheme. It compensates for the non-uniformity of the detector response by applying correction factors that depend on the longitudinal electromagnetic calorimeter layer an electron is measured with. The energy resolution is improved by using a multivariate boosted decision tree with multiple input variables in simulation. An additional energy scale calibration is derived in $Z \to ee$ events in data [121].

Muons

In order to reconstruct muons, signals from both the ID and the muon system are used. First, tracks are identified in each of the subdetectors individually. Then the information is combined to enhance the angular resolution. The track finding in the ID is the same as that of electrons and other charged particles.

In the muon system hits in each of the subsystems MDT, TGC, RPC and CSC are fed into a search algorithm to reconstruct segments. Afterwards the segments in different layers are combined into track candidates requiring at least two matching segments in the barrel and only one if the particle is detected in the barrel-end-cap. Segments can initially be part of multiple track candidates before the most promising ones are selected. A global fit combines the hits of each track candidate and only track candidates that fulfil selection criteria on fit quality and the number of hits are kept. A more detailed discussion of the muon reconstruction in ATLAS can be found in Ref. [122].

For the combination of muon system and ID tracks four types of muons are considered in order to reconstruct each with one of four specialized algorithms:

- Combined (CB) muons: Here, the hits in ID and muon system are combined with one fit. This is done either by extrapolating muon system tracks to the ID or vice versa.

- Segment-tagged (ST) muons: In case the muon crosses only one layer of the muon system or is so low-p_T that it does not reach further into the subdetector, the ID track is matched to a single segment in the MDT or CSC.

- Calorimeter-tagged (CT) muons: In pseudo-rapidity ranges where the muon system has many uninstrumented regions (mostly $|\eta| < 0.1$) an ID track can be matched to a calorimeter energy deposit to recover lost acceptance.

- Extrapolated (ME) muons: The region $2.5 < |\eta| < 2.7$ is out of acceptance of the ID, but tracks in the muon system are still reconstructed here. They serve as muon candidates if they pierce through two layers in the muon system and point to the interaction point.

In case of overlaps of different muon types priority is given in the order CB $\rightarrow$ ST $\rightarrow$ CT from highest to lowest. ME muons take priority over all others if they have a better fit quality and a larger number of hits.

In order to separate prompt muons from hadron decay products and other backgrounds four muon identification working points are provided to analysis teams. Loose, medium and tight are inclusive selections based on the number of hits, muon type and other criteria. This means that tight muons also pass the medium selection and medium muons also pass the loose selection. High p_{T} muons are a fourth, separate category that maximizes the resolution of muons with $p_{\mathrm{T}} > 100$ GeV. Here, muon system regions with imperfect alignments are excluded. Medium is the default selection and has an identification efficiency of more than 95%. This is measured in $Z \rightarrow \mu\mu$ and $J/\psi \rightarrow \mu\mu$ events.

Muons that are decay products of heavy particles like W, Z and Higgs bosons are typically well isolated but muons from semi-leptonic decays are not. Therefore, muon isolation can help distinguish between the two. Similar to the electron isolation requirements the most important variables are the signal activity in the calorimeter within $\Delta R = 0.2$ and the tracks within $\Delta R = \min(0.3, 10 \text{ GeV}/p_{\mathrm{T}})$. There are a total of seven isolation working points with different thresholds on the aforementioned requirements currently in use: LooseTrackOnly, Loose, Tight, Gradient, GradientLoose, FixedCutTightTrackOnly and FixedCutLoose [122].

The muon calibration follows a recipe similar to the electron/photon calibration. The correction factors are derived using Z and J/ψ decays again. However, as opposed to the electron calibration no corrections are applied to data.

3.3.4 Missing transverse energy

Not all objects that are produced in hadron collisions can be reconstructed with the ATLAS detector. Neutrinos and potentially particles that are not part of the SM may elude detection. However, because of momentum conservation in the transverse plane there is the possibility to infer their existence via missing transverse energy ($E_{\mathrm{T}}^{\mathrm{miss}}$). This describes so-called real $E_{\mathrm{T}}^{\mathrm{miss}}$. There is also fake $E_{\mathrm{T}}^{\mathrm{miss}}$ resulting from mismeasurements of physics objects. A more detailed discussion of the $E_{\mathrm{T}}^{\mathrm{miss}}$ reconstruction in ATLAS can be found in Ref. [123].

There is also a distinction between the missing transverse momentum ($\vec{p}_{\mathrm{T}}^{\mathrm{miss}}$), which is the negative vectorial sum of all reconstructed objects in the event as defined in Eq. 3.14, and its magnitude the missing transverse energy ($E_{\mathrm{T}}^{\mathrm{miss}}$):

$$\begin{aligned}
\vec{p}_{\mathrm{T}}^{\mathrm{miss}} &= -\sum_{e} \vec{p}_{\mathrm{T}}^{e} - \sum_{\mu} \vec{p}_{\mathrm{T}}^{\mu} - \sum_{\gamma} \vec{p}_{\mathrm{T}}^{\gamma} - \sum_{\tau} \vec{p}_{\mathrm{T}}^{\tau} - \sum_{\mathrm{jet}} \vec{p}_{\mathrm{T}}^{\mathrm{jet}} - \sum_{\mathrm{track}} \vec{p}_{\mathrm{T}}^{\mathrm{track}} \\
&= \vec{E}_{\mathrm{T}}^{\mathrm{miss},e} + \vec{E}_{\mathrm{T}}^{\mathrm{miss},\mu} + \vec{E}_{\mathrm{T}}^{\mathrm{miss},\gamma} + \vec{E}_{\mathrm{T}}^{\mathrm{miss},\tau} + \vec{E}_{\mathrm{T}}^{\mathrm{miss,jet}} + \vec{E}_{\mathrm{T}}^{\mathrm{miss,soft}} \\
&= \vec{E}_{\mathrm{T}}^{\mathrm{miss,hard}} + \vec{E}_{\mathrm{T}}^{\mathrm{miss,soft}},
\end{aligned} \tag{3.14}$$

where $\vec{p}_{\mathrm{T}}^{\,i}$ is the transverse momentum of an object i, $\vec{E}_{\mathrm{T}}^{\mathrm{miss,soft}}$ is the vectorial sum of the transverse momenta of all tracks or topoclusters that cannot be matched to any physics object and $\vec{E}_{\mathrm{T}}^{\mathrm{miss,hard}}$ is the vectorial sum of all reconstructed particles and jets in the event.

$\vec{E}_{\mathrm{T}}^{\mathrm{miss,soft}}$ is called the soft term. It is mostly comprised of objects below reconstruction thresholds. There are two main approaches to determining the soft term:

- Calorimeter soft term (CST): Here, the calorimeter topoclusters that cannot be associated with physics objects are combined into the negative soft term. They follow the LCW calibration of jets regarding the energy scale.

- Track soft term (TST): The tracks that are not matched to physics objects form the basis of this term. Tracks that are close to physics objects or can be assigned to jets are excluded from this. All the tracks under consideration must be matched to the first primary vertex, which makes the definition relatively resistant to pile-up.

Resulting from this there are two $E_{\mathrm{T}}^{\mathrm{miss}}$ definitions called TST $E_{\mathrm{T}}^{\mathrm{miss}}$ and CST $E_{\mathrm{T}}^{\mathrm{miss}}$. A third option is the so-called track $E_{\mathrm{T}}^{\mathrm{miss}}$, which uses tracking information for both the hard and the soft term. This ignores the contributions of neutral particles and objects out of the acceptance of the ID ($|\eta| < 2.5$). However, the definition also leads to an excellent pile-up resistance. TST $E_{\mathrm{T}}^{\mathrm{miss}}$ is favoured in Run 2 because a higher luminosity leads to more pile-up and thus the resistance against pile-up gains ever more importance.

The $E_{\mathrm{T}}^{\mathrm{miss}}$ definitions gain an ever greater variety when considering the fact that all object definitions of a physics study affect $E_{\mathrm{T}}^{\mathrm{miss}}$. Some analyses (like the one described in Chapter 5) may even exclude objects from the hard term for some of their studies.

Performance

The $E_{\mathrm{T}}^{\mathrm{miss}}$ performance is generally tested with $E_{\mathrm{T}}^{\mathrm{miss}}$ distributions of simulated $Z \to ee$ or $Z \to \mu\mu$ events, since neither of these processes cause real $E_{\mathrm{T}}^{\mathrm{miss}}$. The $E_{\mathrm{T}}^{\mathrm{miss}}$ resolution can be measured as the standard deviation of an $E_{\mathrm{T}}^{\mathrm{miss}}$ distribution, while a non-vanishing mean would hint at a bias. CST $E_{\mathrm{T}}^{\mathrm{miss}}$ typically produces higher $E_{\mathrm{T}}^{\mathrm{miss}}$ as a result of pile-up. TST $E_{\mathrm{T}}^{\mathrm{miss}}$ and Track $E_{\mathrm{T}}^{\mathrm{miss}}$ are very similar in the absence of additional jets. At high jet multiplicities Track $E_{\mathrm{T}}^{\mathrm{miss}}$ produces larger tails.

The $E_{\mathrm{T}}^{\mathrm{miss}}$ scale is tested with simulated $W \to e\nu$ and $W \to \mu\nu$ events because of the presence of real $E_{\mathrm{T}}^{\mathrm{miss}}$. An evaluation shows that track $E_{\mathrm{T}}^{\mathrm{miss}}$ underestimates the scale at high values, but TST and CST $E_{\mathrm{T}}^{\mathrm{miss}}$ are both within 5% of the correct scale [123].

To discern between fake and real $E_{\mathrm{T}}^{\mathrm{miss}}$ the so-called missing transverse momentum significance $\mathscr{S}$ is defined. It is a measure for the likelihood that the $E_{\mathrm{T}}^{\mathrm{miss}}$ is caused by invisible particles as opposed to mismeasurements and resolution effects. This is calculated by taking the resolution of each constituent object of the $E_{\mathrm{T}}^{\mathrm{miss}}$ calculation given its four momentum into account [124].

Systematic uncertainties

Because $E_{\mathrm{T}}^{\mathrm{miss}}$ is a sum of multiple terms, its systematic uncertainty is also propagated from the individual contributions. The systematic uncertainty of the hard term is a result of the

systematic uncertainty estimation for each of the physics objects. This only leaves the soft term to be considered. Since only TST $E_{\mathrm{T}}^{\mathrm{miss}}$ is used in the following chapters, only its systematic uncertainty calculation is presented here.

The uncertainty estimation is based on the variable $\vec{p}_{\mathrm{T}}^{\,\mathrm{hard}}$, which is the vectorial sum of all hard objects in the event including neutrinos as defined in:

$$\vec{p}_{\mathrm{T}}^{\,\mathrm{hard}} = \sum_{e} \vec{p}_{\mathrm{T}}^{\,e} + \sum_{\mu} \vec{p}_{\mathrm{T}}^{\,\mu} + \sum_{\gamma} \vec{p}_{\mathrm{T}}^{\,\gamma} + \sum_{\tau} \vec{p}_{\mathrm{T}}^{\,\tau} + \sum_{\mathrm{jet}} \vec{p}_{\mathrm{T}}^{\,\mathrm{jet}} + \sum_{\nu} \vec{p}_{\mathrm{T}}^{\,\nu}. \tag{3.15}$$

Therefore, in the case of vanishing fake transverse momentum $\vec{p}_{\mathrm{T}}^{\,\mathrm{hard}}$ is the negative of the soft term. It follows that scale uncertainties of the soft term are visible only in the direction parallel to $\vec{p}_{\mathrm{T}}^{\,\mathrm{hard}}$ while resolution effects have components in longitudinal and transverse directions.

The systematic uncertainty is then estimated by comparing the root mean square and mean of the soft term both parallel and perpendicular to the $\vec{p}_{\mathrm{T}}^{\,\mathrm{hard}}$ axis between simulations made with different generators (an introduction into Monte Carlo simulation and event generators can be found in Section 3.4). The resulting uncertainties are largely on the order of 10% [123].

Overlap removal

It can occur that an object meets the identification requirements of two different objects. This is called overlap and is especially prevalent in jets because it is the nature of jets to spread in a wide cone that encompasses many constituents. In order to not count the energy and transverse momentum of a particle overlapping with a hadronic shower towards the jet, an overlap removal is employed on analysis level. This entails checking the jet for radial proximity to other objects.

The overlap removal is especially important for the calculation of $E_{\mathrm{T}}^{\mathrm{miss}}$ where physics objects of different kinds enter into the definition. Here, the overlap is typically removed at cell level. Cells that belong to two kinds of object are simply counted towards the first association [125]. The analysis discussed in Chapter 5 for example uses the overlap removal described below.

Electrons almost always also fit the criteria for a jet, since the jet algorithms search for energy deposits in both calorimeters. Therefore, if a jet's and an electron's angular direction coincide within $\Delta R = 0.2$, the electron is kept and the jet is removed. Conversely, if an electron is within $\Delta R = 0.4$ of a jet without fitting the other criterion, that electron candidate is likely to actually be a charged hadronic object that is part of the jet. It is therefore discarded.

In the case of an overlap between two kinds of objects usually the one with the tighter selection criteria is kept and the other one is removed. Following that logic a conflict between a muon and a jet within $\Delta R = 0.4$ of each other is resolved in one of two ways: If the jet has less than three associated tracks, it is removed and the muon is kept. If the jet has three or more associated tracks, the jet is kept and the muon is discarded.

3.4 Monte Carlo simulation

The link between the theoretical predictions presented in Chapter 2 and the data taking in the current chapter is MC simulation. MC simulations attempt to model the particle interactions after hadronic collisions from first principles. This is a challenging problem considering the

huge number of interactions from collisions to decays that have to be considered. As such the simulation is also a test of the current theoretical understanding of physics. Discrepancies between MC prediction and recorded data can hint at problems or new physics. With MC simulations it is also possible to implement physics beyond the Standard Model (BSM) to make predictions on how data would look like in the presence of new physics. Hypothesis testing would simply be impossible in high energy physics (HEP) without the help of simulation. A schematic of how a simulated dataset that is comparable to the recorded dataset is generated is depicted in Figure 3.16.

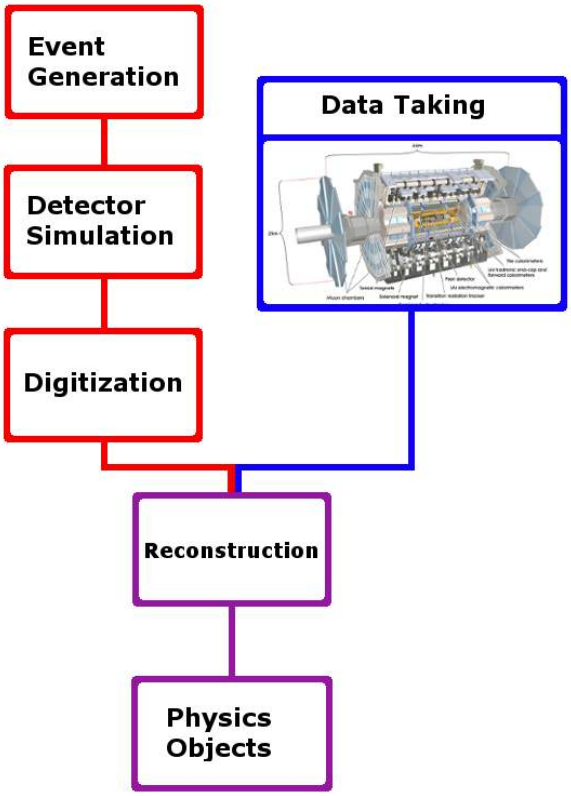

Figure 3.16: Schematic overview of the process chain that generates datasets. MC simulation exclusive steps (red). Data exclusive steps (blue). Common steps (purple).

Event generation is the process of simulating the interaction of particles from collisions to showering. This involves several steps, which are detailed below. Apart from that the detector itself and the particle interaction with the detector material have to be simulated. This is done with a toolkit such as `Geant4` (geometry and tracking) [126]. In order to get an actual electronic signal that can be compared with data the step called digitization is employed. It is after this step that pile-up modelling is added by overlaying the event with generic collision events. Afterwards MC simulation and recorded data have the same format. Therefore, the process of reconstruction can be done the same way for both simulation and data. Finally, the physics objects can be studied on an equal footing.

3.4.1 Event generation

The process of generating events is in itself highly non-trivial. Especially at hadron colliders due to the composite nature of the interacting objects, hundreds of particles are produced on a wide range of energy scales. The calculations that are necessary for the simulation have to make use of perturbative series (see Section 2.1.2 for an introduction) if that is applicable [127]. At the most simple level the calculations are done at leading-order (LO), which refers to the amount of vertices above two the underlying Feynman diagrams have. With the current technology it is often still practical to demand the precision of next-to-leading-order (NLO) or sometimes even higher orders (NNLO, N3LO, ...). The event generation of a hadron–hadron collision can be understood with the schematic in Figure 3.17 as a guideline.

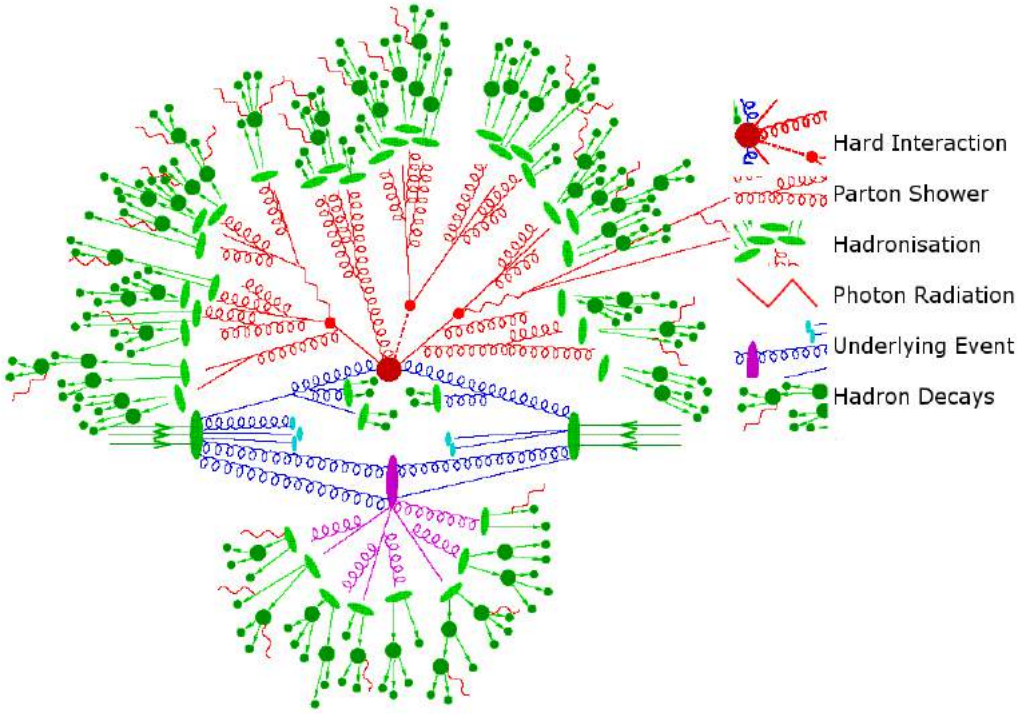

Figure 3.17: Simplified depiction of the MC simulation of a hadron–hadron collision. Hard interaction (dark red circle). Bremsstrahlung simulated by parton showers (light red curled lines). Secondary hard scattering event (purple). Parton to hadron transition (light green). Hadron decay (dark green). Soft photon radiation (red staggered) [128].

The event generation can thus be divided into five steps [128]:

- Hard scattering: This first step calculates the matrix element at a given order in perturbation theory. The matrix element is the result of the Feynman calculus and is proportional to the amplitude of the process (see Ref. [129] for a more detailed discussion). This is always done with an assumed model (the SM for example) and with the use of an event generator program. The physics process of interest and its cross-section is calculated as the interaction of the hadronic partons. Therefore, a parton distribution function (PDF) is given as an input to be a measure of the spectrum of partons that are the initial state for the interaction.

- Parton shower: Since colour charged particles are involved both in the initial state and often also in the final state, a cascade of further quantum chromodynamics (QCD) interactions is initiated. This is called showering. Perturbation theory is not applicable to these QCD processes as discussed in Section 2.1.6. However, they are also independent of the hard scattering, which means that they can be constrained by other measurements. The calculation is then based on the colour string model [130] or other phenomenological models. The transition between hard scattering and parton showering is given by an energy scale in order to use the correct kind of event generation method for each part of the event. The scale choice usually gives rise to a systematic uncertainty (see Section 5.6.2 for the application in an analysis).

- Matching and merging: Some QCD results can be derived perturbatively to complement the phenomenological parton shower calculations. In the process of matching the QCD results are subtracted to avoid double counting. In the process of merging the results are combined.

- Underlying event (UE): The remaining partons inside the hadrons can contribute to the event with their interactions. Typically these interactions are soft. They necessarily contribute to the total cross-section of the process.

- Hadronization: Finally, the colour charged partons are bound into colourless states. This can be calculated with the string model that was first proposed in Ref. [131]. It is based on the linear increase of the potential between a quark-antiquark pair.

After the event generation the simulated dataset is referred to as at "truth level". This means that it describes the actual particle physics interaction without any impact from detector effects and mismeasurement. Truth level datasets cannot reasonably be compared with data, but they are still useful for several studies.

3.4.2 Simulation software

Several kinds of generator software are currently in use, each with their individual strengths, weaknesses and general purpose. The ones used in later chapters are introduced here:

- Comix [132]: A tree-level matrix element generator. It is aimed especially at processes with large multiplicities.

- HAWK [133]: As the name "Higgs boson is attached to weak bosons" suggests the MC integrator was designed specifically for Higgs boson production in vector-boson fusion and Higgsstrahlung. HAWK includes electroweak and QCD corrections.

- ME+PS@NLO [134]: The software serves as a link between parton-level results of different jet multiplicities calculated at NLO and parton showering. By incorporating other matrix element and parton shower generators it is successful at preserving the accuracy of parton-level and parton shower results.

- OpenLoops [135]: The software is able to calculate scattering amplitudes at a varying momentum range with the help of loop-momentum polynomials.

- `Powheg-Box` [136]: Here, the speciality is the production of heavy quarks (charm, bottom and top). The NLO QCD simulation can then be interfaced with parton showering software.

- `Pythia` [137]: As a multi-purpose event generator Pythia is able to calculate a long list of processes. These include beam remnants, string fragmentation, initial- and final state parton showering. The main focus is on strong interactions.

- `Sherpa` [138]: Another multi-purpose generator. Sherpa is also able to describe a large variety of phenomena. However, in contrast to Pythia it is able to fully incorporate spin correlations.

Furthermore, there is a distinction between full simulation [139] and fast simulation [140]. The latter is the less precise, quicker method. Typically, it circumvents the simulation of the detector with `Geant4` by replacing the simulated interaction of electromagnetic particles with the calorimeter with a library of showers, which were generated before. This part would otherwise be the most extensive. Skipping the detector simulation does therefore save a lot of time and resources [141]. Of course it would be most ideal to simulate every process to the highest detail with full simulation. However, that is not always practical and the decision whether accuracy or speed is more important has to be made on a case by case basis.

3.4.3 Simulation properties

An important property of a MC simulated process is the cross-section. It needs to be known to interpret results and generate samples that are an actual equivalent of recorded datasets. Several steps are needed to determine the full cross-section. Each MC generator calculates the cross-section of the simulated process up to LO, NLO or higher orders using the matrix element method and the Feynman calculus. With the so-called k-factor the cross-section up to higher orders is expressed through a multiplicative factor. In many cases the cross-section of a process is known up to higher orders than is practical to calculate with each new simulation. Also the cross-section calculation only needs to be as precise as the measurement the simulation is compared to.

Furthermore, certain areas of the phase space may be enhanced by applying generator filters. These exclude events based on filter criteria. The filter efficiency is a measure for how often events are excluded. It is a single factor that needs to be multiplied with the total cross-section because the events were not generated according to the full cross-section.

Chapter 4

Jet calibration

The jet is one of the most common objects in the final state of any event recorded with the ATLAS detector. Furthermore, the only reconstructed physics objects in the final state of the search for new physics presented in Chapter 5 are two jets. It is therefore of utmost importance to work with the most precisely reconstructed jets possible. Any increase in precision and any decrease in the uncertainties is likely to have positive consequences on search and measurement results.

The jet calibration does just that. In its different stages it optimizes the jet energy scale, minimizes the jet energy resolution and accounts for various effects from the detector response to pile-up. This chapter focusses on electromagnetic energy scale (EM scale) topocluster (EM-Topo) and EM scale particle flow (EMPFlow) jets. A description of other jet definitions can be found in Section 3.3.2.

4.1 Overview

Seven individual corrections of the jet calibration in ATLAS are applied in sequence. As such they build up on each other and later corrections are designed to preserve the improvements of earlier ones. The goal is to calibrate the energy scale of reconstructed jets to particle level and correct for various detector level effects by correcting the four-momentum in each step. This is illustrated in Figure 4.1. A description of these seven corrections, which are applied to both EM scale and local hadronic cell weighting (LCW) scale jets, is given in the following sections.

In Section 4.1.1 the construction of jets from topological clusters is reintroduced briefly. Referring back to Section 3.3.2 it focusses on EM scale jets exclusively to lay the foundation for the jet calibration. Section 4.1.2 goes into the origin correction, which ensures that the jets are pointing towards the correct primary vertex. The pile-up correction is divided into two steps. The jet area based pile-up correction and the residual pile-up correction are both presented in Section 4.1.3. The absolute Monte-Carlo-based (MC-based) etaJES calibration is the topic of Section 4.1.4. Afterwards Section 4.1.5 contains a description of the residual in-situ calibration, which is only applied to data.

Due to contributions of the author the global sequential calibration (GSC) is discussed in much greater detail in Section 4.2. There, recent improvements to the method are discussed especially in the context of the comparison between topocluster and particle flow jets. The impact of these calibration efforts are presented in Section 4.3. This includes a discussion of

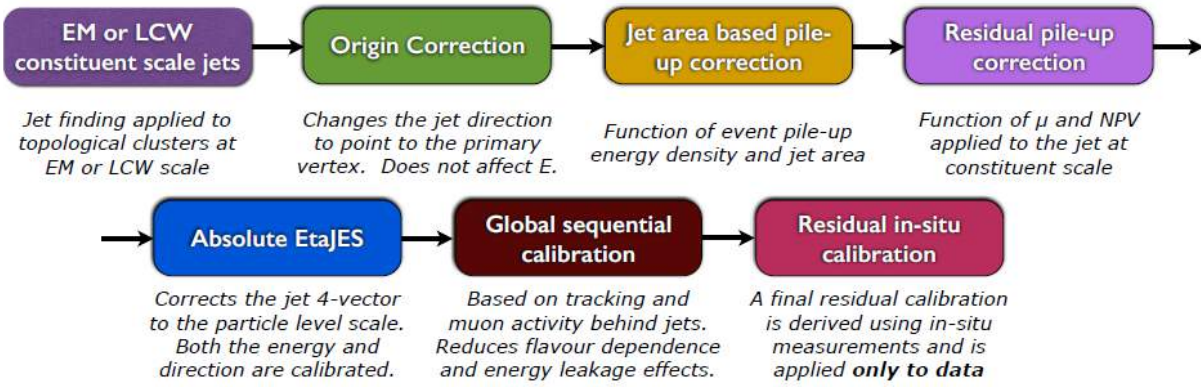

Figure 4.1: The steps in the calibration of both EM and LCW jets in ATLAS. Each part of the calibration builds on the one that comes before [142].

uncertainties and further jet collection comparisons. The effect on an actual analysis is part of Chapter 5.

4.1.1 Electromagnetic scale jets

The starting point of the jet calibration is a jet collection. A more detailed description of jet collections can be found in Section 3.3.2. Here, the focus is solely on EM scale topocluster jets and EM scale particle flow jets. Both are reconstructed with the anti-k_t ($R = 0.4$) clustering algorithm by identifying topological clusters of energy deposits in the calorimeters as part of one collimated shower. These energy deposits have to be significantly more energetic than the noise threshold, which differs between different parts of the calorimeter where the energy is deposited. The response of the calorimeter leads to energies not necessarily being measured at the correct scale. Therefore, an energy scale needs to be chosen. This is done at the electromagnetic scale, leading to the same response as electrons and photons.

For particle flow jets the reconstruction algorithm uses inner detector information in addition to calorimeter clustering. Tracks measured in the inner detector are assigned to topoclusters as described in Section 3.3.2. Since the tracks and energy deposits are now considered to originate form the same hard scattering object, an overlap removal is needed so that the reconstructed energies of tracks and topoclusters are not added and double counted. This is especially important considering missing transverse energy ($E_{\mathrm{T}}^{\mathrm{miss}}$).

4.1.2 Origin correction

During the reconstruction of jets a four-vector is constructed from the measured topoclusters that are identified as a jet. Therefore, an assumption on the origin of the jet is made, which is the centre of the detector by default. After the full event is reconstructed, however, a "first primary vertex" is identified. It is defined as the primary vertex that has the largest $\sum p_{\mathrm{T}}^2$ of tracks associated with it and is assumed to be the point of the hard-scatter interaction. The four-vector is then corrected to point to the first primary vertex, while leaving the jet energy unchanged.

Because the colliding proton bunches are elongated along the beam axis as discussed in Section 3.1, the point of interaction has a resolution of 40–55 mm in length [142]. As a result the improvement of the η-resolution of the jets is quite sizeable lowering it from about 0.06 to 0.045 in 2015 [143]. The resolution improvement in the ϕ-direction is not as big, since the spread in the plane perpendicular to the beam axis is much smaller. For particle flow jets the origin correction is not applied because the inner detector tracks already point to the primary vertex.

4.1.3 Pile-up correction

Pile-up has already been discussed in Section 3.3.2. It is a problem for the precise reconstruction of jets because it adds a large number of soft particles that do not originate from the hard-scatter interaction to the event. These particles often overlap with jets and complicate the jet reconstruction. This is less of a problem if the particles can be associated with a primary vertex. Particles that do not originate from the first primary vertex are simply removed from the event. This does only work for charged particles, which have a good angular resolution. Since particle flow jets do not rely on calorimeters alone to reconstruct the original primary vertex, they automatically have a good pile-up suppression, which is quantified in Section 4.3.2.

To remove pile-up from reconstructed jets ATLAS uses the pile-up subtraction method described in Ref. [144] and Ref. [145]. At its core the pile-up correction is a subtraction of three terms from the reconstructed jet with $p_{\mathrm{T}} = p_{\mathrm{T}}^{\mathrm{reco}}$ to get a new corrected transverse momentum $p_{\mathrm{T}}^{\mathrm{corr}}$. This is summarized by:

$$p_{\mathrm{T}}^{\mathrm{corr}} = p_{\mathrm{T}}^{\mathrm{reco}} - \rho \times A - \alpha \times (N_{\mathrm{PV}} - 1) - \beta \times \mu, \tag{4.1}$$

where ρ is the median p_{T} density of jets in the η-ϕ plane and A is the area of the jet. The variable N_{PV} is the number of reconstructed primary vertices in the event and μ is the average number of interactions per bunch crossing. Furthermore, α and β are correction factors that model the dependence of the reconstructed p_{T} on N_{PV} and μ, respectively.

In more detail the three terms correspond to the following distinct steps:

- Area-based pile-up correction ($-\rho \times A$): The jet area A is determined by creating simulated ghost particles that are uniformly distributed in the η-ϕ plane before reconstruction. After reconstruction all the ghost particles clustered into the jet are counted to get A. The p_{T} divided by the thus determined jet area is the energy density of the jet. To determine ρ all central ($|\eta| < 2.0$) positive-energy jets are taken into account. The median of the energy densities of these jets is defined as ρ. The impact of this correction can be seen in Figure 4.2.

- In-time pile-up correction ($-\alpha \times (N_{\mathrm{PV}} - 1)$): The jet area-based correction cannot fully account for the forward regions, which is why residual corrections are necessary. With linear fits the N_{PV} dependence of the jet p_{T} is probed and expressed with the coefficient α. This is done in bins of $|\eta|$ as can be seen in Figure 4.2. After the subtraction the N_{PV} dependence of the pile-up is removed.

- Out-of-time pile-up correction ($-\beta \times \mu$): Determining the β coefficient for the out-of-time pile-up correction is very analogous to α. Again linear fits in several $|\eta|$ bins model the μ dependence and determine β.

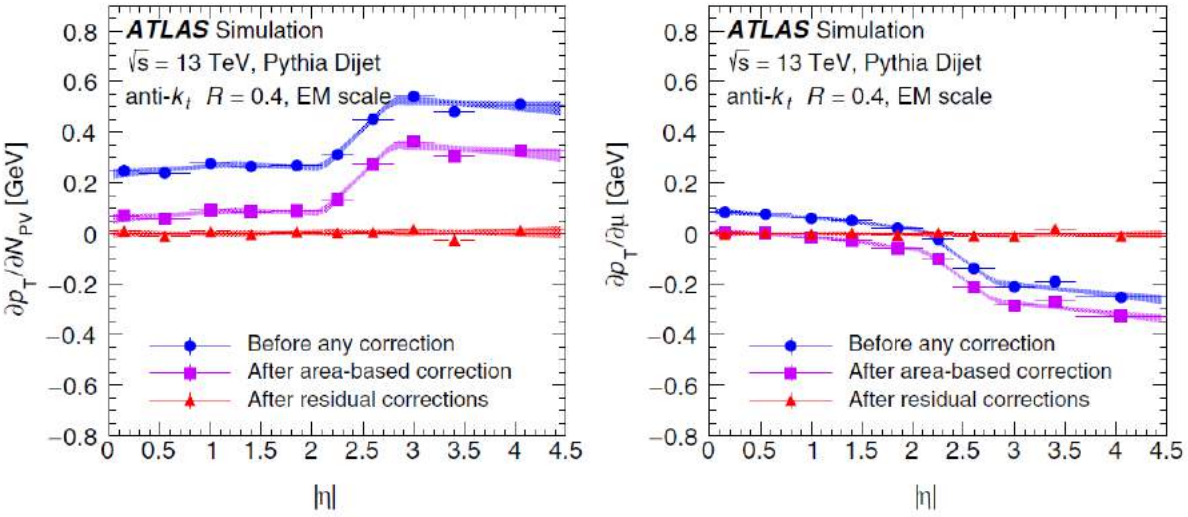

Figure 4.2: Number of primary vertices N_{PV} (left) and μ (right) dependence of the jet p_{T} before the pile-up removal (blue dots), after the area-based pile-up correction (purple squares) and after the residual pile-up corrections (red triangles). The variable N_{PV} is averaged over μ on the left and vice versa on the right. The shaded bands are 68% confidence intervals to fits of the distributions [143].

4.1.4 Absolute etaJES calibration

There are certain biases in the reconstruction of jets. Over the entire η range of the calorimeter different technologies are used and the detector cells have a changing granularity. This is especially prominent in transition regions between barrel and end-cap as well as between end-cap and forward calorimeters. The absolute etaJES calibration is a correction of the entire four-momentum of the jet that addresses these biases. It seeks to improve the η and jet energy scale (JES) measurements.

To correct for biases they first have to be derived from simulated events. To do so well isolated jets are selected and matched to nearby truth jets within $\Delta R = 0.3$. By requiring good isolation it is made sure that the reconstructed jet is matched to the correct truth jet. The jets are binned in the energy of the matched truth jet E^{truth} and η_{det}, which is the η direction pointing from the centre of the detector to the hit in the calorimeter. With this η definition instead of the one pointing to the primary vertex of the hard-scatter interaction the jet properties can be discussed in the context of the detector geometry. This is important, since detector effects that depend on the calorimeter geometry and its technologies lead to the biases that are supposed to be removed by the correction.

In each bin a Gaussian fit is applied to the distribution of the energy response $E^{\mathrm{reco}}/E^{\mathrm{truth}}$ to determine an average energy response in each E^{truth}-η_{det}-bin as the mean of the Gaussian distribution. The resulting energy response distribution in dependence of η_{det} in various bins of E^{truth} is depicted on the left of Figure 4.3. Here, the clear η_{det}-dependent bias can be seen in the transition regions around $|\eta_{\mathrm{det}}| = 1.4$ and $|\eta_{\mathrm{det}}| = 3.1$. The energy response is significantly lower because some of the energy is lost in the uninstrumented regions between subdetectors. The effect is corrected for by applying the inverse of the response distribution to all jets. This method is called the numerical inversion.

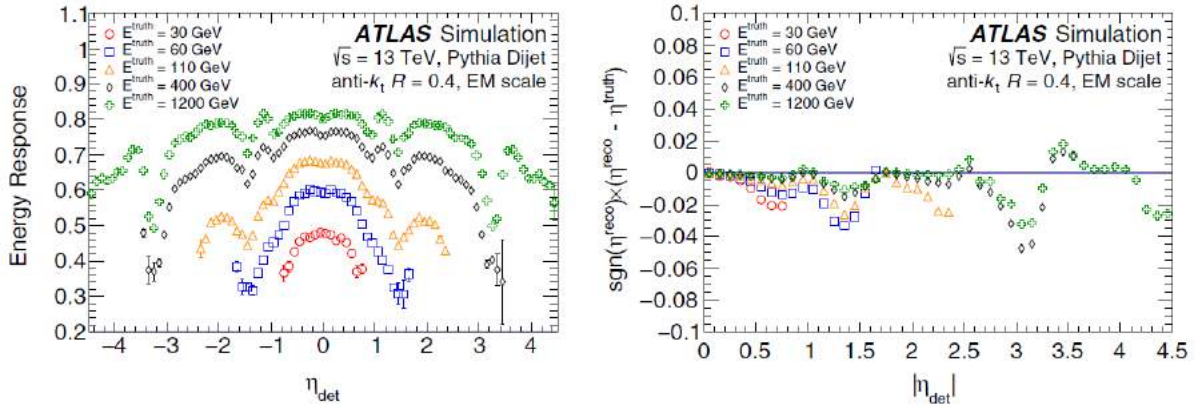

Figure 4.3: Jet energy response versus η_{det} (left) and η-bias versus η_{det} (right) after origin and pile-up corrections. Both distributions are evaluated at five different jet energy working points. The η-bias is expressed as the signed difference between η^{reco} and η^{truth} [143].

Another bias exists in the η measurement as a function of η_{det}, which is clear from looking at the right of Figure 4.3. Again the effect is most prominent in the transition regions. It occurs mostly when a jet deposits energy in different parts of the detector, which have varying technologies and granularity. As a result the energy of the jet is over- or underestimated between different sides of the jet, altering the η-measurement. The correction to η^{reco} is derived in bins of E^{truth} and η_{det}. However, in contrast to the JES correction the η correction is only applied to the p_{T} and η of jets and not the entire four-momentum.

The absolute etaJES calibration is followed by the GSC. Because that calibration step has its own section, the residual in-situ calibration is covered first.

4.1.5 Residual in situ calibration

The in-situ calibration is a set of three data-driven calibrations, which are applied in sequence to cover different η_{det} and p_{T} ranges. The in-situ calibration is applied after the global sequential calibration described in Section 4.2. Therefore, the jets already benefited from an improvement to the jet energy resolution (JER).

The purpose of the in-situ calibration is to account for differences between the jet responses in data and MC simulation. Therefore, in each step the jet transverse momentum $p_{\text{T}}^{\text{jet}}$ is compared with the transverse momentum of a reference $p_{\text{T}}^{\text{ref}}$ object in order to determine the ratio:

$$\frac{\mathscr{R}_{\text{data}}}{\mathscr{R}_{\text{MC}}} = \frac{< p_{\text{T}}^{\text{jet}} / p_{\text{T}}^{\text{ref}} >^{\text{data}}}{< p_{\text{T}}^{\text{jet}} / p_{\text{T}}^{\text{ref}} >^{\text{MC}}}, \tag{4.2}$$

where $< ... >$ denotes the average. The output of each step is a set of calibration factors to the four-momentum in bins of p_{T} and η_{det} of the jet. Of course the calibration factors are derived such that the ratio of the responses becomes one.

Eta-intercalibration

The jets that are calibrated with the η-intercalibration are forward jets ($0.8 < |\eta_{\text{det}}| < 4.5$). The reference object is a central jet ($|\eta_{\text{det}}| < 0.8$) in a dijet event. Therefore, the η-intercalibration is not used to calibrate central jets. The method works because central jets are generally measured more precisely than forward jets.

As per Eq. 4.2 the ratio of data and MC response is determined in bins of $|\eta_{\text{det}}|$ and the average p_{T} of the two jets. From the distribution of these ratios correction factors are derived with a smoothing curve. The corrections typically do not exceed 2%. A more detailed description of the method can be found in Ref. [146].

Boson + jet balance

In the case of the boson + jet balance the reference object is either a Z boson or a photon. Here, jets are calibrated in a p_{T} range of $20 \leq p_{\text{T}} \leq 500$ GeV for Z + jets and at $36 \leq p_{\text{T}} \leq 950$ GeV for γ + jets [143]. With this step only central jets ($|\eta_{\text{det}}| < 0.8$) are covered, since they were left out in the η-intercalibration.

If they decay into charged leptons, Z bosons can be well reconstructed from the tracks of their decay products and both bosons are measured with very high precision compared with jets. As a result this is a very good test of the simulation of the energy response. The method is discussed more thoroughly in Ref. [147].

Multijet balance

The final in-situ step is the multijet balance. It covers a range of $300 \leq p_{\text{T}} \leq 2000$ GeV and thus complements the boson + jet balance. It follows the same principle as the rest of the in-situ calibration with the leading jet in the event as the jet that is calibrated and a recoil system as the reference object. The recoil system is the vectorial sum of at least two jets with $p_{\text{T}} \leq 950$ GeV. Because of the p_{T} requirement these jets are calibrated by the boson + jet balance and all previous steps of the jet calibration.

However, the p_{T} requirement on the recoil jets also cuts out events with a very large leading jet p_{T}. The multijet balance calibration is therefore applied repeatedly, reaching ever higher p_{T} ranges and increasing the value of the recoil jet p_{T} requirement.

After the multijet balance a final combination of the in-situ calibrations is done. Special care is taken with the overlap regions at $|\eta_{\text{det}}| = 0.8$ and $300 < p_{\text{T}} < 950$ GeV. Since the agreement between the different methods is good, the techniques are considered validated and enter the recommendations for analysis groups [143].

4.2 Global sequential calibration

The GSC is applied after the absolute etaJES calibration. It is therefore essential that it preserves the achievements of the etaJES, the calibrated jet energy scale, and those of any other previous step of the jet calibration.

The reconstructed jet four-momentum generally deviates from the measurement in a hypothetical perfect detector. There is a correlation between these mismeasurements and several jet observables that are discussed in the following. The dependencies on the jet observables

are a feature of the detector and exist due to the uninstrumented region between subdetectors, non-uniform responses to energy deposits and other reasons. Their effect can be summarized with the jet response, since it compares the true jet energy or transverse momentum to the reconstructed counterpart. With the GSC the dependencies on each jet observable are removed sequentially, as the name of the calibration implies.

By removing theses dependencies the GSC is able to improve the jet energy resolution, which improves the reconstruction of the entire event. Especially the measurement of missing transverse energy profits from a precise jet reconstruction. This also has a direct effect on searches for new physics like the one described in Chapter 5.

In Section 4.2.1 the theoretical principles of the GSC are explained in general terms. Furthermore, the expected improvements to the jet measurement are detailed. Section 4.2.2 is the presentation of the used datasets and in Section 4.2.3 the event selection and binning for the derivation of the GSC in the 2016 ATLAS jet calibration are listed. The jet observables that were considered in the study are discussed in Section 4.2.4. The implementation of the method and derivation of correction factors is covered in Section 4.2.5. The results are the topic of Section 4.2.6 with special attention being paid to the comparison between topocluster and particle flow jets.

4.2.1 Theory behind the GSC

The purpose of the GSC is to improve the JER and the jet p_{T} resolution. The p_{T} resolution is defined as the width of the jet p_{T} response distribution, which is the reconstructed jet transverse momentum divided by the p_{T} of a matched truth jet $p_{\mathrm{T}}^{\mathrm{reco}}/p_{\mathrm{T}}^{\mathrm{truth}}$. The response typically has a Gaussian shape because of the random mismeasurements from detector effects. The jet response partially depends on truth information, which means that the GSC necessarily has to be a MC-driven technique. The GSC was first described in Ref. [148].

The average jet p_{T} response $< p_{\mathrm{T}}^{\mathrm{reco}}/p_{\mathrm{T}}^{\mathrm{truth}} >$ correlates with the general shower shapes of the jet, which can be expressed through multiple observables. If for example a jet has such a shape that it deposits a large part of its energy in an uninstrumented area of the detector, the reconstructed p_{T} is typically lower than the true p_{T} of the jet. This fact can be exploited by increasing the p_{T} of such jets with correction factors in order to gain a more accurate measurement. With a global factor the jet energy scale is preserved through all of these corrections. The JES calibration corrects for some of the mismeasurement of jet energies, but does so only for the absolute energy scale and not in dependence of additional jet observables.

The GSC is applied and derived in several GSC steps each corresponding to one jet observable x_i. Each step derives correction factors that remove the dependence on that one observable. Therefore, in the next step the correction based on the observable x_{i+1} is applied to jets that already went through such corrections. The corrections are applied independently and negligible correlations between the steps are assumed. This assumption was tested by changing the order of the GSC steps and no significant improvement was found by varying the order of the GSC.

The correction factors are derived through numerical inversion very similar to the absolute etaJES calibration. In this method the response $R(p_{\mathrm{T}}^{\mathrm{reco}}, x_i)$ is determined as a function of the reconstructed jet p_{T} and the observable x_i. Afterwards the jet $p_{\mathrm{T}}^{\mathrm{reco}}$ is multiplied by the inverse

of the response to determine the corrected jet $p_{\mathrm{T}}^{\mathrm{corr}}$ as shown in:

$$p_{\mathrm{T},i}^{\mathrm{corr}} = \frac{p_{\mathrm{T},i-1}^{\mathrm{reco}}}{R(p_{\mathrm{T},i-1}^{\mathrm{reco}}, x_i)}. \tag{4.3}$$

The basic principle behind the GSC is illustrated in Figure 4.4 with a generic jet response distribution. Due to the correlation of an observable x with the jet p_{T} response subsets of the sample with low-x and high-x jets have different response distributions with a differing average p_{T} response. By removing that correlation using Eq. 4.3 the mean of low-x and high-x jet response distributions becomes the same. As can be seen on the right of Figure 4.4, this typically lowers the width of the overall response distribution and thus improves the jet resolution. This example is of course a simplification, since the binning in x_i is much finer than just two bins.

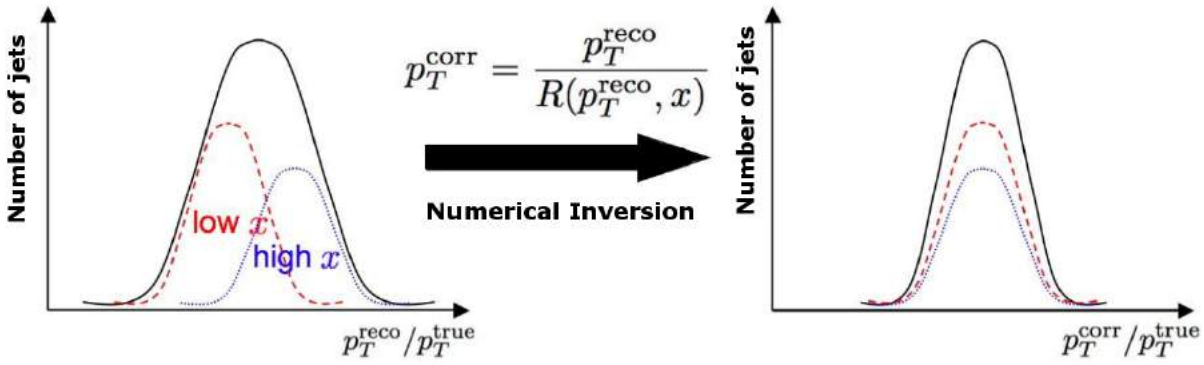

Figure 4.4: Basic principle of the GSC. Left: Illustration of a jet response distribution before the GSC is applied. The distribution is divided into two subsets of jets with high values of a variable x (blue) and low values of the same variable (red). Right: The same distributions after the GSC step that removes the dependence on the variable x.

Another purpose of the GSC is to lessen the difference in the response to light quark (LQ) and gluon jets. This difference of up to 8% would otherwise result in a large uncertainty of the jet calibration [149]. The reason why the response varies between LQ and gluon jets is the difference in the particle composition of the jet shower and its shape. Gluon jets typically contain softer particles, which leads to a wider shower. Quark-initiated jets on the other hand tend to have higher transverse momenta and contain more hadrons. By removing the dependencies of the jet response on the jet shapes the difference between gluon and quark jet responses is lowered.

Without the GSC the average jet response for a specific flavour can differ from one because there are systematic flavour-dependent effects that cause a shift of the response distribution. Consequently, the difference between the jet response in LQ and gluon jets is a source of a systematic uncertainty of the jet energy scale. This is because the jet flavour composition of a given sample is unknown and can differ between MC simulation and data. MC-driven methods to calibrate the jet energy scale using the jet response like the absolute etaJES calibration described above might therefore work imperfectly on a given dataset. By removing this flavour dependence the uncertainty is removed as well. This effect was also studied in Ref. [150] and Ref. [151].

4.2.2 Simulated samples

Given that the GSC is a purely MC-driven technique, there is no dataset and just a list of simulated samples that were used in the calibration. The multijet Monte Carlo samples were simulated at a centre-of-mass energy of 13 TeV using `Pythia 8` [137]. For the simulation the samples are divided into 13 different slices to simulate events with many different cross-sections. The slices each cover a different range of the leading jet truth p_{T}. When used together the samples gain weights such that all slices add up to smooth distributions despite being generated independently. Because of the large cross-section of multijet processes in proton–proton collisions the MC samples necessarily also have to be large, which necessitates splitting the production.

The list of simulated samples can be found in Appendix A.1.1. The validations discussed in Section 4.2.6 that are described in Ref. [150] and Ref. [151] use 38 pb^{-1} of data recorded at 7 TeV and 20 fb^{-1} recorded at 8 TeV, respectively.

4.2.3 Event selection

The GSC is derived for both topocluster and particle flow jets. The event selection is the same for both of them. Because the calibration is supposed to be applied to all jets, the selection is relatively loose. The only purpose is to reject pile-up and find clean collision events with well reconstructed and isolated jets.

The considered events have to fulfil the following requirements:

- There is at least one primary vertex with at least four associated tracks. This removes most of the non-collision background.
- There are at least two jets with $p_{\mathrm{T}} > 7$ GeV and $|\eta_{\mathrm{det}}| < 5.0$.
- All considered jets are well isolated and matched to a truth jet. The isolation criteria are optimized for jets reconstructed with the anti-k_t algorithm with distance parameter $R = 0.4$:
  - All jets are matched to a truth jet within $\Delta R = 0.3$.
  - There is no additional truth jet within $\Delta R = R \times 2.5$.
  - There is no additional reconstructed jet within $\Delta R = R \times 1.5$.
- MC quality requirement: $0.6 < p_{\mathrm{T}}^{\mathrm{ave}} / p_{\mathrm{T,j1}}^{\mathrm{truth}} < 1.4$

Here, $p_{\mathrm{T}}^{\mathrm{ave}}$ is the average p_{T} of the two leading jets $p_{\mathrm{T}}^{\mathrm{ave}} = (p_{\mathrm{T,j1}} + p_{\mathrm{T,j2}})/2$. The MC quality requirement removes events with low-p_{T} jets that have large event weights and migrate to higher-p_{T} bins. The effect distorts the jet p_{T} spectrum and is unphysical. It exists because of multijet events being simulated in slices divided by the leading jet p_{T} and because pile-up is added as an overlay simulated separately from the hard scattering. Weighting of the events than leads to the distortion [152].

Binning

The multijet sample is subdivided into p_T and $|\eta_{det}|$ bins. Furthermore, in each step the dataset is separated into bins in the observable x_i that the current correction is based on. The $|\eta_{det}|$ binning and the binning in each GSC observable x_i is equidistant with 10 x_i bins and 35 bins of $|\eta_{det}|$ between 0.0 and 3.5. The binning in p_T is more complex. It is listed in Table 4.1.

Table 4.1: Binning in p_T for the global sequential calibration.

p_T [GeV]	20–25	25–30	30–40	40–50	50–60	60–80	80–100
p_T [GeV]	100–120	120–140	140–160	160–180	180–200	200–250	250–300
p_T [GeV]	300–350	350–400	400–500	500–600	600–800	800–1000	1000–1200

For one of the correction steps, the Punch-Through correction, a binning in the jet energy instead of the transverse momentum is used for reasons that are discussed below. The binning is reported here in Table 4.2.

Table 4.2: Energy binning for the Punch-Through correction of the global sequential calibration.

E [GeV]	0–10	10–20	20–30	30–40
E [GeV]	40–50	50–60	60–80	80–100
E [GeV]	100–150	150–200	200–400	400–600
E [GeV]	600–800	800–1000	1000–1200	1200–1600
E [GeV]	1600–2000	2000–3000		

The binning is designed to allow for corrections that are as granular as possible in p_T, $|\eta_{det}|$ and x_i while still ensuring enough statistics in each bin. The detector response and dependence on a variable x_i is expected to differ as a function of the direction and transverse momentum of the jet.

4.2.4 GSC variables

As explained in Section 4.2.1 the GSC is subdivided into multiple steps, each of which corrects for a different jet observable x_i. These observables are called the GSC variables. As a result of the calibration a set of correction factors $R(p_T^{reco}, x_i)$ is acquired. These can then be applied to any suitable dataset as per Eq. 4.3.

The selection of GSC variables makes use of the detector geometry, especially the calorimeter.[1)] The ATLAS calorimetry is divided into electromagnetic (liquid argon) calorimeter and hadronic (tile) calorimeter. Each of these two is further divided into layers. The space between the two calorimeters houses readout systems, other infrastructure and therefore an uninstrumented region. Jets that deposit a large part of their energy in layers near an uninstrumented region therefore necessarily tend to have a low jet response. The corrections corresponding to each variable are applied in the order they are listed.

[1)] A detailed description of the ATLAS calorimetry can be found in Section 3.2.3.

For topocluster jets the GSC variables are the following:

- f_{Tile0}: The fraction of jet energy deposited in the first layer of the tile calorimeter.
- f_{EM3}: The fraction of jet energy deposited in the third layer of the electromagnetic calorimeter. Another designation for f_{EM3} is f_{Lar3}.
- n_{Trk}: The number of tracks associated with the jet.
- σ_{Trk}: The p_{T}-weighted width of the jet. This "trackwidth" is defined in Eq. 4.4.
- $n_{\mu,\text{Seg}}$: The number of muon segments associated with the jet. The corresponding GSC step is the Punch-Through correction. Another designation for $n_{\mu,\text{Seg}}$ is Nsegments.

$$\sigma_{\text{Trk}} = \frac{\sum_i \left[p_{\text{T},i}^{\text{track}} \Delta R(\text{track}_i, \text{jet}) \right]}{\sum_i \left[p_{\text{T},i}^{\text{track}} \right]}. \tag{4.4}$$

Here, $p_{\text{T},i}^{\text{track}}$ is the transverse momentum of a track i with $p_{\text{T}} > 1$ GeV associated with the jet and $\Delta R(\text{track}_i, \text{jet}) = \sqrt{\Delta\eta(\text{track}_i, \text{jet})^2 + \Delta\phi(\text{track}_i, \text{jet})^2}$ is the angular distance between a track i associated with a jet and its centre.

For particle flow (PFlow) jets the GSC variables are the following:

- f_{charged}: The p_{T} weighted fraction of charged tracks associated with the jet.
- f_{Tile0}: The fraction of jet energy deposited in the first layer of the tile calorimeter.
- f_{EM3}: The fraction of jet energy deposited in the third layer of the electromagnetic calorimeter.
- $n_{\mu,\text{Seg}}$: The number of muon segments associated with the jet. The corresponding GSC step is the Punch-Through correction.

The transition region between the two calorimeters lies directly between the first layer of the tile calorimeter (Tile0) and the third layer of the electromagnetic calorimeter (EM3). Therefore, jets that have high fractions of their energy deposited in these layers tend to have a low response. This strong dependence makes the two variables f_{Tile0} and f_{EM3} great choices for the GSC.

The variables n_{Trk} and σ_{Trk} on the other hand make use of the flavour-dependent shower shape. Gluon-initiated jets consist of more particles and softer ones. As a result they tend to be wider and have a lower calorimeter response. Finally, the Punch-Through correction handles the high energy tails of the jet energy distribution. The jets with a high number of muon segments associated with them necessarily are highly energetic and not contained in the calorimeter. Therefore, not all of their energy is recorded and the jet response is low. The Punch-Through correction is exceptionally derived in energy bins because it is more correlated with that quantity than the jet p_{T}.

For particle flow jets the tracking variables n_{Trk} and σ_{Trk} cannot be used because the jet reconstruction already uses tracking information. The charged fraction takes their place. This is due to gluon jets containing fewer hadronic tracks. Therefore, a smaller portion of particles

in a gluon initiated shower is charged. As mentioned before gluon jets have a lower response and this dependence can be used by the GSC.

All of the observables are well modelled in MC simulation, showing only small differences to data. With the dijet balance method it was determined that none of these differences affect the result [143]. The validation of this is discussed in Section 4.2.6.

Because the corrections are based on measurements in specific subdetectors, they cannot be applied to the entire $|\eta|$ range. For example it would make little sense to derive tracking-based corrections like n_{Trk} and σ_{Trk} outside of the acceptance of the tracker. Therefore, the ranges are $|\eta| < 1.7$ for f_{Tile0}, $|\eta| < 2.5$ for n_{Trk} and σ_{Trk} and $|\eta| < 2.7$ for f_{charged} and $n_{\mu,\mathrm{Seg}}$. There are no additional restrictions on the f_{EM3} correction.

4.2.5 Derivation of the GSC calibration factors

In Figure 4.5 the average jet p_{T} response against n_{Trk} is shown for topocluster jets calibrated up to the absolute etaJES calibration. The MC sample is divided into the aforementioned p_{T}, $|\eta_{\mathrm{det}}|$ and in this case n_{Trk} bins. In each bin the jet p_{T} response distribution is plotted and fitted with a Gaussian function. The mean of this fit is the average jet response and its width is depicted as the error bars on the data points in the figure.

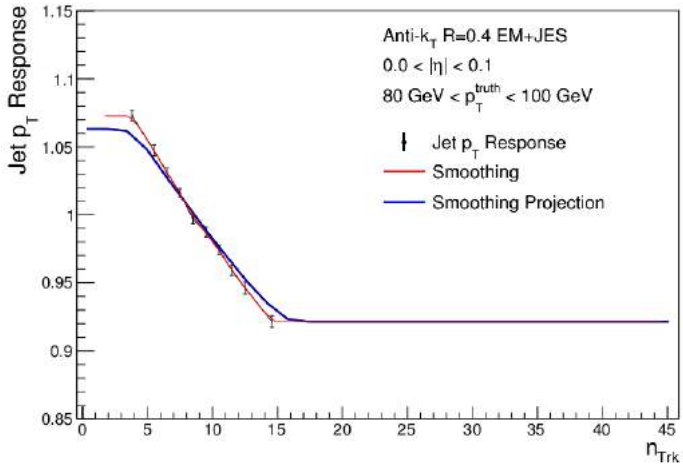

Figure 4.5: Average p_{T} response as a function of n_{Trk} before the GSC step based on n_{Trk} (black data points) for central intermediate-p_{T} jets. The GSC correction factors are obtained from a curve constructed via two-dimensional smoothing (red). The projection of the smoothed curve onto the n_{Trk}-axis (blue) is shown for comparison.

The distribution in Figure 4.5 is visibly non-flat. This means that n_{Trk} was indeed well chosen as a GSC variable because a strong dependence on a variable leads to a large improvement of the jet resolution after the GSC step. Considering Figure 4.4 again the width of the jet response distribution is larger if the response of jets with high x_i is differs more from the response of jets with low x_i. After the dependence is removed this detector-caused resolution effect also vanishes.

The average jet response against each observable is interpolated via a smoothing procedure using two-dimensional Gaussian kernels. The approach assumes Gaussian fluctuations

and enables the propagation of statistical uncertainties. The smoothing function $F_{\text{rel}}(p_{\text{T}}^{\text{jet}}, x_i)$ is determined in each $|\eta_{\text{det}}|$ bin and it is this smoothed curved that is evaluated at each point in the three-dimensional p_{T}-$|\eta_{\text{det}}|$-x_i space to determine the correction factors for the numerical inversion. The correction factors are the inverse of the response, following the logic of Eq. 4.3. The factors are applied iteratively in each GSC step as shown in:

$$p_{\text{T}}^{i} = F_{\text{rel}}^{i}(x_i) \times p_{\text{T}}^{i-1} = F_{\text{rel}}^{i}(x_i) \times F_{\text{rel}}^{i-1}(x_{i-1}) \times p_{\text{T}}^{i-2} = ..., \tag{4.5}$$

where p_{T}^{i} is the jet p_{T} after the ith GSC step. The smoothing function itself is given in Eq. 4.6 and Eq. 4.7:

$$F_{\text{rel}}(p_{\text{T}}^{\text{jet}}, x) = \frac{\sum_{j=1}^{N_{\text{bins}}} C_j w_j}{\sum_{j=1}^{N_{\text{bins}}} w_j}, \tag{4.6}$$

$$w_j = \frac{1}{\Delta C_j^2} \times \text{Gauss}\left(\frac{\log(p_{\text{T}}^{\text{jet}}) - \log < p_{\text{T}}^{\text{jet}} >_j}{\sigma_{p_{\text{T}}}} \oplus \frac{\log(x) - \log < x >_j}{\sigma_x} \right), \tag{4.7}$$

where j is the bin index over p_{T}-x bins and ΔC_j the statistical uncertainty of the smoothing parameters C_j. Furthermore, $< ... >_j$ is the average over a bin j. The function $\text{Gauss}(x)$ is a Gaussian function with vanishing mean and unit width and $\oplus$ denotes quadratic addition. Both $\sigma_{p_{\text{T}}}$ and σ_x are width parameters that are determined through the smoothing [151]. In addition, the smoothing function is projected to the x_i-axis to study its overall behaviour.

In principle the smoothing could be skipped and instead the average jet response distributions could be evaluated at each p_{T}-$|\eta_{\text{det}}|$-x_i bin to derive correction factors. However, that would also disregard the impact of statistical fluctuations, which the smoothing does take into account. Some of the data points in the average p_{T} response distributions could be subject to some extreme fluctuations, which should not be passed on to the correction factors that are applied to data and other simulated samples. The smoothing naturally compensates for those fluctuations to some extend.

4.2.6 Results of the sequential calibration steps

One of the tests of the GSC and especially the smoothing is whether the jet response in dependence of the GSC variables flattens after the corresponding calibration step. In Figure 4.6 this is shown for the Punch-Through correction. Here, the jet p_{T} response distribution over $n_{\mu,\text{Seg}}$ flattens a bit especially at $p_{\text{T}} \simeq 1$ TeV. The effect is not stronger because the Punch-Through correction only concerns high energy tails and is binned in the jet energy instead of the transverse momentum. This step is especially significant because the Punch-Through correction to particle flow jets was new at the time.

The removal of the jet response dependence on a GSC variable can be seen more clearly in the other GSC steps. Figure 4.7 depicts the f_{charged}-dependent p_{T} response distribution before and after the f_{charged} correction. As expected, the low-f_{charged} jets have a low response because many of them are gluon jets. After the GSC step this dependence is removed almost entirely.[2)] Overall the dependence of the jet response on the GSC variables is typically lowered to less than 2%.

[2)] It is not fully removed because the correction factors were determined with the smoothing described above and not directly taken from the data points.

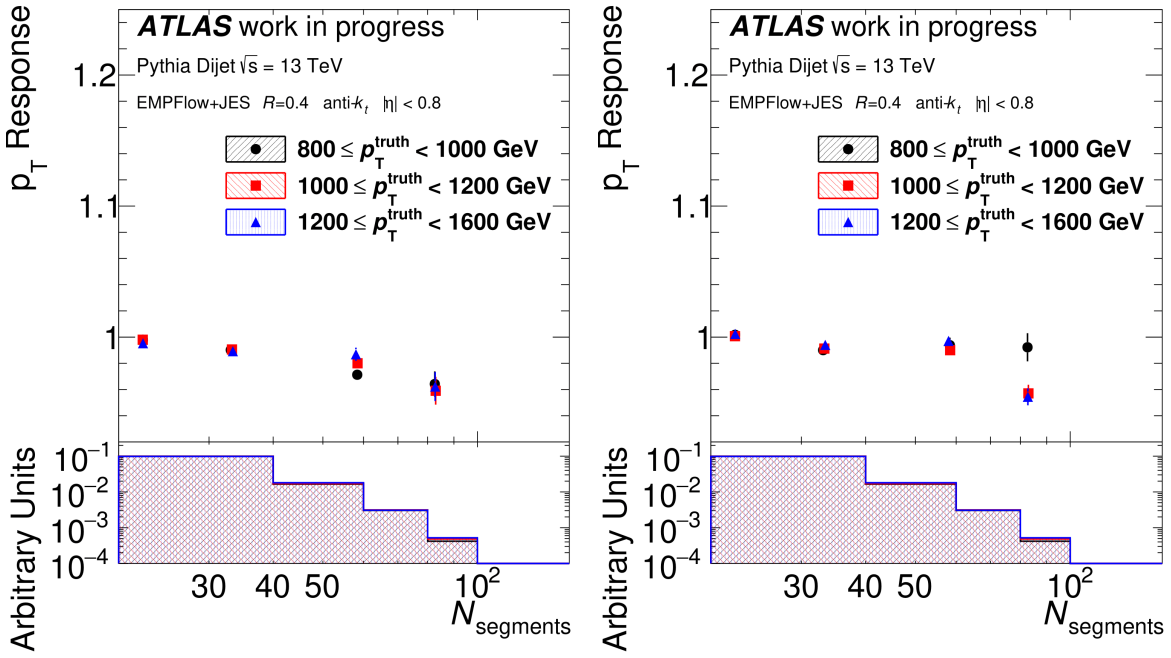

Figure 4.6: Top panels: average p_{T} response of particle flow jets as a function of $n_{\mu,\mathrm{Seg}}$ before (left) and after (right) the GSC step based on $n_{\mu,\mathrm{Seg}}$ in three bins of $p_{\mathrm{T}}^{\mathrm{truth}}$. Bottom panels: $n_{\mu,\mathrm{Seg}}$ distributions in the three $p_{\mathrm{T}}^{\mathrm{truth}}$ bins.

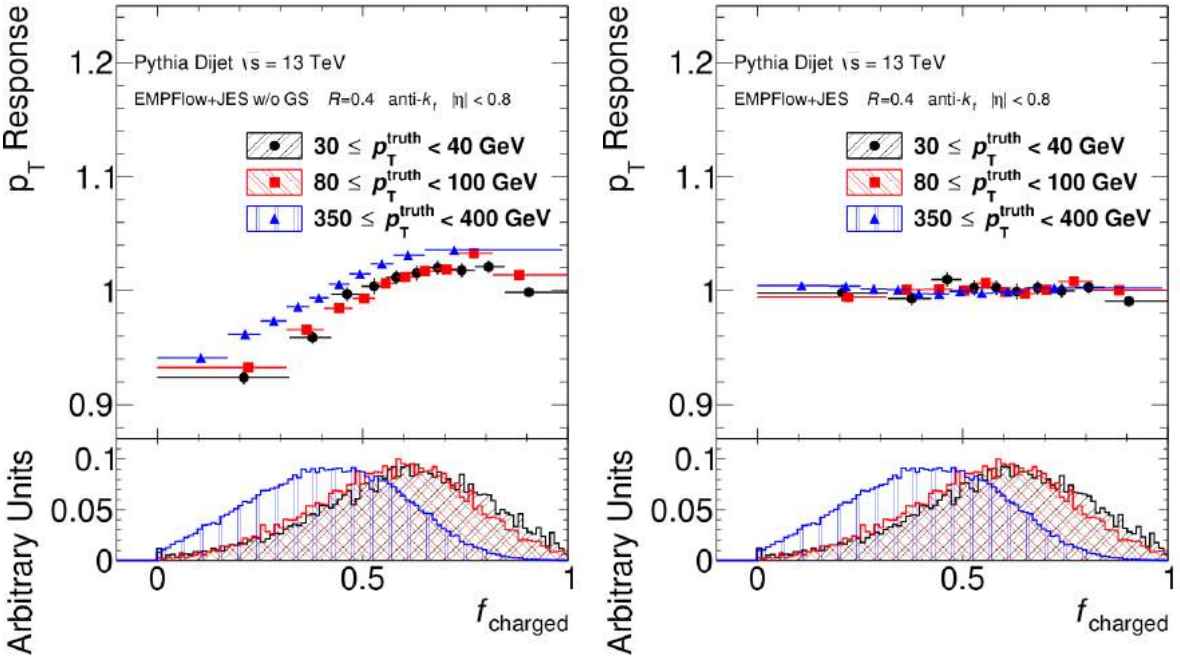

Figure 4.7: Top panels: average p_{T} response of particle flow jets as a function of f_{charged} before (left) and after (right) the GSC step based on f_{charged} in three bins of $p_{\mathrm{T}}^{\mathrm{truth}}$. Bottom panels: f_{charged} distributions in the three $p_{\mathrm{T}}^{\mathrm{truth}}$ bins.

Finally, Figure 4.8 and Figure 4.9 show how the f_{Tile0} and f_{EM3} dependencies vanish with the GSC. They both show the expected behaviour that jets with high values of either observable have a low response because the two calorimeter layers are near the gap between electromagnetic and hadronic calorimetry, which is uninstrumented. The bottom panels in both plots show negative tails for low-p_{T} jets. This is unphysical and caused by noise fluctuations in the calorimeter.

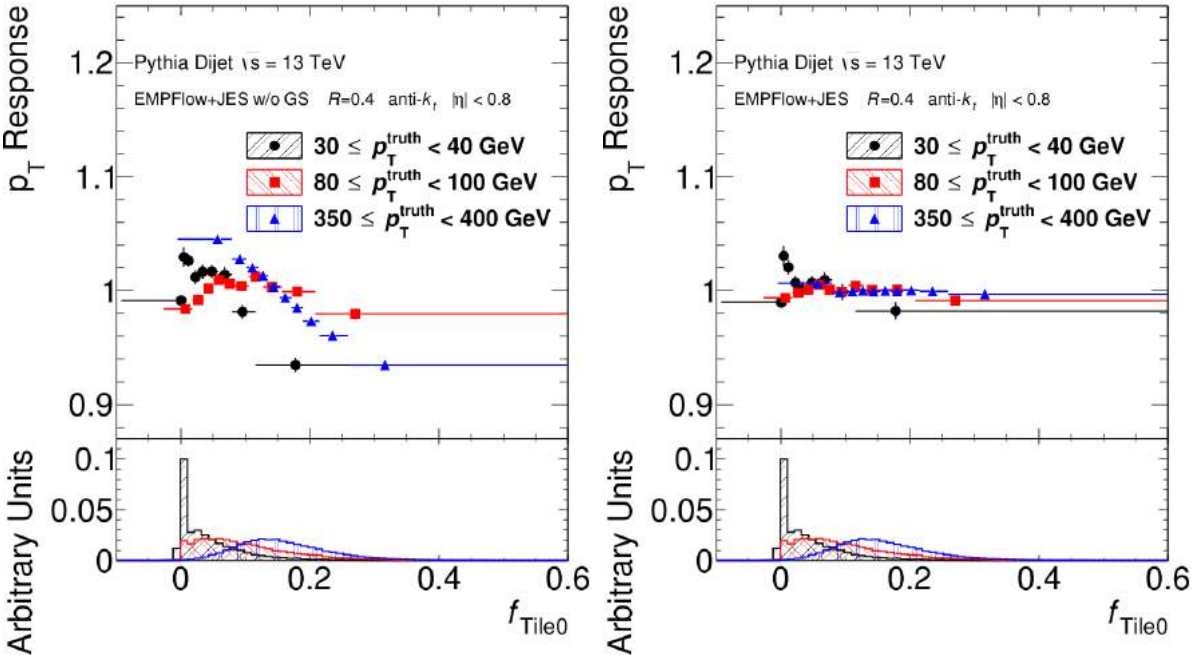

Figure 4.8: Top panels: average p_{T} response of particle flow jets as a function of f_{Tile0} before (left) and after (right) the GSC step based on f_{Tile0} in three bins of $p_{\text{T}}^{\text{truth}}$. Bottom panels: f_{Tile0} distributions in the three $p_{\text{T}}^{\text{truth}}$ bins.

Another effect of the GSC is flattening the jet response as a function of $|\eta|$. In Figure 4.10 this is shown for just the f_{EM3} and Punch-Through corrections in two high-p_{T} bins. The effect of the Punch-Through is largest in the transition region around $|\eta| = 1.5$, since the GSC removes detector effects in general. The comparison with jets corrected up to the f_{EM3} step is shown in order to show the effects of the relatively new particle flow Punch-Through correction in isolation.

The most important result of the GSC is the improvement of the jet p_{T} resolution. This is shown as a function of $p_{\text{T}}^{\text{truth}}$ in Figure 4.11. Here, the jet resolution is divided by the jet response to normalize it. The response is very close to one, so this normalization does not have a large impact. The Punch-Through correction is omitted here, since the improvement in this last step is small compared with the other ones. This is attributable to the Punch-Through correction only affecting a small portion of the jets. Since the corrections are applied sequentially the resolution after the later steps profits from the first corrections.

There is a steady improvement with every step of the GSC. The largest impact results from the first corrections. These diminishing returns with later GSC steps stem from the fact that many detector effects are corrected for at that point. Therefore, adding more GSC variables

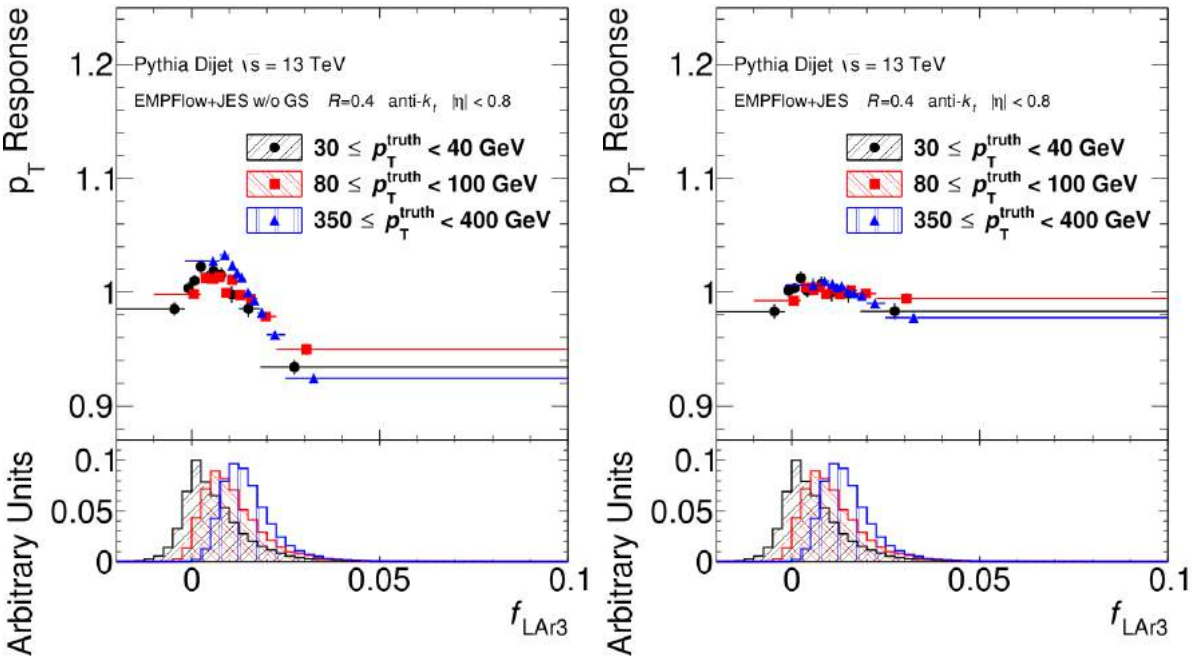

Figure 4.9: Top panels: average p_{T} response of particle flow jets as a function of f_{EM3} before (left) and after (right) the GSC step based on f_{EM3} in three bins of $p_{\mathrm{T}}^{\mathrm{truth}}$. Bottom panels: f_{EM3} distributions in the three $p_{\mathrm{T}}^{\mathrm{truth}}$ bins.

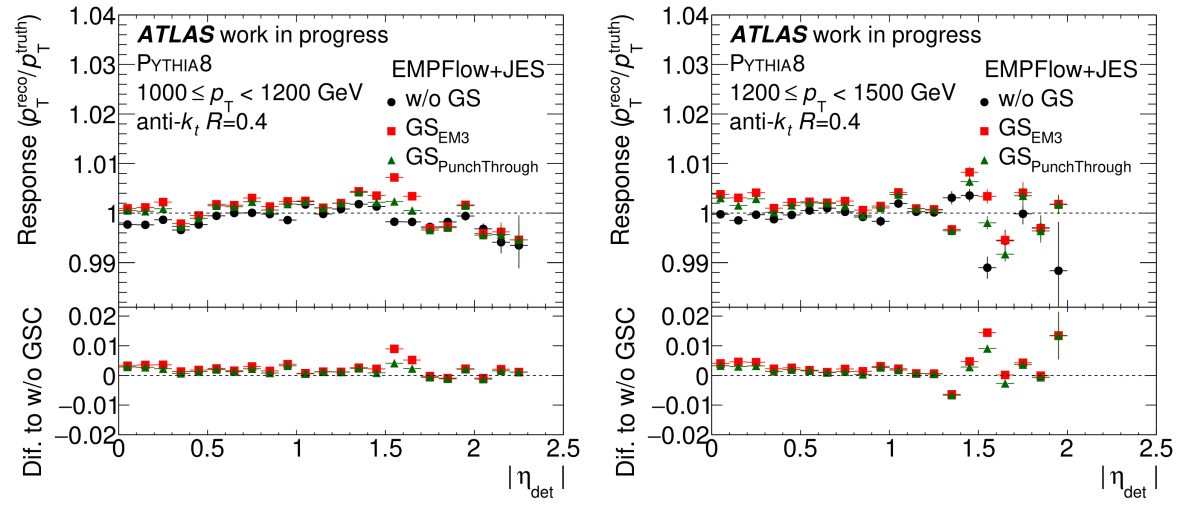

Figure 4.10: Top panels: average p_{T} response of particle flow jets as a a function of $|\eta|$ before any GSC correction and after the steps based on f_{EM3} and $n_{\mu,\mathrm{Seg}}$ in two different jet p_{T} bins. Bottom panels: Quadratic difference between uncorrected jets, f_{EM3} and $n_{\mu,\mathrm{Seg}}$ corrections.

does very little to improve the resolution even further. Also, the chosen GSC variables are already the most effective that were tested.

The resolution improvement is at its highest for intermediate-p_{T} jets of the order of 100 GeV. There, it reaches up to 20%. The resolution improvement is less consistent at low p_{T}.

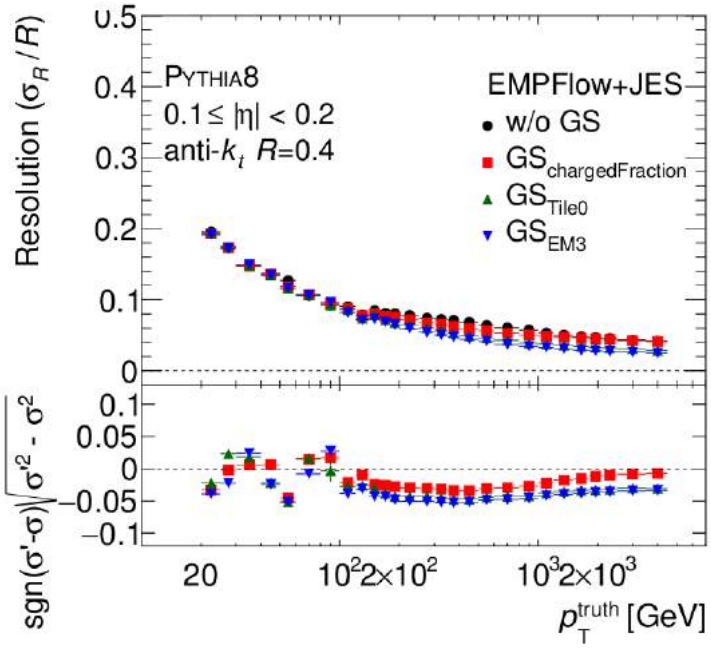

Figure 4.11: Top panel: Jet resolution σ_R normalized to the response R of particle flow jets as a function of $p_{\mathrm{T}}^{\mathrm{truth}}$. The resolution is shown before any correction is applied and after the first three steps of the GSC. Bottom panels: Quadratic difference between the resolution after each correction and the resolution before any correction is applied.

A comparison of the jet resolution improvement in both jet collections is depicted in Figure 4.12. The comparison is favourable towards particle flow jets below 10^2 GeV. Particle flow jets use tracking information to bolster their resolution whereas topocluster jets need to "catch up" with the corrections based on the n_{Trk} and σ_{Trk} dependencies.

At high p_{T} the advantage of particle flow jets diminishes or vanishes entirely. Here, the dense core of highly energetic jets causes the tracking efficiency to decrease. In addition, the multiple showers within the jet tend be closer together, which is more difficult to reconstruct for the algorithm.[3)] Between 100 GeV and 1000 GeV particle flow jets are a little bit worse with regards to the resolution.

Validation

The GSC was validated using a dijet balance method. With the data-driven validation the dependence of the response $\mathscr{R}(x_i)$ on a variable x_i is measured. Since this is a data-driven technique, the response cannot be defined with the truth jet p_{T} and instead relies on a pair of back-to-back jets. The dependence of the probe jet with the transverse momentum $p_{\mathrm{T}}^{\mathrm{probe}}$ on a variable is

[3)] See for example Ref. [103] for more information on this.

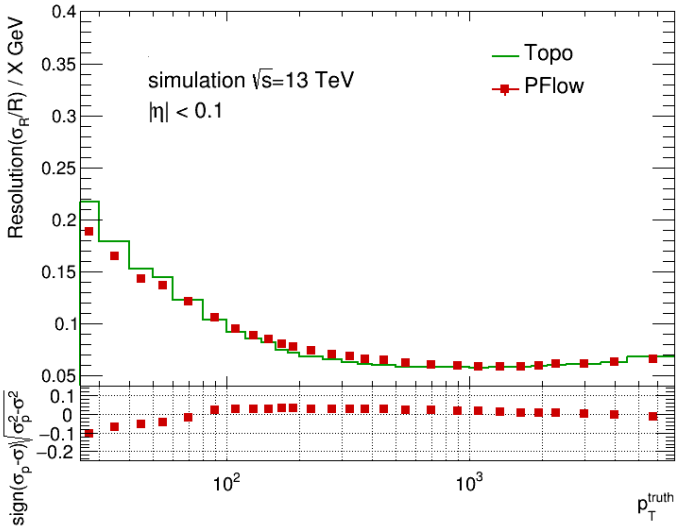

Figure 4.12: Top panel: Jet resolution σ_R normalized to the response R of topocluster jets (Topo, green) and particle flow jets (PFlow, red data points) as a function of $p_{\mathrm{T}}^{\mathrm{truth}}$. The resolution is shown after all corrections of the GSC are applied. Bottom panel: Quadratic difference between the particle flow resolution (σ_{p}) and the topocluster resolution (σ).

measured. The second jet is the reference jet, which is required to be in the same $|\eta_{\mathrm{det}}|$ range in order to have a similar resolution. Probe and reference jet are arbitrarily chosen among the two leading jets. Each event is used twice by inverting the arbitrary choice the second time. The average response $< \mathscr{R}(x_i) >$ is defined by:

$$< \mathscr{R}(x_i) >= \left\langle \frac{p_{\mathrm{T}}^{\mathrm{probe}}}{p_{\mathrm{T}}^{\mathrm{ref}}} \right\rangle . \tag{4.8}$$

The so defined response is not a Gaussian distribution in bins of $p_{\mathrm{T}}^{\mathrm{ref}}$, which means that the calculation of the average $< ... >$ is non-trivial. Instead the asymmetry $A(x_i)$ defined in Eq. 4.9 is used because the asymmetry is a Gaussian distribution in bins of the average p_{T} of the probe and reference jet $p_{\mathrm{T}}^{\mathrm{ave}} = (p_{\mathrm{T}}^{\mathrm{probe}}(x_i) + p_{\mathrm{T}}^{\mathrm{ref}})/2$. With the relation in Eq. 4.10, which follows from Eq. 4.8 and Eq. 4.9, conclusions about the response can be drawn:

$$A(x_i) = \frac{p_{\mathrm{T}}^{\mathrm{probe}}(x_i) - p_{\mathrm{T}}^{\mathrm{ref}}}{(p_{\mathrm{T}}^{\mathrm{probe}}(x_i) + p_{\mathrm{T}}^{\mathrm{ref}})/2} = \frac{p_{\mathrm{T}}^{\mathrm{probe}}(x_i) - p_{\mathrm{T}}^{\mathrm{ref}}}{p_{\mathrm{T}}^{\mathrm{ave}}(x_i)}, \tag{4.9}$$

$$< \mathscr{R}(x_i) >= \frac{2 + < A(x_i) >}{2 - < A(x_i) >}. \tag{4.10}$$

With these relations it is possible to apply the GSC to data and check whether it removes the dependence on x_i and improves the resolution. This was done at $\sqrt{s} = 7$ TeV in Ref. [150] and at 8 TeV in Ref. [151]. Indeed data and MC simulation compare well and an agreement within 2–4% was found.

4.3 Important results of the ATLAS jet calibration

4.3.1 Systematic uncertainties

The jet calibration brings with it a number of uncertainties due to assumptions made in the calibration steps, potential MC mismodelling and other reasons. In total 80 JES systematic uncertainty contributions are identified and need to be propagated to analyses. The contribution from the GSC results from the modelling of the Punch-Through. The largest contributor to the systematic uncertainties are the in-situ corrections with 67 out of the 80 JES systematic uncertainty terms.

The 67 in-situ uncertainties are combined into a set of 6 nuisance parameters (NPs) by adding the individual contributions quadratically. This is done to enable analyses to implement the uncertainties in a practical fashion. This requires treating some of the uncertainties as independent and losing information about their correlation. To deal with this correlation loss, which has an effect on the single percent scale, new p_{T}-$|\eta|$-dependent NPs are introduced. An example of the application of the jet uncertainties in an analysis can be found in Section 5.6.1. The systematic uncertainties are discussed in more detail in Ref. [143].

In Figure 4.13 the combined systematic uncertainty is shown as a function of p_{T} with constant $|\eta|$ and as a function of $|\eta|$ at a constant p_{T} value of 80 GeV. The main contributions are shown individually. These include pile-up, which shows the potential importance of particle flow jets in the future. They also include flavour response and composition, which are affected positively by the GSC.

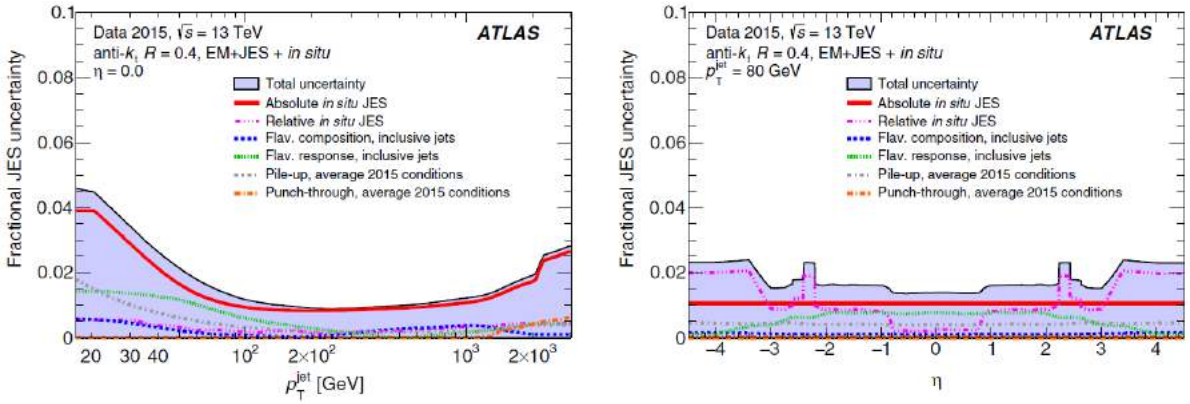

Figure 4.13: Combined systematic uncertainty and dominant systematic uncertainty contributions of topocluster jets fully calibrated up to the in-situ calibration. Absolute in-situ JES stands for Z/γ + jets and multijet balance, relative in-situ JES stands for η-intercalibration [143].

The combined systematic uncertainty is always below 4.5% reaching its highest point at very low p_{T}. It becomes as small as 1.5% around 200 GeV. A sharp incline can be observed at 2 TeV because the in-situ calibration only reaches that far.

4.3.2 Particle flow performance

With multiple jet collections to choose from it is important to know the strengths and weaknesses of each so that analysis teams can make an informed decision. The most important

properties of particle flow jets with regards to that issue are discussed here for that reason.

In Section 4.2.6 it is shown that particle flow jets offer a better jet p_T resolution at low to intermediate p_T. This is an important result because the event selection of many analyses uses either the jet p_T or the closely correlated missing transverse energy. In addition, the particle flow algorithm improves the directional resolution of jets by adding tracking information, which have a better angular resolution compared to calorimeter information, to the use of topoclusters.

The resolution of η and ϕ depending on the jet p_T is depicted in Figure 4.14 for LC topocluster and EM particle flow jets. LC topocluster jets are comparable to EM topocluster jets in that neither collection uses tracking information. However, LC jets do undergo an additional weighting, which makes them an interesting standard to compare particle flow jets to. Section 3.3.2 goes more into detail about their differences. As expected, Figure 4.14 shows that the angular resolution of particle flow jets is superior, especially for low-p_T jets.

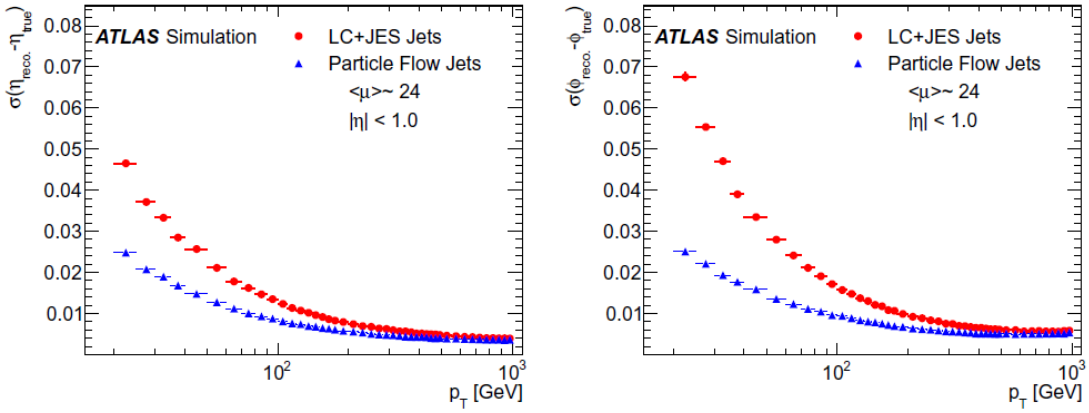

Figure 4.14: Pseudo-rapidity resolution of jets in simulated multijet events for both LC topocluster (LC+JES, red) and particle flow (blue) jets (left) for central jets. The same comparison for ϕ on the right. This is part of a particle flow performance study in Ref. [103].

A comparison of EM topocluster jets and EM particle flow jets is shown in Figure 4.15. The figure depicts the response of the η-direction of jets ($\eta_{\text{reco}} - \eta_{\text{truth}}$) in multijet events[4)] for high-p_T central jets. The peak is significantly narrower in the case of particle flow jets or, in other words, the resolution is better. Its root mean square (RMS) is 0.024 compared with 0.033 for topocluster jets. Similarly, the response of the $\Delta\eta$ between the two leading jets is resolved significantly better for central jets at intermediate p_T. Here, the resolution is defined as $(\Delta\eta_{\text{jj,reco}} - \Delta\eta_{\text{jj,truth}})/\Delta\eta_{\text{jj,truth}}$ and its RMS is 0.055 and 0.039 for topocluster and particle flow jets, respectively. For this comparison both reconstructed leading jets are required to be matched to the two leading truth jets within $\Delta R = 0.4$.

As mentioned before particle flow jets have a better pile-up suppression because of the removal of charged tracks that do not come from the primary process. This effect can be seen in Figure 4.16. Its right shows the number of fake jets per event as a function of η. Fake jets are defined as jets that cannot be matched to truth jets with a transverse momentum larger than 4 GeV and within $\Delta R = 0.4$. Especially for central jets where the particle flow algorithm can make use of the tracking system it does a lot better even surpassing LC topocluster jets with

[4)] The multijet sample used for this comparison is the same as the one used in the GSC.

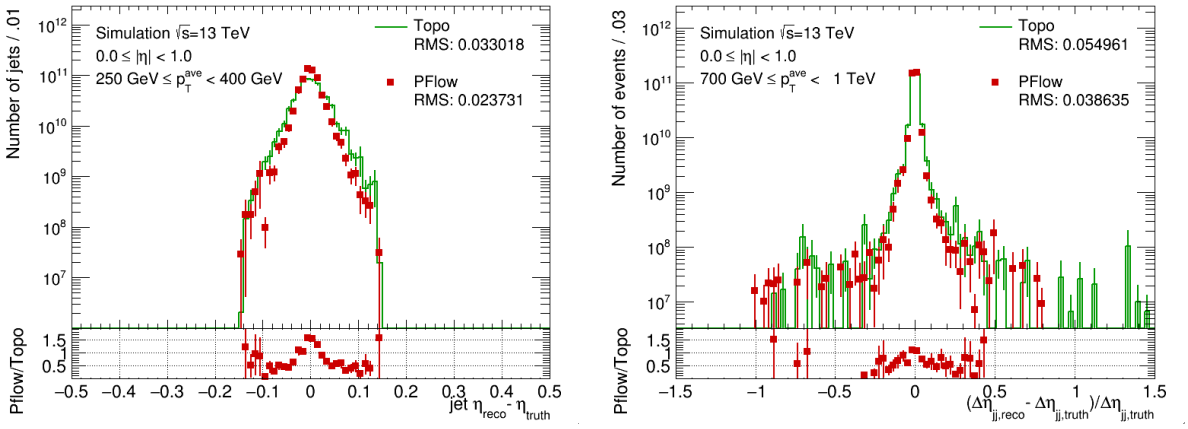

Figure 4.15: Jet η response in simulated multijet events for both topocluster (Topo, green) and particle flow (PFlow, red) jets on the left. The same comparison for the $\Delta\eta$ of the two leading jets is on the right.

additional pile-up removal [113]. The reconstruction efficiency is the rate, at which hard-scatter jets ($p_{\mathrm{T}} > 15$ GeV) are reconstructed within $\Delta R = 0.4$ of a truth jet. Here too, particle flow jets have a higher quality at low $p_{\mathrm{T}}^{\mathrm{truth}}$. Note that the additional pile-up removal hurts the efficiency of LC jets. A drawback that is not present in particle flow.

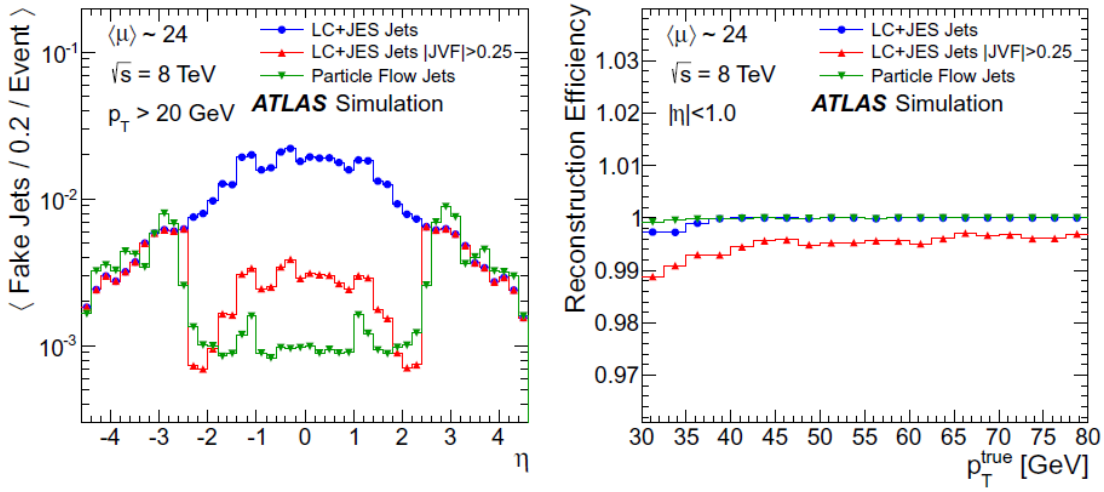

Figure 4.16: Average number of fake jets per event versus η (left) and reconstructions efficiency versus the truth jet p_{T} (right). Particle flow jets (green) are compared with LC topocluster jets with (red) and without (blue) an added pile-up suppression. This is part of a particle flow performance study in Ref. [103].

The good pile-up removal for central jets is further motivation to improve the pile-up suppression of forward jets. Here, new technologies like the forward jet vertex tagger (fJVT) [116] promise further improvements. Particle flow jets will be especially important for the future of the ATLAS experiment, as the ever increasing instantaneous luminosity will also mean an increase of pile-up.

4.3.3 Conclusion

The Run 2 ATLAS jet calibration is presented for EM scale topocluster and particle flow jets reconstructed with the anti-k_t ($R = 0.4$) algorithm. In it the origin of the jet is corrected and the pile-up contamination is removed with an area-based and a residual correction. The jet four-momentum is corrected, calibrating the jet energy scale to particle level and improving the angular resolution with the absolute EtaJES calibration. Jets are calibrated starting at $p_{\mathrm{T}} = 20$ GeV, below which they are not recommended for usage in analyses outside of dedicated tests.

The jet energy resolution is improved by removing dependencies on detector level variables with the GSC. This also lessens the differences between the energy response to light quark and gluon jets. The global sequential calibration is successfully applied to topocluster and particle flow jets. For the first time the latter jet collection is calibrated with the Punch-Through correction, the last step of the GSC. The impact of the Punch-Through correction is small. However, it allows a fair comparison between the jet collections. Finally, the data-driven in-situ calibration balances forward jets against central jets, bosons against jets and jets against each other to calibrate for differences between MC simulation and data jet responses.

As a result the jet resolution is improved by up to 20%. Around 100 GeV the resolution in both jet collections shows the largest improvement. Dependencies on detector level variables are lowered to less than 2% and the combined systematic uncertainty is as low as 4.5%. Particle flow jets exhibit some advantages over topocluster jets with a superior pile-up suppression and a better jet resolution for central jets with low to intermediate p_{T}.

4.3.4 Outlook

The improvement of the calibration is an ongoing effort. One potential area of improvement is the correlation of GSC steps and the selection of jet observables to correct for. The correlation may have been found to be negligible, but as ATLAS thrives for ever higher precision it might be worthwhile to improve even in this area. The GSC variables were selected with the good reasons listed above and lead to the outstanding results presented in this chapter. However, this does not mean that they are guaranteed to be the best GSC variables possible or will remain optimal as detector conditions change.

Both topics can be addressed with the regression method presented in Ref. [153]. Regression is a multivariate analysis technique and part of the TMVA package [154], which is commonly used in ATLAS. The method uses dozens of jet observables including the GSC variables in one simultaneous correction step. It is based on measuring the correlations between jet observables and the jet response. With that the dependencies on the jet observables can be measured and removed via correction factors. In contrast to the GSC this takes correlations between jet observables into account and can even construct new optimized variables as combinations of the input observables. Since the regression can effectively make use of more input variables and does not have to rely on the same approximations, it is expected to improve the jet resolution even further. However, further testing and validation is necessary before it is ready for use in the jet calibration.

Chapter 5

Search for invisible decays of the Higgs boson produced in vector-boson fusion

5.1 Introduction

As discussed in Section 2.2.5 there are several beyond the Standard Model (BSM) models [11, 155, 156, 157] that predict invisible particles that couple to the Higgs boson. These particles could therefore be part of the final state of Higgs boson decays. Even in the Standard Model (SM) there is a process producing invisible decay products of Higgs boson decays in $H \to ZZ^* \to \nu\bar{\nu}\nu\bar{\nu}$. However, the branching ratio (BR) is very low at about 0.12%. If one of the BSM predictions were to be correct, it might be possible to observe a Higgs boson to invisible branching fraction ($\mathscr{B}_{\text{inv}}$) larger than the SM prediction at the LHC.

The collider experiments searching for invisible decays of the Higgs boson can be divided into two categories: indirect constraints and direct searches. Indirect constraints on $\mathscr{B}_{\text{inv}}$ are determined by combining the findings in searches for visible decays of the Higgs boson. A global fit to all Higgs boson couplings in which the couplings to BSM particles are left as free parameters is used to calculate the constraints. The thus determined upper limit on $\mathscr{B}_{\text{inv}}$ is 34% at 95% CL [158].

Direct searches for invisible decays of Higgs bosons like the one described here seek to select events with final states matching the expected decay products from the studied interaction. Since the invisible decay products cannot be detected with the ATLAS detector, they appear as missing transverse energy ($E_{\text{T}}^{\text{miss}}$). Other features of the event topology are unique to each particular search and are described in detail below. Either way the Higgs boson needs to carry enough momentum to cause $E_{\text{T}}^{\text{miss}}$ above a trigger threshold in the final state.

The most sensitive search channel is the invisible decay of a Higgs boson produced in vector-boson fusion (VBF). VBF Higgs boson production only has the second highest cross-section behind gluon–gluon fusion (ggF), but because of the smaller backgrounds, searches for VBF Higgs boson to invisible events have a higher sensitivity with regards to invisible decays [159]. The process is depicted in Figure 5.1.

A secondary signal of invisibly decaying Higgs bosons produced in ggF is considered. Figure 5.2 shows two Feynman diagrams of such processes, the right of which also contributes to the signal region described in Section 5.4.4. There is assumed to be no interference between the two signals. Since ggF does not necessarily cause the production of particles other than

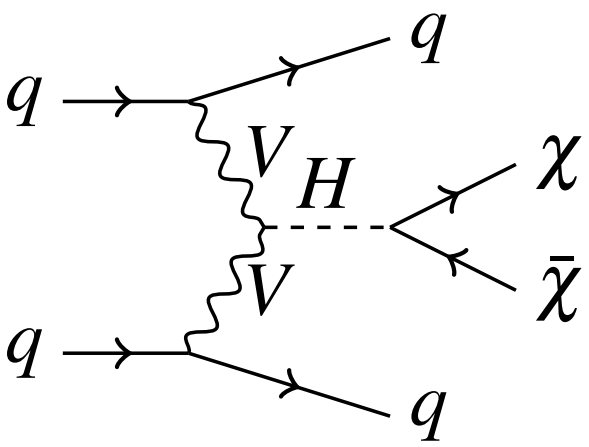

Figure 5.1: Example diagram of VBF Higgs boson to invisible production, the main signal considered in the search.

the Higgs boson, there is no detectable signal in the simplest form of the process (left of Figure 5.2). A final state with no reconstructed object makes it impossible to define any sort of expected event topology to select for. Instead events with $E_{\mathrm{T}}^{\mathrm{miss}}$ and two jets caused by initial state radiation (ISR) as depicted on the right of Figure 5.2 are considered because of the overlap with the VBF signal.

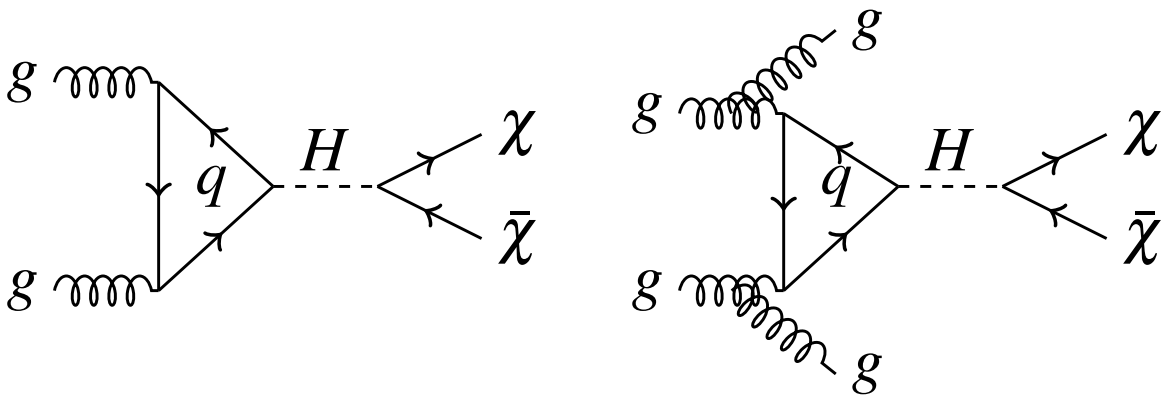

Figure 5.2: Example diagrams of ggF Higgs boson to invisible production. Right: initial state radiation leading to two jets in the final state.

Both ATLAS and CMS have performed searches in the past. In Run 1 with centre-of-mass energies up to 8 TeV the upper limit on the branching fraction of a 125 GeV Higgs boson produced in vector-boson fusion decaying into invisible particles was 0.30 (0.35) observed (expected) [160]. The combination with other direct searches and constraints from visible decays lead to a 0.24 (0.23) observed (expected) limit [161]. The comparable VBF search in CMS yielded an observed (expected) limit of 0.65 (0.49) [162]. CMS was also able to deliver results with $\sqrt{s} = 13$ TeV data. The limit of the invisible branching fraction is 0.28 (0.21) with VBF

production and 0.24 (0.18) for the combination of multiple direct searches [163]. In addition to VBF and ggF there are other production modes for invisibly decaying Higgs bosons that are not considered here. The list includes $b\bar{b}H$, $t\bar{t}H$, VH [70], monojet [164] and associated production [165]. The processes are also discussed in Section 2.2.5.

5.2 Analysis strategy

The data for the analysis were collected using proton–proton collisions at $\sqrt{s} = 13$ TeV. The analysis strategy is optimized for a SM Higgs boson with a mass of 125 GeV and all couplings in both the VBF and the ggF process are assumed to be SM couplings. The signal region (SR) selection is chosen using a multivariate optimization that simultaneously varies all jet related selection requirements to find the most strict expected limit on the Higgs boson to invisible BR.

The main background comes from decays of vector bosons. First of all the process $Z \to \nu\bar{\nu}$ + jets is an irreducible background, since the neutrinos are invisible decay products for the purpose of their detection with the ATLAS detector. For the process $W \to \ell\nu$ + jets the background can come from charged leptons not being reconstructed or "lost" in the case of muons and electrons. In the case of $W \to \tau\nu$ there are multiple reasons for an event with such a process to end up in the SR depending on whether the τ decays leptonically or hadronically.

Control regions (CRs) to study $Z \to \ell^+\ell^-$ + jets and $W \to \ell\nu$ + jets where the lepton is reconstructed are defined. These processes are similar in their interactions to $Z \to \nu\bar{\nu}$ and $W \to \ell_{\text{lost}}\nu$, but are much easier to reconstruct. The backgrounds in the signal region are then normalized with a simultaneous fit using data in the CRs in order to reduce their uncertainties.

Backgrounds from $t\bar{t}$ and $single-top$ processes are relatively minor and are handled with estimates from simulation. Quantum chromodynamics (QCD) events produce a multijet background from jets being mismeasured. This background is also small, but its estimate is difficult to determine and produces relatively large uncertainties. The analysis selection is in part optimized to mostly reject the multijet background, but the data-driven rebalance and smear (R+S) method is still needed to predict the background with good precision.

All the optimization described below is undertaken without looking at SR data to avoid bias. Before the SR is included the analysis is called "blinded". After all decisions are finalized, the analysis is unblinded and the SR data is included. This step is only needed to produce the final results.

This chapter details the search for invisible decays of the Higgs boson. Section 5.3 is the description of the data and simulated samples used in the analysis. In Section 5.4 the selection is presented, discussing signal and control regions. The presentation of SM backgrounds and how they are estimated is the subject of Section 5.5. All systematic uncertainties are covered in Section 5.6. With the fit model described in Section 5.7 the results of the analysis are calculated leading to their discussion in Section 5.8. Section 5.9 deals with the interpretation of the results of the search in the context of dark matter (DM) and several theoretical models. Finally, Section 5.10 summarizes the findings and offers a look at the future of the analysis.

5.3 Data and simulated samples

5.3.1 Data

The search for invisible decays of the Higgs boson is performed with data recorded in 2015 and 2016 at a centre-of-mass energy of $\sqrt{s} = 13$ TeV. The dataset amounts to an integrated luminosity of 36.1 fb^{-1}. The uncertainty in the integrated luminosity is 2.1%. Only data recorded with a fully operational ATLAS detector and with stable beams are taken into consideration.

5.3.2 Simulated samples

Both full simulation [139] and fast simulation [140] are used for this analysis. Full simulation seeks to simulate the entire detector and how it reconstructs the generated events, while fast simulation simply parametrizes the calorimeter response. Both types of simulation are discussed in Section 3.4.

The fully simulated samples are:

- VBF $H \to inv$ signal sample with the Higgs boson mass set to 125 GeV
- $Z \to \nu\bar{\nu}$ and $W \to \ell\nu$ background samples as well as $Z \to \ell^+\ell^-$
- $t\bar{t}$ and single-top background samples
- Multijet background samples

The fast simulated samples are:

- VBF $H \to inv$ signal sample with Higgs boson masses different from 125 GeV. The full list of mass points is: 75 GeV, 200 GeV, 300 GeV, 500 GeV, 750 GeV, 1 TeV, 2 TeV and 3 TeV.
- ggF $H \to inv$ signal sample with the Higgs boson mass set to 125 GeV
- Pure weakly interacting massive particles (WIMP) triplet samples for the dark matter interpretation

All Monte Carlo (MC) samples used in the analysis are listed in Appendix A.1.2. All of them mimic the 25 ns bunch spacing conditions that were present during data taking.

Background

V+ jets: The main backgrounds of the analysis are $Z \to \nu\bar{\nu}$, $W \to \tau\nu$ and $W \to \ell_{\text{lost}}\nu$ events or W/Z + jets for short. Here, ℓ_{lost} describes a charged lepton that is not reconstructed within the detector, which can lead to missing transverse energy. The primary processes of both main backgrounds were modelled using `Sherpa` 2.2.1 [138]. They include electroweak (EWK) and strongly produced components, which can be categorized by their order in the coupling constant α_{EW}.

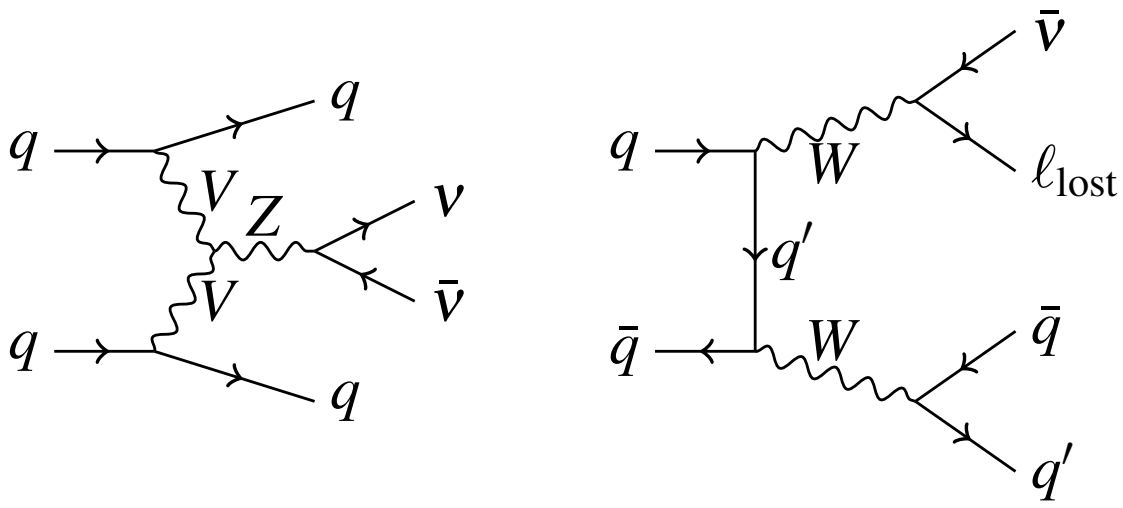

Figure 5.3: Example diagram of electroweak-produced $Z \to \nu\bar{\nu}$ (left) and diboson production (right), each of which contributes to the background of the search.

The strong component is of order α_{EW}^2 and the EWK component is of order α_{EW}^4. An example diagram for EWK V + jets events can be found in Figure 5.3. Strong-produced examples are in Figure 5.4. Separate MC samples are simulated for each component. Strong V + jets production is simulated up to next-to-leading-order (NLO) for matrix elements with up to two final state partons and up to leading-order (LO) with up to four partons. The EWK component is further split into diboson diagrams with no t-channel boson (for example Figure 5.3 right) and VBF diagrams with at least one t-channel boson (for example Figure 5.3 left). Here, the VBF process is simulated up to LO in α_{S} in the cases of three or fewer final state partons.

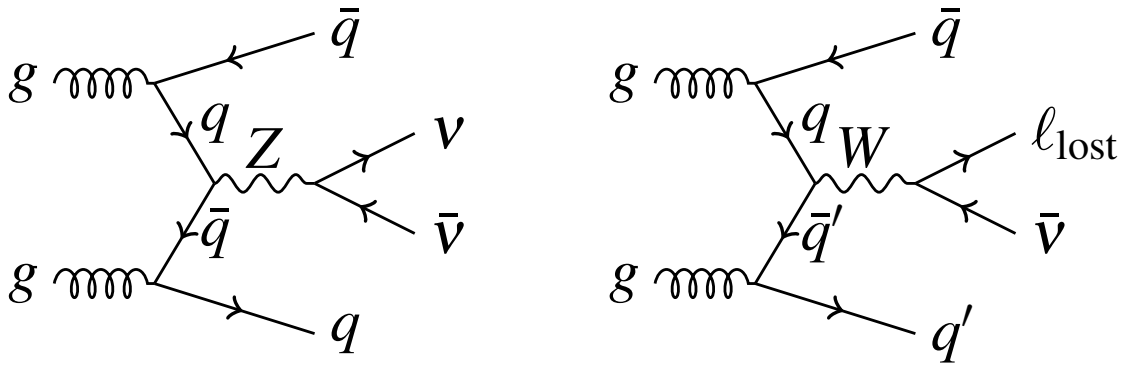

Figure 5.4: Example diagrams of strongly produced $Z \to \nu\bar{\nu}$ (left) and $W \to \ell_{\text{lost}}\nu$ production (right), the largest background contributions of the search.

Diboson diagrams are computed up to NLO with three or fewer final state partons and up to LO with four or five. Additional partons are produced through ISR or final state radiation (FSR). VBF and diboson processes are assumed to not interfere significantly for the purpose of the analysis.

In addition, there are $Z \to \ell^+\ell^-$ samples with both strong and EWK production, which are simulated with Sherpa 2.2.1 as well. Here, a generator-level filter that requires the dilepton mass to be larger than 40 GeV is applied in order to avoid processes involving off-shell photons. These processes are negligible in the $H \to inv$ signal region. For all of the samples described above the Matrix elements are calculated with Comix [132] and OpenLoops [135]. The showering is done with the Sherpa parton shower [166] and the ME+PS@NLO prescription [134]. At next-to-next-to-leading-order (NNLO) the PDF set NNPDF3.0 NNLO PDF [167] is used together with a Sherpa parton shower tuning.

$t\bar{t}$, single top: For all simulations of processes involving top-quarks its mass is set to 172.5 GeV and its spin correlations are preserved. The primary processes are simulated using Powheg-Box v2 [136]. The CT10 PDF sets [168] are used in the calculation of matrix elements. The exception are EWK t-channel single top-quark events, which are simulated with Powheg-Box v1. For the underlying event (UE), parton shower and fragmentation Pythia 6.4 [169] with the CTEQ6LI PDF sets and Perugia 2012 tune is used. Bottom-quark and charm-quark decays are simulated with the EvtGen v1.2.0 program.

Multijet: The background from simulated multijet events in the signal region is small, since it only exists due to the rarely occurring fake $E_{\mathrm{T}}^{\mathrm{miss}}$.[1)] The reason why there is any multijet background is that these processes have large cross-sections. This leads to a vanishing amount of MC events in the signal region. Statistics that are large enough to produce multijet events in the signal region would require more resources than were available for the analysis. The multijet samples that are produced with Pythia 8 [137] are instead used for the validation of the data-driven R+S method that is covered in Section 5.5.4.

Signal

Both VBF and ggF Higgs boson to invisible signal samples are simulated in Powheg up to NLO in α_{S}. The showering is done in Pythia and the NLO electroweak corrections are calculated with HAWK [133]. The fact that the Higgs boson is always produced on-shell for processes considered in this analysis is exploited by simulating the invisible decay as a Higgs boson decaying into two Z bosons that then decay into two neutrinos each. As the neutrinos are invisible to the detector, this process is indistinguishable from the signal. However, the SM branching ratio of this process is only 1.2×10^{-3}. Therefore, the search for a BSM signal can actually be performed by letting the branching ratio float freely as a fit parameter later.

The PDF set for the ggF sample is PDF4LHC15_nnlo_100 allowing for the calculation of the cross-section up to N3LO. The VBF sample is split into two: one with $E_{\mathrm{T}}^{\mathrm{miss}} < 125$ GeV and one with $E_{\mathrm{T}}^{\mathrm{miss}} > 125$ GeV, the latter of which has more statistics. Additional mass points are simulated with the same parameters except for the mass of the Higgs boson.

Pile-up reweighting

Several experimental features of a dataset cannot be simulated in advance and are only known after data taking. These have to be measured in data and the reweighting procedure can later correct for them. One of the most important ones of those features is pile-up. It scales with

[1)] Technically, some amount of fake $E_{\mathrm{T}}^{\mathrm{miss}}$ occurs all the time but not with such a magnitude that it would be mistaken for a signal.

the average amount of interactions per bunch crossing μ, since a higher number of interactions also causes a higher amount of objects that do not come from the primary process. Each MC sample is generated with some μ distribution, before the actual distribution is measured in data. After data taking a set of weights is derived and applied to the simulated sample. The weights are defined in such a way that the simulated μ distribution after reweighting is the same as in data [170].

Other features include identification, isolation and lepton reconstruction efficiencies as well as trigger efficiencies. The MC samples are also reweighted to the luminosity L of the dataset, such that a process with the cross-section σ produces a number of events N according to the equation $N = L\sigma$ as discussed in Section 3.1. Other effects need to be taken into account when calculating the event weight w. They are covered in Appendix A.1.2. There can also be an additional weight from the event generator. The total weight applied to each event is simply a product of all the individual weights.

5.4 Selection

5.4.1 Preselection

During data taking with the ATLAS detector several effects can inhibit the recording of events at the highest precision. There can be noise bursts in the electromagnetic calorimeter, modules can be inactive for a brief period of time or there can be general bad detector conditions. These problems are usually fixed within seconds or minutes either by automatic recovery protocols or through the work of the control room personnel. The periods in which data taking is optimal are recorded on the so called good runs list (GRL). Only events that are on the GRL are used in the analysis and all others are rejected.

5.4.2 Trigger

Missing transverse energy triggers

The $E_{\mathrm{T}}^{\mathrm{miss}}$ triggers at level 1 (L1) set a requirement at 50 GeV. At the high level trigger stage the calorimeter jets are reconstructed using energy clusters in a way that is very similar to the description in Section 3.3.2. The vectorial sum of all these jets with $p_{\mathrm{T}} > 7$ GeV is taken as the trigger level missing transverse energy. Its high level trigger (HLT) threshold changed over the course of data taking. The purpose of this change was to always use the unprescaled trigger with the lowest threshold to get the maximum amount of statistics. All of these triggers are listed in Table 5.1. Due to a firmware bug some events that should have passed the L1 trigger did not. These events were recovered using the jet trigger HLT_noalg_J400, which requires a 400 GeV jet at L1 and has no HLT selection, in addition to the $E_{\mathrm{T}}^{\mathrm{miss}}$ triggers.

The turn-on curves $\varepsilon(T, x_i)$ of the $E_{\mathrm{T}}^{\mathrm{miss}}$ triggers are studied using muon triggers as reference triggers. It is determined that the triggers listed in Table 5.1 are fully efficient at $E_{\mathrm{T}}^{\mathrm{miss}} > 200$ GeV and at $E_{\mathrm{T}}^{\mathrm{miss}} = 180$ GeV their efficiency is greater than 0.98.

Table 5.1: List of $E_{\mathrm{T}}^{\mathrm{miss}}$ triggers used in the analysis per data taking period.

Period	Trigger
All 2015	HLT_xe70_mht
2016, Runs $\leq$ 304008	HLT_xe90_mht_L1XE50
2016, Runs $>$ 304008	HLT_xe110_mht_L1XE50
All	HLT_noalg_J400

Lepton triggers

Lepton momenta are measured with a higher precision than missing transverse energy. As a result their turn-on curves are steeper [171, 172]. The lepton triggers listed in Table 5.2 were used to select data in the control regions described in Section 5.5.1. Where multiple triggers are listed, an event is required to pass at least one of these triggers. Requiring a lepton $p_{\mathrm{T}} > 30$ GeV is enough to be in the plateau of the lepton triggers.

Table 5.2: List of lepton triggers used in the analysis per data taking period.

Period	Electron Trigger	Muon Trigger
All 2015	HLT_e24_lhmedium_L1EM20VH HLT_e60_lhmedium HLT_e120_lhloose	HLT_mu20_iloose_L1MU15 HLT_mu50
2016, Runs $\leq$ 304008	HLT_e24_lhtight_nod0_ivarloose HLT_e60_lhmedium_nod0 HLT_e140_lhloose_nod0	HLT_mu50 HLT_mu26_ivarmedium
2016, Runs $>$ 304008	HLT_e26_lhtight_nod0_ivarloose HLT_e60_lhmedium_nod0 HLT_e140_lhloose_nod0	HLT_mu50 HLT_mu26_ivarmedium

Triggers used for the multijet background estimate

For the multijet background estimate, which is discussed in Section 5.5.4, low-p_{T} jets become important. Therefore, low-threshold prescaled triggers are used (see also Section 3.2.5). A prescale ps_i is a measure for how likely that is to happen. For each trigger i with a prescale ps_i only $1/ps_i$ of the events are recorded.

EVent weights are applied to restore the number of events at a given p_{T} to the number of events that would be recorded if no prescale existed [170]. Given a number of events that would be recorded without prescales $N_{\mathrm{triggered}}$ and a number of recorded events N_{recorded}, the following relation is considered:

$$N_{\mathrm{recorded}} = p(\text{triggered and selected}|p_{\mathrm{T}}^{\mathrm{online}}) \times N_{\mathrm{triggered}}, \tag{5.1}$$

where $p(\text{triggered and selected}|p_{\text{T}}^{\text{online}})$ is the probability that an event containing a jet with a large enough $p_{\text{T}}^{\text{online}}$ for a trigger to have fired is actually selected despite the application of a prescale. Its inverse is the effective prescale ps_{eff}. Considering that $1-1/ps_i$ is the probability for an event to not have been selected by a trigger i, $p(\text{triggered and selected}|p_{\text{T}}^{\text{online}})$ can be expressed with:

$$p(\text{triggered and selected}|p_{\text{T}}^{\text{online}}) = 1 - \prod_{i=1}^{N_t}(1 - \frac{1}{ps_i}), \tag{5.2}$$

where N_t is the number of triggers that could have fired. The list of single jet triggers that were used can be found in Table 5.3. An event used in the analysis passed a logical OR of all of these triggers.

Table 5.3: List of single jet triggers for the selection of multijet events. The data recorded by these triggers were used for the multijet background estimate.

Trigger						
HLT_j15	HLT_j25	HLT_j35	HLT_j55	HLT_j60	HLT_j85	HLT_j110
HLT_j150	HLT_j175	HLT_j200	HLT_j260	HLT_j300	HLT_j320	HLT_j360
HLT_j380	HLT_j400	HLT_j420	HLT_j440	HLT_j460		

5.4.3 Analysis objects

The following is a short description of the objects relevant for the analysis with definitions specific to the search. Section 3.3 is a more detailed and general look into the reconstruction of these physics objects with the ATLAS detector.

Jets

For the search for invisible decays of the Higgs boson electromagnetic (EM) scale topocluster jets reconstructed with the anti-k_t algorithm (topocluster jets or Topo jets from now on) were used [101]. In addition, the use of EM scale particle flow jets reconstructed with the anti-k_t algorithm (particle flow jets or PFlow jets from now on) in the analysis is studied especially in Section 5.10.1 and later in Chapter 6. As seen in Chapter 4 there are several advantages to using particle flow jets like the superior energy resolution for intermediate p_{T} jets. However, it is unclear as to how these effects may propagate to the results of the analysis. For both types of jets the distance parameter of the anti-k_t algorithm is $R = 0.4$. The algorithm is discussed in Section 3.3.2.

Jets used in the analysis have to fulfil the following criteria:

- $p_{\text{T}} > 25$ GeV
- $|\eta| < 4.5$

- Jets need to pass the medium jet vertex tagger (JVT) (see Section 3.3.2 for more details) requirement. In other words, jets with $p_{\mathrm{T}} < 60$ GeV and $|\eta| < 2.4$ need to have a JVT score of more than 0.59.
- For particle flow jets JVT > 0.2 is required. The inherent pile-up suppression of particle flow jets allows a more loose criterion.
- Jets need to satisfy tight cleaning requirements (JetCleanTight, as defined in Section 3.3.2).
- In order to remove non-collision background the entire event is discarded if a jet does not satisfy the jet cleaning requirements after overlap removal and JVT selection.

Non-collision background can arise because of beam gas interactions that cause particle cascades, which sometimes reach the detector. Cosmic rays can also have a similar effect. Energy deposits that are caused by these effects are not momentum balanced, since they do not originate from proton–proton collisions in the centre of the detector. Therefore, they are especially problematic for analyses with jet and missing transverse energy in the final state and can be picked up by $E_{\mathrm{T}}^{\mathrm{miss}}$ triggers.

Other analysis objects

The other analysis objects have to meet a list of requirements as well:

- Primary vertex
  - The primary vertex with the largest $\sum p_{\mathrm{T}}^2$ of associated tracks is defined as the location of the hard-scatter interaction.
  - One primary vertex needs at least two associated tracks with $p_{\mathrm{T}} > 400$ MeV or the event is discarded.
- Electrons
  - EM calorimeter energy cluster matched to inner detector track.
  - $p_{\mathrm{T}} > 7$ GeV
  - $|\eta| < 2.47$, but not in the EM end-cap transition region at $1.37 < |\eta| < 1.52$
  - Primary vertex consistency criteria: $z_0 \times \sin\theta < 0.5$ mm and $|d_0|/\sigma(d_0) < 5$, where z_0 and d_0 are the longitudinal and transverse impact parameters as defined in Section 3.3.1.
  - Tight identification criteria as defined in Section 3.3.3
  - Isolated. The Gradient isolation criteria used here have an efficiency of 90% (99%) for truth electrons with $p_{\mathrm{T}} > 25$ GeV (> 60 GeV).
- Muons
  - Muon-spectrometer track matched to inner detector track

  - $p_{\mathrm{T}} > 7$ GeV
  - $|\eta| < 2.5$
  - Primary vertex consistency criteria: $z_0 \times \sin\theta < 0.5$ mm and $|d_0|/\sigma(d_0) < 3$
  - Medium identification criteria as defined in Section 3.3.3
  - Isolated. The Gradient isolation criteria used here have an efficiency of 90% (99%) for truth muons with $p_{\mathrm{T}} > 25$ GeV (> 60 GeV).

- $E_{\mathrm{T}}^{\mathrm{miss}}$
  - Similar to Eq. 3.14 in Section 3.3.4 $E_{\mathrm{T}}^{\mathrm{miss}}$ is defined as the negative vectorial sum of the transverse momenta of all analysis objects (electrons, muons and jets).
  - The negative vectorial sum of all tracks not matched to analysis objects but consistent with the primary vertex — the so-called track soft term (TST) $E_{\mathrm{T}}^{\mathrm{miss}}$ as defined in Section 3.3.4 — is added as well.
  - Only jets with $p_{\mathrm{T}} > 20$ GeV and satisfying the medium JVT requirement are included in the $E_{\mathrm{T}}^{\mathrm{miss}}$ definition.
  - The closely related $E_{\mathrm{T}}^{\mathrm{miss}}$ significance ($E_{\mathrm{T}}^{\mathrm{miss,sig}}$) is defined in Section 5.5.2.

- $MHT(\mathrm{noJVT})$
  - Magnitude of the vectorial sum of the momenta of all jets in the event.
  - Only jets with $p_{\mathrm{T}} > 20$ GeV are included in this definition.
  - The variable compliments $E_{\mathrm{T}}^{\mathrm{miss}}$ by being sensitive to fake $E_{\mathrm{T}}^{\mathrm{miss}}$ from jets not satisfying the medium JVT requirement.

5.4.4 Signal region

Three signal region bins SR1, SR2 and SR3 are defined. They are optimized to deliver a large signal efficiency for invisible decays of a Higgs boson produced in vector-boson fusion assuming SM interactions. All signal region bins share the following selection:

- $E_{\mathrm{T}}^{\mathrm{miss}}$ trigger requirement
- No electrons or muons
- Leading jet: $p_{\mathrm{T,j1}} > 80$ GeV
- Subleading jet: $p_{\mathrm{T,j2}} > 50$ GeV
- Third jet veto: No additional jets with $p_{\mathrm{T}} > 25$ GeV
- $E_{\mathrm{T}}^{\mathrm{miss}} > 180$ GeV
- $MHT(\mathrm{noJVT}) > 150$ GeV
- $\Delta\Phi(j_1, E_{\mathrm{T}}^{\mathrm{miss}}) > 1$ and $\Delta\Phi(j_2, E_{\mathrm{T}}^{\mathrm{miss}}) > 1$

- $\Delta\phi_{jj} < 1.8$
- $\eta_{j1} \times \eta_{j2} < 0$
- $\Delta\eta_{jj} > 4.8$
- $m_{jj} > 1$ TeV

The first five requirements select for events with exactly two jets, no lepton and large E_T^{miss} in the final state, as would be expected from Figure 5.1. Large E_T^{miss} follows logically from the invisible decay products and therefore has to account for the energy carried by the Higgs boson. The $MHT(\text{noJVT})$ requirement can be understood as an auxiliary E_T^{miss} requirement. Because of the removal of jets as a result of the JVT requirement fake E_T^{miss} is introduced. The $MHT(\text{noJVT})$ requirement is able to discriminate against these events.

The other requirements make use of knowledge of the topology that is expected from a signal event. In a signal event the two quark jets are recoiling from the Higgs boson and are therefore well separated from the E_T^{miss} direction ($\Delta\Phi(j_{1,2}, E_T^{miss}) > 1$) and they are not back-to-back ($\Delta\phi_{jj} < 1.8$). It follows from the VBF process that the two jets are well separated in η ($\Delta\eta_{jj} > 4.8$) and in opposite z-hemispheres ($\eta_{j1} \times \eta_{j2} < 0$). Here, the former implies the latter, since only jets with $|\eta| < 4.5$ are considered, but both requirements are kept for consistency when the $\Delta\eta_{jj}$ requirement is changed in the validation region.

The three signal region bins only differ in their requirements on the dijet invariant mass m_{jj}. SR1 requires 1 TeV $< m_{jj} <$ 1.5 TeV, SR2 requires 1.5 TeV $< m_{jj} <$ 2 TeV and SR3 requires 2 TeV $< m_{jj}$. These m_{jj} bins differ in their signal purity, which is clear from the discussion of the results below. Instead of trusting the simulation to accurately model the m_{jj} shape, the signal is normalized to data in each bin.

Furthermore, a two-jet validation region (2j VR) is defined. Here, the $\Delta\eta_{jj} > 4.8$ requirement becomes $\Delta\eta_{jj} < 2.5$ and the m_{jj} requirement is flipped to $m_{jj} < 1$ TeV. The 2j VR is orthogonal to the SR and has a small signal contamination of 8% of the background assuming all Higgs bosons decay into invisible particles. The purpose of the VR is to have a region in that the background behaviour is very similar to the SR without actually containing much signal. This allows several checks during the blinded stage of the analysis.

5.5 Analysis backgrounds

5.5.1 Vector bosons

$Z \to \nu\bar{\nu}$ and $W \to \ell_{\text{lost}}\nu$ events form the dominant backgrounds. The $Z \to \nu\bar{\nu}$ background is irreducible meaning it is so similar to the signal that it can barely be reduced by selection requirements. For the $W \to \ell_{\text{lost}}\nu$ background it is crucial to estimate how frequently a charged lepton is not reconstructed with the detector. Typical reasons for not reconstructing a lepton are that the object is outside of p_T or η acceptance. Figure 5.3 and Figure 5.4 show four example Feynman diagrams of such processes, all of which have two jets and E_T^{miss} in the final state.

To estimate this background in the SR $Z \to \ell^+\ell^-$ and $W \to \ell\nu$ events with two jets in the final state are studied. The couplings causing these processes are of course very similar to the couplings of the dominant background processes, which leads to very similar event topologies.

Both for $Z \to \ell^+\ell^-$ and $W \to \ell\nu$ additional CRs are defined. They differ from the signal region as follows:

- $Z \to e^+e^-$ and $Z \to \mu^+\mu^-$ control regions:
  - The $E_{\mathrm{T}}^{\mathrm{miss}}$ trigger requirement is replaced with a single lepton trigger requirement
  - The electron/muon veto is replaced by requiring exactly two electrons in electron triggered events and two muons in muon triggered events.
  - $p_{\mathrm{T}} > 30$ GeV for the leading lepton
  - The two leptons have opposite charge.
  - Invariant dilepton mass within 25 GeV of the Z boson mass of 91.2 GeV
  - The lepton transverse momenta are vectorially added to $E_{\mathrm{T}}^{\mathrm{miss}}$.
  - The requirements on $\Delta\Phi(E_{\mathrm{T}}^{\mathrm{miss}}, j_1)$ and $\Delta\Phi(E_{\mathrm{T}}^{\mathrm{miss}}, j_2)$ use the modified $E_{\mathrm{T}}^{\mathrm{miss}}$.
- $W \to e^+\nu, W \to e^-\nu, W \to \mu^+\nu$ and $W \to \mu^-\nu$ control regions:
  - The $E_{\mathrm{T}}^{\mathrm{miss}}$ trigger requirement is replaced with a single lepton trigger requirement.
  - The electron/muon veto is replaced by requiring exactly one electron in electron triggered events and one muon in muon triggered events.
  - $p_{\mathrm{T}} > 30$ GeV for the leading lepton
  - The lepton p_{T} is vectorially added to $E_{\mathrm{T}}^{\mathrm{miss}}$.
  - The requirements on $\Delta\Phi(E_{\mathrm{T}}^{\mathrm{miss}}, j_1)$ and $\Delta\Phi(E_{\mathrm{T}}^{\mathrm{miss}}, j_2)$ use the modified $E_{\mathrm{T}}^{\mathrm{miss}}$.

The CRs are also subdivided into the three m_{jj} bins because they are used to separately constrain the background in each of the SR bins. The lepton p_{T} requirements make sure that the CRs are in the lepton trigger efficiency plateau. The charge distinction for W decays is made because of the asymmetric production of W + jets in pp collisions in contrast to the charge symmetric multijet background. This allows a better discrimination later as discussed in Section 5.5.2.

The CR selection requirements aim to select events that are very similar to the events that contaminate the signal region except that one or two charged leptons are reconstructed, respectively. The motivation for the CR requirements can be understood when thinking of the final state leptons as the replacement of the invisible decay products of the Higgs boson. By modifying $E_{\mathrm{T}}^{\mathrm{miss}}$ with the lepton transverse momenta, the $E_{\mathrm{T}}^{\mathrm{miss}}$ spectrum is preserved and an equivalence to the background process without leptons in the final state is achieved.

In contrast to light leptons, τ leptons are not considered as decay products appearing in the final state of background events. They themselves can decay into muons or electrons and both of these cases are already covered by the CR selection. The other possibility is that the τ decays hadronically producing additional jets, which contributes to neither the SR nor the CRs because of the third jet veto. In total, there are three reasons for a $W \to \tau\nu$ event to contribute to the SR:

- The τ decays hadronically (for example $\tau \to \pi\nu$) and the resulting jet is below the 25 GeV threshold of the third jet veto. This is evaluated with toy MC simulations, showing that in events with a transverse momentum of the W larger than 150 GeV about 30% of the produced pions are below $p_{\mathrm{T}} = 25$ GeV.

- The τ decays leptonically and the lepton is lost. Generally this lepton is outside of η acceptance or too low in p_{T} to be reconstructed.
- The τ appears as one of the two leading jets. This behaviour is studied by evaluating the angular distance between τ leptons and jets at truth level. If there is a spatial overlap between a jet and a τ within $\Delta R = 0.4$, the jet is the product of a hadronically decaying τ.

With studies using truth information it was determined that $W \to \tau\nu$ events are causing 24% of the total background. About 70% of these are coming from hadronically decaying τ leptons where the jet is too low in p_{T} to be vetoed. About 30% are caused by leptonically decaying τ leptons. The cases with a τ appearing as one of the two leading jets are very rare.

To estimate the background predictions in each m_{jj} bin, the CR yields are scaled by the free parameters $k_{i,W}$ and $k_{i,Z}$ with $i = 1,2,3$ being the m_{jj}-bin index. As a result the backgrounds are normalized with:

$$\begin{aligned} Z_{\mathrm{SR}} &= \frac{Z_{\mathrm{CR}}^{\mathrm{data}}}{Z_{\mathrm{CR}}^{\mathrm{MC}}} \times Z_{\mathrm{SR}}^{\mathrm{MC}} = k_{\mathrm{Z}} \times Z_{\mathrm{SR}}^{\mathrm{MC}}, \\ W_{\mathrm{SR}} &= \frac{W_{\mathrm{CR}}^{\mathrm{data}}}{W_{\mathrm{CR}}^{\mathrm{MC}}} \times W_{\mathrm{SR}}^{\mathrm{MC}} = k_{\mathrm{W}} \times W_{\mathrm{SR}}^{\mathrm{MC}}. \end{aligned} \tag{5.3}$$

Here, $Z_{\mathrm{SR}}/W_{\mathrm{SR}}$ are the normalized number of Z/W events in the signal region. The parameters $Z^{\mathrm{data}}/W^{\mathrm{data}}$ and $Z^{\mathrm{MC}}/W^{\mathrm{MC}}$ describe event yields measured in data or obtained from MC simulation. It is assumed that the parameters $k_{i,Z/W}$ are the same for charged lepton and invisible decays, which is a necessary assumption in order to normalize the background. The normalization is performed using a simultaneous fit of all m_{jj} bins with individual normalization factors in each m_{jj} region. With this normalization the actual number of background events in the SR can be inferred from the MC simulation, while using the CR to lessen the uncertainty and to not solely rely on the background being well simulated. The fit model together with the normalization is described in Section 5.7.

5.5.2 Misidentified leptons

Furthermore, multijet events with one of the jets being misidentified as a lepton are considered. These jets are the so-called misidentified leptons. The misidentification of a jet as a lepton is a relatively rare occurrence, but the enormous cross-section of multijet events turns misidentified leptons into a relevant contribution. Multijet events with misidentified leptons contaminate the $W(\to e\nu/\mu\nu)$ CRs. The amount of fake muons is negligible, since it requires jets to punch through to the muon spectrometer and still be misidentified. However, the frequency of electron fakes has to be determined to improve the quality of the W + jets background estimation. This is done with a fit to $E_{\mathrm{T}}^{\mathrm{miss,sig}}$, which is defined as:

$$E_{\mathrm{T}}^{\mathrm{miss,sig}} = \frac{E_{\mathrm{T}}^{\mathrm{miss}}}{\sqrt{p_{\mathrm{T,j_1}} + p_{\mathrm{T,j_2}} + p_T(el)}}, \tag{5.4}$$

where $E_{\mathrm{T}}^{\mathrm{miss}}$ is the missing transverse energy. However, in contrast to the $E_{\mathrm{T}}^{\mathrm{miss}}$ definition for the $W \to \ell\nu$ CR in Section 5.5.1 the $E_{\mathrm{T}}^{\mathrm{miss}}$ in Eq. 5.4 is not corrected by adding the lepton p_{T}. In

the case of the $E_{\mathrm{T}}^{\mathrm{miss}}$ definition for the $W \to \ell\nu$ CR the goal is to normalize $W \to \ell_{\mathrm{lost}}\nu$ events and the lost leptons are reconstructed as missing transverse energy in $W \to \ell_{\mathrm{lost}}\nu$ events. While evaluating the contamination from misidentified leptons in the $W \to e\nu$ CR, $E_{\mathrm{T}}^{\mathrm{miss}}$ does not need to be an equivalent of the boson p_{T}. $E_{\mathrm{T}}^{\mathrm{miss,sig}}$ is a good discriminating variable because multijet events have no neutrino and therefore lower $E_{\mathrm{T}}^{\mathrm{miss,sig}}$.

An anti-ID control sample is produced using the W + jets selection in Section 5.5.1 with one difference: the reconstructed electrons are required to pass the loose selection while at the same time not passing the tight selection. In practice this leads to most of these reconstructed electrons to actually be jets. The expected W/Z + jet contribution in the anti-ID control sample is then subtracted from the sum of the observed yields in that region. Afterwards an $E_{\mathrm{T}}^{\mathrm{miss,sig}}$ shape template is obtained from these anti-ID control samples that are enriched in fakes.

As an input to the final fit presented in Section 5.7 the ratio R_i between fake events in the multijet-enriched region ($E_{\mathrm{T}}^{\mathrm{miss,sig}} < 4\sqrt{\mathrm{GeV}}$) and in the complementary region ($E_{\mathrm{T}}^{\mathrm{miss,sig}} > 4\sqrt{\mathrm{GeV}}$) is computed, where i is the m_{jj}-bin index. With R_i the shape templates are expressed as single parameters, which are used to normalize the multijet background in the W + jets CR region. Furthermore, the fact that the W + jets background is charge-asymmetric and the multijet background is expected to be almost charge-symmetric is used. The W production tends to positive charges because it is the product of pp collisions. Multijet processes on the other hand originate predominantly from gluon and sea-quark interactions. The ratios R_i are obtained with a charge-inclusive selection, but during the fit the $W \to \ell\nu$ CRs are split by the lepton charge. The number of misidentified leptons $N_{\mathrm{mis-ID}}$ and ratios R_i are given in Table 5.4.

Table 5.4: Expected multijet background due to misidentified leptons in the $W \to e\nu$ CR. Here, R_i is the ratio of events in the multijet-enriched region of the $W \to e\nu$ CR to the number of events in complementary region. The number of misidentified lepton events $N_{\mathrm{mis-ID}}$ is taken from the post-fit results [173].

m_{jj}-bin [TeV]	R_i	$N_{\mathrm{mis-ID}}$
$1.0 < m_{\mathrm{jj}} < 1.5$	9.0 ± 0.4	7.8 ± 3.9
$1.5 < m_{\mathrm{jj}} < 2.0$	9.7 ± 0.6	3.8 ± 2.3
$m_{\mathrm{jj}} > 2.0$	5.0 ± 0.4	4.0 ± 2.9

5.5.3 Top quarks

The top related backgrounds are $t\bar{t}$ and single top events including Wt. After the selection requirements their contribution to the SR is very small and does not introduce large uncertainties like the multijet background. Their event yields are therefore estimated with MC simulation and entered into the final fit described in Section 5.7. There is no dedicated top control region as a result. A b-jet veto was considered to reduce this background further, but is ultimately not needed.

5.5.4 Estimation of the multijet background

Multijet events that produce light jets exclusively have only jets and no real $E_{\mathrm{T}}^{\mathrm{miss}}$ in the final state, but $E_{\mathrm{T}}^{\mathrm{miss}}$ can come into existence as a result of jet mismeasurements. Given that the analysis is looking for large amounts of $E_{\mathrm{T}}^{\mathrm{miss}}$ this is only of interest in the case of severe mismeasurements. These mismeasurements happen rarely, but the multijet cross-section is so large that it becomes a sizeable contribution. The multijet background in the signal region is also small because of a selection that efficiently separates it from the signal. In multijet events, $E_{\mathrm{T}}^{\mathrm{miss}}$ can also be created as a result of the decay of heavy flavour jets that decay leptonically. However, these events would also produce leptons, which are excluded by the lepton veto unless they are lost similar to the $W \to \ell_{\mathrm{lost}}\nu$ background.

Figure 5.5 illustrates the good separation of the multijet background with the examples of $E_{\mathrm{T}}^{\mathrm{miss}}$ and dijet mass distributions. Both are good discriminants to discern whether an event is multijet-like or signal-like. However, as is shown below, the uncertainties on the background estimate are relatively large. That requires us to handle the multijet background with care and is a further motivation to optimize the selection to reject this background to a large degree. Predominantly the $E_{\mathrm{T}}^{\mathrm{miss}} > 180$ GeV, $MHT(\mathrm{noJVT}) > 150$ GeV, $\Delta\Phi(E_{\mathrm{T}}^{\mathrm{miss}}, j_i) > 1$ and $\Delta\phi_{\mathrm{jj}} < 1.8$ requirements are responsible for rejecting most of the multijet background.

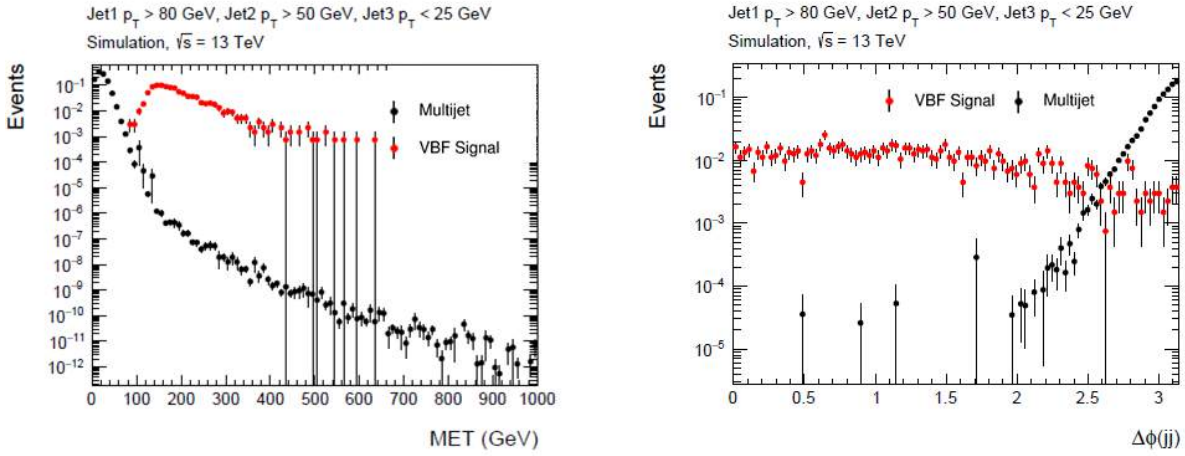

Figure 5.5: Missing transverse energy (left) and $\Delta\phi_{\mathrm{jj}}$ (right) distributions with a selection including a third jet veto. The simulated multijet events (black) can be separated from the simulated signal events (red) with great success by cuts on both variables [173].

A standard ABCD method was considered but ultimately not used. An ABCD method defines four regions A, B, C and D using two variables x_1 and x_2. One of the regions is the signal region D and another is the background dominated control region C. Both C and D have large x_1, while A and B are defined through the orthogonal requirement to have low x_1.[2)] In addition, A and D are defined to both have large x_2, while B and C orthogonally both have low x_2. If x_1 and x_2 are uncorrelated, it follows for the number of events in each region that $N_D = N_C \cdot N_A / N_B$. In the case of the multijet background estimation the ABCD method would define a multijet control region with high $E_{\mathrm{T}}^{\mathrm{miss}}$ and low $\Delta\Phi(E_{\mathrm{T}}^{\mathrm{miss}}, j_i)$ to extrapolate the multijet

[2)] This can also be turned around by picking high x_1 for A and B as long as the definition is orthogonal.

content of the signal region. Since the correlation between $\Delta\Phi$ and $E_{\mathrm{T}}^{\mathrm{miss}}$ is hard to understand among other challenges, this was discarded.

Furthermore, the multijet cross-section is huge and as a result the statistics that can be acquired from the MC samples described in Section 5.3.2 is small compared with the available data. In fact the simulation of the multijet background leads to no event in the signal region. Also the multijet background exists solely due to mismeasurements and it is uncertain whether these random non-physics effects are simulated well. This makes it impossible to use simulation to constrain the background and a data-driven method is needed. Therefore, the Rebalance and Smear Method is used.

Rebalance and smear method

The R+S method seeks to model the jet response of each individual jet to quantify how often jets fake high $E_{\mathrm{T}}^{\mathrm{miss}}$ and multijet events appear as signal. The used sample is selected with a series of single-jet triggers, which are discussed in Section 5.4.2 and can be found in Table 5.3.

The method is illustrated in Figure 5.6. It shows a simplified momentum picture of jets in a single event that are first "rebalanced" and then smeared. Rebalancing means that the jet momenta are modified by a kinematic fit to balance the transverse momenta. When a jet momentum is smeared, random mismeasurements are simulated by changing the jet momentum according to a distribution. This can lead to missing transverse energy in the event. This is the equivalent of a jet being misreconstructed.

The main difference to a simple smearing method lies in the first step. Simple jet smearing would work with a QCD enriched sample that has low $E_{\mathrm{T}}^{\mathrm{miss,sig}}$ and no leptons. The R+S method on the other hand creates an unbiased seed sample. This makes it possible that the used seed events come from inclusive jet samples, which have large statistics and contain the background of interest.

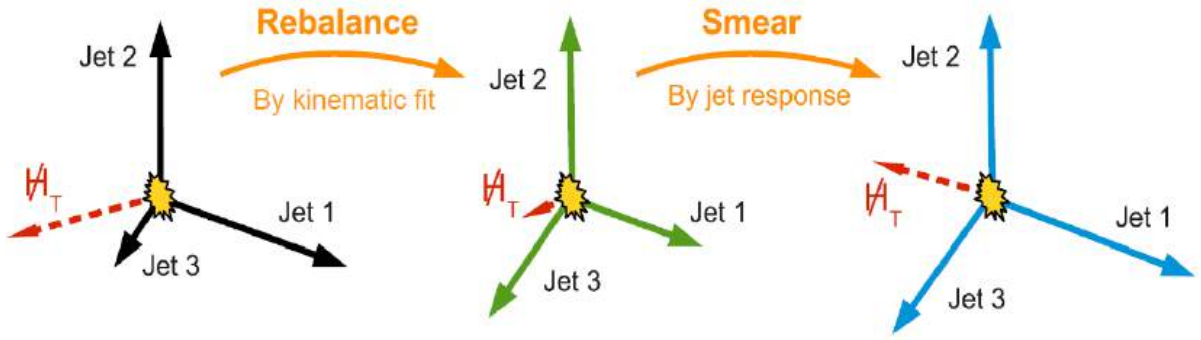

Figure 5.6: Illustration of the rebalance and smear (R+S) method.

Before the rebalancing an MHT significance cut $MHT/\sqrt{H_T} < 5$ removes most of the contributions from non-multijet events from the seed sample, where MHT is the magnitude of the vectorial sum of all jet momenta in the event and H_T is the scalar sum of all jet momenta. After the rebalancing the events have no $E_{\mathrm{T}}^{\mathrm{miss}}$ except for the soft term $E_{\mathrm{T}}^{\mathrm{miss,soft}}$, which is defined in Section 3.3.4.

In the second step the mismeasurement of jets is simulated. Random mismeasurement effects are expressed through the jet response $< p_{\mathrm{T}}^{\mathrm{reco}}/p_{\mathrm{T}}^{\mathrm{truth}} >$, which compares the reconstructed

transverse momentum of jets to their matched truth counterparts. From simulated samples jet response distributions called jet response templates are produced. These response templates are binned in non-b and b jets as well as E and η.

The jet response templates are produced using reconstructed jets with tight matching to truth jets ($\Delta R < 0.1$, no additional truth jets within $\Delta R = 0.8$, no additional reconstructed jets within $\Delta R = 0.6$). Unphysical tails resulting from truth jets matched to the wrong reconstructed jet are largely avoided because of the matching. The templates include neutrinos in the definition of the simulated $E_{\mathrm{T}}^{\mathrm{miss}}$.

An example of such a template is Figure 5.7. The core of the response distribution can be described by a Gaussian function (green curve) due to the random nature of deviations between the reconstructed and the true transverse momentum of a jet. However, there are also tails in the high (purple) and low response (red) regime. The green Gaussian curve was obtained through a fit to the core of the distribution. The red and purple functions are the difference between the response distribution and the Gaussian fit. The tails are discussed in Chapter 6 in detail.

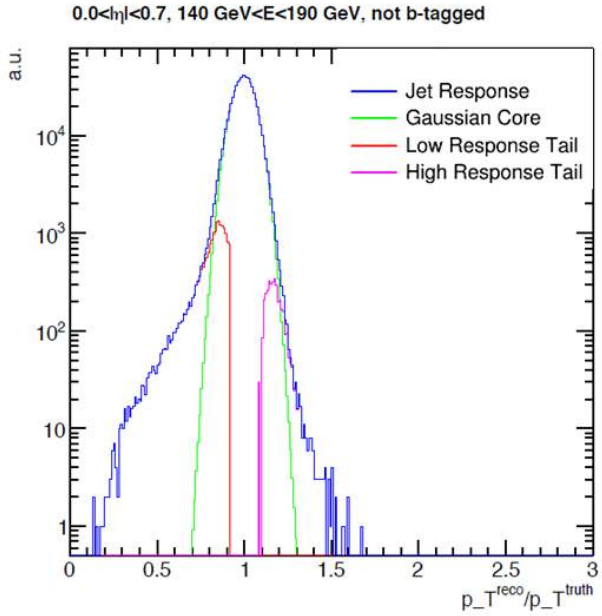

Figure 5.7: An example jet response template as it is used for the smearing. Central ($0.0 < |\eta| < 0.7$) low-energy ($140\ \mathrm{GeV} < E < 190\ \mathrm{GeV}$) not b-tagged jets. The Gaussian core is identified with a fit (green). The high (purple) and low response (red) tails are the difference between fit and distribution [173].

The jets are then smeared 20 times creating 20 pseudo-datasets to estimate how often jets fake large missing transverse energy. The prediction of the multijet background is the mean resulting from 20 different predictions. The square root of the variance over 20 attempts is assigned as the statistical uncertainty. The highly weighted events are smeared additionally to reduce the effect of single events with large prescales on the results. To do so every data event is smeared a number of times equal to the prescale (or weight). Meanwhile, the weights are reduced accordingly. If the prescale (or weight) is larger than 1000, the smearing is done 1000 times instead to avoid excessive amounts of smearing.

The Rebalance and Smear Method is verified with a closure test, applying it to simulated multijet events. Furthermore, it is applied to W + jet events in order to account for possible effects on a contamination from non-multijet (non-QCD) backgrounds in the data sample. The latter yields a vanishing increase of the background prediction.

In order to ensure a good comparison between the background predicted with R+S and simulation, a QCD enriched control region is defined: $1.8 < \Delta\Phi < 2.7$, $25 < p_{\mathrm{T,j_3}} < 50$ GeV, no fourth jet with $p_T > 25$ GeV, $\Delta\eta_{\mathrm{jj}} > 3.0$, $E_{\mathrm{T}}^{\mathrm{miss}} > 100$ GeV, $m_{\mathrm{jj}} > 600$ GeV. The comparison for several distributions is shown in Figure 5.8. Overall the agreement is good. In data in Figure 5.9 events with $E_{\mathrm{T}}^{\mathrm{miss}}$ between 100 and 120 GeV for all distributions but missing transverse momentum are selected. This is done in order to deal with a discrepancy at high $E_{\mathrm{T}}^{\mathrm{miss}}$ that is attributed to the non-multijet background, as can be seen in the top left of Fig 5.9. Between 100 and 120 GeV this discrepancy is vanishing in the $E_{\mathrm{T}}^{\mathrm{miss}}$ distribution.

Finally, the multijet background prediction in the signal region is listed in Table 5.5. Because of the small probability for smeared events to fall into the SR, the prediction has an uncertainty on the order of 100%. The variance of the 20 different smearing procedures described above is the statistical uncertainty. For the systematic uncertainty two contributions are considered. One is the jet energy resolution (JER). To estimate its impact the jet energy is varied by +10%, before new results are calculated. The other contribution comes from the non-Gaussian tails in the jet response templates and is discussed in Chapter 6 in detail. Despite only few events being part of the tails, the systematic uncertainty resulting from their variation is of the same order as the JER uncertainty. This makes it important to take a closer look at the simulation of the tails. The statistical uncertainty of the systematic variations is so large that it needs to be taken into account. The combined uncertainty σ_{comb} is calculated with:

$$\sigma_{\mathrm{comb}} = \sqrt{\sigma_{\mathrm{nom}}^2 + |N_{\mathrm{JER}} + \sigma_{\mathrm{JER}} - N_{\mathrm{nom}}|^2 + |N_{\mathrm{tail}} + \sigma_{\mathrm{tail}} - N_{\mathrm{nom}}|^2}, \tag{5.5}$$

where N_{nom} is the number of expected multijet events or, in other words, the nominal result and σ_{nom} is its statistical uncertainty. Furthermore, N_{JER} and N_{tail} are the varied results, σ_{JER} and σ_{tail} are the statistical uncertainties of the varied results. The statistical uncertainty of the varied result is added and not subtracted because the background is a result of mismeasurement, so any kind of uncertainty is expected to increase the number of fake $E_{\mathrm{T}}^{\mathrm{miss}}$ events.

Table 5.5: Multijet background prediction with 36.1 fb^{-1} [173].

Bin	Nominal	JER up	Tail up	Combined uncertainty
SR	9.82 ± 5.52	8.18 ± 4.38	7.34 ± 4.00	6.35
SR1	7.13 ± 4.71	4.52 ± 2.19	5.39 ± 3.60	5.08
SR2	2.24 ± 2.80	2.75 ± 3.69	1.40 ± 1.60	5.10
SR3	0.45 ± 0.59	0.90 ± 0.88	0.55 ± 0.71	1.67

5.5.5 Data-to-MC comparison

Data and MC simulation are compared in several distributions to understand the accuracy of the MC prediction. Two example distributions are shown in Figure 5.10. Both distributions add the

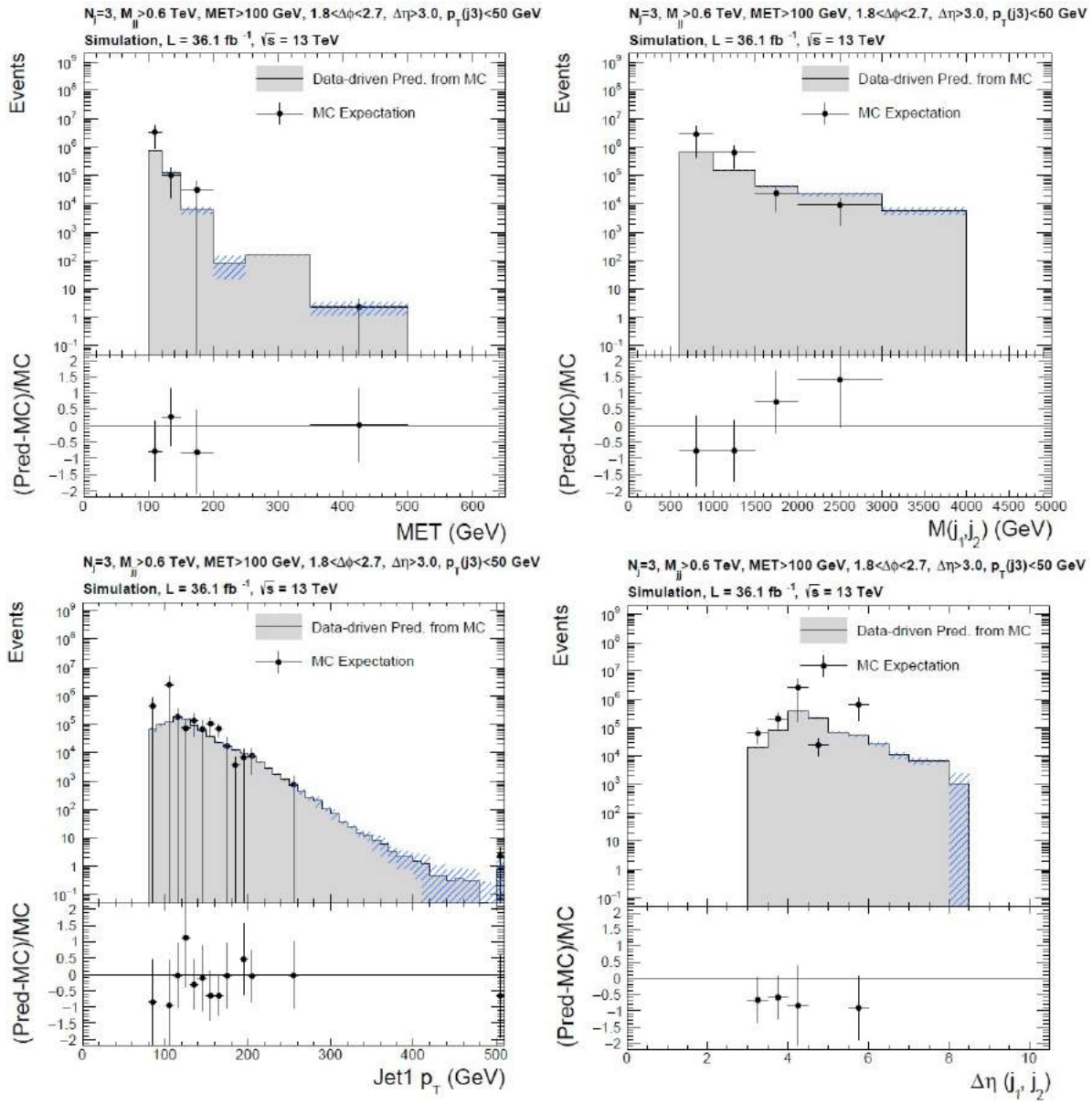

Figure 5.8: Kinematic distributions that compare the data-driven R+S prediction from MC of the multijet background in a QCD enriched control region (selection in the text) with simulated multijet events. Here, $E_{\mathrm{T}}^{\mathrm{miss}}$ is referred to as MET [173].

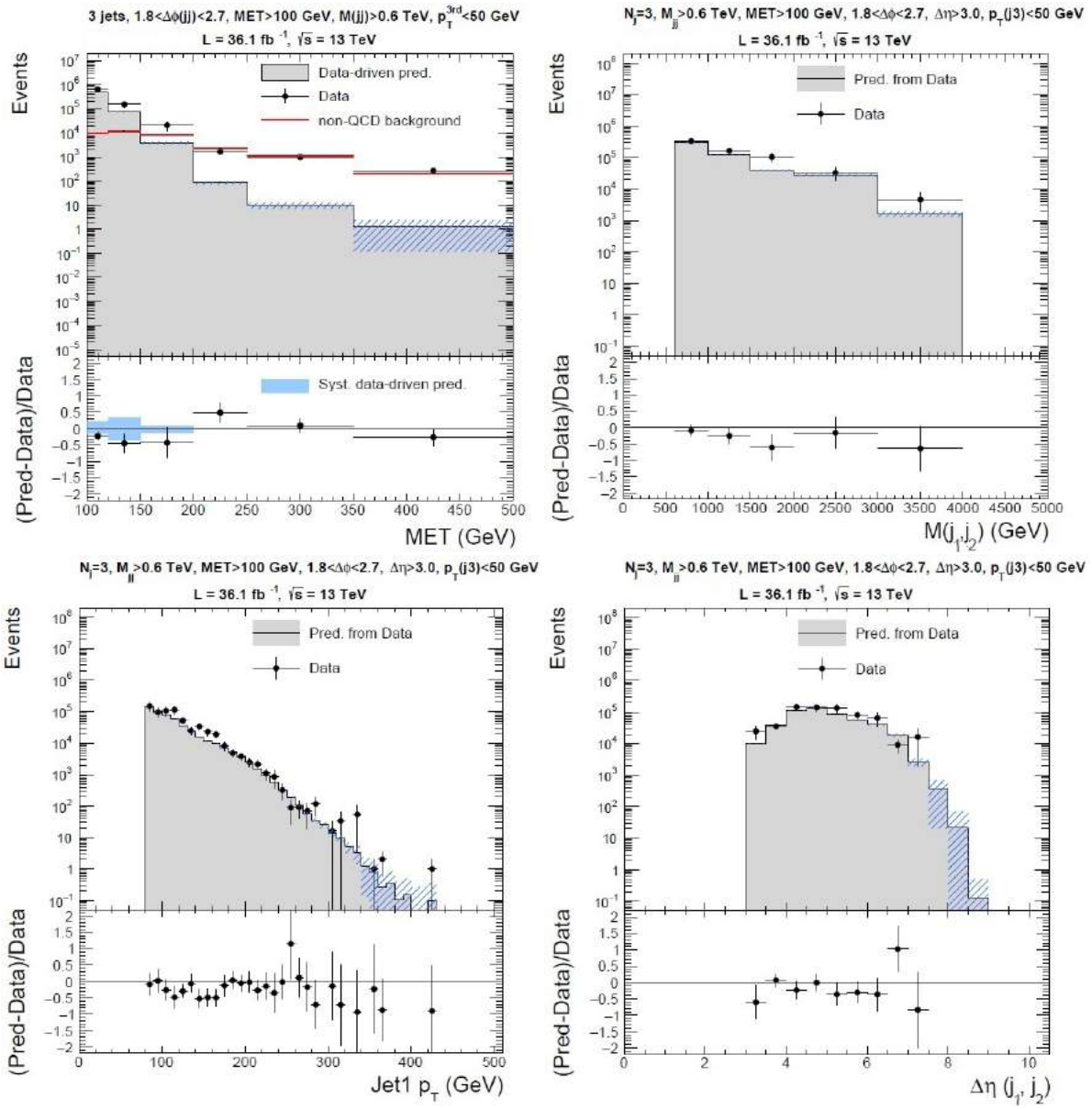

Figure 5.9: Kinematic distributions that compare the data-driven R+S prediction from data of the multijet background in a QCD enriched control region (selection in the text) with multijet events obtained from data. The $E_{\mathrm{T}}^{\mathrm{miss}}$ (MET) distribution (top left) includes the simulated non-multijet background as an individual contribution instead of a stacked plot. The other three distributions have an additional $E_{\mathrm{T}}^{\mathrm{miss}} < 120$ GeV requirement [173].

events from all m_{jj} bins. The full data-to-MC comparison of each bin is depicted in Figure 5.11. Here, the electron fakes that are also called misidentified leptons are shown despite only being estimated in the fit and not directly predicted from counting MC events after the CR selection. The agreement between data and simulation is already pretty good and normalization factors close to one are expected as a result.

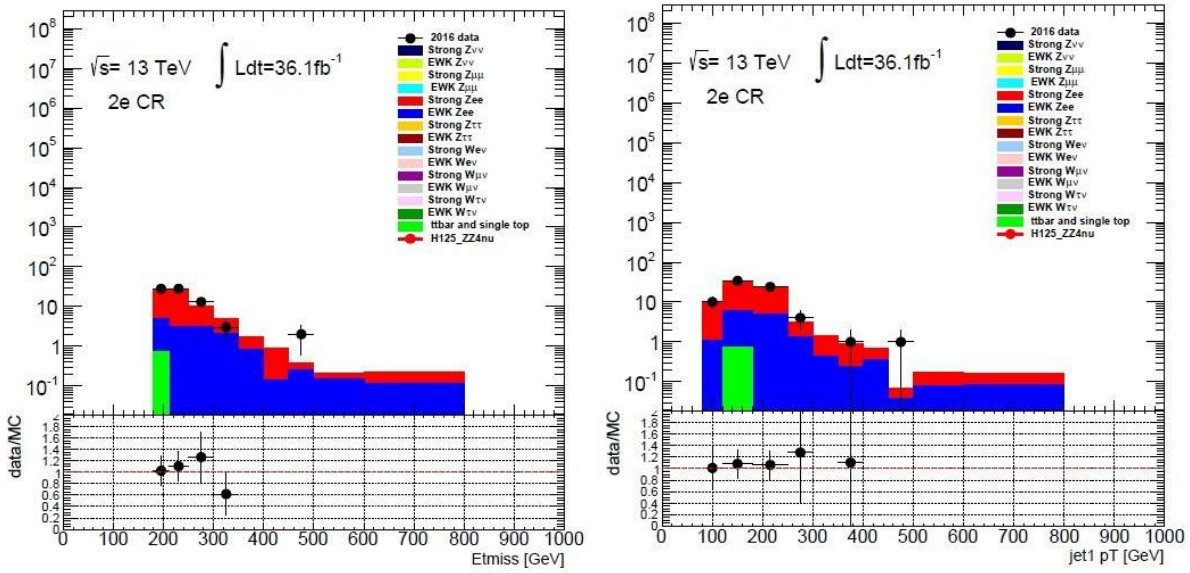

Figure 5.10: Pre-fit comparison of the observed data (black data points) and MC prediction (stacked histogram) in the $Z \to e^+e^-$ CR. The entire selection is applied except for the requirement on the variable that is depicted. The variable $E_{\mathrm{T}}^{\mathrm{miss}}$ is shown on the left and $p_{\mathrm{T,j1}}$ is shown on the right [173].

To put the importance of each of the background contributions into perspective, their expected event yields in the SR are summarized in Table 5.6. This is discussed in more detail in Section 5.7 and especially Section 5.8.

Table 5.6: Summary of expected event yields of backgrounds and signal in the SR. The signal yields assume a 100% branching fraction for the Higgs boson to decay invisibly. The post-fit results are shown in Table 5.14. The multijet (QCD) background is estimated with the R+S method presented in Section 5.5.4.

Region	MC prediction					QCD	Signal	Total
	Strong Z	EWK Z	Strong W	EWK W	Top			Background
SR	964.9	170.7	906.8	170.7	23.0	9.8	1063.6	2245.9

5.6 Systematic uncertainties

The approach to estimate the systematic uncertainties of the analysis is presented below. Unless stated otherwise, the established recommendations of the ATLAS collaboration are followed.

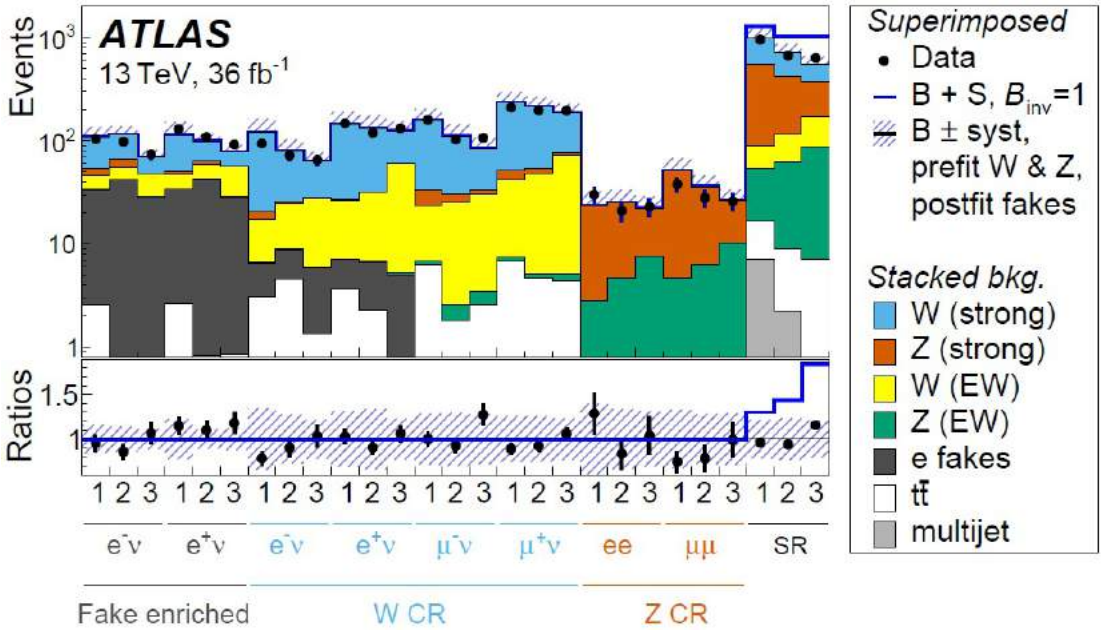

Figure 5.11: Pre-fit comparison of the observed data (black data points), MC prediction (stacked histogram) and background plus signal prediction under the assumption that the Higgs boson only decays invisibly (blue line). The numbers 1, 2 and 3 denote the m_{jj} bins. The error bars include the statistical uncertainty from the MC statistics and poisson uncertainty of the data events as well as the systematic uncertainty described in Section 5.6. The number of electron fakes in the $W \to e\nu$ CRs are estimated with the fit, but are included in the pre-fit plot to show the goodness of the background modelling. The region that is "enriched in e fakes" is defined by a low $E_{\mathrm{T}}^{\mathrm{miss,sig}}$ [12].

5.6.1 Experimental uncertainties

The experimental uncertainties can be categorized by the analysis objects in addition to pile-up modelling. The approach is similar to that of other searches with jets and missing transverse momentum in the final state [174]. In ATLAS, systematic uncertainties are derived by specialized working groups dedicated to electrons, jets, $E_{\mathrm{T}}^{\mathrm{miss}}$ and other analysis objects.

The ATLAS working groups provide sets of nuisance parameters (NPs) that account for these uncertainties as well as simplified sets of groups of NPs. Samples with variations based on these uncertainty contributions are built. The distributions studied below are generated with each of the variations. When applicable, the sample is varied up and down by one standard deviation. The maximum difference to the nominal result between up and down is determined as a contribution to the systematic uncertainty.

Missing transverse energy

As $E_{\mathrm{T}}^{\mathrm{miss}}$ is constructed from multiple objects, all uncertainties of the various objects propagate to the $E_{\mathrm{T}}^{\mathrm{miss}}$ uncertainty. The contribution from the $E_{\mathrm{T}}^{\mathrm{miss}}$ track soft term is derived separately from the lepton and jet contributions. The $E_{\mathrm{T}}^{\mathrm{miss}}$ track soft term uncertainty has three contributions, which are included in the fit described in Section 5.7 as NPs:

- The $E_{\mathrm{T}}^{\mathrm{miss}}$ track soft term scale uncertainty.
- The $E_{\mathrm{T}}^{\mathrm{miss}}$ tacks soft term resolution uncertainty evaluated parallel to the p_{T} of the hard activity component of the missing transverse energy.
- The $E_{\mathrm{T}}^{\mathrm{miss}}$ tacks soft term resolution uncertainty evaluated perpendicular to the p_{T} of the hard activity component of the missing transverse energy.

The uncertainties are determined through data-to-MC comparisons of distributions of parallel and perpendicular $E_{\mathrm{T}}^{\mathrm{miss}}$ soft terms in the plane defined by the hard activity. The parallel component of the soft term is independent of the event topology, making the separation meaningful.

Jets

Jet uncertainties are derived alongside the jet calibration, which is both calibrating the jet energy scale (JES) and the JER. The uncertainties mostly result from assumptions made in the calibration and potential MC mismodelling. The uncertainties are expressed as NPs and the analysis uses a reduced set of them to enable a better implementation into the fit. There are four groups of contributions to the jet systematic uncertainty:

- A group of NPs connected to the η-intercalibration (see Section 4.1.5).
- Three groups of NPs accounting for the uncertainty of the jet energy scale. Together with the NPs above these are 29 in total.
- Uncertainty on the jet energy resolution.
- Uncertainty on the efficiency of the JVT pile-up removal.

The derivation of jet systematic uncertainties in the ATLAS jet calibration is discussed in detail in Section 4.3.1.

Leptons

The uncertainties in the reconstruction of muons and electrons are applied analogously to the jet uncertainties. The following uncertainties are considered for muons:

- Muon identification uncertainty.
- Muon momentum scale uncertainty.
- Muon momentum scale variations due to charge-dependent bias and Z-based corrections.
- Muon trigger uncertainty.
- Systematic and statistical components of muon identification scale factors.
- Uncertainty on the muon spectrometer track associated with the muon.
- Systematic and statistical components of the muon track-to-vertex association uncertainties.

The electron/photon uncertainties are listed here:

- Electron/photon energy scale uncertainty.
- Electron reconstruction, isolation and identification efficiency scale factors.
- Uncertainty on the electron trigger efficiency.

These uncertainties in the electron and muon reconstruction are the results of extensive studies described in Ref. [117] and Ref. [122].

Pile-up modelling

The pile-up systematic uncertainties are accounted for with a single NP, which parametrizes the uncertainty in the number of interactions per bunch crossing. These uncertainties were studied in Ref. [175].

5.6.2 Theoretical uncertainties

The theoretical uncertainties describe how well the MC simulation predicts the signal and background yields. The different contributions are detailed below.

Signal

The contributions to the uncertainty of the VBF Higgs boson to invisible signal are the Higgs boson parton shower uncertainties, PDF uncertainties, QCD scale uncertainties and electroweak corrections.

To determine the Higgs boson parton shower uncertainties the parton-level signal is showered using `Pythia` with several variations. The variations are applied to the parameters describing the underlying event, the initial and final state showers as well as the scale of the multi-parton interaction cut-off and ISR/FSR renormalization. Finally, the showering is done with `Herwig` instead of `Pythia` as a comparison. For each variation the difference to the nominal showering result is calculated. The `Herwig` result exhibits the largest deviation from the nominal result at 7.7%.

For the PDF uncertainties, the signal events produced with `Powheg` 19.2.2.5 and the PDF set NNPDF30_nlo_as_0118 with 100 statistical replicas are used. The signal selection is applied to the 100 replicas and the signal efficiency is calculated for each of them. These signal efficiency distributions are then evaluated in the three m_{jj} bins of the signal region. With Gaussian fits the width of each distribution is determined as a systematic uncertainties unique to its m_{jj}-bin. The uncertainties are $0.64\%, 1.02\%$ and 1.53% in ascending order of m_{jj}.

Regarding the QCD scale uncertainty, both the factorization and renormalization scale are varied independently around the Higgs boson mass by a factor of two using MCFM [176] generated VBF signal samples according to the Stewart-Tackmann technique [177], leading to a total of seven[3)] variations. The resulting acceptances, after the VBF selection is applied to each variation, are compared in order to determine a QCD scale uncertainty of 7.6%; the uncertainty of the third jet veto alone is 6.0%.

Electroweak corrections are calculated with the HAWK [133] program, which has reweighting factors as the output. The difference between the signal yields resulting from the reweighted sample and the nominal sample is taken as the systematic uncertainty. For the inclusive $m_{jj} > 1.0$ TeV SR bin it is only 0.26%.

The contributions to the uncertainty of the ggF Higgs boson to invisible signal are resulting from jet bin migration and the Higgs boson parton showers. The jet bin uncertainty is essentially a scale uncertainty and as a result the Stewart-Tackmann technique is used again. The uncertainty is especially impactful on the selection requirements. The jet bin migration uncertainty amounts to 67.8%. The Higgs boson parton shower uncertainty is determined in the exact same way as for the VBF example above, yielding an uncertainty of 7.7%.

Background

The most important theoretical background uncertainties are those in the W and Z backgrounds because they are the dominant backgrounds. The uncertainties of the multijet background are covered in Section 5.5.4. The W/Z theoretical background uncertainty results from the choices of renormalization, factorization, resummation and CKKW scales [179], which are fixed during event generation. For the factorization and renormalization scale, the Stewart-Tackmann technique is applied in the same manner as it is used for the signal above.

[3)] In principle a total of $3 \times 3 = 9$ variations could be obtained from varying two quantities across three workings points independently. However, it was shown that the factorization and renormalization scale should not be varied simultaneously in opposite directions in Ref. [178].

For the CKKW and resummation scale, the varied samples are generated only at truth level. From that point, reweighting factors are determined instead of performing the full reconstruction, which would be computing resource intensive. The nominal CKKW scale of 20 GeV is varied to 15 and 30 GeV, respectively. The other scales are varied by a factor of 2. For CKKW and resummation scale uncertainties, the maximum of the statistical uncertainty of the variation and the variation itself is propagated to deal with a relatively small sample size. The CKKW and resummation scale are symmetrized by defining the varied yields as half the difference between the up and down variations. Due to the limited size of the varied samples, the statistical uncertainty of the size of the variations is problematic for the strong-production samples. This is mitigated by evaluating the variations at low m_{jj} and extrapolating to the SR and CRs with a linear fit. The statistical uncertainties are then calculated from the fit parameter uncertainties.

The results of the variations of the factorization, renormalization, CKKW and resummation scales are reported in Tables 5.7–5.10 (The selections referred to in the tables can be found in Section 5.4.4 and Section 5.5.1, respectively.).

Table 5.7: Relative impact on the W/Z background event yields because of factorization and renormalization "up" variation [173].

Selection	Process	CR1	CR2	CR3
0-lepton ($E_{\mathrm{T}}^{\mathrm{miss}}$)	Strong Z	33.2%	35.3%	37.4%
	Strong W	33.7%	41.2%	38.1%
	EWK Z	16.4%	15.5%	20.6%
	EWK W	7.9%	13.1%	15.7%
1-lepton ($W \to \ell\nu$)	Strong W	31.0%	33.7%	34.6%
	EWK W	14.7%	8.9%	14.0%
2-lepton ($Z \to \ell^+\ell^-$)	Strong Z	31.5%	31.2%	34.4%
	EWK Z	17.2%	15.5%	18.1%

Table 5.8: Relative impact on the W/Z background event yields because of factorization and renormalization "down" variation [173].

Selection	Process	CR1	CR2	CR3
0-lepton ($E_{\mathrm{T}}^{\mathrm{miss}}$)	Strong Z	-19.7%	-20.8%	-21.4%
	Strong W	-20.3%	-23.5%	-21.6%
	EWK Z	-7.04%	-11.17%	-12.73%
	EWK W	-25.81%	-9.76%	-16.13%
1-lepton ($W \to \ell\nu$)	Strong W	-18.9%	-20.0%	-20.4%
	EWK W	-8.41%	-15.73%	-25.11%
2-lepton ($Z \to \ell^+\ell^-$)	Strong Z	-19.0%	-18.9%	-20.4%
	EWK Z	-6.52%	-10.56%	-15.34%

Table 5.9: Relative impact on the W/Z background event yields because of resummation "down" variation. The variations are symmetrized. Therefore, the "up" variation is omitted. Statistical variations are not listed for the sake of brevity [173].

Selection	Process	CR1	CR2	CR3
0-lepton ($E_{\mathrm{T}}^{\mathrm{miss}}$)	Strong Z	2.6%	4.2%	6.7%
	Strong W	3.7%	5.7%	9.9%
	EWK Z	$9.8\% \pm 3.0\%$	$7.7\% \pm 3.0\%$	$8.7\% \pm 2.7\%$
	EWK W	$14.8\% \pm 3.1\%$	$12.8\% \pm 3.0\%$	$12.3\% \pm 2.6\%$
1-lepton ($W \to \ell\nu$)	Strong W	1.9%	2.4%	3.5%
	EWK W	$17.8\% \pm 3.5\%$	$14.6\% \pm 3.3\%$	$10.3\% \pm 2.8\%$
2-lepton ($Z \to \ell^+\ell^-$)	Strong Z	2.9%	3.6%	4.8%
	EWK Z	$4.1\% \pm 8.3\%$	$20.1\% \pm 9.9\%$	$1.8\% \pm 7.0\%$

Table 5.10: Relative impact on the W/Z background event yields because of CKKW "up" variation. The variations are symmetrized between the 15 GeV and 30 GeV scale. Therefore, the "down" variation is omitted. Statistical variations are not listed for the sake of brevity [173].

Selection	Process	CR1	CR2	CR3
0-lepton ($E_{\mathrm{T}}^{\mathrm{miss}}$)	Strong Z	2.0%	2.5%	3.3%
	Strong W	6.8%	11.1%	17.5%
	EWK Z	$5.7\% \pm 3.2\%$	$1.2\% \pm 3.1\%$	$3.0\% \pm 2.7\%$
	EWK W	$8.5\% \pm 3.1\%$	$-0.4\% \pm 3.2\%$	$-0.3\% \pm 2.7\%$
1-lepton ($W \to \ell\nu$)	Strong W	2.1%	3.9%	6.57%
	EWK W	$11.4\% \pm 3.5\%$	$-1.6\% \pm 3.6\%$	$-1.1\% \pm 3.9\%$
2-lepton ($Z \to \ell^+\ell^-$)	Strong Z	2.6%	3.6%	4.8%
	EWK Z	$11.9\% \pm 9.1\%$	$-8.5\% \pm 8.5\%$	$6.1\% \pm 7.9\%$

The PDF uncertainties of the backgrounds are determined with a procedure analogous to the signal uncertainties. 100 PDF replicas are produced and the background yields are determined with each of them. This leads to several distributions of yields in the SR and all the CRs. The widths of these distributions are determined via Gaussian fits, assigning the standard deviation as the systematic uncertainty. The results of this procedure are listed in Tab 5.11.

The only correlation that is assumed is the one between processes in the CR and the equivalent process in the SR. An example of this is the correlation between EWK $W \to \ell\nu$ in the CR and EWK $W \to \ell_{\mathrm{lost}}\nu$ in the SR. This has to be the case for the CR yields to be able to constrain the background yields in the SR. No correlation between W and Z, electroweak and strong processes or between the different m_{jj} bins is assumed. This is all in line with the fit model described in the next section, which uses separate parameters for the different m_{jj} bins and processes.

Table 5.11: Relative impact on the W/Z background event yields because of PDF variations from an ensemble of 100 PDF sets [173].

Selection	Process	CR1	CR2	CR3
0-lepton ($E_{\mathrm{T}}^{\mathrm{miss}}$)	Strong Z	1.44%	2.51%	2.95%
	Strong W	2.27%	1.50%	3.12%
	EWK Z	1.73%	1.91%	3.76%
	EWK W	2.46%	2.00%	2.40%
1-lepton ($W \to \ell\nu$)	Strong W	1.02%	2.13%	2.13%
	EWK W	1.65%	1.51%	4.60%
2-lepton ($Z \to \ell^+\ell^-$)	Strong Z	1.99%	1.81%	1.65%
	EWK Z	2.88%	2.21%	3.79%

5.7 Fit model

At its core, the fit model is based on a transfer factor (TF) method. The underlying logic is the generalization of Eq. 5.3 with Eq. 5.6 and Eq. 5.7. It is an expression for the estimated event yield N_{SR} of a generic background N in the SR:

$$N_{\mathrm{CR}} = k \times N_{\mathrm{CR}}^{\mathrm{MC}}; N_{\mathrm{SR}} = k \times N_{\mathrm{SR}}^{\mathrm{MC}}. \tag{5.6}$$

It follows, that:

$$N_{\mathrm{SR}} = N_{\mathrm{CR}} \times \left[\frac{N_{\mathrm{SR}}^{\mathrm{MC}}}{N_{\mathrm{CR}}^{\mathrm{MC}}}\right] = N_{\mathrm{CR}} \times T_F. \tag{5.7}$$

Therefore, data can be used to estimate the background yields in the CRs and determine the yields in the SR by calculating the eponymous transfer factors T_F with a maximum likelihood fit. This approach lowers the detector modelling uncertainty and theoretical uncertainty compared with a MC-driven approach in which the background yields are only estimated from simulation. In the ratios of predicted SR and CR events (the transfer factors), the systematic uncertainties partially cancel out.

The fit parameters are listed below. With the exception of μ, which is universal to all m_{jj} bins, an index i is implied but omitted for the sake of simplicity:

- μ: The combined signal strength in all m_{jj} bins
- k_W: W background normalization factor as defined in Eq. 5.3
- k_Z: Z background normalization factor as defined in Eq. 5.3
- S: Expected number of signal events assuming a 100% BR for the Higgs boson to decay invisibly
- N_W: Expected number of W events
- N_Z: Expected number of Z events

- β^e: Expected number of events with misidentified leptons contaminating the $W \to e\nu$ CR
- R: Ratio of events with high $E_{\mathrm{T}}^{\mathrm{miss,sig}}$ over events with low $E_{\mathrm{T}}^{\mathrm{miss,sig}}$ as detailed in Section 5.5.2. In addition, the ratio $\mathscr{R}(E_{\mathrm{T}}^{\mathrm{miss,sig}})$ is defined with $\mathscr{R}(E_{\mathrm{T}}^{\mathrm{miss,sig}}) = R$ at $E_{\mathrm{T}}^{\mathrm{miss,sig}} < 4\sqrt{\mathrm{GeV}}$ and $\mathscr{R}(E_{\mathrm{T}}^{\mathrm{miss,sig}}) = 1$ at $E_{\mathrm{T}}^{\mathrm{miss,sig}} > 4\sqrt{\mathrm{GeV}}$.

The multijet background is exempt from this fitting procedure, since its yield in the SR is estimated using the Rebalance and Smear method described in Section 5.5.4. Therefore, the amount of multijet background in the SR $N_{\mathrm{SR}}^{\mathrm{QCD}}$ and its uncertainties are actually fixed parameters for the purpose of the fit. The contribution of $t\bar{t}$, single top and Wt events in the SR and all CRs is not normalized like the dominating backgrounds. Instead the yields are taken directly from MC simulation.

The $Z \to \ell^+\ell^-$ events are fitted simultaneously with invisible Z decays. This has the advantage that it allows a data-driven estimate of the $Z \to \nu\bar{\nu}$ background. The simulation is only used to determine the effects of the lepton selection.

The free parameters of the fit are also listed in Table 5.12 in the context of the several CRs and the SR. Again the m_{jj}-bin indices i are implied but omitted except for the μ parameter, which is the same in every m_{jj}-bin. The $W \to \ell\nu$ CRs are additionally divided by their lepton charge. Since the misidentified leptons are produced in a charge symmetric process, the corresponding fit parameters R and β^e must be equal, while the W + jets TFs are not.

Table 5.12: The free parameters of the fit model. When applicable, the m_{jj}-bin index i is omitted and implied. The fit is repeated for each m_{jj}-bin. The $W \to e\nu$ and $W \to \mu\nu$ CRs are separated by the lepton charge, which is simplified in the table.

Region	SR	$Z \to ee$	$Z \to \mu\mu$	$W \to e\nu$	$W \to \mu\nu$
Signal	$\mu \times S$				
Z + jets	$k_Z \times N_Z$	$k_Z \times N_Z$	$k_Z \times N_Z$	$k_Z \times N_Z$	$k_Z \times N_Z$
W + jets	$k_W \times N_W$	$k_W \times N_W$	$k_W \times N_W$	$k_W \times N_W$	$k_W \times N_W$
$t\bar{t}$	from MC	from MC	from MC	from MC	from MC
Multijet/fakes	R+S			$\mathscr{R}(E_{\mathrm{T}}^{\mathrm{miss,sig}}) \times \beta^e$	

The inputs for the likelihood function are the yields in MC simulation and data, which are normalized with the normalization parameters described in Table 5.12. The NPs θ (see Section 5.6) account for systematic and statistical uncertainties. The likelihood function is:

$$\mathscr{L}(k_Z, k_W, \mu, \theta) = \prod_r \prod_i \mathrm{Poiss}(N_{r,i}^{\mathrm{obs}} | \mu N_{r,i}^{\mathrm{exp,sig}}(\theta) + N_{r,i}^{\mathrm{exp,bkg}}(\theta, k_Z^i, k_W^i)) \cdot \mathscr{L}_{\mathrm{constr}} \cdot \mathscr{L}_{\mathrm{stat}}, \quad (5.8)$$

where $N_{r,i}^{\mathrm{exp,bkg}}(\theta, k_Z^i, k_W^i)$ is the sum of all expected background yields. This is defined as:

$$N_{r,i}^{\mathrm{exp,bkg}}(\theta, k_Z^i, k_W^i) = k_Z^i \sum_z N_{r,i}^z + k_W^i \sum_w N_{r,i}^w + N_{r,i}^t + N_{\mathrm{SR,i}}^{\mathrm{QCD}} + \mathscr{R}_i(E_{\mathrm{T}}^{\mathrm{miss,sig}}) \times \beta_i^e. \quad (5.9)$$

The terms in the two expressions above describe the following:

- z, w: Process indices standing for the different decay modes of the Z and W backgrounds, respectively.
  - $z = (Z \to \nu\bar{\nu}), (Z \to \mu^+\mu^-), (Z \to e^+e^-), (Z \to \tau^+\tau^-)$
  - $w = (W \to \mu\nu), (W \to e\nu), (Z \to e^+e^-), (W \to \tau\nu)$
- r: Region index running over the SR and CRs.
- i: m_{jj}-bin index
- $N_{r,i}^{\mathrm{obs}}$: Number of observed data events in bin i of region r
- $N_{r,i}^{\mathrm{exp,sig}}(\theta)$: Number of expected events in bin i of region r
- $N_{r,i}^{z}$ and $N_{r,i}^{w}$: Number of expected Z-events and W-events in bin i of region r with process z/w, respectively
- $N_{r,i}^{t}$: Number of expected top events in bin i of region r
- $N_{\mathrm{SR,i}}^{\mathrm{QCD}}$: Number of expected multijet events in bin i of the signal region
- $\mu, k_Z, k_W, \beta^e, \theta, R, \mathscr{R}_i(E_{\mathrm{T}}^{\mathrm{miss,sig}})$: defined above

The purpose of the fit is to test several theoretical models, which are interpreted in Section 5.9. This is done by setting limits on the Higgs boson to invisible branching ratio. In principle the data can randomly fluctuate to an extreme case that looks like a signal. Therefore, the limits are set in the sense that the probability for the measured outcome given the no-signal hypothesis is less than 5%. The hypothesis is expressed through a probability distribution, which can be determined via toy simulations [180], but these are computationally resource demanding so an asymptotic approximation [181] is used instead.

The confidence level C_L is defined from the p-values of the signal plus background hypothesis $p_{\mathrm{s+b}}$ and the pure background hypothesis p_{b} as:

$$C_L = \frac{p_{\mathrm{s+b}}}{1 - p_{\mathrm{b}}}. \tag{5.10}$$

This is a useful definition for cases like this analysis where the signal is small compared to the background, resulting in their probability distributions overlapping to a large extent. With this definition a search for an upper limit on $\mathscr{B}_{\mathrm{inv}}$ expressed via the signal strength μ in the fit such that $C_L < 0.05$ is performed. This is often referred to as calculating the limit at 95% confidence level.

An observed and an expected limit is defined. To calculate the former, the fit is used as described above. For the latter, the observed data yields in the SR are replaced by the prediction for the background-only hypothesis. The background-only prediction is determined as the best-fit parameters in the case $\mu = 0$. The expected limit is a measure of the sensitivity of the analysis. The observed limit is sensitive to statistical fluctuations and as a result misleading when interpreting the impact of improvements on the analysis.

5.7.1 Fit results

A two step process is employed to determine the signal yields, the normalization factors and the limits on the Higgs boson to invisible branching fraction. First, a background-only fit is used to check the consistency between different control regions. Afterwards, a simultaneous fit of the control regions and signal region is performed with the signal strength as a free parameter.

Background-only fit

The signal region is ignored for the background-only fit. The signal strength μ is not a fit parameter and only events that lie in one of the CRs are relevant for determining the best-fit result for the normalization factors. This has the purpose of checking the fit model and evaluating the MC modelling. Since no signal is expected in the control regions, a good agreement between MC simulation and data is expected.

Table 5.13 reports the results of the background-only fit by listing the normalization factors k_Z and k_W as well as the fake electron contamination β^e. Indeed the normalization factors are compatible with one, indicating that the simulation fits the data well. This is not surprising considering the pre-fit studies presented in Section 5.5.5. The number of fake electrons is also small as expected. Another way to look at the results of the background-only fit is shown in Figure 5.12. Here, the post-fit MC predictions are compared with the observed data in each of the CRs. Data and SM prediction are in good agreement. The SR with the background plus signal prediction under the assumption that the BR for the $H \to inv$ process equals one are also shown. Since the signal strength is not a free parameter in the background-only fit, the data are trivially compatible with the background-only hypothesis.

Table 5.13: Best-fit values for the normalization factors of the W and Z backgrounds as well as the number of events with fake electrons contaminating the high-$E_{\mathrm{T}}^{\mathrm{miss,sig}}$ $W \to e\nu$ CR. The numbers are obtained via a background-only fit that ignores the SR [173].

m_{jj}-bin	k_Z	k_W	β^e
$1.0-1.5$ TeV	1.10 ± 0.27	0.91 ± 0.18	3.63 ± 1.76
$1.5-2.0$ TeV	0.98 ± 0.23	0.94 ± 0.18	4.0 ± 1.47
> 2.0 TeV	1.13 ± 0.27	1.07 ± 0.19	6.8 ± 2.13

Figure 5.13 depicts the post-fit distributions of the lepton p_{T} corrected $E_{\mathrm{T}}^{\mathrm{miss}}$ as well as the corresponding m_{jj} distributions in the $W \to e^+\nu$ control region. The number of electron fakes cannot be shown in these plots because only the total number in a given CR is a parameter of the fit and not the shape. In the distributions a good data-to-MC agreement is observed as well. Given these results, it is justified to move on to the signal region fit in order to derive the new limit on the Higgs boson to invisible BR. Further post-fit distributions can be found in Appendix A.3.

The post-fit distributions in the SR after the background-only fit are shown in Figure 5.14. Here, the data points are not an actual input to the fit. Therefore, the fact that they agree well with the SM prediction indicates that the SM describes the data well. These distributions are used as a cross-check and the SR information is used in the next step.

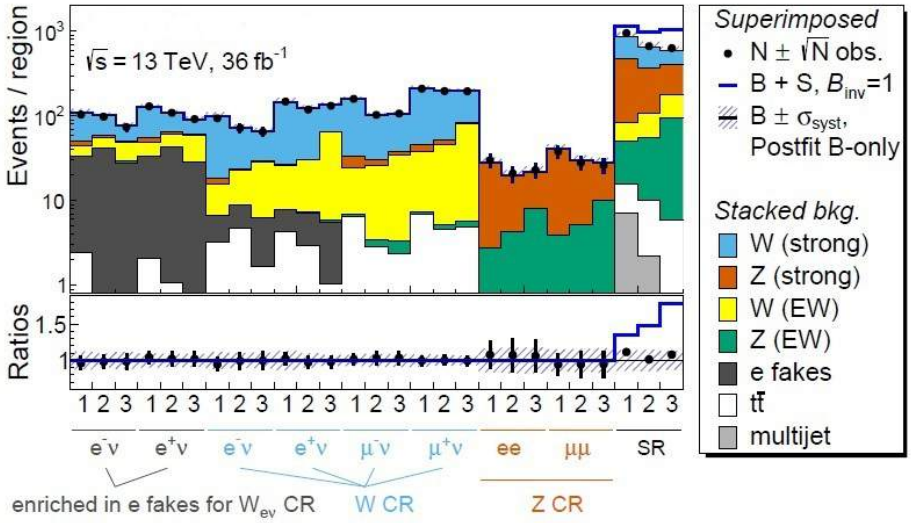

Figure 5.12: Results of the background-only fit: Comparison of the observed data (black data points), MC prediction of the background based on the fit (stacked histogram) and background plus signal prediction under the assumption that the Higgs boson only decays invisibly (blue line). The numbers 1, 2 and 3 denote the m_{jj} bins. The error bars include the statistical uncertainty from the MC statistics and poisson uncertainty of the data events as well as the systematic uncertainty described in Section 5.6. The number of electron fakes in the $W \to e\nu$ CRs are a result of the fit and derived from the β^e parameters. The region that is "enriched in e fakes" is defined by $E_{\mathrm{T}}^{\mathrm{miss,sig}} < 4\ \sqrt{\mathrm{GeV}}$ [173].

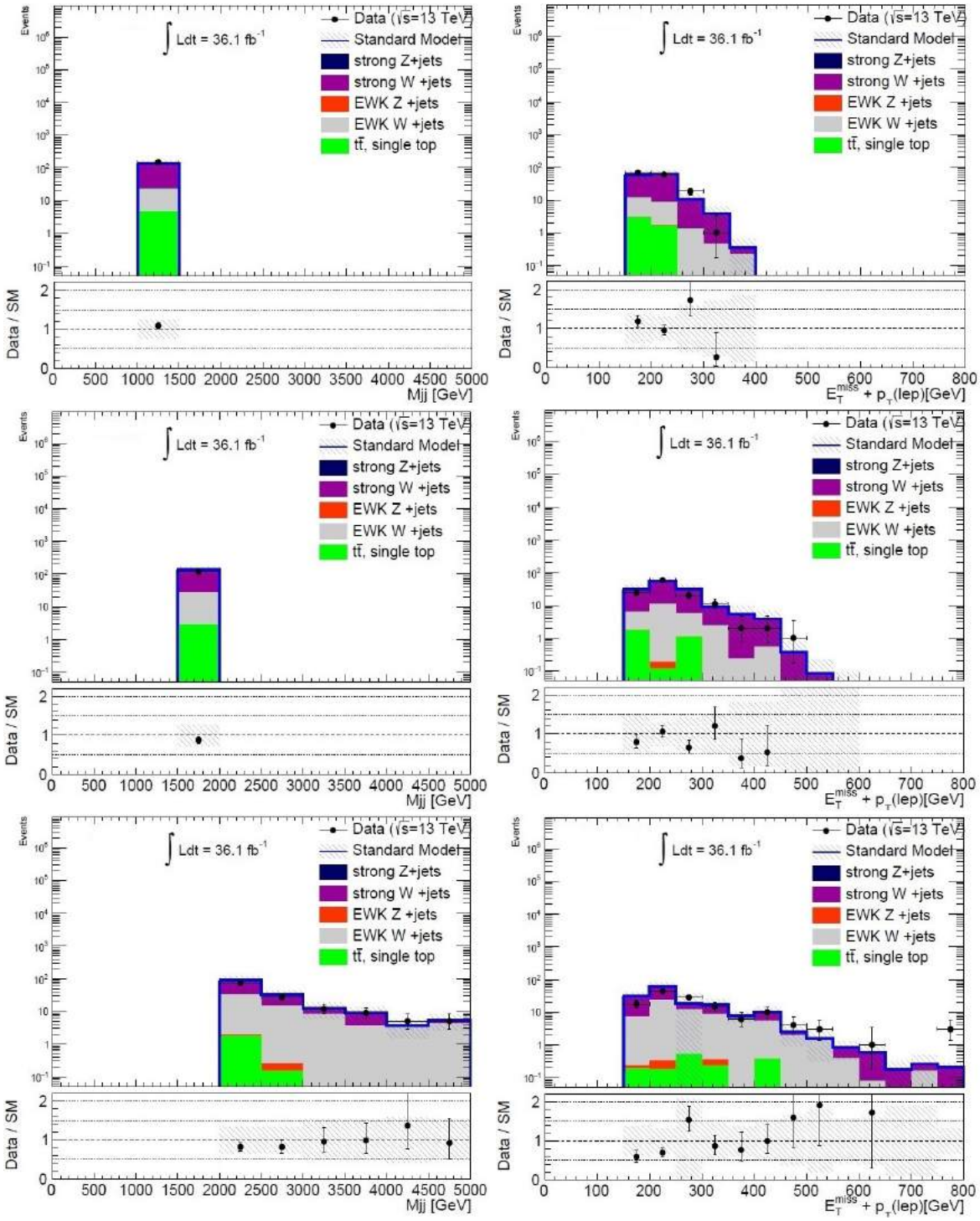

Figure 5.13: Results of the background-only fit: Dijet mass distributions (left) and lepton p_{T} corrected $E_{\mathrm{T}}^{\mathrm{miss}}$ distributions (right) in the $W \to e^{+}\nu$ control region. The plots show the distributions in the three different bins: 1.0 TeV $< m_{\mathrm{jj}} <$ 1.5 TeV (top), 1.5 TeV $< m_{\mathrm{jj}} <$ 2.0 TeV (middle) and $m_{\mathrm{jj}} >$ 2.0 TeV (bottom) [173].

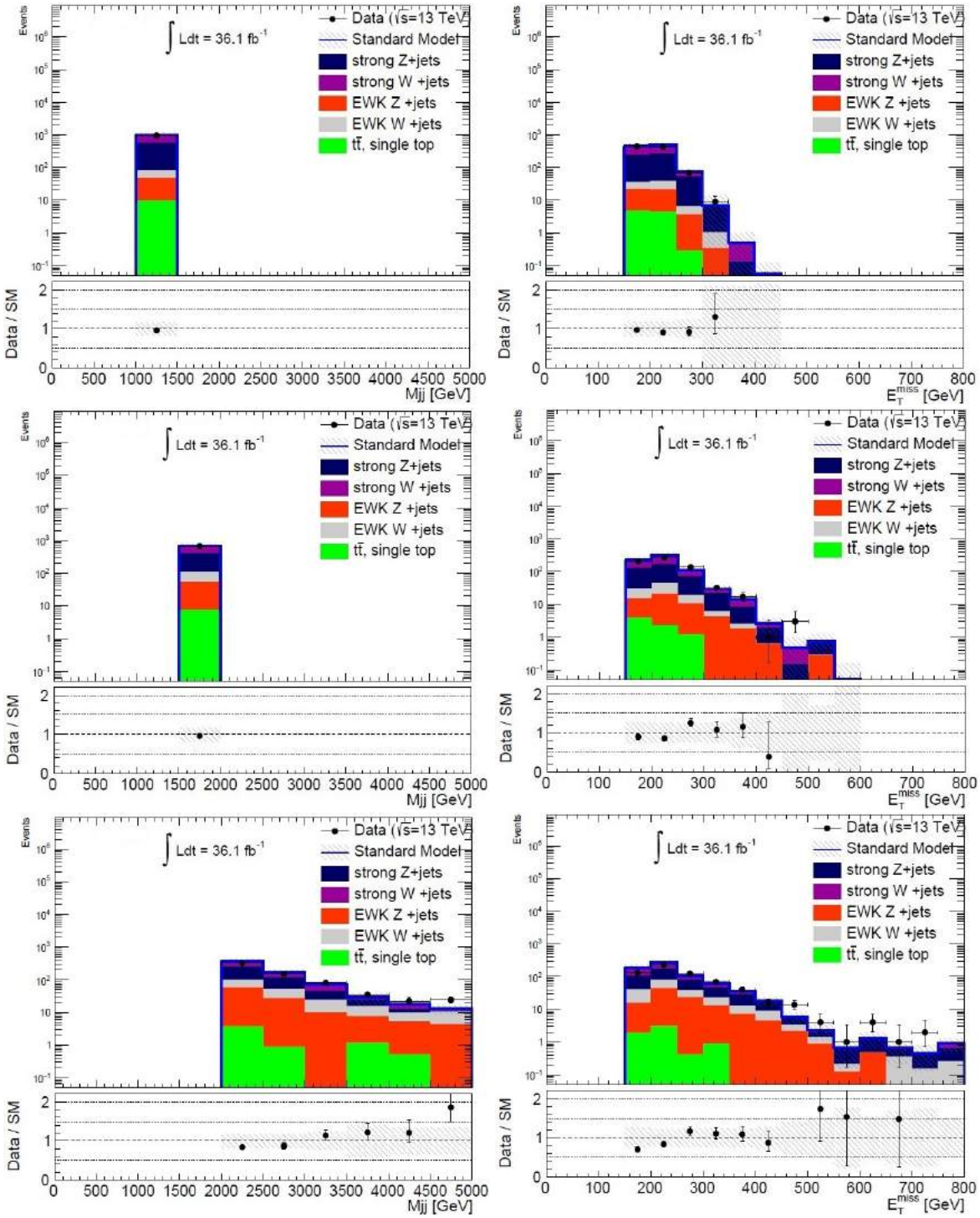

Figure 5.14: Results of the fit in the SR: Dijet mass distributions (left) and lepton p_{T} corrected $E_{\mathrm{T}}^{\mathrm{miss}}$ distributions (right). The plots show the distributions in the three different bins: 1.0 TeV $< m_{\mathrm{jj}} <$ 1.5 TeV (top), 1.5 TeV $< m_{\mathrm{jj}} <$ 2.0 TeV (middle) and $m_{\mathrm{jj}} >$ 2.0 TeV (bottom) [173].

5.8 Limits on the Higgs boson to invisible branching fraction

After the background-only validation, the data are unblinded and the fit is repeated including the signal region with the signal strength μ as a free parameter. Table 5.14 summarizes the MC expectation that enters the fit and the post-fit event yields in the SR. The best-fit parameter values after the final fit are reported in Table 5.15. The signal strength μ is compatible with zero and no significant excess above the SM prediction is found.

Table 5.14: Summary of event yields in the three SR bins. The expected yields are the pre-fit values that are the input of the fit. The fitted yields have the normalization factors applied. The signal yields assume a 100% branching fraction for the Higgs boson to decay invisibly [173].

Region	Exp. signal		Total exp.	Fitted signal		Total fitted	Observed
	VBF	ggF	background	VBF	ggF	background	events
SR1	297.0	52.8	988.4	$35.1^{+40.0}_{-35.1}$	$6.4^{+8.3}_{-6.4}$	947.2 ± 41.4	952
SR2	308.5	27.3	710.2	$36.2^{+40.9}_{-36.2}$	$3.1^{+4.1}_{-3.1}$	669.6 ± 31.3	667
SR3	458.1	56.5	547.4	$53.7^{+60.8}_{-53.7}$	$7.1^{+9.1}_{-7.1}$	633.5 ± 26.4	633

Table 5.15: Best-fit values for the normalization factors of the W and Z backgrounds as well as the number of events with fake electrons contaminating the high-$E_{\mathrm{T}}^{\mathrm{miss,sig}}$ $W \to e\nu$ background. Finally, the signal strength μ is also listed. The numbers are obtained via a simultaneous fit to signal and control regions [173].

m_{jj}-bin	k_Z	k_W	β^e
$1.0-1.5$ TeV	0.94 ± 0.25	0.94 ± 0.23	4.5 ± 1.6
$1.5-2.0$ TeV	0.80 ± 0.22	0.95 ± 0.25	4.8 ± 1.3
> 2.0 TeV	1.04 ± 0.28	1.11 ± 0.26	6.2 ± 2.0
$\mu = -3.66 \times 10^{-2} \pm 0.17$			

In the absence of a clear signal, a limit on $\mathcal{B}_{\mathrm{inv}}$ is set at 95% confidence level. The expected and observed limits are listed in Table 5.16. The uncertainties of the expected limit are listed as well, showing that the observed limit is within 1σ of the expected limit.

Table 5.16: Expected and observed limits on the Higgs boson to invisible branching fraction at 95% confidence level [173].

Observed	Expected	$+1\sigma$	-1σ	$+2\sigma$	-2σ
0.37	0.28	0.39	0.20	0.58	0.15

Systematic and statistical limitations

In order to get a sense of where possible improvements in the analysis could be achieved, it is important to study the uncertainties and their influence on the results. To gauge the impact of each uncertainty, it is removed from the fit by fixing it to its overall best-fit value. The uncertainty is turned off, and the fit is repeated resulting in a new limit on $\mathscr{B}_{\text{inv}}$. This limit is then compared with the 0.28 expected limit, which is presented above.

By turning off the MC statistical uncertainty, the impact of having abundant MC statistics is simulated. By turning off systematic uncertainties, the hypothetical case of vanishing systematic uncertainties is studied. However, the dataset that is used for the estimate is still limited and affected by fluctuations. The relative change of the limits due to turning off particular uncertainties or groups thereof is listed in Table 5.17.

Table 5.17: Impact of various uncertainties on the expected limit. The right column lists the relative change of the limit on the Higgs boson to invisible branching ratio as a result of turning off a respective group of uncertainties. Experimental uncertainties and MC statistics are considered separate categories [173].

Group	Relative limit improvement [%]
Jet energy scale	10
Jet energy resolution	2
MET soft term	1
Lepton ID veto	2
Pile-up	1
Total Experimental	17
Resummation scale	1
Factorization and renormalization scale	2
CKKW matching	4
Third jet veto	2
Total Theoretical	10
Experimental and Theoretical	28
Exp., Theory and MC statistics	42

MC statistics are a big contributor and they threaten to continue to be a problem, as the recorded data increase and it becomes increasingly difficult to generate samples with similar statistics. The most important datasets in that regard are the W and Z background simulated samples.

Determining the so-called pulls offers a more detailed view on the impact of various systematic uncertainties. They are calculated using three fits for each NP. The first is a standard fit as described above that determines a signal strength μ and best-fit values for all NPs. Then the NP in question is fixed to its best-fit value $\pm 1\sigma$ pre-fit and the fit is repeated recording a new signal strength $\hat{\mu}$. The difference between the two signal strengths $\Delta\hat{mu} = \mu - \hat{\mu}$ is a measure for the impact of the NP on the signal strength. Finally, the second fit is repeated, but now the NP is fixed to $\pm 1\sigma$ post-fit instead of pre-fit. This results in the post-fit impact on $\hat{mu}$. The

difference between pre-fit and the best-fit value for the NP is the pull, a measure for how well an NP is constrained by the fit.

The pulls and the results in Table 5.17 suggest potential areas of improvement:

- MC statistics: Measures to improve on this are mentioned in Section 5.10.1.
- Jet energy resolution: The fact that the JER shows up so high in the rankings is a testament to how important the efforts to get a better JER with the global sequential calibration (GSC) described in Section 4.2 are. Potential ways to improve on this are discussed in Section 4.3.4.
- Jet energy scale: Improving on the JES is a big effort, which will affect more than just this analysis. The jet energy calibration is discussed of Chapter 4.
- W/Z background theory uncertainties: Section 5.10.1 contains a discussion on new ways to constrain these backgrounds.
- Pile-up reweighting uncertainty: Particle flow jets with their inherent pile-up suppression will potentially improve on this uncertainty. This is discussed in Section 4.3.2.
- $E_{\mathrm{T}}^{\mathrm{miss}}$: Since $E_{\mathrm{T}}^{\mathrm{miss}}$ is constructed from all other physics objects and jets have the largest systematic uncertainties associated with them, the $E_{\mathrm{T}}^{\mathrm{miss}}$ systematic uncertainties are likely to profit from the improvements in that area.

The large impact of jet systematic uncertainties of the analysis can be explained by the heavy use of forward jets, which are the jets with the largest uncertainties, and the third jet veto.

5.9 Interpretation

The limit on the Higgs boson to invisible branching fraction determined above is model independent. This allows the widest range of theoretical models to be affected by the result and avoids a bias towards a particular hypothesis. However, in order to compare the limit to other experiments and gauge the impact on the search for dark matter overall, it is important to interpret the results via a small selection of models below.

5.9.1 Dark matter

The results are interpreted in the context of a Higgs portal model (see also Section 2.2.5) in which the Higgs boson couples to an invisible sector containing dark matter candidates [64]. These dark matter candidates can be WIMPs (see Section 2.2.2 for an explanation) and therefore limits are put on the interaction between WIMPs and nucleons. This offers the proper context to compare the results with those from direct detection methods (see Section 2.2.4 for more details). The invisible branching ratio and WIMP-nucleon cross-section are interpreted as part of an effective field theory with new physics existing at the scale of 1 TeV, which is significantly larger than the considered Higgs boson mass.

For simplicity a dark sector consisting of only one particle χ that couples only to the Higgs boson and no other SM particle is assumed. The DM candidate χ can be a scalar, a Majorana

fermion or a vector, its mass is m_χ and it couples to the Higgs boson with strength λ_χ. These are the only two parameters of this model. Given that the nucleon form factor is known, the relation between $\mathcal{B}_{\text{inv}}$ and λ_χ for a given m_χ can be exploited to derive exclusion limits. The nucleon form factor is taken from Ref. [182]. Given that WIMP masses below 70 GeV are studied, the Higgs portal model can indeed be treated as an effective field theory.

Figure 5.15 shows the exclusion limits at 90% confidence level of the direct detection experiments LUX [183], PandaX-II [184] and Xenon1T [58] and the search with the ATLAS detector in the WIMP mass - WIMP-nucleon cross-section plane. The two approaches cover different regions of the phase space and together they are able to exclude a large range of WIMP masses for the Higgs portal and similar models. The direct detection experiments are more sensitive at higher masses because the recoil against nuclei is stronger. The collider search needs a large phase space for the scalar particle to decay into, which is present at low masses.

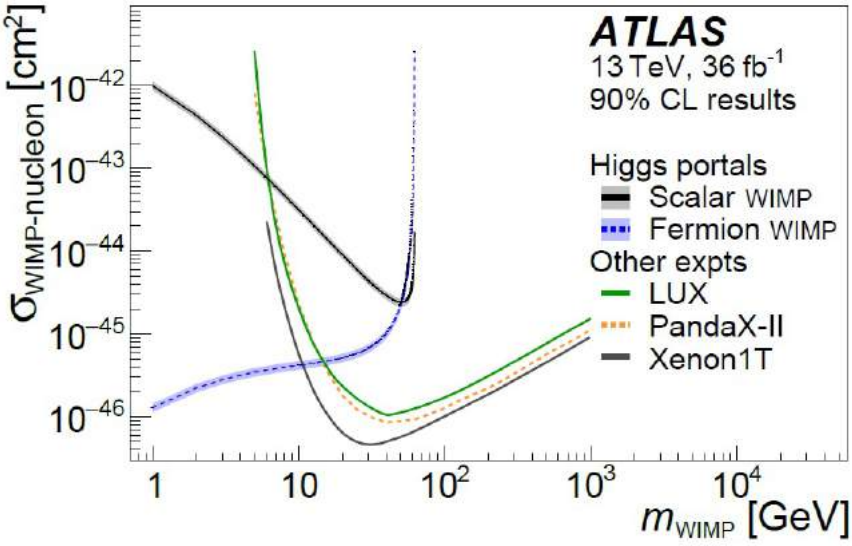

Figure 5.15: Upper limits on the WIMP-nucleon cross-section from the ATLAS search and direct detection experiments. Both the interpretations as scalar (black) and fermionic (blue) dark matter are shown. The direct detection experiments LUX [183] (green), PandaX-II [184] (orange) and Xenon1T [58] (dark blue) assume a local DM density of 0.3 GeV$/c^2/cm^3$ for the limit calculation [12].

5.9.2 Cross section vs. scalar mass

While the search was aimed at invisible decays of the Higgs boson, it is possible to extend the interpretation to other scalar particles with the same properties as the Higgs boson but with different masses. Seven mass points between 75 GeV and 3 TeV are considered. The list of additional VBF samples is presented in Section 5.3.2. The 95% confidence level limits of their cross-sections $\sigma^{\text{VBF}}_{\text{scalar}}$ times $\mathcal{B}_{\text{inv}}$ are depicted in Figure 5.16. The scalar to invisible branching ratio cannot be determined directly without making additional assumptions about the production cross-section.

Because the same couplings are assumed, the kinematics of the decay process are largely the same at other scalar masses. However, in the case of heavier mediators the tails of m_{jj} and

$\Delta\eta_{jj}$ distributions tend to be larger. This allows a better discrimination against the background and thus leads to the improved limit at higher scalar masses that can be seen in Figure 5.16.

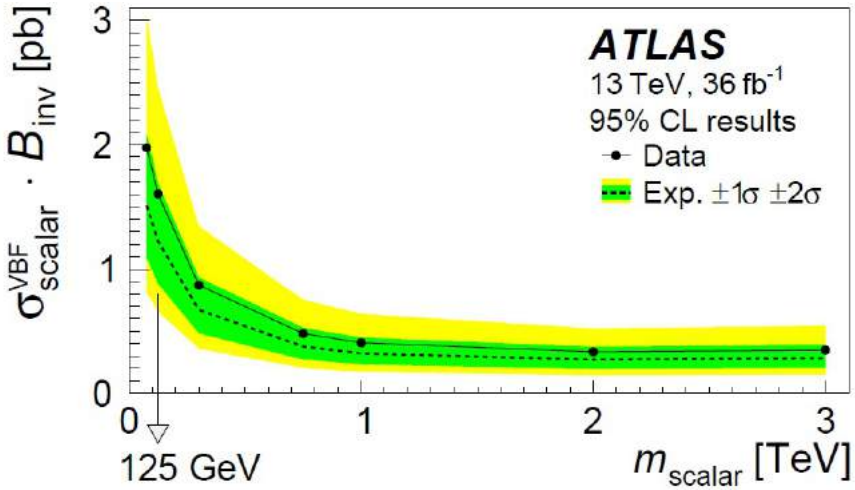

Figure 5.16: Upper limits on $\sigma^{\text{VBF}}_{\text{scalar}} \cdot \mathscr{B}_{\text{inv}}$ as a function of the mass of a scalar particle similar to the Higgs boson produced in vector-boson fusion [12].

There are multiple BSM models that predict additional heavy particles that are similar to the Higgs boson. Examples include a heavy scalar mediator as mentioned in Section 2.2.4, the two Higgs doublet models and supersymmetry discussed in Section 2.2.5. All of these models are constrained by the limits in Figure 5.16.

5.10 Conclusion

A search for invisible decays of a Higgs boson produced in vector-boson fusion in pp-collisions recorded with the ATLAS detector at a centre-of-mass energy of 13 TeV is performed and presented. The final state includes two jets with large invariant mass and η separation as well as invisible particles, which are registered as missing transverse energy. No leptons are expected in the final state and yet $W \to \ell\nu$ events where the lepton is lost are one of the dominant backgrounds together with $Z \to \nu\bar{\nu}$. Multijet events contribute little to the background, but are hard to quantify and much effort is put into their estimation.

A good agreement between data and the Standard Model prediction is found. As a result an observed (expected) limit is put on the invisible branching ratio $\mathscr{B}_{\text{inv}}$ of 0.37 (0.28). Furthermore, the results are interpreted with a Higgs portal model excluding WIMP-nucleon cross-sections above 10^{-46} cm^2 to 10^{-42} cm^2 for WIMP masses between 1 GeV and 70 GeV, which is complementary to direct detection methods. Additional limits are placed on the VBF cross-section times invisible branching fraction of hypothetical particles that are similar to the Higgs boson between $m_{\text{scalar}} = 75$ GeV and 3 TeV. The limits range from $\sigma^{\text{VBF}}_{\text{scalar}} \cdot \mathscr{B}_{\text{inv}} = 2$ pb to 0.3 pb.

Compared to the Run 1 result using 8 TeV data with an observed (expected) limit of 0.30 (0.35) an improvement of the expected limit and thus the sensitivity of the search is achieved. The search also contributed to a combination with searches for invisible decays of the Higgs

boson produced as Higgsstrahlung either from a Z boson decaying into a pair of electrons/muons or from a hadronically decaying vector boson. The combined limit is 0.26 (0.17) observed (expected) [185].

At the same time in CMS a search for invisible decays of a Higgs boson produced in vector-boson fusion at $\sqrt{s} = 13$ TeV yielded an observed (expected) limit of 0.28 (0.21) and a combination with other searches for invisible decays lead to 0.24 (0.18) [163].

5.10.1 Looking ahead, analysis with the full Run 2 dataset

Of course there is a constant effort to improve on these results even further. As such the work on the full Run 2 analysis, which makes use of an expected integrated luminosity of 140 fb^{-1}, has already begun. In addition to having access to a larger dataset the following improvements are likely to lead to an even higher sensitivity for new physics:

- The method described in Section 5.5.1 uses data from the control regions to constrain the background yields in the signal region. The W and Z backgrounds are handled separately, but in principle the W CRs can be used to normalize the $Z \to \nu\bar{\nu}$ background, as is illustrated in Figure 5.17. In order to constrain the Z to invisible background with W events it is necessary to understand the correlation between the two processes. Otherwise the additional theoretical uncertainties would undo the advantages of higher statistics for the estimate.

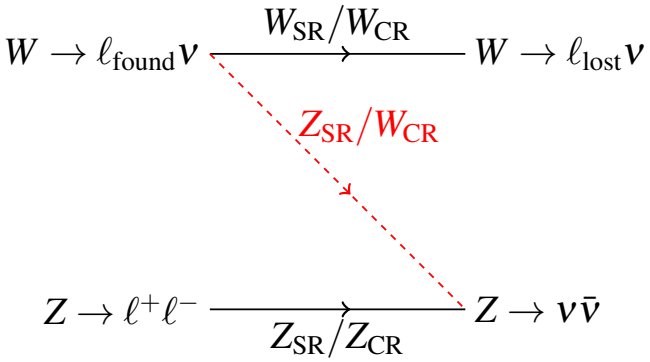

Figure 5.17: Illustration of a new method to constrain the $Z \to \nu\bar{\nu}$ background. In contrast to the method summarized by Eq. 5.3 and presented in Section 5.5.1 (straight arrows) an additional constraint from the W CR is shown (red dashed arrow).

- Monte Carlo statistics are another limiting factor especially for the W and Z background samples. Potential ways to improve statistics in the future include the definition of a parton level filter on m_{jj} after generating a large amount of events at EVTGEN level with an LO generator. Afterwards the resulting theoretical systematic uncertainties are gauged with comparisons to NLO samples.

- The $E_{\mathrm{T}}^{\mathrm{miss}}$ requirement has potential for improvement. For now it is necessary to use an $E_{\mathrm{T}}^{\mathrm{miss}}$ requirement as high as 180 GeV together with an $MHT(\mathrm{noJVT}) > 150$ GeV requirement in order to suppress the uncertainty prone multijet background. However, an $E_{\mathrm{T}}^{\mathrm{miss}}$ requirement at 150 GeV would lead to a better signal to background ratio. It might be possible to serve both needs with an $E_{\mathrm{T}}^{\mathrm{miss}}$ definition more suitable for the analysis.

- Some of the largest systematic uncertainties and therefore some of the most fruitful areas of improvement relate to jets. The use of particle flow jets is studied in Chapter 6 but is yet to touch every aspect of the analysis. Furthermore, the jet calibration described in Chapter 4 is undergoing constant improvement and has already shown several advantages of the new jet collection compared with the old one. If the jet energy scale, jet energy resolution and pile-up reweighting uncertainty could be lowered, it would be a big step for the analysis. A study of the potential impact of the use of particle flow jets is presented below.

Particle flow jets as a possible area of improvement

As discussed in Section 3.3.2 there are multiple jet collections that are currently in use in ATLAS. The VBF Higgs boson to invisible analysis published in 2018 [12] uses topocluster jets. For the full Run 2 study the possible advantages and challenges of switching to particle flow jets are studied and the most important findings are discussed below.

In general, there are multiple expected advantages for any analysis seeking to use particle flow instead of topocluster jets. The reasons for possible improvements are twofold: the particle flow jet algorithm uses tracks to determine η and ϕ directions, which is more precise than using topoclusters. Furthermore, the pile-up suppression is superior, as charged particles that do not come from the primary process are removed [103]. These effects are discussed in more detail in Section 4.3.2. A better jet energy resolution of particle flow jets is also observed for intermediate p_{T} in Section 4.2.6.

Despite all of these improvements, it is not immediately obvious if these advantages affect the phase space this analysis is sensitive to. Most improvements only take effect for central jets where the tracker can help with the reconstruction, and for low-p_{T} jets. The analysis selection requirements on the jet transverse momentum might lessen the impact of the improvements. An example of this is the $p_{\mathrm{T,j_1}} > 80$ GeV requirement. As discussed in Section 4.2.6 the p_{T} resolution of particle flow jets is only better below 100 GeV, leaving only a small window of leading jets with an improved resolution.

One of the greatest hopes connected to the incorporation of particle flow jets is a decrease of the systematic uncertainties from jet reconstruction. Figure 5.18 shows the number of events in two VBF Higgs boson to invisible simulated signal samples after each of the signal region selection requirements is applied. This distribution is called a selection sequence. One of the samples uses topocluster jets the other particle flow jets. The bottom pad shows the combined systematic uncertainty based on the jet contributions listed in Section 5.6.1. The combined uncertainty is the quadratic sum of the individual contributions. The difference between the two jet collections is negligible because of the small amount of central low-p_{T} jets in the sample. In fact the final requirement $|\Delta\eta_{\mathrm{jj}}| > 4.8$ ensures that the jets cannot both have $|\eta| < 2.4$ and it is likely that neither of them is central given that only jets up to $|\eta| = 4.5$ are considered in the analysis.

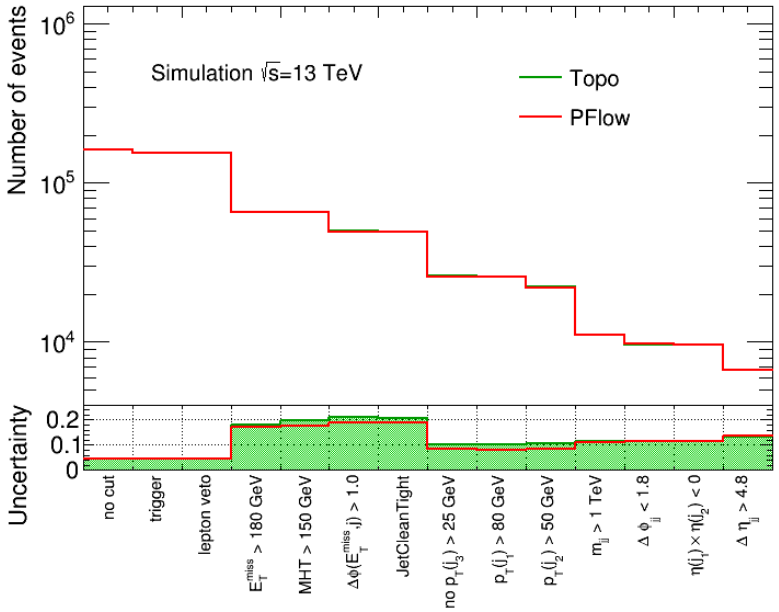

Figure 5.18: Comparison of topocluster jets (green) and particle flow jets (red) for a simulated signal sample of an invisibly decaying Higgs boson produced in vector-boson fusion. Top pad: "selection sequence" — the number of events after each of the SR requirements is applied. Bottom pad: combined systematic uncertainties. MHT is short for MHT(noJVT) and jetCleanTight is defined with the jet object definition in Section 5.4.3.

This is slightly different for the ggF Higgs boson to invisible samples studied in Figure 5.19. Although the selection sequences for both jet collections look largely the same, the uncertainties differ starting at the dijet mass requirement. Here, particle flow jets outperform topocluster jets, as the jets produced in the gluon–gluon fusion process (see for example Figure 5.2) typically are softer ISR jets.

At the third jet veto (no $p_{\mathrm{T,j3}} > 25$ GeV) there is a sharp decline of the uncertainty. Intuitively the jet uncertainties should have a big impact on the measurement of the third jet p_{T} causing uncertainty in whether or not a jet is above the threshold. However, the selection sequence is determined by the requirements in aggregate. For the $E_{\mathrm{T}}^{\mathrm{miss}}$ requirement, which is still in effect, the uncertainty now decreases as a result of the third jet veto. Events that pass the veto have fewer jets and thus the constructed $E_{\mathrm{T}}^{\mathrm{miss}}$ contains fewer objects that contribute to its uncertainty. The two plots indicate that the latter effect is dominant.

In conclusion, the impact on the systematic uncertainties as a result of switching to particle flow jets is small in case of the VBF signal and noticeably positive in case of the ggF signal. Therefore, it is expected to be an overall improvement of the search for invisible decays of the Higgs boson to use particle flow jets in future analyses.

5.10.2 High-luminosity LHC prospects

The High-Luminosity LHC is expected to provide up to 3000 fb^{-1} at $\sqrt{s} = 14$ TeV within the next two decades. This enormous amount of data is obviously very promising for the future of the analysis. There are already crude estimates of the potential in this next era of Higgs

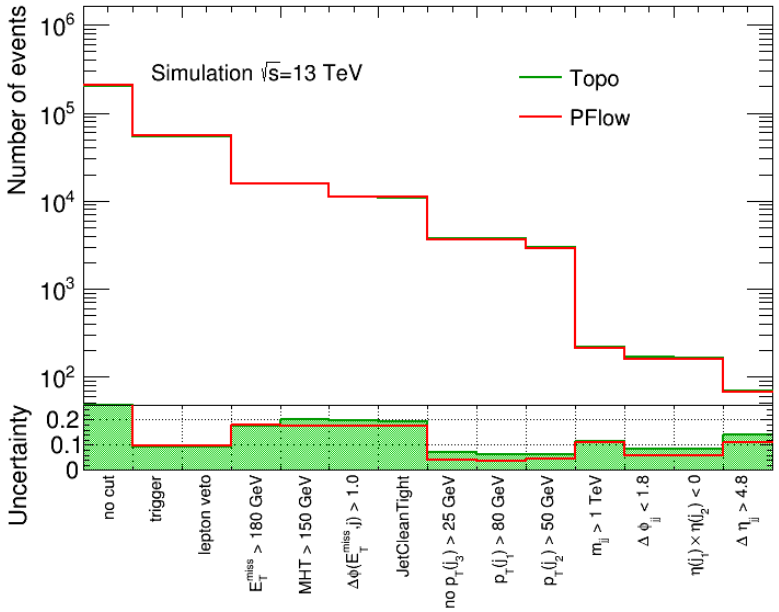

Figure 5.19: Comparison of topocluster jets (green) and particle flow jets (red) for a simulated signal sample of an invisibly decaying Higgs boson produced in gluon–gluon fusion. Top pad: "selection sequence" — the number of events after each of the SR requirements. Bottom pad: combined systematic uncertainties. MHT is short for MHT(noJVT) and jetCleanTight is defined with the jet object definition in Section 5.4.3.

boson physics and the challenges for analyses [186]. The prospects for new physics in Higgs boson decay channels was studied and the sensitivity is expected to improve greatly. Looking at the Higgs portal model the limit on the invisible branching fraction is predicted to improve significantly as shown in Table 5.18.

Table 5.18: Expected limits on the Higgs boson to invisible branching fraction as projected for the High-Luminosity LHC compared to the current result [187].

Luminosity [fb^{-1}]	36.1	300	3000
Expected Limit	0.28	0.22	0.13

In addition to higher luminosities the ATLAS detector itself will undergo a number of upgrades to cope with the new environment. One of them is the replacement of the entire inner detector with the all-silicon inner tracker. The latter covers a larger range in $|\eta|$, up to 4.0 instead of 2.5 [188]. This is advantageous to the analysis because many forward jets are expected in the final state and a large separation in η of the two leading jets is one of the SR requirements.[4)]

[4)] See for example Figure 4.16 in Section 4.3.2 where the pile-up suppression sees a clear decline beyond $|\eta| = 2.4$.

Chapter 6

Modelling of jet transverse momentum response tails

6.1 Motivation

The goal of the multijet background estimation presented in Section 5.5.4 is to quantify the number of events with only jets in the final states where a jet is mismeasured such that the event appears to have large $E_{\mathrm{T}}^{\mathrm{miss}}$. This does not happen typically and is more likely in regions of extreme mismeasurement. Looking at the transverse momentum response $p_T^{\mathrm{reco}}/p_T^{\mathrm{truth}}$, the tails of the distribution are therefore of interest. The tails are the regions with a very high or a very low response in which only few events lie. The central, Gaussian part, which contains the bulk of the events, was studied extensively (see for example the description of the global sequential calibration (GSC) in Section 4.2 or the following sources [142, 143, 148, 149]), but for the tails it is a priori unknown how precise the simulation is. As mentioned in Section 5.5.4, jet response templates like the one in Figure 5.7 are used for the smearing that leads to the multijet background prediction. The size of the non-Gaussian tails has a big impact on the results of the rebalance and smear (R+S) method. Therefore, the tails have to be understood well to evaluate the contribution of potential mismodelling of the non-Gaussian tails to the uncertainty of the multijet background prediction in the search for invisible decays of a Higgs boson produced in vector-boson fusion.

The tails of the jet response distributions are not Gaussian in shape and they are caused by effects that are different from the behaviour of the core. In fact, the tails are caused by effects resulting from instrumentation, calibration and physics processes.

The physics effects include the following:

- Semi-leptonic heavy flavour decays: Heavy-flavour jets (from b and c quarks) can decay semi-leptonically and tend to have a smaller response than light-flavour jets (from u, d and s quarks), since the neutrino decay products are undetected. This effect is the strongest if the jet originates from a b or c quark and does not just contain a heavy-flavour quark in the shower. Its main contribution is to the low response tail.

- Gluon jets: These jets contain more particles, which are also softer. As a result they cause a lower response due to non-linear effects in the measurement with the calorimeters.

Both physics effects are also reasons why the low response tails are expected to be larger. Instrumental and calibration effects include the following:

- Electronic noise: The direction of a jet, and therefore its transverse momentum, correlate with the underlying process and the centre-of-mass energy. Electronic noise, however, is completely random, which can alter the reconstructed jet momentum vector in directions that are atypical for the (Gaussian) spread expected in a particular physics process. This in turn can lead to non-Gaussian effects.

- Inhomogeneities of the detector material: Necessarily some of the jet energy is deposited in parts of the detector that are not instrumented. Parts of the jets can even traverse the calorimeter as Punch-Through, as discussed in Chapter 4. Both of these effects cause the measurement to miss energy, leading to low response tails [142].

- Inactive channels: Malfunctioning detector components can cause the measurement to miss some of the jet energy or create artificial signal, which is prevalent both in the high- and low response tails. Similarly, detector regions can be inactive during part of data taking, which contributes to part of the jet energy deposit being missed by the reconstruction [189]. These effects are mitigated by the use of the good runs list (GRL) mentioned in Section 5.4.1, but they still contribute.

- Miscalibration: Other than simple mismeasurements, the effects of miscalibration depend on the choices made during the jet calibration and the experimental limitations of its application. For example, in the in-situ step of the jet calibration (see Section 4.1.5), miscalibration effects are removed through corrections to data. These corrections are designed to cover a wide kinematic phase space by using γ+jet, Z+jet and multijet-based corrections. However, this finite number of corrections still does not perform equally well in every energy range [190].

In the following, two jet collections described in detail in Section 3.3.2 are studied. Topocluster jets are the jet collection of choice for the first search for invisible decays of the Higgs boson produced in vector-boson fusion at $\sqrt{s} = 13$ TeV with $\int L = 36.1$ fb^{-1} [12]. For the next iteration of the analysis, particle flow jets are used because of their better resolution at intermediate p_{T}, superior pile-up suppression and other advantages discussed in Chapter 4. An additional goal of the study of non-Gaussian tails is to see whether particle flow jets have disadvantages in this area that would dissuade from switching to the new jet collection or if there are even better results that support the decision to use particle flow jets.

This chapter details the various steps that are undertaken to estimate how well the non-Gaussian tails are simulated in jet response distributions. The chosen approach is new to the ATLAS experiment. However, non-Gaussian tails were studied in CMS in Ref. [191]. The discussion begins with the introduction of the basic principle of the method in Section 6.2. The datasets used in the study as well as selection and binning are presented in Section 6.3. The modelling of Gaussian cores with a fit and the quantification of the non-Gaussian tail are detailed in Section 6.4. The systematic uncertainties of the study are discussed in Section 6.5, before the results are presented and interpreted in Section 6.6. Finally, the discussion of alternative methods in Section 6.7 serves as an outlook towards future efforts to quantify non-Gaussian tails of jet response distributions.

6.2 Basic principle of the jet response tail study

The study seeks to measure the goodness of the simulation of non-Gaussian tails in jet transverse momentum response distributions. In order to do so, the tails are identified with Gaussian fits and the number of tail events are counted. Afterwards, tail fraction factors are determined. These are defined as the number of tail events in data divided by the number of tail events in Monte Carlo (MC).

Because the quality of the simulation is tested, this needs to be a data-driven study. There is no such thing as a response distribution in data, since the variable uses information about the truth jet. The closest equivalent is the asymmetry distribution where the asymmetry A is defined as:

$$A = \frac{p_{\mathrm{T,j_1}} - p_{\mathrm{T,j_2}}}{p_{\mathrm{T,j_1}} + p_{\mathrm{T,j_2}}}. \tag{6.1}$$

Here, the transverse momentum of the leading jet $p_{\mathrm{T,j_1}}$ is compared with the transverse momentum of the subleading jet $p_{\mathrm{T,j_2}}$ instead of comparing a jet with the corresponding truth jet. The underlying logic is that the random mismeasurements that lead to a Gaussian response distribution have a corresponding effect on the asymmetry distribution where both jets are randomly mismeasured. This leads to both distributions having a proportional width. Furthermore, the rarely occurring tail effects lead to a large asymmetry, as one jet transverse momentum massively deviates from the other, which is typically part of the Gaussian core in the response distribution. Therefore, the fraction of events in the tails of response and asymmetry distributions is expected to be very similar. The asymmetry distribution is strictly positive by definition, which disqualifies it from being a measure for the prevalence of effects that contribute at different rates to the low and high response tails.

In general, multijet events have more than two jets in the final state. The recoil of additional jets affects the asymmetry distribution, which becomes apparent below. Therefore, an extrapolation to pure dijet events is used before deriving tail fraction factors. By using an extrapolation instead of selecting events with exactly two jets, the large statistics of multijet events can be exploited.

Inserting Eq. 6.1, the following conclusion can be made in the regime where the transverse momenta of the two leading jets and their resolutions are similar ($p_{\mathrm{T}} \simeq p_{\mathrm{T,j_1}} \simeq p_{\mathrm{T,j_2}}$, $\sigma_{p_{\mathrm{T}}} \simeq \sigma_{p_{\mathrm{T,j_1}}} \simeq \sigma_{p_{\mathrm{T,j_2}}}$):

$$\begin{aligned} \sigma_A^2 &= \left[\frac{\partial A}{\partial p_{\mathrm{T,j_1}}}\right]^2 \sigma^2_{p_{\mathrm{T,j_1}}} + \left[\frac{\partial A}{\partial p_{\mathrm{T,j_2}}}\right]^2 \sigma^2_{p_{\mathrm{T,j_2}}}, \\ \Rightarrow \left(\frac{\sigma p_{\mathrm{T}}}{p_{\mathrm{T}}}\right) &\simeq \sqrt{2}\sigma_A. \end{aligned} \tag{6.2}$$

Therefore, for a given jet p_{T} the width of the asymmetry distribution is proportional to the corresponding transverse momentum resolution. Since the resolution of jets depends on $|\eta|$, this approximation only holds with both leading jets in the same $|\eta|$ regime. This relation was used in other analyses and experiments such as DØ [192], CMS [193] and even ATLAS [194].

6.3 Data and simulated samples

The study of non-Gaussian tails in jet response distributions uses datasets and simulated samples that are very similar to those of the main analysis presented in Chapter 5. The only difference is the use data of recorded in 2017 in addition to the dataset recorded in 2015 and 2016. In total this more recent study has access to 80 fb^{-1} of integrated luminosity with 2.0% uncertainty. As usual, a fully operational ATLAS detector with stable beams is the prerequisite for data to be taken into consideration. The single-jet triggers of the dataset are discussed in Section 5.4.2 and are listed in Table 5.3.

Non-Gaussian tails in jet response distribution were also studied with a dataset of 36.1 fb^{-1}. This lead to parts of the results presented in Table 5.5 in Section 5.5.4. The study discussed in this chapter is a more refined and current version of that study. Therefore, it uses a larger dataset.

The multijet MC samples are a subset of the ones used for the validation of the multijet background estimate discussed in Section 5.5.4. They are listed in Table A.12 in Appendix A.1.2. The samples were produced with full simulation [139] using `Pythia 8` [137].

6.3.1 Binning and selection

The goal is to study pure dijet events where every jet beyond the subleading one does not contribute to the hard scattering event. Selecting for events without a third jet is problematic. In reconstructing jets with the ATLAS experiment there is a threshold at 20 GeV, below which jets are not recommended for use. Therefore, there could always be another jet just below threshold that changes the asymmetry of the event even if third jets are vetoed. Instead, an extrapolation technique is used to examine the trend of the influence of the third jet on the dijet event as a function of its transverse momentum.

Figure 6.1 shows the momenta of the three leading jets of a multijet event in the transverse plane. A dijet-axis $\hat{p}_{\text{T},jj}$ is defined as the vectorial difference between the two leading jets as in:

$$\hat{p}_{\text{T},jj} = \frac{\vec{p}_{\text{T,j1}} - \vec{p}_{\text{T,j2}}}{|\vec{p}_{\text{T,j1}} - \vec{p}_{\text{T,j2}}|}. \tag{6.3}$$

Only the vector component of the third jet parallel to the dijet axis affects the asymmetry of the event. Therefore, $\alpha_{||}$ is defined in Eq. 6.4 in a way that ignores the perpendicular component:

$$\alpha_{||} = \frac{\vec{p}_{\text{T,j3}} \cdot \hat{p}_{\text{T},jj}}{p_{\text{T}}^{\text{ave}}}, \tag{6.4}$$

where $p_{\text{T}}^{\text{ave}}$ is the average transverse momentum of the two leading jets: $p_{\text{T}}^{\text{ave}} = 0.5 \times (p_{\text{T,j1}} + p_{\text{T,j2}})$.

The jet response can be tested most clearly in events with negligible third jet influence on the hard-scatter event. In other words, the region of interest is the limit $\alpha_{||} \to 0$. To analyse these events, the sample is binned in $\alpha_{||}$ with the binning given in Table 6.3.1. As is shown below, the behaviour of the dijet asymmetry is dependent on $p_{\text{T}}^{\text{ave}}$ and the $|\eta|$ direction of the two leading jets. Therefore, a binning in $p_{\text{T}}^{\text{ave}}$ and $|\eta|$ is done as well. As is shown in Chapter 4, the resolution of jets depends on their $|\eta|$-direction. As a consequence, both jets are demanded to be in the same $|\eta|$-bin in order to get asymmetry distributions with one clear width. With

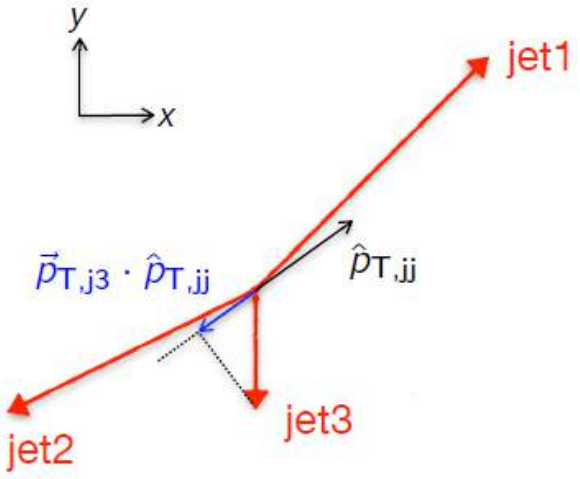

Figure 6.1: Momenta of the three leading jets in a multijet event. The transverse momentum of the third jet projected onto the dijet axis is $\alpha_{||}$, a measure of the "dijet-ness" of the event.

the same argument, it could be demanded that both jets are in the same p_T bin. However, that restriction would prevent the difference between the jet transverse momenta to be larger than the bin size and thus cut off part of the tails of the asymmetry distribution. The p_T^{ave} and $|\eta|$ binning can be found in Table 6.3.1 as well.

Table 6.1: The binning of multijet events for the study of non-Gaussian tails.

$\|\eta\|$	0.0–1.0	1.0–1.9	1.9–4.5			
p_T^{ave} [GeV]	45–80	80–150	150–250	250–400	400–700	700–1000
$\alpha_{\|\|}$	0.0–0.02	0.02–0.04	0.04–0.06	0.06–0.08	0.08–0.11	0.11–0.14
	0.14–0.17					

The dijet events are required to satisfy the following selection criteria:

- At least two good jets, defined according to the following requirements:
  - $p_T > 25$ GeV
  - $|\eta| < 4.5$
  - Jet vertex tagger (JVT) (see Section 3.3.2 for more details) requirement:
    - For topocluster jets: JVT > 0.59 if $p_T < 60$ GeV and $|\eta| < 2.4$
    - For particle flow jets: JVT > 0.2 if $p_T < 60$ GeV and $|\eta| < 2.4$
  - MC quality requirement: $0.6 < p_T^{ave}/p_{T,j_1}^{truth} < 1.4$
- No reconstructed lepton or photon
- $\Delta\phi_{jj} > 2.5$

- Both leading jets are in the same $|\eta|$-bin

The JVT cuts are applied to reduce the amount of pile-up in the events. For particle flow jets the requirement is a lot less strict because particle flow jets have an inherent pile-up suppression as discussed in Section 4.3.2. The jets are required to be back-to-back in order to measure their momentum balance. The MC quality requirement is implemented to remove events, in which low-p_{T} jets with large event weights migrate to higher-p_{T} bins and distort the jet p_{T} spectrum. The effect exists because of multijet events being simulated in slices divided by the leading jet p_{T} and receiving a pile-up overlay, before the samples are weighted. The effect is unphysical [152].

6.4 Technical implementation

Figure 6.2 shows an asymmetry distribution. The chosen bin is $|\eta| < 1.0$, 80 GeV $\leq p_T <$ 150 GeV, $0.02 \leq \alpha_{||} < 0.04$ and therefore contains central jets in events with relatively low $p_{\mathrm{T}}^{\mathrm{ave}}$ and $\alpha_{||}$. The distribution can be understood considering two regions: one is the Gaussian core, which encompasses the vast majority of the events; the other is the non-Gaussian tail, which exists because of the phenomena described above.

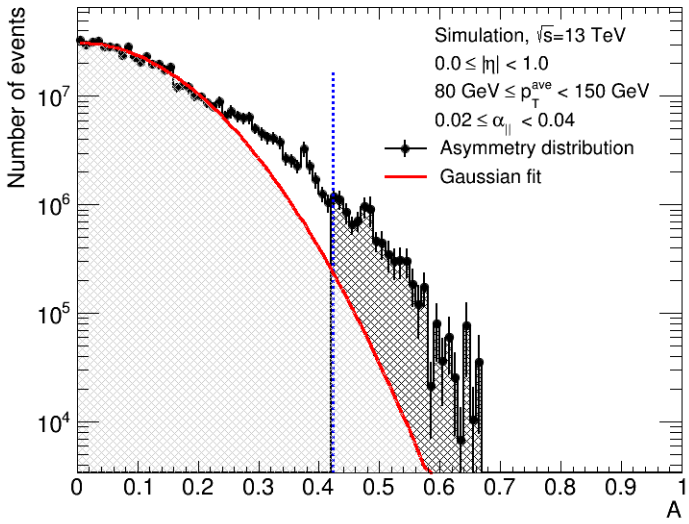

Figure 6.2: Asymmetry distribution (black dots and histogram) of topocluster jets in the bin $|\eta| < 1.0$, 80 GeV $\leq p_T <$ 150 GeV, $0.02 \leq \alpha_{||} < 0.04$. Gaussian fit (red line) and definition of the tail region (blue, dashed line). The grey hashed area is identified as tail-like events.

The Gaussian core is modelled with a fit. Furthermore, a tail region is defined above an asymmetry value (blue, dashed line) that depends on the distribution and is discussed below. The events below the Gaussian fit are defined as "core-like events" and the events above it that are in the tail region are defined as "tail-like events[1)]" (grey hashed area in Figure 6.2). The

[1)] Of course it is unknown, which individual event is the result of a non-Gaussian effect. As such, for many asymmetry values there are both events that are considered tail-like events and core-like events with no reason to decide which is which. Because only the quantity of tail-like events is of interest and no attempt to label individual events is made, the distinction based on the fit serves its purpose.

tail-like events are the difference between the events in the distribution and the Gaussian fit in the tail region. With the definitions of tail region, core-like event and tail-like event in hand, the tail fraction is defined as:

$$f_{\text{tail}} = \frac{N_{\text{tr}} - N_{\text{g,tr}}}{N_{\text{total}}}, \tag{6.5}$$

where N_{tr} is the number of events in the tail region, $N_{\text{g,tr}}$ is the number of core-like events in the tail region and N_{total} is the total number of events in the distribution.

An alternative definition would be to simply subtract the Gaussian fit from the asymmetry distribution and divide that number by N_{total} without defining a tail region. This does not lead to reliable results for the following reason: the asymmetry distribution naturally fluctuates as a statistical effect. Especially in the lowest asymmetry bins, there can be sizeable differences between the fitted curve and the distribution. These differences can be large compared with the number of events in the tail because the Gaussian core contains orders of magnitudes more events than the tail. By counting only tail-like events in the tail region it is avoided that these fluctuations dominate the calculation.

Returning to the overall goal, which is the comparison of pure dijet events between data and MC events, the asymmetry tail factor ρ_{tail} is defined as:

$$\rho_{\text{tail}} = \frac{f_{\text{tail}}^{\text{data}}(\alpha_{||} \to 0)}{f_{\text{tail}}^{\text{MC}}(\alpha_{||} \to 0)}. \tag{6.6}$$

If the value is equal or close to unity, it can be concluded that the simulation does a good job of simulating the tails quantitatively.[2)] Is the value larger than 1, the tail effects are underestimated by the simulation. If the value is smaller than 1, they are overestimated.

In the general case, the third jet introduces an imbalance to the dijet interaction because of its recoil. This fact is also illustrated by Figure 6.1. It leads to higher asymmetry values independent of the mismeasurements that lead to the Gaussian width and other effects that result in the tails. The effect causes the Gaussian mean to shift to higher asymmetry values. This becomes clear when looking at asymmetry distributions in a higher $\alpha_{||}$-bin like the example in Figure 6.3.

6.4.1 Fitting

Since the recoil from the third jet causes the Gaussian mean to increase, the mean of the fit function differs from zero if $\alpha_{||} \neq 0$. Mathematically this is modelled by summing two Gaussian functions with the same amplitude and width as well as means that only differ by their sign. The fit function is illustrated in Figure 6.4 and defined as:

$$F_{\text{gauss}} = a \times \left[e^{-\frac{(x-\mu)^2}{2\sigma^2}} + e^{-\frac{(x+\mu)^2}{2\sigma^2}} \right]. \tag{6.7}$$

The figure shows a mostly positive Gaussian function (red line) and a mostly negative one (green line). The mostly negative Gaussian function has a positive flank, which is added (blue shaded area) to the mostly positive Gaussian function, which leads to the overall expected shape (blue line). However, what is actually happening is that the negative flank (red shaded area) of

[2)] However, it is unknown whether each phenomenon that contributes to the tail size is simulated well.

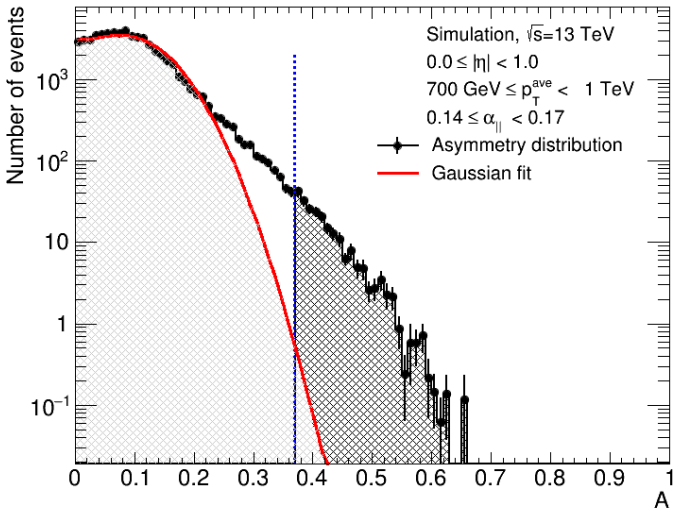

Figure 6.3: Asymmetry distribution (black dots and histogram) of particle flow jets in the bin $|\eta| < 1.0$, 700 GeV $\leq p_T <$ 1 TeV, $0.14 \leq \alpha_{||} < 0.17$. Gaussian fit (red line) and definition of the tail regions (blue, dashed line). The grey hashed area is identified as tail-like events.

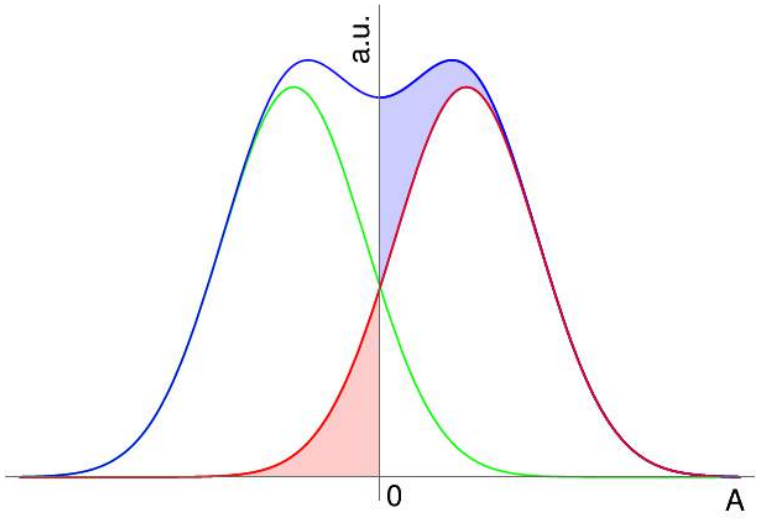

Figure 6.4: Illustration of the fit function, which is the sum (blue) of two Gaussian functions (green and red) that differ only by the sign of their mean.

the mostly positive Gaussian function has its sign changed and is then added to the positive part of the same function. Since the asymmetry is positive by definition, there is no need to consider the negative side. If the mean equals zero, the function is indistinguishable from a single Gaussian function with twice the amplitude.

Looking back at Figure 6.3 there is some prior knowledge about the mean μ. Under the assumptions that the main reason for the mean shift away from zero is the third jet and the recoil from further non-pile-up jets is negligible, the mean μ_{est} can be estimated as follows:

$$\mu_{\text{est}} = \frac{p_{\text{T},1} - p_{\text{T},2}}{p_{\text{T},1} + p_{\text{T},2}} = \frac{p_{\text{T},1} - p_{\text{T},2}}{2p_{\text{T}}^{\text{ave}}} \simeq \frac{\vec{p}_{\text{T},3} \cdot \hat{p}_{\text{T},jj}}{2p_{\text{T}}^{\text{ave}}} = \frac{\alpha_{||}}{2}. \tag{6.8}$$

The approximation in Eq. 6.8 describes the average case where the asymmetry is shifted as a result of the influence of the third jet. It does not consider the reconstruction effect that leads to the Gaussian width because the mean of the Gaussian distribution is the parameter of interest here. In the limit $\alpha_{||} \to 0$ there is no third jet, no shift and the mean is at zero as well.

Fixing the mean to $\alpha_{||}/2$ leads to better fit results, but introduces a source of systematic uncertainty. This is further discussed in Section 6.5. Additional studies on the goodness of this approximation are presented in Appendix A.2.1.

The statistical uncertainty of the tail fraction determined from each asymmetry distribution has three components resulting from Eq. 6.5: the uncertainties of the total number of events in the distribution, the number of events in the tail region and the uncertainty of the fit integral. The first two are straightforward and result from the poisson error in each bin. The latter is estimated with a sampling method to ensure results that are always comparable between data and MC even in low statistics bins. For this method, each bin content is statistically varied by its poisson uncertainty. This is repeated until 1000 different histograms are produced. A fit to each histogram is performed and the fits are ordered by their integral in the tail region. The median result is selected as the nominal fit result. Furthermore, the fit result at the 16th percentile and the result at the 84th percentile are selected, creating a 68% window in the middle. The maximum difference of the nominal fit integral to the two selected results is taken as the statistical uncertainty. Only converging fits are considered, which in all but the very low statistics bins are all of the 1000 fits. The sampling method is illustrated in Figure 6.5, which depicts all fits to the ensemble of statistically varied distributions.

Improvements of the fit method

Several measures are taken to ensure that the fits adequately model the Gaussian core. First of all, the fit is only applied to the low-asymmetry bins, such that the non-Gaussian tails do not hinder the Gaussian fit. The size of the fit window w_c is determined via:

$$w_c = \mu_{\text{est}} + c_{\text{corr}} \times c_{\text{range}} \times \sigma_d, \tag{6.9}$$

where σ_d is the root mean square of the asymmetry distribution, c_{range} is the fit range factor, a global factor, which is set to 1.5, and c_{corr} is an $|\eta|$-dependent fit correction factor. The width of the Gaussian core and the shape of the tail differ from bin to bin. This makes it impossible to determine good fit results with the same fit window. The fit correction factor is set to $c_{\text{corr}} = 0.5$ for $|\eta| < 1.9$ and $c_{\text{corr}} = 1.0$ for $|\eta| \geq 1.9$ with a few exceptions, which

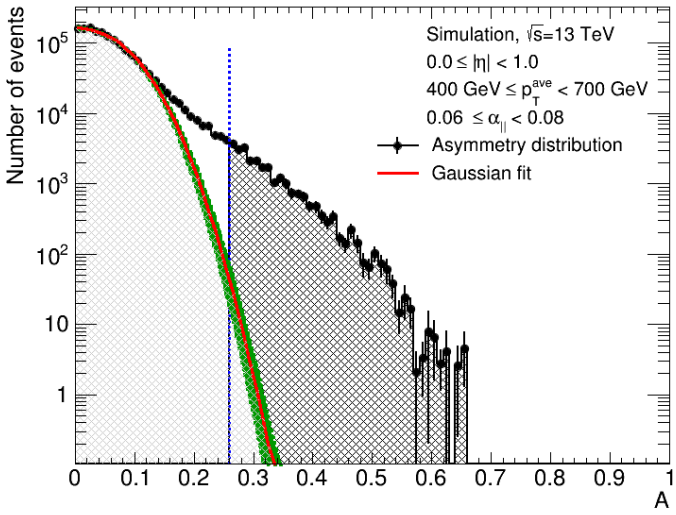

Figure 6.5: Asymmetry distribution (black dots and histogram) of simulated topocluster jets in the bin $|\eta| < 1.0$, 400 GeV $\leq p_T <$ 700 GeV, $0.06 \leq \alpha_{||} < 0.08$. Fits to the varied distributions obtained with the sampling method (green lines).

are discussed in Appendix A.2.3. The exceptions are determined empirically to ensure reliably converging fits.

Furthermore, suitable starting values for the two free fit parameters are chosen. The amplitude a of the Gaussian function starts as the maximum of the distribution.[3)] The width σ is empirically estimated to be 0.06. Finally, the parameters are restricted within reasonable limits. The amplitude can only take values between 0.1 and 7 times the maximum of the asymmetry distribution. These are generous limits and the fit routine has no problem to find the correct amplitude. The width σ is limited between 0.02 and 0.5.

As alluded to above, a high asymmetry region called the tail region is defined as having asymmetry values larger than the parameter x_{tr}, which is defined as:

$$x_{\text{tr}} = \mu_{\text{est}} + c_{\text{t,reg}} \cdot \sigma_d, \tag{6.10}$$

where $c_{\text{t,reg}}$ is a tail region factor and $c_{\text{t,reg}}$ is set to 2.5 as a result of the typical widths of tails, but other values could be reasonable, which is the source of a systematic uncertainty discussed in Section 6.5.

6.4.2 Extrapolation to pure dijet events

After the fraction of tail events is determined, the next step is the extrapolation $\alpha_{||} \to 0$. In this limit, the asymmetry distribution is the closest equivalent to the jet response because no additional jet activity affects the dijet event. Figure 6.6 shows the extrapolation of the tail fraction to the pure dijet event in the 250 GeV $\leq p_{\text{T}}^{\text{ave}} <$ 400 GeV, $|\eta| < 1.0$ bin.[4)] The corresponding

[3)] From Eq. 6.7 a maximum around $2a$ would be expected at least for low $\alpha_{||}$, but the fit routine has no trouble finding the correct amplitude regardless and the starting value is chosen for the sake of simplicity.

[4)] In Appendix A.2.4 extrapolations of tail fractions in different jet collections are compared.

fit function is:

$$f_{\text{tail}}(\alpha_{||}) = a_f \cdot \exp(b_f \cdot \alpha_{||}), \tag{6.11}$$

where a_f and b_f are the two fit parameters of the function. No special steps are necessary to perform this fit, and the tail fraction extrapolated to $\alpha_{||} = 0$ is the parameter $f_{\text{tail}}(0) = a_f$. The 68% confidence interval at $\alpha_{||} = 0$ is the statistical uncertainty, which is propagated to the next step. The result of this step is very sensitive to changes in the first $\alpha_{||}$ bins, but is not hugely affected by variations in the higher $\alpha_{||}$ bins. This observation could be interesting for further studies that might try a different binning.

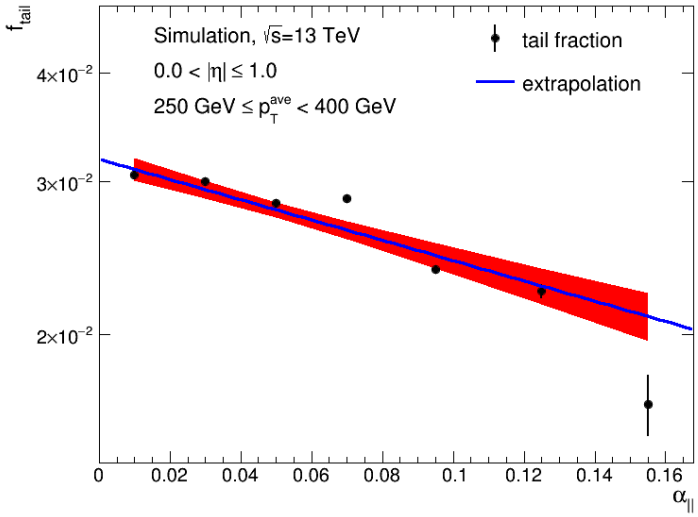

Figure 6.6: Tail fractions extrapolated to $\alpha_{||} = 0$ in the bin $|\eta| < 1.0$, 250 GeV $\leq p_{\text{T}}^{\text{ave}} <$ 400 GeV. The error bars around the data points result from the statistical uncertainty described above and the error band around the fit function is the 68% confidence interval of the fit.

6.5 Systematic uncertainties

Four contributions to the systematic uncertainty are considered:

- Tail region definition
- Non-multijet background contamination
- Jet momentum resolution
- Gaussian mean estimate

In each case the uncertainty is calculated by determining a varied result using either a modified dataset or some changed parameter. The difference between the varied and nominal results is then taken as the systematic uncertainty.

6.5.1 Tail region definition

The definition of the tail region in Eq. 6.10 with $c_{\mathrm{t,reg}} = 2.5$ is well-motivated from the shape of typical asymmetry distributions, but $c_{\mathrm{t,reg}}$ could take different values. Alternative values of 1.5 and 3.5 are tested, as illustrated in Figure 6.7. To gauge how much this choice affects the results, the study is repeated with the alternative definitions. The resulting uncertainty u_{tr} is calculated via:

$$u_{\mathrm{tr}} = \max(|\rho_{1.5} - \rho_{\mathrm{nom}}|, |\rho_{3.5} - \rho_{\mathrm{nom}}|), \tag{6.12}$$

where ρ_{nom} is the ratio of the extrapolated tail fractions of data and MC as defined in Eq. 6.6 with the notation ρ_{tail}. This is the nominal result, which can also be called $\rho_{2.5}$ analogous to $\rho_{1.5}$ and $\rho_{3.5}$, which are the extrapolated tail fractions from the tail region variation.

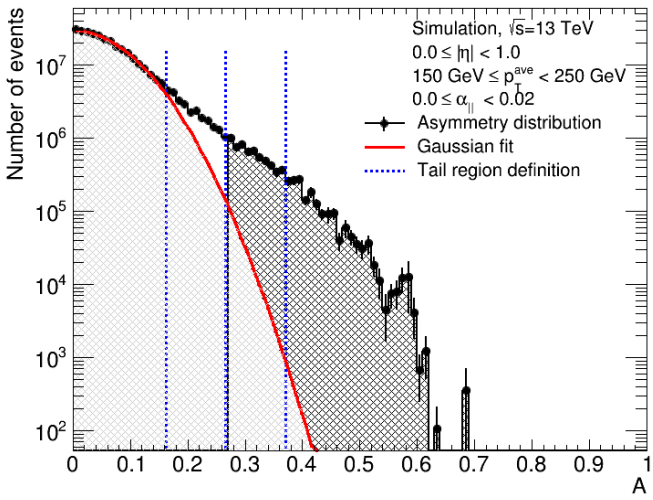

Figure 6.7: Asymmetry distribution (black dots and histogram) of particle flow jets in the bin $|\eta| < 1.0$, 150 GeV $\leq p_T <$ 250 GeV, $0.0 \leq \alpha_{||} < 0.02$. Gaussian fit (red line) and definitions of the tail regions (blue, dashed lines). The grey hashed area is identified as tail-like events in the nominal case.

6.5.2 Non-multijet background contamination

The examination of the non-multijet (non-QCD) background contamination is important because the MC used here does not simulate all of the physics processes contained in the data. For MC only multijet events are simulated and selected, since no other process is of interest for this study. In data, the events are pre-selected using the triggers listed in Table 5.3, before they are required to satisfy the same selection as MC events. This means that most of the events in the data sample are multijet events but not all of them. Some non-multijet processes can lead to events that are sufficiently similar to multijet events and pass both trigger and selection. Examples of this include $W \to \tau\nu$ events, where the τ decays hadronically, and $W \to \ell_{\mathrm{lost}}\nu$, where ℓ_{lost} is an electron or muon that is not identified.

The number of non-multijet events that meet the selection criteria can be estimated using the $W \to \ell\nu$ and $W \to \tau\nu$ background samples discussed in Section 5.3.2. This is illustrated in Figure 6.8.

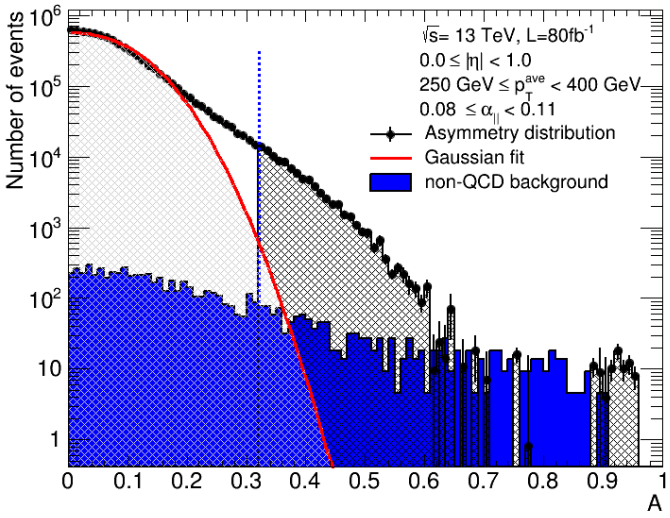

Figure 6.8: Asymmetry distribution (black dots and histogram) of particle flow jets in the bin $|\eta| < 1.0$, 250 GeV $\leq p_T <$ 400 GeV, $0.08 \leq \alpha_{||} < 0.11$. Gaussian fit (red line). Definition of the tail region (blue, dashed line). Non-multijet background (blue histogram).

The shape of the non-QCD background is different, non-Gaussian and has a higher tail fraction than multijet events. These simulated non-multijet events are subtracted from data. If the non-multijet simulation has more events in a bin than data, the number of entries in the bin is set to 0. The MC simulation cannot be trusted enough to take the dataset with the subtracted non-QCD background as corrected data and proceed. However, it is reasonable to assume that the simulation is good enough for us to derive a systematic uncertainty. To do so, the study is repeated with the new data asymmetry distributions that have their non-multijet content removed. The new extrapolated tail fraction $\rho_{\text{non-QCD}}$ is derived with the corrected data, leading to the systematic uncertainty $u_{\text{non-QCD}}$, which is defined as:

$$u_{\text{non-QCD}} = |\rho_{\text{nom}} - \rho_{\text{non-QCD}}|. \tag{6.13}$$

6.5.3 Jet momentum resolution

A jet smearing is incorporated to account for jets being slightly misreconstructed, as it is done in the R+S method discussed in Section 5.5.4. In ATLAS, jets in the p_{T} range considered in the study have a p_{T} resolution of up to 10%. This means that the true jet transverse momentum can be over- or underestimated by up to 10%. In order to account for this, the p_{T} of the reconstructed jets is varied up and down by 10% of the difference between the p_{T} of the reconstructed and the matched truth jet using:

$$\begin{aligned} p_{\text{T,smear}} &= p_{\text{T,reco}} - 0.1 \cdot (p_{\text{T,true}} - p_{\text{T,reco}}), \\ p_{\text{T,smear}} &= p_{\text{T,reco}} + 0.1 \cdot (p_{\text{T,true}} - p_{\text{T,reco}}). \end{aligned} \tag{6.14}$$

As a result two additional MC samples are generated: one in which the reconstructed jet p_T is smeared upward and another in which it is smeared downward. The truth matching is done by selecting the three leading jets and matching them to the closest generator-level jet in ΔR.

The study is repeated with the additional samples, which leads to more extrapolated tail fractions $\rho_{\text{res,up}}$ and $\rho_{\text{res,down}}$. The contribution to the systematic uncertainty u_{res} is calculated in an equation analogous to Eq. 6.12:

$$u_{\text{res}} = \max(|\rho_{\text{res,up}} - \rho_{\text{nom}}|, |\rho_{\text{res,down}} - \rho_{\text{nom}}|). \tag{6.15}$$

This estimate of the jet resolution uncertainty derived from a global upper limit on the jet p_{T} resolution is conservative. It might be better to do this estimation taking into account the differing jet resolutions depending on the jet p_{T}. This would also make use of the fact that the jet resolution in particle flow jets is better for intermediate p_{T}. However, the implementation would require further testing to make sure that the uncertainty is not underestimated, which is the reason why the conservative approach is used here.

6.5.4 Gaussian mean estimate

Finally, the estimate of the mean of the Gaussian core is connected to an uncertainty. According to Eq. 6.8, the estimate $\mu_{\text{est}} = \alpha_{||}^{*}/2$ is used. Here, $\alpha_{||}^{*}$ is the centre of the $\alpha_{||}$-bin. The approximation is justified with studies presented in Appendix A.2.1.

However, the width of the bin is non-vanishing and all $\alpha_{||}$ values have to be considered in the estimate to avoid bias. To do so, $\alpha_{||}^{*}$ is varied according to the width of the bin. Both at the upper and lower edge of the $\alpha_{||}$-bin a different fit result is obtained. The maximum difference between either of these two fit results and the nominal result is used to scale up the statistical uncertainty of the fit integral in each p_T-$|\eta|$ bin. With this new statistical uncertainty the normal procedure is followed, calculating the extrapolated tail fraction and the varied asymmetry tail factor ρ_{μ}. The last contribution to the systematic uncertainty is determined as:

$$u_{\mu} = |\rho_{\mu} - \rho_{\text{nom}}|. \tag{6.16}$$

In this method of estimating the last contribution to the systematic uncertainty, no assumptions are made about the shape of the $\alpha_{||}$ distribution inside one bin. It serves as an upper estimate independent of the general behaviour of $\alpha_{||}$. Regardless, $\alpha_{||}$ distributions are studied and are presented in Appendix A.2.2.

6.6 Results

Combining the definition of ρ_{tail} in Eq. 6.6 and taking the limit $\alpha_{||} \to 0$ in Eq. 6.11 the asymmetry tail factors are determined from the extrapolation with:

$$\rho_{\text{tail}} = \frac{f_{\text{tail}}^{\text{data}}(\alpha_{||} \to 0)}{f_{\text{tail}}^{\text{MC}}(\alpha_{||} \to 0)} = \frac{a_f^{\text{data}}}{a_f^{\text{MC}}}. \tag{6.17}$$

This is done for every bin in $p_{\text{T}}^{\text{ave}}$ and $|\eta|$ that is considered in the study. Figure 6.9 shows the asymmetry tail factors for particle flow and topocluster jets in all bins. The breakdown of the systematic uncertainties is depicted in each of the bottom plots. Overall, the asymmetry tail factors are compatible with 1, from which it is concluded that the tails of the jet response are well simulated and that there is no systematic over- or underestimation of the tail sizes. If the

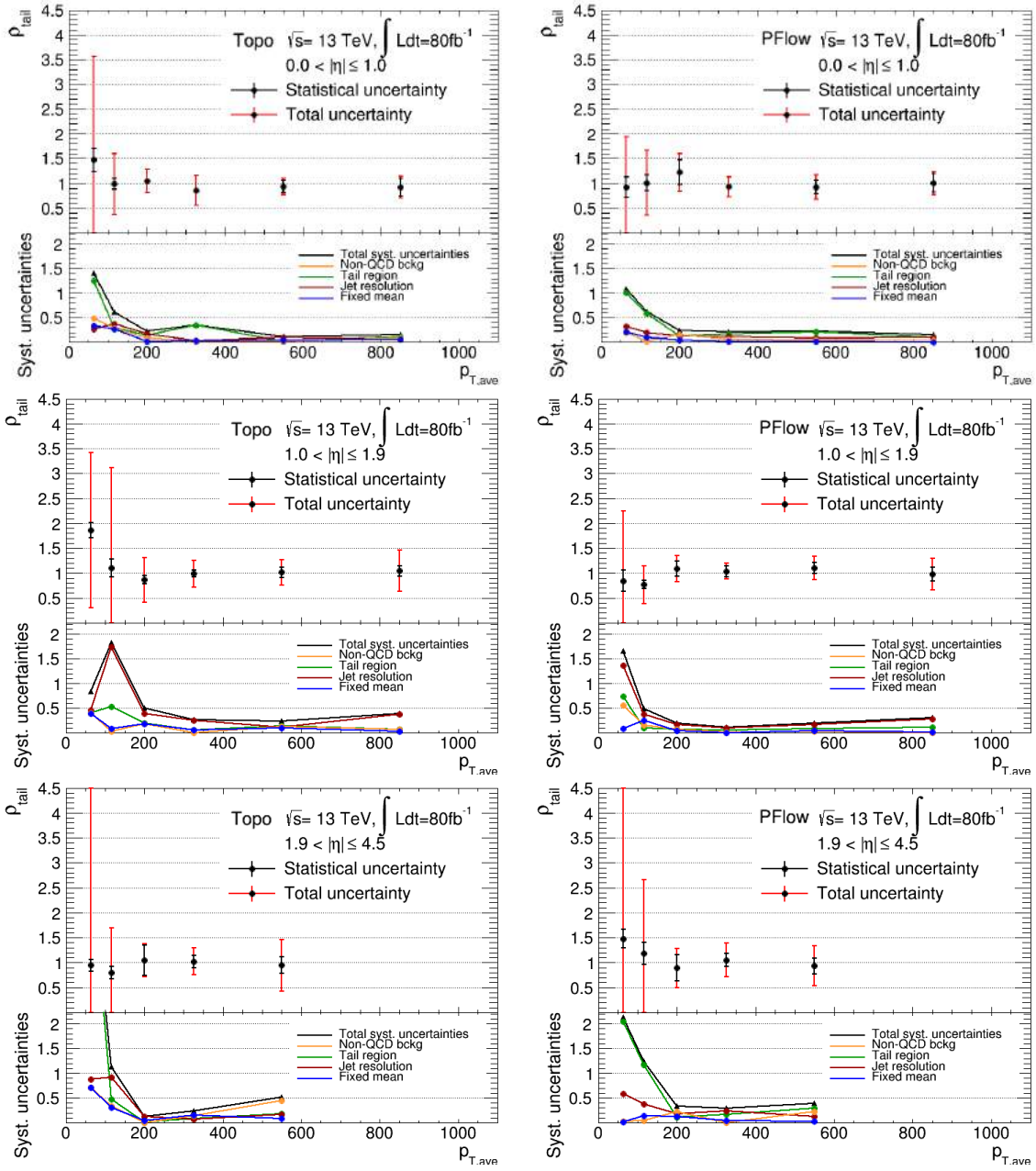

Figure 6.9: Asymmetry tail factors that are derived using 80 fb^{-1} of multijet data (top plots). Total systematic uncertainty and contributions to the systematic uncertainties (bottom plots). Topocluster jets (left) and particle flow jets (right). For forward jets at high $p_{\mathrm{T}}^{\mathrm{ave}}$ (> 700 GeV) there is not enough statistics to obtain useful results.

asymmetry tail factors were significantly different from 1, it might be necessary to introduce a correction factor to correct for effects that are not well understood.

The asymmetry tail factors together with the various uncertainty contributions are also listed in Table 6.2–6.7. The uncertainty contributions $u_{\text{non-QCD}}$, u_{tr}, u_{res} and u_{μ} are defined in Eq. 6.13, Eq. 6.12, Eq. 6.15 and Eq. 6.16. The statistical uncertainty and the quadratic sum of all systematic uncertainties are u_{stat} and $u_{\text{sys,total}}$, respectively. The combined uncertainty is u_{total}. Note that the uncertainties in the table are absolute, while systematic uncertainties in the bottom panels of Figure 6.9 are relative uncertainties.

Table 6.2: Asymmetry tail factors and uncertainties for central ($0.0 < |\eta| \leq 1.0$) topocluster jets.

p_{T}-bin [GeV]	ρ_{tail}	u_{stat}	$u_{\text{non-QCD}}$	u_{tr}	u_{res}	u_{μ}	$u_{\text{sys,total}}$	u_{total}
45 – 80	1.48	0.24	0.71	1.84	0.39	0.50	2.07	2.09
80 – 150	0.99	0.11	0.28	0.29	0.37	0.25	0.60	0.61
150 – 250	1.04	0.03	0.08	0.14	0.17	0.01	0.23	0.24
250 – 400	0.86	0.05	0.01	0.30	0.03	0.03	0.30	0.30
400 – 700	0.93	0.13	0.01	0.02	0.09	0.03	0.10	0.16
700 – 1000	0.92	0.18	0.07	0.10	0.05	0.05	0.14	0.23

Table 6.3: Asymmetry tail factors and uncertainties for intermediate ($1.0 < |\eta| \leq 1.9$) topocluster jets.

p_{T}-bin [GeV]	ρ_{tail}	u_{stat}	$u_{\text{non-QCD}}$	u_{tr}	u_{res}	u_{μ}	$u_{\text{sys,total}}$	u_{total}
45 – 80	1.86	0.15	0.74	0.75	0.86	0.73	1.55	1.55
80 – 150	1.11	0.18	0.04	0.59	1.92	0.10	2.01	2.01
150 – 250	0.86	0.08	0.16	0.17	0.33	0.16	0.44	0.44
250 – 400	0.99	0.07	0.00	0.06	0.25	0.05	0.26	0.27
400 – 700	1.01	0.10	0.13	0.14	0.11	0.10	0.24	0.26
700 – 1000	1.04	0.10	0.08	0.07	0.39	0.03	0.41	0.42

At high transverse momenta ($p_{\text{T}}^{\text{ave}} > 250$ GeV) the asymmetry tail factors including their uncertainties are well constrained between 0.6 and 1.4. At low transverse momenta the systematic uncertainties are dominant. Especially the uncertainty coming from the tail region definition is a large contributor. This can be understood with a look at Figure 6.10: At low $p_{\text{T}}^{\text{ave}}$ the asymmetry distributions are very wide and the Gaussian core is hard to distinguish from the tails. As can be seen from Eq. 6.10, the three different tail region definitions that are considered to estimate the systematic uncertainty drift further apart as the width of the distribution σ_d increases. Thus the contribution to the systematic uncertainties captures the difficulty in identifying the correct tail region.

Another big contributor at low $p_{\text{T}}^{\text{ave}}$ is the jet resolution uncertainty. Again this can be understood, looking at low-$p_{\text{T}}^{\text{ave}}$ asymmetry distributions. The width of the distribution and thus

Table 6.4: Asymmetry tail factors and uncertainties for forward ($1.9 < |\eta| \leq 4.5$) topocluster jets. For forward jets at high $p_{\mathrm{T}}^{\mathrm{ave}}$ (> 700 GeV) there is not enough statistics to obtain useful results.

p_{T}-bin [GeV]	ρ_{tail}	u_{stat}	$u_{\mathrm{non-QCD}}$	u_{tr}	u_{res}	u_{μ}	$u_{\mathrm{sys,total}}$	u_{total}
$45-80$	0.95	0.12	0.67	5.25	0.83	0.67	5.40	5.40
$80-150$	0.79	0.12	0.26	0.37	0.73	0.24	0.89	0.90
$150-250$	1.05	0.30	0.00	0.02	0.12	0.05	0.13	0.33
$250-400$	1.02	0.12	0.13	0.09	0.07	0.16	0.24	0.27
$400-700$	0.94	0.16	0.43	0.17	0.16	0.08	0.49	0.52

Table 6.5: Asymmetry tail factors and uncertainties for central ($0.0 < |\eta| \leq 1.0$) particle flow jets.

p_{T}-bin [GeV]	ρ_{tail}	u_{stat}	$u_{\mathrm{non-QCD}}$	u_{tr}	u_{res}	u_{μ}	$u_{\mathrm{sys,total}}$	u_{total}
$45-80$	0.92	0.20	0.18	0.92	0.30	0.20	1.00	1.02
$80-150$	1.01	0.16	0.02	0.59	0.20	0.09	0.63	0.65
$150-250$	1.22	0.25	0.19	0.15	0.15	0.05	0.29	0.38
$250-400$	0.93	0.04	0.05	0.16	0.10	0.01	0.19	0.20
$400-700$	0.92	0.13	0.04	0.19	0.08	0.02	0.21	0.25
$700-1000$	1.01	0.18	0.04	0.10	0.10	0.01	0.15	0.24

the width of the jet response is larger. Slightly mismeasured jets end up in the tail region more often and the impact on the asymmetry tail factors is higher than in other $p_{\mathrm{T}}^{\mathrm{ave}}$ bins. This can be seen when comparing the low-$p_{\mathrm{T}}^{\mathrm{ave}}$ asymmetry distribution in Figure 6.2 with higher $p_{\mathrm{T}}^{\mathrm{ave}}$ bins that are shown in Figure 6.3 and Figure 6.5. The p_{T} resolution as a function of p_{T} is also shown in Figure 4.12, which affirms the observation.

In the forward region at high $p_{\mathrm{T}}^{\mathrm{ave}}$ (> 700 GeV) statistics become a limiting factor. At low $p_{\mathrm{T}}^{\mathrm{ave}}$ the systematic uncertainties become so large that no reliable statement about the asymmetry tail factor can be made, since the usual effects at low $p_{\mathrm{T}}^{\mathrm{ave}}$ are even more prevalent.

The impact of the non-multijet background and mean estimate on the systematic uncertainties is negligible in most bins.

Finally, there is no significant difference between the asymmetry tail factors in particle flow and topocluster jets. The advantages of particle flow jets discussed in Chapter 3 still persist and it is important to know that there is no problem with the simulation of the tails that would challenge the decision of transitioning the analysis to particle flow jets.

Comparing the sizes of the non-Gaussian tails between the jet collections with the method described above is not very meaningful, since the definition of the tail region in Eq. 6.10 depends on the width of the distributions. This width, which is roughly proportional to the jet energy resolution according to Eq. 6.2, differs between jet collections. Further understanding of all the processes that cause non-Gaussian tails could help model them and make such a comparison possible in the future.

Table 6.6: Asymmetry tail factors and uncertainties for intermediate ($1.0 < |\eta| \leq 1.9$) particle flow jets.

p_T-bin [GeV]	ρ_{tail}	u_{stat}	$u_{non-QCD}$	u_{tr}	u_{res}	u_{μ}	$u_{sys,total}$	u_{total}
45 – 80	0.84	0.21	0.47	0.62	1.15	0.07	1.39	1.40
80 – 150	0.77	0.08	0.12	0.08	0.29	0.19	0.37	0.38
150 – 250	1.09	0.15	0.07	0.08	0.18	0.04	0.21	0.26
250 – 400	1.04	0.11	0.02	0.06	0.10	0.00	0.12	0.16
400 – 700	1.10	0.11	0.02	0.08	0.18	0.04	0.21	0.24
700 – 1000	0.98	0.14	0.00	0.11	0.27	0.02	0.29	0.32

Table 6.7: Asymmetry tail factors and uncertainties for forward ($1.9 < |\eta| \leq 4.5$) particle flow jets. For forward jets at high p_T^{ave} (> 700 GeV) there is not enough statistics to obtain useful results.

p_T-bin [GeV]	ρ_{tail}	u_{stat}	$u_{non-QCD}$	u_{tr}	u_{res}	u_{μ}	$u_{sys,total}$	u_{total}
45 – 80	1.48	0.19	0.04	3.02	0.86	0.03	3.14	3.15
80 – 150	1.19	0.22	0.04	1.38	0.45	0.16	1.46	1.48
150 – 250	0.89	0.26	0.20	0.10	0.16	0.10	0.30	0.40
250 – 400	1.05	0.13	0.00	0.18	0.24	0.05	0.31	0.33
400 – 700	0.93	0.16	0.21	0.27	0.11	0.03	0.36	0.40

6.6.1 Application in the analysis

As mentioned in Section 5.5.4, the non-Gaussian tails of asymmetry distributions are studied to get a measure of the goodness of jet response templates, which are used to estimate the multijet background in the search for invisible decays of the Higgs boson produced in vector-boson fusion. Trust in the modelling of the tails is translated into a systematic uncertainty, which is determined by scaling up the tails in the response templates and repeating the multijet estimate with the new varied jet response template. The difference between the varied and nominal result is taken as the systematic uncertainty. In the study of non-Gaussian tails of jet response distributions performed with 36.1 fb^{-1} of data the tail scaling factor were between 0.5 and 1.5 at high p_T where the signal is expected. Thus the tails of jet response templates were scaled by 50% to determine the results in Table 5.5. Now with 80 fb^{-1} the asymmetry tail scaling factors lie between 0.6 and 1.4, which should improve the multijet estimate.

6.7 Alternative methods

Other methods of testing the simulation of non-Gaussian tails were considered. One proposed method is to use Z + jet events instead of multijet events. An example for such a production mechanism is depicted in Figure 6.11. In this case, the plan involves reconstructing and tagging a Z boson using its leptonic decay products to probe the leading jet in the event.The uncertainty

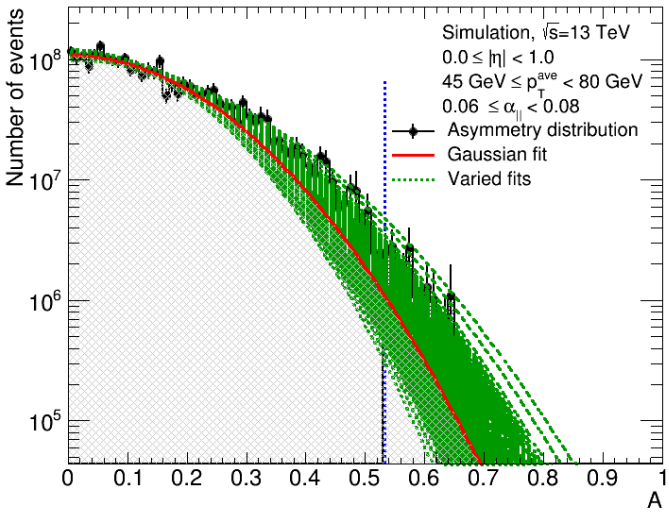

Figure 6.10: Asymmetry distribution (black dots and histogram) of particle flow jets in the bin $|\eta| < 1.0$, 45 GeV $\leq p_T <$ 80 GeV, $0.06 \leq \alpha_{||} < 0.08$. Gaussian fit (red line) and definition of the tail regions (blue, dashed lines). Fits to varied distributions obtained with the sampling method (green lines).

from the measurement of Z bosons is negligible because they are measured precisely by reconstructing their charged leptonic decay products [143]. Instead of an asymmetry a response $\mathscr{R}_Z$ is defined as:

$$\mathscr{R}_Z = \frac{p_{\mathrm{T,j1}}}{p_{\mathrm{T},Z}}. \tag{6.18}$$

Therefore, $\mathscr{R}_Z$ is the equivalent of the jet response $p_T^{\mathrm{reco}}/p_T^{\mathrm{truth}}$ with the Z boson momentum acting as the stand-in for the truth jet momentum. This definition offers an interesting advantage over the multijet method above. The asymmetry stops being strictly positive, which allows the separate analysis of high and low response tails. Furthermore, it would be easier to probe the forward region, since the requirement for both analysis objects to be in the same $|\eta|$-bin is no longer necessary.

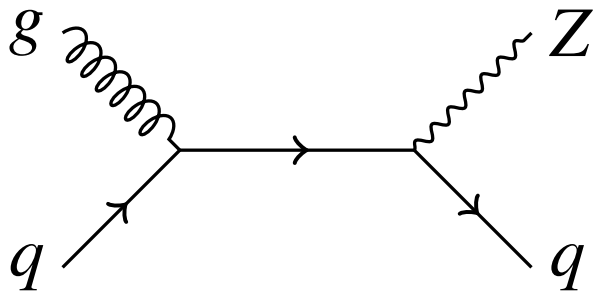

Figure 6.11: Example diagram of Z boson production in association with a quark jet.

The same can be done with γ + jet events, using photons to probe the jet response. Like Z bosons photons are also measured precisely [143]. Both approaches have a problem with statistics compared with the multijet method.[5)] This means that a boson + jet analysis would require larger bins to deliver good enough response distributions that would lead to smooth fits. As the study examines small tails in extreme phase space regions, the importance of good statistics cannot be understated. However, this is also a chance for the future. As larger MC samples are generated and ATLAS records more data, it is worth revisiting this approach to gain a greater understanding of the jet response.

Both γ + jet and Z + jet are also used for the calibration of the jet energy scale in ATLAS [143] as discussed in Section 4.1.5. They are limited to a p_{T} range with sufficient statistics with $36 < p_{\mathrm{T}} < 950$ GeV for γ + jet and $20 < p_{\mathrm{T}} < 500$ GeV for Z + jet. This range would be even more restrictive when studying response tails because only a small portion of events end up in this region. However, as the results above showed, the dijet asymmetry method has an especially high precision at high p_{T}, while Z/γ + jet does well at low p_{T}. Together with the advantages in the forward region this makes this alternative complementary to the method described above. It might therefore be interesting to use both approaches in the future, relying on each in different ranges of p_{T} and $|\eta|$.

Another consideration is to replace the variable $\alpha_{||}$ defined in Eq. 6.4 with a new variable α_{MET} defined as:

$$\begin{aligned} \alpha_{\mathrm{MET}} &= \frac{\vec{E}^{\mathrm{miss}}_{\mathrm{T,j_3}} \cdot \hat{p}_{\mathrm{T},jj}}{p^{\mathrm{ave}}_{\mathrm{T}}}, \\ \vec{E}^{\mathrm{miss}}_{\mathrm{T,j_3}} &= \vec{E}^{\mathrm{miss,soft}}_{\mathrm{T}} + \sum_{i=3}^{N} \vec{p}_{\mathrm{T,j_i}}, \end{aligned} \tag{6.19}$$

where $\hat{p}_{\mathrm{T},jj}$ is defined in Eq. 6.3 and N is the number of jets in the event. Therefore, $\vec{E}^{\mathrm{miss}}_{\mathrm{T,j_3}}$ is an $E^{\mathrm{miss}}_{\mathrm{T}}$ definition that contains all objects that could cause a recoil to the dijet event. Where with $\alpha_{||}$ the influence of missing transverse energy and additional jets beyond the third jet on asymmetry distributions is unclear, α_{MET} includes them in the definition. Therefore, narrower peaks and a more clear mean shift effect are expected. That said, the next-to-next-to-leading jet is the main cause of the recoil and the results are not expected to change by a large amount.

[5)] This is well illustrated in Appendix A.1.2 where the multijet samples are listed with statistics on the order of mb and $Z \to \mu\mu$ samples on the order of pb.

Chapter 7

Conclusion and outlook

Several astrophysical observations are consistent with the existence of dark matter (DM), a new type of matter that is not part of the Standard Model of particle physics (SM). This demands new theories of particle physics that include an explanation for this phenomenon. Other open questions of the SM serve as a motivation for finding new models as well.

So far no interaction between SM particles and DM has been observed in particle physics experiments. However, the newly discovered Higgs boson may be a window into this dark world because multiple models beyond the SM predict a coupling between the boson and DM candidates. Some of them even suggest that an observation of such a coupling is accessible to modern methods of detection. However, in colliders, DM itself cannot be detected directly with current state-of-the-art particle detectors and would therefore appear as invisible particles.

With this main motivation in mind, a search for invisible decays of the Higgs boson produced in vector-boson fusion is performed using 36.1 fb^{-1} of proton–proton collision data recorded at $\sqrt{s} = 13$ TeV with the ATLAS detector and presented in this work. The decay process leads to two well-separated jets and missing transverse energy in the final state. As a result the dominant backgrounds are Z bosons decaying into neutrinos and leptonically decaying W bosons where the charged lepton escapes detection. The multijet background is small but especially challenging to estimate.

The multijet background of the search for invisible decays of the Higgs boson results from rare extreme mismeasurements to a large extent. These are in the phase space characterized as the tails of jet response distributions. To understand how well these tails are simulated a study is performed using data recorded with the ATLAS detector in proton–proton collisions at $\sqrt{s} = 13$ TeV. In the study the cores of the distributions are modelled using Gaussian fits in order to quantify the non-Gaussian tails. With an extrapolation to events with exactly two jets in the final state the dijet balance is studied to gain insight into random mismeasurements with data events.

The results are compatible with a simulation that quantitatively describes the non-Gaussian tails well. Including statistical and systematic uncertainties the data-to-simulation ratios lie between 0.6 and 1.4 for jets with $p_{\text{T}} > 250$ GeV jets. This result is used to derive a systematic uncertainty on the multijet background. The result is relevant to all other ATLAS analyses using jets in areas of extreme mismeasurement.

The two dominant systematic uncertainties of the study are the jet energy resolution and the definition of a tail region. The latter can potentially be lessened in the future by not only

modelling the core of the distributions with a fit but also the tails. In order to access low-p_{T} jets with a higher precision the use of Z + jets and photons + jets events in addition to dijet events is potentially useful.

Among the limiting factors on the sensitivity of the search are the systematic uncertainties. Two of the most dominant ones are the jet energy scale and the jet energy resolution uncertainty. Both jet energy scale and resolution are improved with the jet calibration, which contains several steps. One of them is the global sequential calibration (GSC), a simulation-driven technique that is presented in this thesis. The calibration improves the resolution of jets by removing the dependence of the jet transverse momentum on a selection of detector level variables. The GSC is performed with a simulation of proton–proton collisions that are recorded with the ATLAS detector at a centre-of-mass energy of $\sqrt{s} = 13$ TeV using proton beams provided by the LHC. The results were validated in data. Through the GSC the jet resolution is improved by up to 20%, leading to a resolution of 10% or less for jets with $p_{\mathrm{T}} > 100$ GeV. As a result of improvements in the jet calibration including the GSC the study of non-Gaussian tails should improve in the future.

The search for invisible decays of the Higgs boson is performed with a maximum likelihood fit, in which control regions are defined to constrain the background estimate from simulation with data events. No excess above the SM prediction is found. Therefore, an observed (expected) limit is set on the branching fraction for the Higgs boson to decay invisibly at 0.37 (0.28) at 95% confidence level. The results are interpreted in a Higgs portal model, setting limits on the DM candidate-nucleon cross-sections between 10^{-46} cm^2 and 10^{-42} cm^2 at 90% confidence level. The limit depends on the mass and spin of the DM candidate. The former varies between 1 GeV and 70 GeV.

Future iterations of the search for invisible decays of the Higgs boson are expected to profit from a better jet energy resolution provided by improvements of the GSC. Advancements in the modelling of tails of jet response distributions are similarly expected to affect the results. In an effort to improve the jet reconstruction a new jet definition called particle flow jets has recently been added and one important result of the GSC is the ability to compare fully calibrated particle flow jets with other jet reconstruction methods. Particle flow jets compare well with other jet reconstruction methods with advantages at low to intermediate p_{T}. Even without these improvements first projections predict the limit to improve down to 0.13 when the LHC is expected to achieve very large data rates in a phase called the high-luminosity LHC.

Finally, the search for invisible decay products of Higgs bosons resulted in constraints on models that predict DM candidates and is therefore helpful in guiding theorists that seek to refine these models.

Appendix A

Appendix

A.1 Simulated samples

The topic of this appendix is a list of all MC samples used in the analyses described in the previous chapters. Section A.1.1 contains the simulated samples that are used in the GSC part of the 2016 Jet calibration. The MC samples used in the search for invisible decays of the Higgs boson are listed in Section A.1.2. Each of the tables listing simulated samples also lists their cross-section, filter efficiency and k-factor (See Section 3.4.3 for more details.).

A.1.1 Global sequential calibration

Table A.1: Simulated multijet samples used for the global sequential calibration. All samples were simulated using `Pythia` 8.

Process (slice)	MC ID	Cross-section [mb]	K-factor	Filter efficiency
Multijet (JZ0W)	361020	78.420	1	0.97550
Multijet (JZ1W)	361021	78.420	1	0.00067198
Multijet (JZ2W)	361022	2.433	1	0.00033264
Multijet (JZ3W)	361023	0.026454	1	0.00031963
Multijet (JZ4W)	361024	2.54630×10^{-4}	1	0.00052982
Multijet (JZ5W)	361025	4.553×10^{-6}	1	0.00092255
Multijet (JZ6W)	361026	2.57530×10^{-7}	1	0.00094016
Multijet (JZ7W)	361027	1.6215×10^{-8}	1	0.00039282
Multijet (JZ8W)	361028	6.25030×10^{-10}	1	0.010176
Multijet (JZ9W)	361029	1.9617×10^{-11}	1	0.012092
Multijet (JZ10W)	361030	1.196×10^{-12}	1	0.0058935
Multijet (JZ11W)	361031	4.2259×10^{-14}	1	0.0027015
Multijet (JZ12W)	361032	1.037×10^{-15}	1	0.00042592

A.1.2 Search for invisible decays of the Higgs boson

The strong-produced V + jets samples are generated in slices of MAXHTPTV, which is the maximum of the transverse momentum of the vector boson p_{T}^{V} and H_{T}, the scalar sum of all the momenta of objects in the event. The samples are further subdivided by applying orthogonal c- and b-quark filters. This has the effect of generating inclusive samples.

Table A.2: Simulated samples of strong $Z \to \nu\nu$ production. All samples were simulated using `Sherpa` 2.2.1.

Process	MC ID	Cross-section [pb]	K-factor	Filter efficiency
MAXHTPTV 0-70 CVetoBVeto	364142	10700	0.9728	0.8216
MAXHTPTV 0-70 CFilterBVeto	364143	10702	0.9728	0.11123
MAXHTPTV 0-70 BFilter	364144	10709	0.9728	0.066175
MAXHTPTV 70-140 CVetoBVeto	364145	603.23	0.9728	0.68924
MAXHTPTV 70-140 CFilterBVeto	364146	608.15	0.9728	0.18243
MAXHTPTV 70-140 BFilter	364147	603.32	0.9728	0.11955
MAXHTPTV 140-280 CVetoBVeto	364148	222.28	0.9728	0.60735
MAXHTPTV 140-280 CFilterBVeto	364149	221.88	0.9728	0.22527
MAXHTPTV 140-280 BFilter	364150	222.4	0.9728	0.15103
MAXHTPTV 280-500 CVetoBVeto	364151	47.375	0.9728	0.55887
MAXHTPTV 280-500 CFilterBVeto	364152	47.397	0.9728	0.26201
MAXHTPTV 280-500 BFilter	364153	47.476	0.9728	0.17514
MAXHTPTV 500-1000	364154	9.9099	0.9728	1
MAXHTPTV 1000_E_CMS	364155	0.81809	0.9728	1

The study of non-Gaussian tails in jet response distributions uses only the subset of slices listed in Table A.12 in contrast to the full 13 multijet slices listed in Table A.11 because it only focuses on a certain $p_{\mathrm{T}}^{\mathrm{ave}}$ range.

Table A.3: Simulated samples of strong $Z \to \mu\mu$ production. All samples were simulated using Sherpa 2.2.1.

Process	MC ID	Cross-section [pb]	K-factor	Filter efficiency
MAXHTPTV 0-70 CVetoBVeto	364100	1983	0.9751	0.8221
MAXHTPTV 0-70 CFilterBVeto	364101	1978.4	0.9751	0.11308
MAXHTPTV 0-70 BFilter	364102	1982.2	0.9751	0.064161
MAXHTPTV 70-140 CVetoBVeto	364103	108.92	0.9751	0.68873
MAXHTPTV 70-140 CFilterBVeto	364104	109.42	0.9751	0.18596
MAXHTPTV 70-140 BFilter	364105	108.91	0.9751	0.11375
MAXHTPTV 140-280 CVetoBVeto	364106	39.878	0.9751	0.60899
MAXHTPTV 140-280 CFilterBVeto	364107	39.795	0.9751	0.23308
MAXHTPTV 140-280 BFilter	364108	39.908	0.9751	0.23308
MAXHTPTV 280-500 CVetoBVeto	364109	8.5375	0.9751	0.55906
MAXHTPTV 280-500 CFilterBVeto	364110	8.5403	0.9751	0.26528
MAXHTPTV 280-500 BFilter	364111	8.4932	0.9751	0.17559
MAXHTPTV 500-1000	364112	1.7881	0.9751	1
MAXHTPTV 1000_E_CMS	364113	0.14769	0.9751	1

Table A.4: Simulated samples of strong $Z \to ee$ production. All samples were simulated using Sherpa 2.2.1.

Process	MC ID	Cross-section [pb]	K-factor	Filter efficiency
MAXHTPTV 0-70 CVetoBVeto	364114	1981.8	0.9751	0.82106
MAXHTPTV 0-70 CFilterBVeto	364115	1980.8	0.9751	0.11295
MAXHTPTV 0-70 BFilter	364116	1981.7	0.9751	0.063809
MAXHTPTV 70-140 CVetoBVeto	364117	110.5	0.9751	0.69043
MAXHTPTV 70-140 CFilterBVeto	364118	110.63	0.9751	0.18382
MAXHTPTV 70-140 BFilter	364119	110.31	0.9751	0.11443
MAXHTPTV 140-280 CVetoBVeto	364120	40.731	0.9751	0.61452
MAXHTPTV 140-280 CFilterBVeto	364121	40.67	0.9751	0.23044
MAXHTPTV 140-280 BFilter	364122	40.694	0.9751	0.14927
MAXHTPTV 280-500 CVetoBVeto	364123	8.6743	0.9751	0.56134
MAXHTPTV 280-500 CFilterBVeto	364124	8.6711	0.9751	0.26294
MAXHTPTV 280-500 BFilter	364125	8.6766	0.9751	0.17223
MAXHTPTV 500-1000	364126	1.8081	0.9751	1
MAXHTPTV 1000_E_CMS	364127	0.14857	0.9751	1

Table A.5: Simulated samples of strong $Z \to \tau\tau$ production. All samples were simulated using Sherpa 2.2.1.

Process	MC ID	Cross-section [pb]	K-factor	Filter efficiency
MAXHTPTV 0-70 CVetoBVeto	364128	1981.6	0.9751	0.82142
MAXHTPTV 0-70 CFilterBVeto	364129	1978.8	0.9751	0.11314
MAXHTPTV 0-70 BFilter	364130	1981.8	0.9751	0.064453
MAXHTPTV 70-140 CVetoBVeto	364131	110.37	0.9751	0.68883
MAXHTPTV 70-140 CFilterBVeto	364132	110.51	0.9751	0.1829
MAXHTPTV 70-140 BFilter	364133	110.87	0.9751	0.110886
MAXHTPTV 140-280 CVetoBVeto	364134	40.781	0.9751	0.60821
MAXHTPTV 140-280 CFilterBVeto	364135	40.74	0.9751	0.22897
MAXHTPTV 140-280 BFilter	364136	40.761	0.9751	0.13442
MAXHTPTV 280-500 CVetoBVeto	364137	8.5502	0.9751	0.56036
MAXHTPTV 280-500 CFilterBVeto	364138	8.6707	0.9751	0.26245
MAXHTPTV 280-500 BFilter	364139	8.6804	0.9751	0.17313
MAXHTPTV 500-1000	364140	1.8096	0.9751	1
MAXHTPTV 1000_E_CMS	364141	0.14834	0.9751	1

Table A.6: Simulated samples of strong $W \to e\nu$ production. All samples were simulated using Sherpa 2.2.1.

Process	MC ID	Cross-section [pb]	K-factor	Filter efficiency
MAXHTPTV 0-70 CVetoBVeto	364170	19127	0.9702	0.82447
MAXHTPTV 0-70 CFilterBVeto	364171	19130	0.9702	0.1303
MAXHTPTV 0-70 BFilter	364172	19135	0.9702	0.044141
MAXHTPTV 70-140 CVetoBVeto	364173	942.58	0.9702	0.66872
MAXHTPTV 70-140 CFilterBVeto	364174	945.67	0.9702	0.22787
MAXHTPTV 70-140 BFilter	364175	945.15	0.9702	0.10341
MAXHTPTV 140-280 CVetoBVeto	364176	339.81	0.9702	0.59691
MAXHTPTV 140-280 CFilterBVeto	364177	339.87	0.9702	0.28965
MAXHTPTV 140-280 BFilter	364178	339.79	0.9702	0.10898
MAXHTPTV 280-500 CVetoBVeto	364179	72.084	0.9702	0.54441
MAXHTPTV 280-500 CFilterBVeto	364180	72.128	0.9702	0.31675
MAXHTPTV 280-500 BFilter	364181	72.113	0.9702	0.13391
MAXHTPTV 500-1000	364182	15.224	0.9702	1
MAXHTPTV 1000_E_CMS	364183	1.2334	0.9702	1

Table A.7: Simulated samples of strong $W \to \mu\nu$ production. All samples were simulated using Sherpa 2.2.1.

Process	MC ID	Cross-section [pb]	K-factor	Filter efficiency
MAXHTPTV 0-70 CVetoBVeto	364156	19143	0.9702	0.82380
MAXHTPTV 0-70 CFilterBVeto	364157	19121	0.9702	0.1303
MAXHTPTV 0-70 BFilter	364158	19135	0.9702	0.044141
MAXHTPTV 70-140 CVetoBVeto	364159	944.85	0.9702	0.67463
MAXHTPTV 70-140 CFilterBVeto	364160	937.78	0.9702	0.23456
MAXHTPTV 70-140 BFilter	364161	944.63	0.9702	0.075648
MAXHTPTV 140-280 CVetoBVeto	364162	339.54	0.9702	0.9702
MAXHTPTV 140-280 CFilterBVeto	364163	340.06	0.9702	0.28947
MAXHTPTV 140-280 BFilter	364164	339.54	0.9702	0.10872
MAXHTPTV 280-500 CVetoBVeto	364165	72.067	0.9702	0.54647
MAXHTPTV 280-500 CFilterBVeto	364166	72.198	0.9702	0.31743
MAXHTPTV 280-500 BFilter	364167	72.045	0.9702	0.13337
MAXHTPTV 500-1000	364168	15.01	0.9702	1
MAXHTPTV 1000_E_CMS	364169	1.2344	0.9702	1

Table A.8: Simulated samples of strong $W \to \tau\nu$ production. All samples were simulated using Sherpa 2.2.1.

Process	MC ID	Cross-section [pb]	K-factor	Filter efficiency
MAXHTPTV 0-70 CVetoBVeto	364184	19152	0.9702	0.82495
MAXHTPTV 0-70 CFilterBVeto	364185	19153	0.9702	0.12934
MAXHTPTV 0-70 BFilter	364186	19163	0.9702	0.044594
MAXHTPTV 70-140 CVetoBVeto	364187	947.65	0.9702	0.67382
MAXHTPTV 70-140 CFilterBVeto	364188	946.73	0.9702	0.22222
MAXHTPTV 70-140 BFilter	364189	943.3	0.9702	0.10391
MAXHTPTV 140-280 CVetoBVeto	364190	339.36	0.9702	0.59622
MAXHTPTV 140-280 CFilterBVeto	364191	339.63	0.9702	0.29025
MAXHTPTV 140-280 BFilter	364192	339.55	0.9702	0.11229
MAXHTPTV 280-500 CVetoBVeto	364193	72.065	0.9702	0.54569
MAXHTPTV 280-500 CFilterBVeto	364194	71.976	0.9702	0.31648
MAXHTPTV 280-500 BFilter	364111	72.026	0.9702	0.13426
MAXHTPTV 500-1000	364112	15.046	0.9702	1
MAXHTPTV 1000_E_CMS	364113	1.2339	0.9702	1

Table A.9: Simulated samples of diboson + jets events. All samples were simulated using Sherpa 2.2.1.

Process	MC ID	Cross-section [pb]	K-factor	Filter efficiency
ZqqZ$\nu\nu$	363355	15.564	1	0.27976
ZqqZll	363356	15.563	1	0.13961
WqqZ$\nu\nu$	363357	6.7973	1	1
WqqZll	363358	3.437	1	1
WpqqWμlν	363359	24.717	1	1
WplνWμqq	363360	112.74	1	1
WlνZqq	363489	11.413	1	1

Table A.10: Simulated samples of electroweak V + jets production. All samples were simulated using `Sherpa` 2.2.1.

Process	MC ID	Cross-section [pb]	K-factor	Filter efficiency
Zee2jets	308092	0.63051	1	1
$Z\mu\mu$2jets	308093	0.63591	1	1
$Z\tau\tau$2jets	308094	0.63287	1	1
$Z\nu\nu$2jets	308095	2.9327	1	1
Weν2jets	308096	6.8072	1	1
W$\mu\nu$2jets	308097	6.81	1	1
W$\tau\nu$2jets	308098	6.791	1	1

Table A.11: Simulated multijet samples used for the study of the multijet background in the search for invisible decays of the Higgs boson. All samples were simulated using `Pythia` 8. The samples are the same as the ones used for the GSC.

Process (slice)	MC ID	Cross-section [mb]	K-factor	Filter efficiency
Multijet (JZ0W)	361020	78.420	1	0.97550
Multijet (JZ1W)	361021	78.420	1	0.00067198
Multijet (JZ2W)	361022	2.433	1	0.00033264
Multijet (JZ3W)	361023	0.026454	1	0.00031963
Multijet (JZ4W)	361024	2.54630×10^{-4}	1	0.00052982
Multijet (JZ5W)	361025	4.553×10^{-6}	1	0.00092255
Multijet (JZ6W)	361026	2.57530×10^{-7}	1	0.00094016
Multijet (JZ7W)	361027	1.6215×10^{-8}	1	0.00039282
Multijet (JZ8W)	361028	6.25030×10^{-10}	1	0.010176
Multijet (JZ9W)	361029	1.9617×10^{-11}	1	0.012092
Multijet (JZ10W)	361030	1.196×10^{-12}	1	0.0058935
Multijet (JZ11W)	361031	4.2259×10^{-14}	1	0.0027015
Multijet (JZ12W)	361032	1.037×10^{-15}	1	0.00042592

Table A.12: Simulated multijet samples used for the study of non-Gaussian tails. All samples were simulated using `Pythia` 8.

Process (slice)	MC ID	Cross-section [mb]	K-factor	Filter efficiency
Multijet (JZ1W)	361021	78.420	1	0.00067198
Multijet (JZ2W)	361022	2.433	1	0.00033264
Multijet (JZ3W)	361023	0.026454	1	0.00031963
Multijet (JZ4W)	361024	2.54630×10^{-4}	1	0.00052982
Multijet (JZ5W)	361025	4.553×10^{-6}	1	0.00092255
Multijet (JZ6W)	361026	2.57530×10^{-7}	1	0.00094016

A.2 Study of non-Gaussian tails in jet response distributions

A.2.1 Additional studies for estimating the mean in Gaussian fits

To justify the approximation $\mu_{\text{est}} \simeq \alpha_{||}/2$ in Eq. 6.8 asymmetry distributions of multijet events with a fourth jet veto are examined. If the third jet is the dominating factor in shifting the mean, this effect should be very similar with and without vetoing the fourth jet.

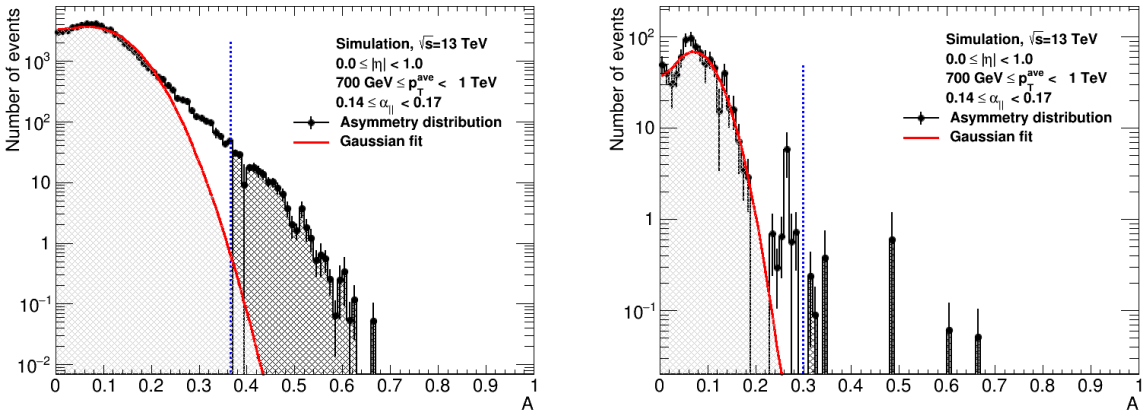

Figure A.1: Asymmetry distribution (black dots and histogram) of simulated topocluster jets in the bin $|\eta| < 1.0$, 700 GeV $\leq p_T <$ 1 TeV, $0.14 \leq \alpha_{||} < 0.17$. Gaussian fit (red line). Without a fourth jet veto (left). With a fourth jet veto (right).

In Figure A.1 two asymmetry distributions are shown each together with a Gaussian fit, where the mean is left as a free parameter. Without the fourth jet veto (left) the mean is determined as 0.0828 ± 0.0016[1)] and with the veto the fit yields a mean of 0.0738 ± 0.0012. The approximation $\mu_{\text{est}} \simeq \alpha^*_{||}/2 = 0.0775$ with $\alpha^*_{||}$ taken as the centre of the $\alpha_{||}$-bin is located between the two results. Taking the non-vanishing width of the $\alpha_{||}$-bin into account, $\alpha_{||}/2$ values run from 0.07 to 0.085 and thus encompass both mean results. From this it is concluded that the approximation is justified. Most importantly the uncertainty calculation in Section 6.5 covers both results and therefore the goodness of the approximation is not overestimated. This behaviour is studied in multiple p_{T}-$|\eta|$ bins yielding similar results.

In principle the sample with a fourth jet veto could be used to get cleaner events and to not be hindered by effects coming from additional jets. However, the loss of statistics is too great and the approximation in Eq. 6.8 too useful in stabilizing the fits to motivate this change of strategy.

Furthermore, the behaviour is compared with the asymmetry distribution of truth jets in Figure A.2. As expected the peak of the distribution is narrower, as instrumental effects are avoided, and the mean at 0.0809 ± 0.0013 does not shift significantly from the mean determined via reconstructed jets. This mean is also within the $\alpha_{||}$-bin width. The non-Gaussian tails in the distribution made with truth jets cannot be caused by effects of instrumentation and calibration. Therefore, they have to be caused by physics effects like semi-leptonic heavy flavour decays and a portion of the jets being gluon jets as discussed in Section 6.1.

[1)] The uncertainty here is determined by using the sampling method described in Section 6.4.1.

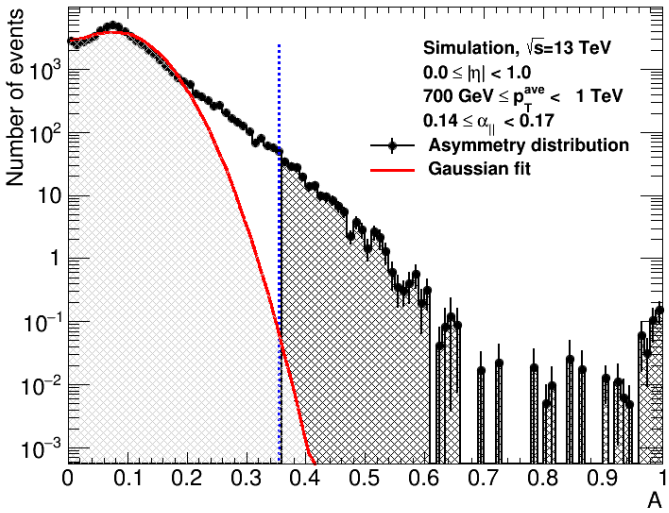

Figure A.2: Asymmetry distribution (black dots and histogram) of truth topocluster jets in the bin $|\eta| < 1.0$, 700 GeV $\leq p_T <$ 1 TeV, $0.14 \leq \alpha_{||} < 0.17$. Gaussian fit (red line).

Using these additional considerations the mean of the Gaussian fit can be fixed, leaving only two parameters to be determined by the fit. Further motivation for this step comes from the following test: In an asymmetry distribution the number of events in each bin is varied randomly using poisson statistics. With this 1000 different distributions are generated and a fit, where the mean is left as a free parameter, is performed for each. These fits are shown in Figure A.3 and the fitted means of the distributions are collected in a histogram for comparison. The means form two populations: one near $\alpha_{||}/2$ where the true mean is expected and another near 0 closing in on the parameter limit. It is likely that many of these fits converge on unphysical results.

Fixing the mean to $\alpha_{||}/2$ avoids those unphysical result, but introduces a source of systematic uncertainty. This is further discussed in Section 6.5. Another test is to look at the distribution of means against $\alpha_{||}$. To obtain Figure A.4 seven asymmetry distribution are fitted, where the mean is left as a free parameter. A linear fit (red line) attempts to model the data points, but does not accurately model the behaviour. In addition, the estimate in Eq. 6.8 is compared with the data points. At high $\alpha_{||}$ this is clearly an accurate description. However, at low $\alpha_{||}$ the fits reach the low parameter limit of μ at 0. This behaviour can be understood by considering Figure A.5. Here, two asymmetry distributions, which are part of the test in Figure A.4, are depicted. The distribution at intermediate $\alpha_{||}$ clearly has a wider peak hinting at the expected shift, but as a result of resolution effects the mean shift is not clearly visible. By fixing the mean its shift can be described accurately despite these effects. At high $\alpha_{||}$ the effect is apparent enough to strengthen the belief in the hypothesis.

This also reveals an advantage over the α definition used in the similar CMS study [191], which was just $\alpha = p_{\mathrm{T,j3}}/p_{\mathrm{T}}^{\mathrm{ave}}$. This simpler definition that lacks the projection onto the dijet axis does not lead to such a clear correlation between the α-bin and the position of the mean.

This is illustrated in Figure A.6. Here, the asymmetry is plotted against $\alpha_{||}$ and α in two-dimensional graphs. Again it is clear that in the case of the $\alpha_{||}$-definition the mean and as a result the maximum shift to higher asymmetry values with the increase of $\alpha_{||}$. With the definition of

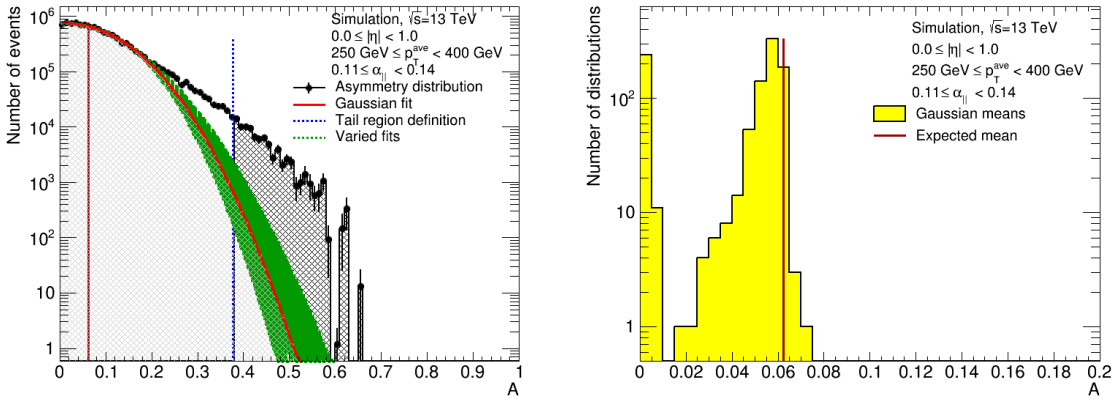

Figure A.3: Left plot: Asymmetry distribution (black dots and histogram) of particle flow jets in the bin $|\eta| < 1.0$, 250 GeV $\leq p_T <$ 400 GeV, $0.11 \leq \alpha_{||} < 0.14$. Gaussian fits to varied histograms obtained with the sampling method (green lines) and Gaussian fit with median integral (red line). Definition of tail regions (blue, dashed line) and expected mean of the fit (red, vertical line). Fits to varied distributions (green lines). Right plot: Distribution of means of the fits to varied histograms (yellow histogram) and expected mean of the fit (red, vertical line).

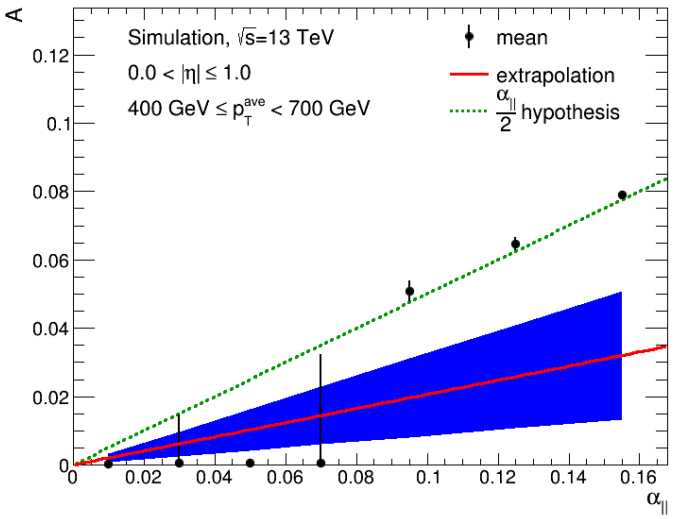

Figure A.4: Gaussian means per $\alpha_{||}$-bin determined through fits without a fixed mean (black data points). The $\alpha_{||}/2$ hypothesis is a linear function with the slope of $1/2$ (green dashed line). The extrapolation (red line) is a linear fit to the data points. Simulated topocluster jets in the bin $|\eta| < 1.0$, 400 GeV $\leq p_T <$ 700 TeV.

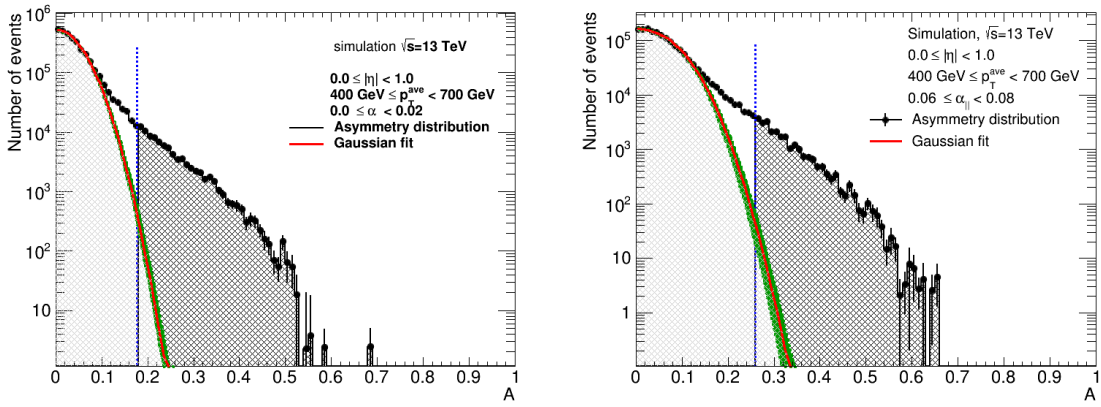

Figure A.5: Left plot: Asymmetry distribution (black dots and histogram) of simulated topocluster jets in the bin $|\eta| < 1.0$, 400 GeV $\leq p_T <$ 7000 GeV, $0.0 \leq \alpha_{||} < 0.02$. Definition of tail regions (blue, dashed line). Fits to varied distributions obtained with the sampling method (green lines). Right plot: Same distribution at $0.06 \leq \alpha_{||} < 0.08$.

$\alpha = p_{\mathrm{T,j_3}}/p_{\mathrm{T}}^{\mathrm{ave}}$ this shift is less pronounced but of course visible because of the high correlation between $\alpha_{||}$ and α. Especially at high values of $\alpha_{||}$ and α the distributions become very similar because most of the third jets are nearly parallel to the dijet axis in that regime.

This is compared with the functions $A = \alpha/2$ and $A = \alpha_{||}/2$, which are expected to coincide with the means of the Gaussian cores of the asymmetry distributions as seen in Figure A.4. However, in the two-dimensional plot without the fits only the maxima, which do not equal the means outside of $\alpha = 0$, are visible. This is can be seen by consulting Figure 6.4 where the maximum is always at a lower asymmetry value than the mean.

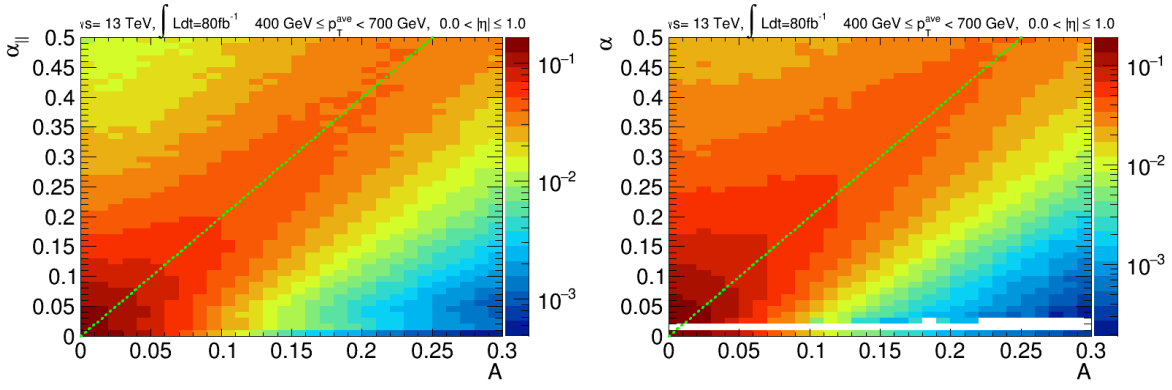

Figure A.6: Number of events in the bin $|\eta| < 1.0$, 400 GeV $\leq p_T <$ 700 TeV as a function of the asymmetry A and $\alpha_{||}$ (left) or α (right) of particle flow jets. The number of events are normalized to one in each $\alpha_{||}$ or α bin. The functions $A = \alpha/2$ and $A = \alpha_{||}/2$ (green dashed lines) act as comparisons to the predicted mean of the Gaussian core.

Another problem with the definition $\alpha = p_{\mathrm{T,j_3}}/p_{\mathrm{T}}^{\mathrm{ave}}$ is apparent on the right of Figure A.6. It shows a clear gap at low non-zero α values. This is due to the fact that jets are not recommended for usage at arbitrarily low p_{T} values. Therefore, an event with a third jet below the $p_{\mathrm{T}} = 20$ GeV

threshold looks like a pure dijet event. As a result in low $p_{\mathrm{T}}^{\mathrm{ave}}$ bins many of the events end up in the lowest α bin despite technically belonging to other ones. The extrapolation procedure with the α definition gains a systematic error from this effect.

A.2.2 "Dijet-ness" behaviour of multijet events

Examples of $\alpha_{||}$ distributions in four $p_{\mathrm{T}}^{\mathrm{ave}}$-$|\eta|$-$\alpha_{||}$ bins are shown in Figure A.7. The distributions illustrate typical behaviour at low $p_{\mathrm{T}}^{\mathrm{ave}}$ where the $\alpha_{||}$ distributions tend to be flat, compared with high $p_{\mathrm{T}}^{\mathrm{ave}}$ where the distributions are falling exponentially. However, this negative slope is only present at $\alpha_{||} > 0.04$. Below $\alpha_{||} = 0.04$ positive slopes are observed at high $p_{\mathrm{T}}^{\mathrm{ave}}$. Many events fill the $\alpha_{||} = 0$ bin because jets below 20 GeV are not recommended for usage in ATLAS. These jets are removed from the events leading to $\alpha_{||} = 0$ if that jet is a third jet.

The behaviour in the other bins can be explained by this threshold effect as well. At a given $p_{\mathrm{T}}^{\mathrm{ave}}$ the third jet p_{T} can have any value as long as it does not exceed the leading and subleading jet. Therefore, the $\alpha_{||}$ distribution has to have the same shape as the $p_{\mathrm{T,j_3}}$ spectrum, which is exponentially falling. This is exactly what is observed at high $p_{\mathrm{T}}^{\mathrm{ave}}$ and high $\alpha_{||}$. In low bins of $p_{\mathrm{T}}^{\mathrm{ave}}$ or $\alpha_{||}$ a portion of the events have a third jet that is either below the 20 GeV threshold or is a higher p_{T} jet that has a large component perpendicular to the dijet axis. The events with a third jet below threshold end up in the $\alpha_{||} = 0$ bin. The lower $\alpha_{||}$ is, the larger the portion of events with a third jet below threshold leading to a rising $\alpha_{||}$ distribution. In Figure A.8 the same distributions are shown for topocluster jets and the behaviour is largely the same.

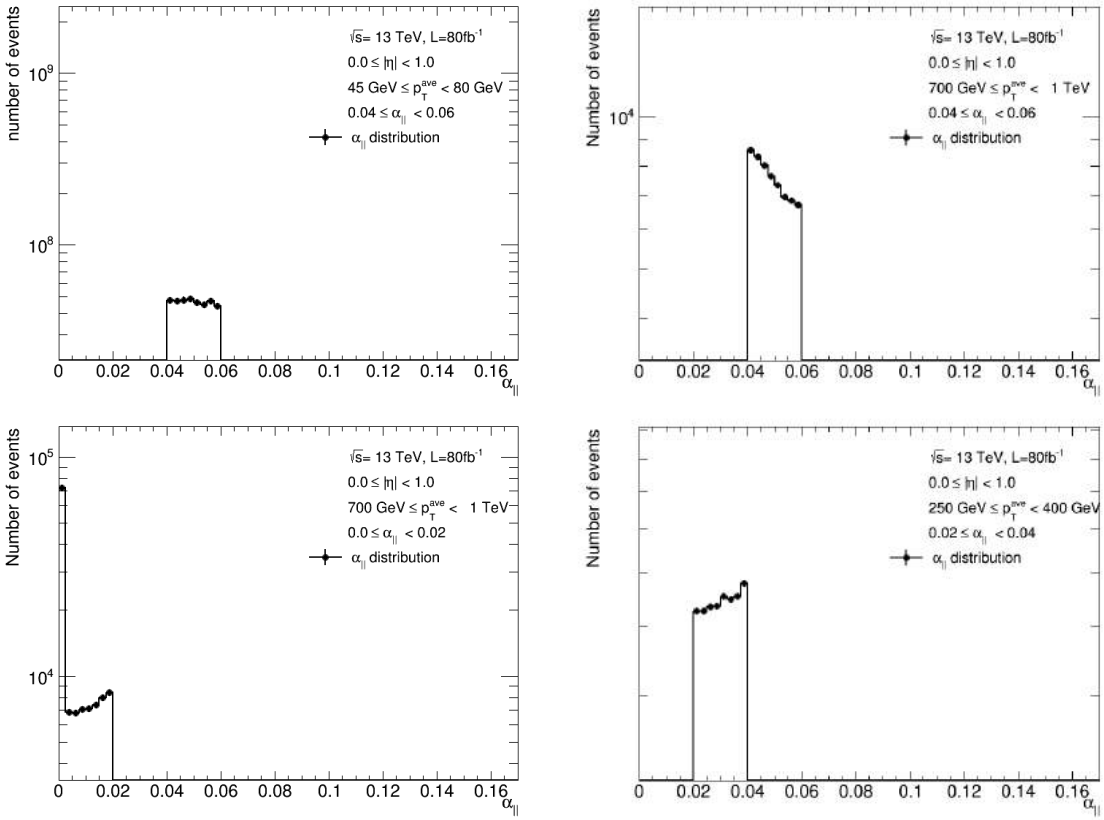

Figure A.7: "Dijet-ness" ($\alpha_{||}$) distributions in four $p_{\mathrm{T}}^{\mathrm{ave}}$-$|\eta|$-$\alpha_{||}$ bins. All distributions are generated with particle flow jets.

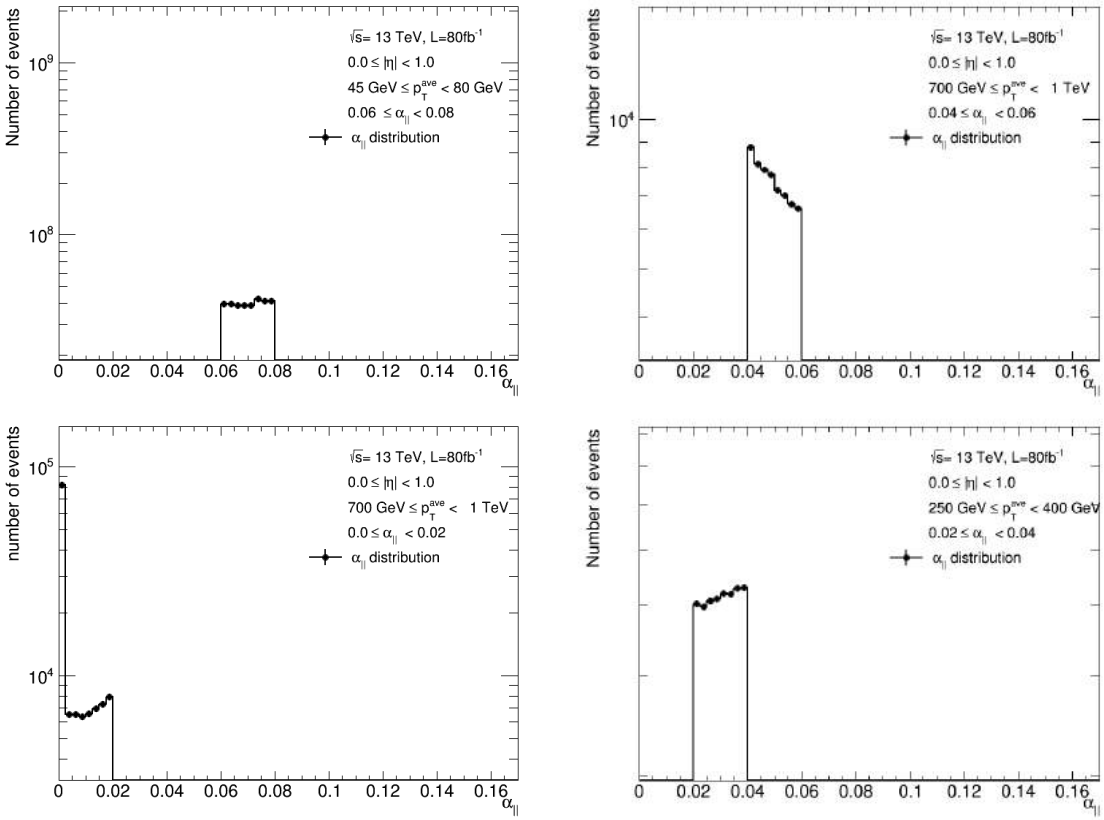

Figure A.8: "Dijet-ness" ($\alpha_{||}$) distributions in four $p_{\mathrm{T}}^{\mathrm{ave}}$-$|\eta|$-$\alpha_{||}$ bins. All distributions are generated with topocluster jets.

A.2.3 Exceptional fit correction factors

The exceptional correction factors c_{corr} according to Eq. 6.9 are listed by bin in Table A.13. These correction factors are determined empirically to yield reliably converging fits.

Table A.13: Exceptional correction factors c_{corr} by bin.

$\lvert\eta\rvert$	p_T [GeV]	$\alpha_{\lvert\rvert}$	Data/MC	Jet collection	c_{corr}
$0.0 \leq \lvert\eta\rvert < 1.0$	$45 \leq p_T < 80$	all	MC	PFlow	0.7
$0.0 \leq \lvert\eta\rvert < 1.0$	$80 \leq p_T < 150$	all	MC	PFlow	0.7
$0.0 \leq \lvert\eta\rvert < 1.0$	$250 \leq p_T < 400$	all	MC	PFlow	0.7
$0.0 \leq \lvert\eta\rvert < 1.0$	$400 \leq p_T < 700$	all	MC	PFlow	0.7
$1.0 \leq \lvert\eta\rvert < 1.9$	$45 \leq p_T < 80$	all	MC	PFlow	0.6
$1.9 \leq \lvert\eta\rvert < 4.5$	$45 \leq p_T < 80$	all	MC	PFlow	0.6
$1.9 \leq \lvert\eta\rvert < 4.5$	$150 \leq p_T < 250$	all	MC	PFlow	0.6
$0.0 \leq \lvert\eta\rvert < 1.0$	$45 \leq p_T < 80$	all	data	PFlow	0.4
$0.0 \leq \lvert\eta\rvert < 1.0$	$150 \leq p_T < 250$	all	data	PFlow	0.4
$0.0 \leq \lvert\eta\rvert < 1.0$	$700 \leq p_T < 1000$	$0.14 \leq \alpha_{\lvert\rvert} < 0.17$	data	PFlow	0.4
$1.9 \leq \lvert\eta\rvert < 4.5$	$45 \leq p_T < 80$	all	data	PFlow	0.4
$1.9 \leq \lvert\eta\rvert < 4.5$	$150 \leq p_T < 250$	all	data	PFlow	0.4
$0.0 \leq \lvert\eta\rvert < 1.0$	$45 \leq p_T < 80$	all	MC	Topo	0.7
$0.0 \leq \lvert\eta\rvert < 1.0$	$80 \leq p_T < 150$	all	MC	Topo	0.7
$0.0 \leq \lvert\eta\rvert < 1.0$	$250 \leq p_T < 400$	all	MC	Topo	0.7
$0.0 \leq \lvert\eta\rvert < 1.0$	$400 \leq p_T < 700$	all	MC	Topo	0.7
$1.0 \leq \lvert\eta\rvert < 1.9$	$80 \leq p_T < 150$	all	MC	Topo	0.7
$1.9 \leq \lvert\eta\rvert < 4.5$	$45 \leq p_T < 80$	all	MC	Topo	0.7
$0.0 \leq \lvert\eta\rvert < 1.0$	$80 \leq p_T < 150$	all	data	Topo	0.6
$0.0 \leq \lvert\eta\rvert < 1.0$	$250 \leq p_T < 400$	all	data	Topo	0.4
$0.0 \leq \lvert\eta\rvert < 1.0$	$700 \leq p_T < 1000$	$0.14 \leq \alpha_{\lvert\rvert} < 0.17$	data	Topo	0.4
$1.0 \leq \lvert\eta\rvert < 1.9$	$80 \leq p_T < 150$	all	data	Topo	0.4
$1.9 \leq \lvert\eta\rvert < 4.5$	$250 \leq p_T < 400$	all	data	Topo	0.4

A.2.4 Example extrapolation plots

Figure A.9 shows the extrapolation to pure dijet events in both jet collections for data and MC simulation. The behaviour in all four configurations is very similar to each other.

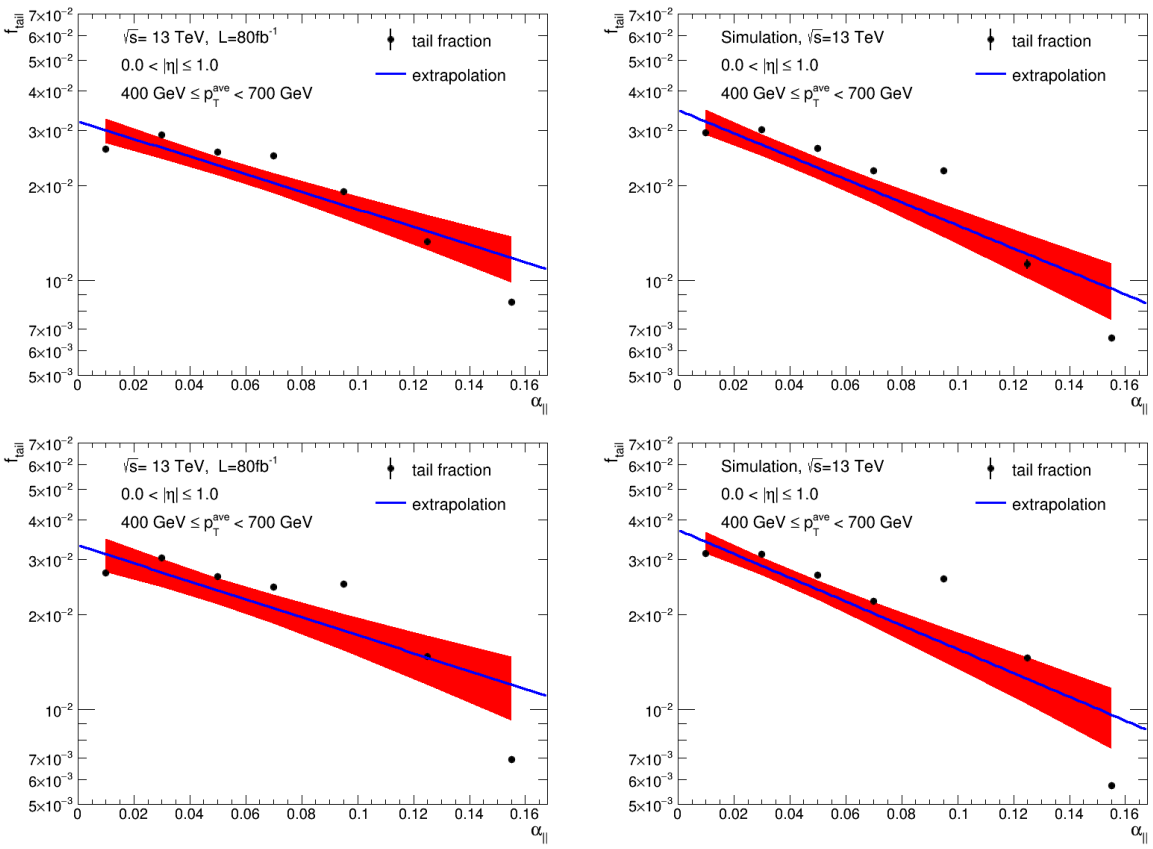

Figure A.9: Tail fractions extrapolated to $\alpha_{||} = 0$ in the bin $|\eta| < 1.0$, 400 GeV $\leq p_{\mathrm{T}}^{\mathrm{ave}} <$ 700 GeV. The two top plots show particle flow jets, topocluster jets are depicted below. Data are studied on the left and MC simulation on the right.

A.3 Post-fit distributions

As an extension of Section 5.7.1 the m_{jj} and lepton p_{T} corrected $E_{\mathrm{T}}^{\mathrm{miss}}$ distributions of the other CRs are shown here:

- $W \to e^{-}\nu$ CR: Figure A.10
- $W \to \mu^{-}\nu$ CR: Figure A.11
- $W \to \mu^{+}\nu$ CR: Figure A.12
- $Z \to \mu^{+}\mu^{-}$ CR: Figure A.13
- $Z \to e^{+}e^{-}$ CR: Figure A.14

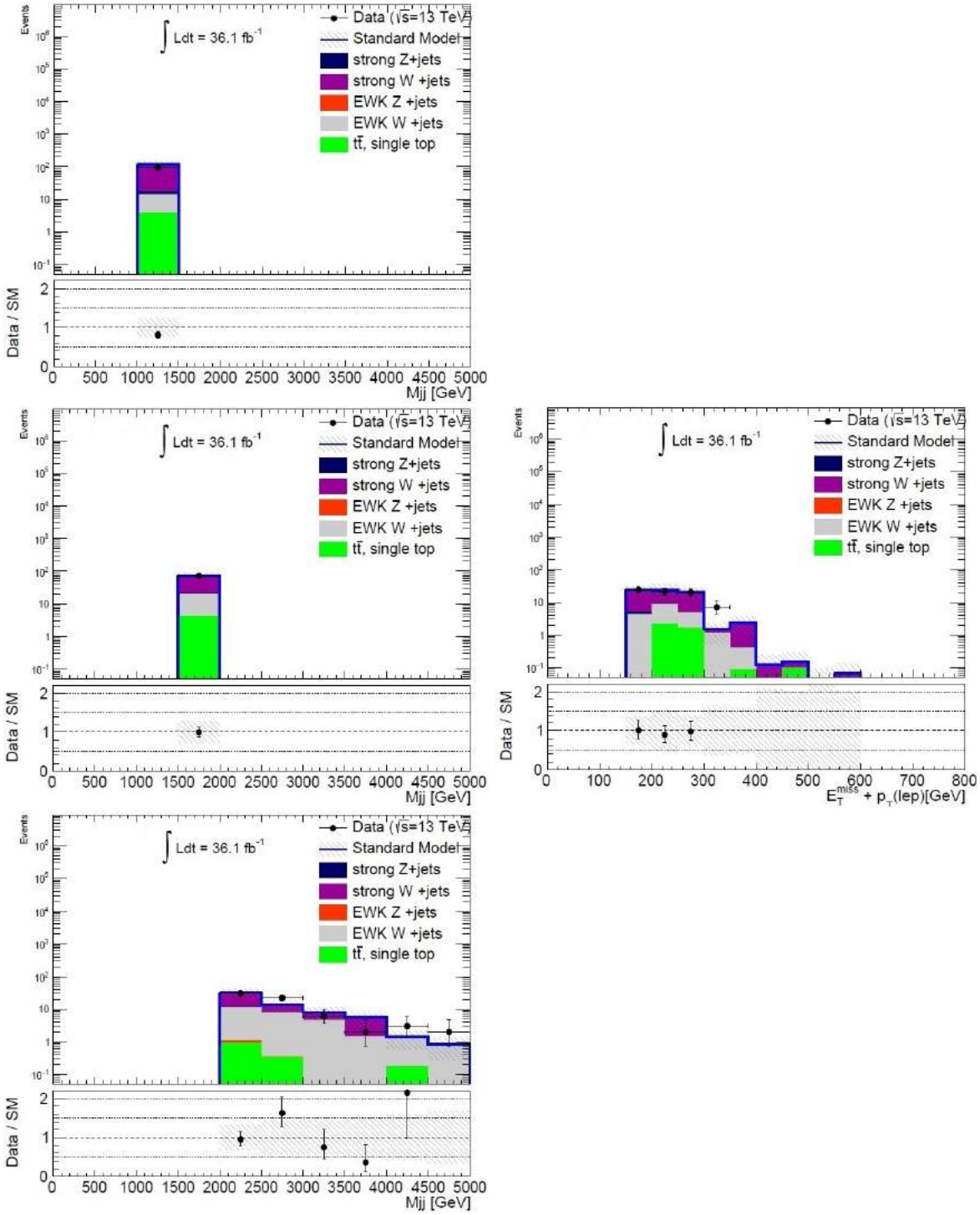

Figure A.10: Results of the background-only fit: Dijet mass distributions (left) and lepton p_{T} corrected $E_{\mathrm{T}}^{\mathrm{miss}}$ distributions (right) in the $W \to e^{-}\nu$ control region. The plots show the distributions in the three different bins 1.0 TeV $< m_{\mathrm{jj}} <$ 1.5 TeV (top), 1.5 TeV $< m_{\mathrm{jj}} <$ 2.0 TeV (middle) and $m_{\mathrm{jj}} >$ 2.0 TeV (bottom) [173].

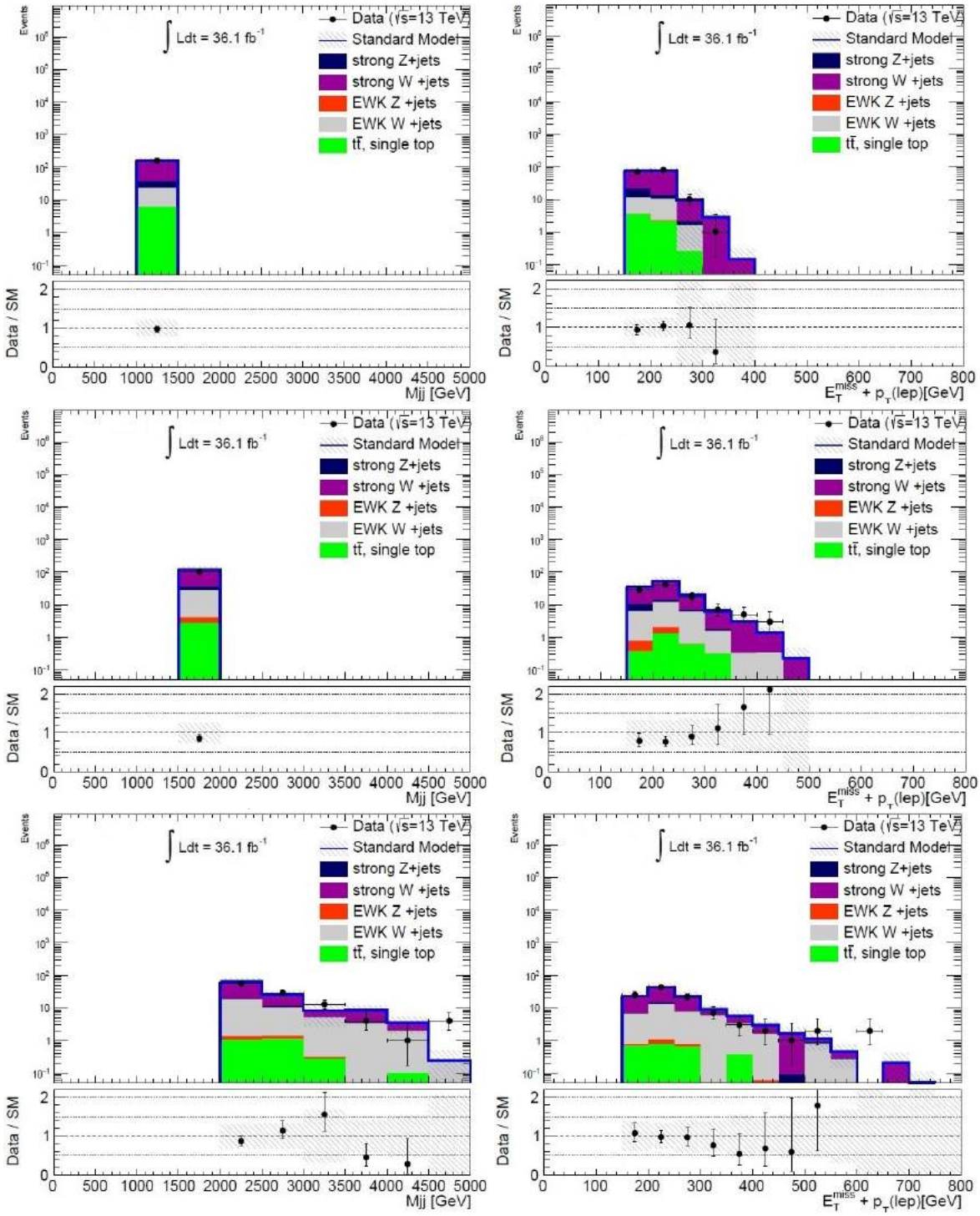

Figure A.11: Results of the background-only fit: Dijet mass distributions (left) and lepton p_{T} corrected $E_{\mathrm{T}}^{\mathrm{miss}}$ distributions (right) in the $W \to \mu^{-}\nu$ control region. The plots show the distributions in the three different bins 1.0 TeV $< m_{\mathrm{jj}} <$ 1.5 TeV (top), 1.5 TeV $< m_{\mathrm{jj}} <$ 2.0 TeV (middle) and $m_{\mathrm{jj}} >$ 2.0 TeV (bottom) [173].

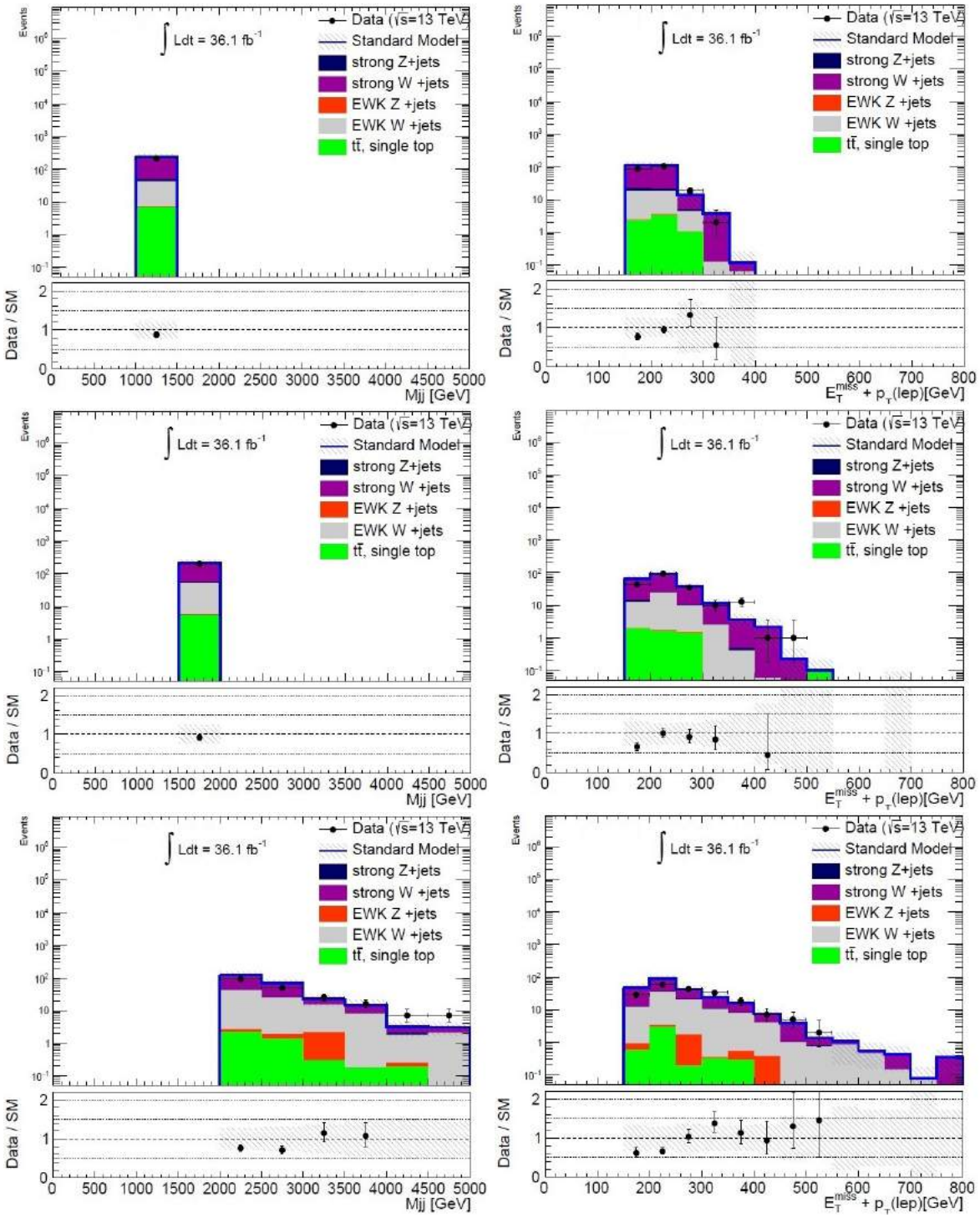

Figure A.12: Results of the background-only fit: Dijet mass distributions (left) and lepton p_{T} corrected $E_{\mathrm{T}}^{\mathrm{miss}}$ distributions (right) in the $W \to \mu^{+}\nu$ control region. The plots show the distributions in the three different bins 1.0 TeV $< m_{\mathrm{jj}} <$ 1.5 TeV (top), 1.5 TeV $< m_{\mathrm{jj}} <$ 2.0 TeV (middle) and $m_{\mathrm{jj}} >$ 2.0 TeV (bottom) [173].

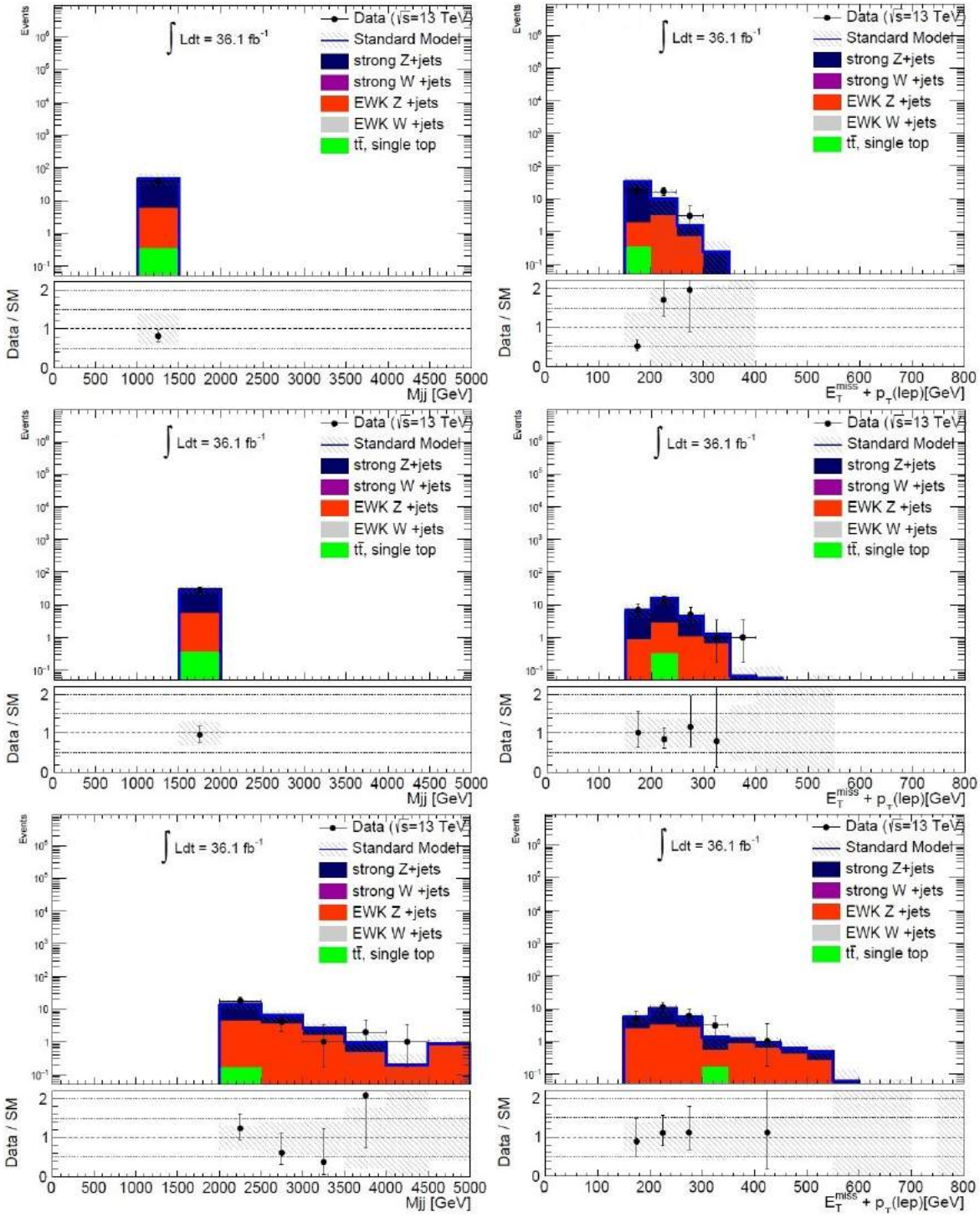

Figure A.13: Results of the background-only fit: Dijet mass distributions (left) and lepton p_{T} corrected $E_{\mathrm{T}}^{\mathrm{miss}}$ distributions (right) in the $Z \to \mu^{+}\mu^{-}$ control region. The plots show the distributions in the three different bins 1.0 TeV $< m_{\mathrm{jj}} <$ 1.5 TeV (top), 1.5 TeV $< m_{\mathrm{jj}} <$ 2.0 TeV (middle) and $m_{\mathrm{jj}} >$ 2.0 TeV (bottom) [173].

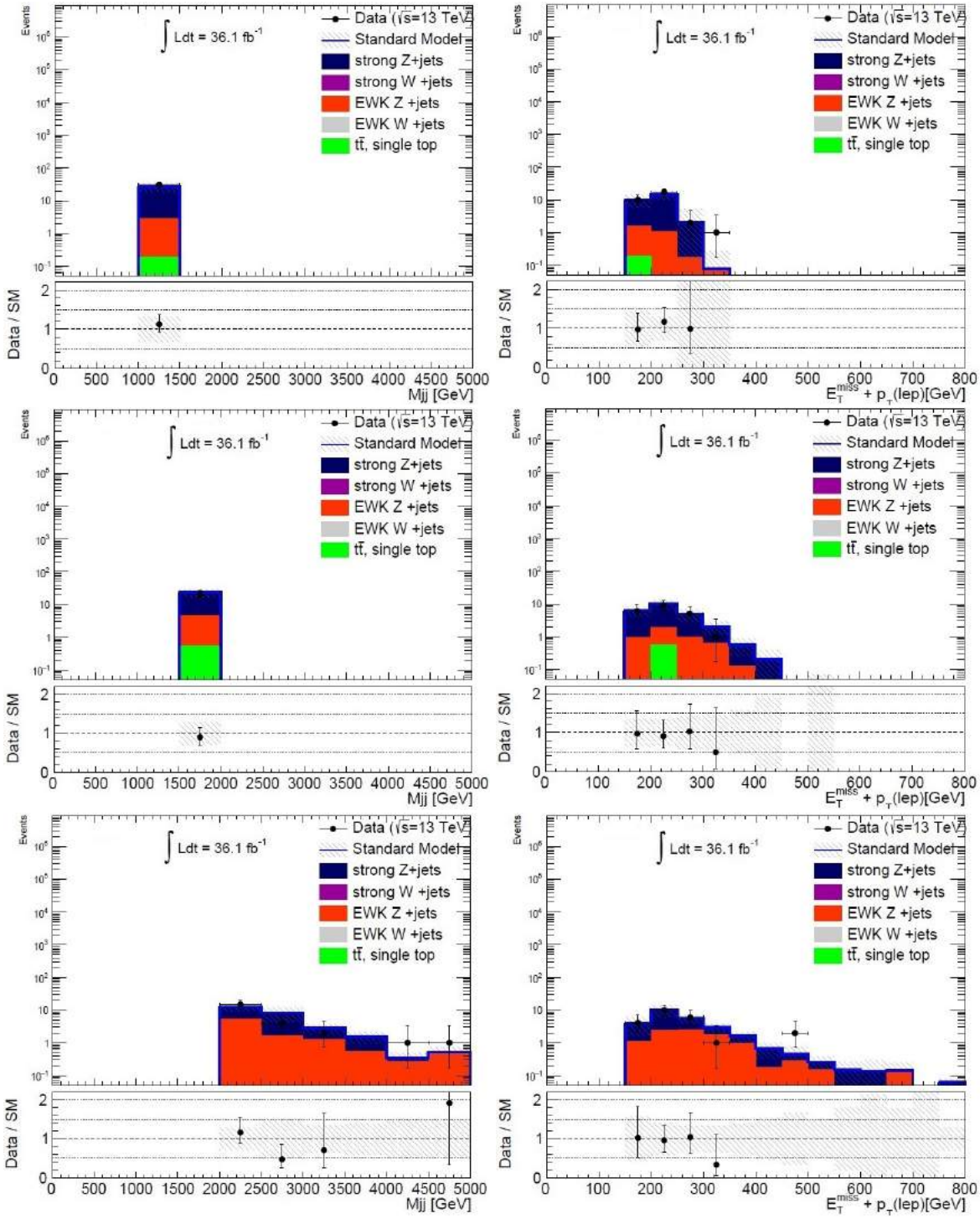

Figure A.14: Results of the background-only fit: Dijet mass distributions (left) and lepton p_{T} corrected $E_{\mathrm{T}}^{\mathrm{miss}}$ distributions (right) in the $Z \to e^{+}e^{-}$ control region. The plots show the distributions in the three different bins 1.0 TeV $< m_{\mathrm{jj}} <$ 1.5 TeV (top), 1.5 TeV $< m_{\mathrm{jj}} <$ 2.0 TeV (middle) and $m_{\mathrm{jj}} >$ 2.0 TeV (bottom) [173].

A.4 Acronym lists

Table A.14: List of acronyms that are used in this thesis (2HDM–EMTopo).

Acronym	Term	Introduced in...
2HDM	two Higgs doublet model	Section 2.2.5
ALICE	a large ion collider experiment	Section 3.1
ATLAS	a toroidal LHC apparatus	Section 3.1
BOOSTER	proton synchrotron booster	Section 3.1
BR	branching ratio	Section 2.1.7, Section 5.1
BSM	beyond the Standard Model	Chapter 1, Section 2.1.8, Section 3.4, Section 5.1
CB muon	combined muon	Section 3.3.3
CDM	cold dark matter	Section 2.2.1
CERN	conseil européen pour la recherche nucléaire	Section 3.1
CKM matrix	Cabibbo-Kobayashi-Maskawa matrix	Section 2.1.5
CMB	cosmic microwave background	Chapter 1, Section 2.2.1
CMS	compact muon solenoid	Section 3.1
CSC	cathode strip chambers	Section 3.2.4
CR	control region	Section 5.2
CST	calorimeter soft term	Section 3.3.4
CT muon	calorimeter-tagged muon	Section 3.3.3
DM	dark matter	Chapter 1, Chapter 2, Section 5.2
EMEC	electromagnetic end-cap	Section 3.2.3
EMPFlow	EM scale particle flow	Chapter 4
EM scale	electromagnetic scale	Section 3.3.2, Chapter 4, Section 5.4.3
EMTopo	EM scale topocluster	Chapter 4

Table A.15: List of acronyms that are used in this thesis ($E_{\mathrm{T}}^{\mathrm{miss}}$–JVF).

Acronym	Term	Introduced in...
$E_{\mathrm{T}}^{\mathrm{miss}}$	missing transverse energy	Chapter 1, Section 2.2.4, Chapter 3, Section 4.1.1, Section 5.1
EWK	electroweak	Chapter 1, Section 2.1.1, Section 5.3.2
FCal	forward calorimeter	Section 3.2.3
fJVT	forward jet vertex tagger	Section 4.3.2
FSR	final state radiation	Section 2.1.6, Section 3.3.2, Section 5.3.2
ggF	gluon–gluon Fusion	Section 2.1.7, Section 5.1
GR	general relativity	Section 2.1.8
GRL	good runs list	Section 3.1.1, Section 5.4.1, Section 6.1
GSC	global sequential calibration	Chapter 1, Section 4.1, Section 5.8, Section 6.1
GUT	grand unified theory	Section 2.1.8
HEC	hadronic end-cap calorimeter	Section 3.2.3
HEP	high energy physics	Section 2.1.6, Section 3.4
HLT	high level trigger	Section 3.2.5, Section 5.4.2
IBL	insertable B-layer	Section 3.2.2
ID	inner detector	Section 3.2
ISR	initial state radiation	Section 2.1.6, Section 3.3.2, Section 5.1
JER	jet energy resolution	Section 4.1.5, Section 5.5.4
JES	jet energy scale	Section 4.1.4, Section 5.6.1
JVF	jet vertex fraction	Section 3.3.2

Table A.16: List of acronyms that are used in this thesis (JVT–QED).

Acronym	Term	Introduced in...
JVT	jet vertex tagger	Section 3.3.2, Section 5.4.3, Section 6.3.1
L1 trigger	level 1 trigger	Section 3.2.5, Section 5.4.2
L2 trigger	level 2 trigger	Section 3.2.5
LAr	liquid argon	Section 3.2
LCW	local hadronic cell weighting	Section 3.3.2, Section 4.1
LEP	Large Electron-Positron Collider	Section 3.1
LHC	Large Hadron Collider	Chapter 1, Chapter 3
LO	leading-order	Section 2.1.2, Section 3.4.1, Section 5.3.2
MACHO	massive compact halo object	Section 2.2.2
MC	Monte Carlo	Chapter 3, Section 4.1, Section 5.3.2, Section 6.2
MDT	monitored drift tube	Section 3.2.4
ME muon	extrapolated muon	Section 3.3.3
MOND	modified newtonian dynamics	Section 2.2.6
MSSM	minimal supersymmetric Standard Model	Section 2.2.5
N3LO	next-to-next-to-next-to-leading-order	Section 2.1.2, Section 3.4.1
NLO	next-to-leading-order	Section 2.1.2, Section 3.4.1, Section 5.3.2
NNLO	next-to-next-to-leading-order	Section 2.1.2, Section 3.4.1, Section 5.3.2
NP	nuisance parameter	Section 4.3.1, Section 5.6.1
PDF	parton distribution function	Section 2.1.6
PFlow	particle flow	Section 1.1, Section 3.3.2, Section 4.2.4, Section 5.4.3
PS	proton synchrotron	Section 3.1
QCD	quantum chromodynamics	Chapter 1, Section 2.1.4, Section 3.4.1, Section 5.2
QED	quantum electrodynamics	Section 2.1.2

Table A.17: List of acronyms that are used in this thesis (RMS–ΛCDM).

Acronym	Term	Introduced in...
RMS	root mean square	Section 4.3.2
RoI	region of interest	Section 3.2.5
RPC	resistive plate chamber	Section 3.2.4
R+S method	rebalance and smear method	Section 5.2, Section 6.1
SCT	semiconductor tracker	Section 3.2.2
SM	Standard Model	Chapter 1, Chapter 2, Section 3.2.3, Section 5.1
SPS	super proton synchrotron	Section 3.1
SR	signal region	Section 5.2
ST muon	segment-tagged muon	Section 3.3.3
TDAQ	trigger and data acquisition	Section 3.2.5
TF	transfer factor	Section 5.7
TGC	thin gap chamber	Section 3.2.4
Topo	topocluster	Section 1.1, Section 4.2.6, Section 5.4.3
TRT	transition radiation tracker	Section 3.2.2
TST	track soft term	Section 3.3.4, Section 5.4.3
UE	underlying event	Section 2.1.6, Section 3.4.1, Section 5.3.2
VBF	vector-boson fusion	Section 2.1.7, Section 5.1
VR	validation region	Section 5.4.4
WIMP	weakly interacting massive particle	Section 2.2.2, Section 5.3.2
WLCG	worldwide LHC computing grid	Section 3.1.2
ΛCDM	Lambda cold dark matter	Section 2.2.1

Bibliography

[1] P. W. Higgs. "Broken Symmetries and the Masses of Gauge Bosons". In: *Physical Review Letters* 13 (Oct. 1964), pp. 508–509. DOI: 10.1103/PhysRevLett.13.508 (page 14).

[2] The ATLAS collaboration. "Observation of a new particle in the search for the Standard Model Higgs boson with the ATLAS detector at the LHC". In: *Physics Letters B* 716.1 (2012), pp. 1–29 (pages 14, 32, 49).

[3] The CMS collaboration. "Observation of a new boson at a mass of 125 GeV with the CMS experiment at the LHC". In: *Physics Letters B* 716.1 (2012), pp. 30–61 (pages 14, 32, 49).

[4] The ATLAS collaboration. "Measurements of $t\bar{t}$ differential cross-sections of highly boosted top quarks decaying to all-hadronic final states in pp collisions at $\sqrt{s} = 13$ TeV using the ATLAS detector". In: *Phys. Rev. D* 98.1 (2018), p. 012003. DOI: 10.1103/PhysRevD.98.012003 (page 14).

[5] The ATLAS collaboration. "Measurement of the cross section for isolated-photon plus jet production in pp collisions at $\sqrt{s} = 13$ TeV using the ATLAS detector". In: *Phys. Lett. B* 780 (2018), pp. 578–602. DOI: 10.1016/j.physletb.2018.03.035 (page 14).

[6] Edvige Corbelli and Paolo Salucci. "The Extended Rotation Curve and the Dark Matter Halo of M33". In: *Mon. Not. Roy. Astron. Soc.* 311 (2000), pp. 441–447. DOI: 10.1046/j.1365-8711.2000.03075.x (page 14).

[7] Steven W. Allen, August E. Evrard, and Adam B. Mantz. "Cosmological Parameters from Observations of Galaxy Clusters". In: *Annual Review of Astronomy and Astrophysics* 49 (Sept. 2011), pp. 409–470. DOI: 10.1146/annurev-astro-081710-102514 (page 14).

[8] The Planck collaboration. "Planck 2018 results. I. Overview and the cosmological legacy of Planck". In: (2018) (pages 14, 36, 38, 44).

[9] A. N. Taylor et al. "Gravitational lens magnification and the mass of abell 1689". In: *Astrophys. J.* 501 (1998), p. 539. DOI: 10.1086/305827 (pages 14, 36).

[10] Douglas Clowe, Anthony Gonzalez, and Maxim Markevitch. "Weak lensing mass reconstruction of the interacting cluster 1E0657-558: Direct evidence for the existence of dark matter". In: *Astrophys. J.* 604 (2004), pp. 596–603. DOI: 10.1086/381970 (page 14).

[11] Christoph Englert et al. "Exploring the Higgs portal". In: *Phys. Lett. B* 703 (2011), pp. 298–305. DOI: 10.1016/j.physletb.2011.08.002 (pages 14, 45, 105).

[12] The ATLAS collaboration. "Search for invisible Higgs boson decays in vector boson fusion at $\sqrt{s} = 13$ TeV with the ATLAS detector". In: *Phys. Lett. B* (2018). DOI: 10.1016/j.physletb.2019.04.024 (pages 15, 127, 143, 144, 146, 150).

[13] Shinya Kanemura et al. "Can WIMP Dark Matter overcome the Nightmare Scenario?" In: *Phys. Rev. D* 82 (2010), p. 055026. DOI: 10.1103/PhysRevD.82.055026 (page 15).

[14] Pierre Binétruy. *Supersymmetry: theory, experiment, and cosmology*. Oxford University Press, 2012 (page 15).

[15] S. L. Glashow. "Partial Symmetries of Weak Interactions". In: *Nucl. Phys.* 22 (1961), pp. 579–588. DOI: 10.1016/0029-5582(61)90469-2 (page 17).

[16] Steven Weinberg. "A Model of Leptons". In: *Phys. Rev. Lett.* 19 (21 Nov. 1967), pp. 1264–1266. DOI: 10.1103/PhysRevLett.19.1264 (page 17).

[17] A. Salam. *Elementary Particle Physics: Relativistic Groups and Analyticity,* Almquvist and Wiksell, 1968 (page 17).

[18] *Go on a particle quest at the first CERN webfest*. Aug. 27, 2019. URL: https://cds.cern.ch/record/1473657 (page 18).

[19] P. A. M. Dirac. "The Quantum Theory of the Electron". In: *Proceedings of the Royal Society of London Series A* 117 (Feb. 1928), pp. 610–624. DOI: 10.1098/rspa.1928.0023 (page 19).

[20] E. Noether. "Invariante Variationsprobleme". ger. In: *Nachrichten von der Gesellschaft der Wissenschaften zu Göttingen, Mathematisch-Physikalische Klasse* 1918 (1918), pp. 235–257 (page 20).

[21] K. A. Olive et al. "Review of Particle Physics". In: *Chin. Phys. C* 38 (2014), p. 090001. DOI: 10.1088/1674-1137/38/9/090001 (pages 21, 22, 25).

[22] Alessandro Bettini. *Introduction to Elementary Particle Physics*. Cambridge University Press, 2008. DOI: 10.1017/CBO9780511809019 (page 21).

[23] Antonio Pich. "The Standard model of electroweak interactions". In: 2008, pp. 1–49 (page 22).

[24] John Ellis, Mary K. Gaillard, and Dimitri V. Nanopoulos. "An Updated Historical Profile of the Higgs Boson". In: *The standard theory of particle physics: Essays to celebrate CERN's 60th anniversary*. Ed. by Luciano Maiani and Luigi Rolandi. 2016, pp. 255–274. DOI: 10.1142/9789814733519_0014 (page 24).

[25] Mark Thomson. *Modern particle physics*. New York: Cambridge University Press, 2013. ISBN: 9781107034266 (page 27).

[26] Makoto Kobayashi and Toshihide Maskawa. "CP-Violation in the Renormalizable Theory of Weak Interaction". In: *Progress of Theoretical Physics* 49.2 (Feb. 1973), pp. 652–657. ISSN: 0033-068X. DOI: 10.1143/PTP.49.652 (page 28).

[27] S. M. Bilenky. "Neutrino in Standard Model and beyond". In: *Phys. Part. Nucl.* 46.4 (2015), pp. 475–496. DOI: 10.1134/S1063779615040024 (page 29).

[28] LHC Higgs Cross Section Working Group. "Handbook of LHC Higgs Cross Sections: 4. Deciphering the Nature of the Higgs Sector". In: (2016). DOI: 10.23731/CYRM-2017-002 (pages 30, 31, 33).

[29] LHC Higgs Cross Section Working Group. "Handbook of LHC Higgs Cross Sections: 2. Differential Distributions". In: (2012). DOI: 10.5170/CERN-2012-002 (page 30).

[30] Johannes Brandstetter. "Higgs boson results on couplings to fermions, CP parameters and perspectives for HL-LHC (ATLAS AND CMS)". In: *International Workshop on Future Linear Collider (LCWS2017) Strasbourg, France, October 23-27, 2017*. 2018 (page 33).

[31] R N Mohapatra. "Physics of the neutrino mass". In: *New Journal of Physics* 6 (July 2004), pp. 82–82. DOI: 10.1088/1367-2630/6/1/082 (page 33).

[32] Renata Zukanovich Funchal, Benoit Schmauch, and Gaëlle Giesen. "The Physics of Neutrinos". In: (2013) (page 33).

[33] David Griffiths. *Introduction to Elementary Particles*. Second, Revised edition. Portland: WILEY-VCH, 2008 (pages 33, 35, 52).

[34] S. P. Martin. "A Supersymmetry Primer". In: *Perspectives On Supersymmetry. Series: Advanced Series on Directions in High Energy Physics. WORLD SCIENTIFIC, Edited by Gordon L Kane, vol. 18, pp. 1-98* 18 (July 1998), pp. 1–98. DOI: 10.1142/9789812839657_0001 (pages 34, 46).

[35] Thomas Mannel. "Theory and Phenomenology of CP Violation". In: *Nuclear Physics B - Proceedings Supplements* 167 (2007). Proceedings of the 7th International Conference on Hyperons, Charm and Beauty Hadrons, pp. 170–174. ISSN: 0920-5632. DOI: https://doi.org/10.1016/j.nuclphysbps.2006.12.083 (page 35).

[36] J. H. Christenson et al. "Evidence for the 2π Decay of the K_2^0 Meson". In: *Phys. Rev. Lett.* 13 (4 July 1964), pp. 138–140. DOI: 10.1103/PhysRevLett.13.138 (page 35).

[37] Dan-di Wu. "A Brief Introduction to the Strong CP Problem". In: vol. 52. Sept. 1991. DOI: 10.1515/zna-1997-1-245 (page 35).

[38] R. D. Peccei and Helen R. Quinn. "CP Conservation in the Presence of Pseudoparticles". In: *Phys. Rev. Lett.* 38 (25 June 1977), pp. 1440–1443. DOI: 10.1103/PhysRevLett.38.1440 (pages 35, 39).

[39] Adam G. Riess et al. "Observational evidence from supernovae for an accelerating universe and a cosmological constant". In: *Astron. J.* 116 (1998), pp. 1009–1038. DOI: 10.1086/300499 (page 35).

[40] The Planck collaboration. "Planck 2015 results. XIII. Cosmological parameters". In: *Astron. Astrophys.* 594 (2016), A13. DOI: 10.1051/0004-6361/201525830 (pages 35, 38).

[41] Gianfranco Bertone and Dan Hooper. "History of dark matter". In: *Rev. Mod. Phys.* 90.4 (2018), p. 045002. DOI: 10.1103/RevModPhys.90.045002 (page 36).

[42] F. Zwicky. "Die Rotverschiebung von extragalaktischen Nebeln". In: *Helvetica Physica Acta* 6 (1933), pp. 110–127 (page 36).

[43] F. Zwicky. "On the Masses of Nebulae and of Clusters of Nebulae". In: *Astrophysical Journal* 86 (Oct. 1937), p. 217. DOI: 10.1086/143864 (page 36).

[44] Vera C. Rubin and Jr. Ford W. Kent. “Rotation of the Andromeda Nebula from a Spectroscopic Survey of Emission Regions”. In: *Astrophysical Journal* 159 (Feb. 1970), p. 379. DOI: 10.1086/150317 (page 36).

[45] A. H. Broeils. “The mass distribution of the dwarf spiral NGC 1560”. In: *Astronomy and Astrophysics* 256 (Mar. 1992), pp. 19–32 (page 37).

[46] Steven Weinberg. *Cosmology*. First edition. Oxford: Oxford University Press, 2008 (page 36).

[47] Gianfranco Bertone and David Merritt. “Dark matter dynamics and indirect detection”. In: *Mod. Phys. Lett. A* 20 (2005), p. 1021. DOI: 10.1142/S0217732305017391 (pages 39, 41).

[48] A. Boyarsky et al. “Sterile Neutrino Dark Matter”. In: *Prog. Part. Nucl. Phys.* 104 (2019), pp. 1–45. DOI: 10.1016/j.ppnp.2018.07.004 (page 39).

[49] The MACHO collaboration. “The MACHO Project: Microlensing Results from 5.7 Years of Large Magellanic Cloud Observations”. In: *The Astrophysical Journal* 542.1 (Oct. 2000), pp. 281–307. DOI: 10.1086/309512 (page 39).

[50] Katherine Garrett and Gintaras Duda. “Dark Matter: A Primer”. In: *Adv. Astron.* 2011 (2011), p. 968283. DOI: 10.1155/2011/968283 (pages 39, 40).

[51] M. Kamionkowski. “WIMP and axion dark matter”. In: *High-energy physics and cosmology. Proceedings, Summer School, Trieste, Italy, June 2-July 4, 1997*. 1997, pp. 394–411 (page 39).

[52] Antonio Boveia and Caterina Doglioni. “Dark Matter Searches at Colliders”. In: *Ann. Rev. Nucl. Part. Sci.* 68 (2018), pp. 429–459. DOI: 10.1146/annurev-nucl-101917-021008 (page 41).

[53] Marc Schumann. “Direct Detection of WIMP Dark Matter: Concepts and Status”. In: *J. Phys.* G46.10 (2019), p. 103003. DOI: 10.1088/1361-6471/ab2ea5 (pages 41, 43).

[54] Tracy R. Slatyer. “Indirect Detection of Dark Matter”. In: *Proceedings, Theoretical Advanced Study Institute in Elementary Particle Physics : Anticipating the Next Discoveries in Particle Physics (TASI 2016): Boulder, CO, USA, June 6-July 1, 2016*. 2018, pp. 297–353. DOI: 10.1142/9789813233348_0005 (pages 41, 44).

[55] The ATLAS collaboration. “Constraints on mediator-based dark matter and scalar dark energy models using $\sqrt{s} = 13$ TeV pp collision data collected by the ATLAS detector”. In: *JHEP* 05 (2019), p. 142. DOI: 10.1007/JHEP05(2019)142 (pages 41, 42).

[56] C. G. Lester and D. J. Summers. “Measuring masses of semiinvisibly decaying particles pair produced at hadron colliders”. In: *Phys. Lett. B* 463 (1999), pp. 99–103. DOI: 10.1016/S0370-2693(99)00945-4 (page 41).

[57] The ATLAS collaboration. “Search for dark matter produced in association with bottom or top quarks in $\sqrt{s} = 13$ TeV pp collisions with the ATLAS detector”. In: *Eur. Phys. J. C* 78.1 (2018), p. 18. DOI: 10.1140/epjc/s10052-017-5486-1 (page 41).

[58] The XENON collaboration. “Dark Matter Search Results from a One Ton-Year Exposure of XENON1T”. In: *Phys. Rev. Lett.* 121.11 (2018), p. 111302. DOI: 10.1103/PhysRevLett.121.111302 (pages 43, 143).

[59] CDEX Collaboration. "Limits on Light Weakly Interacting Massive Particles from the First 102.8 kg × day Data of the CDEX-10 Experiment". In: *Phys. Rev. Lett.* 120 (24 June 2018), p. 241301. DOI: 10.1103/PhysRevLett.120.241301 (page 43).

[60] Juan Cortina, Florian Goebel, and Thomas Schweizer. "Technical Performance of the MAGIC Telescopes". In: *arXiv e-prints*, arXiv:0907.1211 (July 2009) (page 44).

[61] The H.E.S.S. collaboration. "Search for dark matter annihilations towards the inner Galactic halo from 10 years of observations with H.E.S.S". In: *Phys. Rev. Lett.* 117.11 (2016), p. 111301. DOI: 10.1103/PhysRevLett.117.111301 (page 44).

[62] The IceCube collaboration. "Search for Neutrinos from Dark Matter Self-Annihilations in the center of the Milky Way with 3 years of IceCube/DeepCore". In: *Eur. Phys. J. C* 77.9 (2017), p. 627. DOI: 10.1140/epjc/s10052-017-5213-y (page 44).

[63] Farinaldo S. Queiroz. "Dark Matter Overview: Collider, Direct and Indirect Detection Searches". In: *Proceedings, 51st Rencontres de Moriond on Electroweak Interactions and Unified Theories: La Thuile, Italy, March 12-19, 2016*. ARISF. ARISF, 2016, pp. 427–436 (page 44).

[64] Nathaniel Craig et al. "The Higgs Portal Above Threshold". In: *JHEP* 02 (2016), p. 127. DOI: 10.1007/JHEP02(2016)127 (pages 45, 142).

[65] Abdelhak Djouadi et al. "Implications of LHC searches for Higgs–portal dark matter". In: *Phys. Lett.* B709 (2012), pp. 65–69. DOI: 10.1016/j.physletb.2012.01.062 (page 45).

[66] G. C. Branco et al. "Theory and phenomenology of two-Higgs-doublet models". In: *Phys. Rept.* 516 (2012), pp. 1–102. DOI: 10.1016/j.physrep.2012.02.002 (page 46).

[67] Riccardo Barbieri, Lawrence J. Hall, and Vyacheslav S. Rychkov. "Improved naturalness with a heavy Higgs: An Alternative road to LHC physics". In: *Phys. Rev. D* 74 (2006), p. 015007. DOI: 10.1103/PhysRevD.74.015007 (page 46).

[68] M. S. Boucenna and S. Profumo. "Direct and Indirect Singlet Scalar Dark Matter Detection in the Lepton-Specific two-Higgs-doublet Model". In: *Phys. Rev. D* 84 (2011), p. 055011. DOI: 10.1103/PhysRevD.84.055011 (page 47).

[69] Martin Bauer, Ulrich Haisch, and Felix Kahlhoefer. "Simplified dark matter models with two Higgs doublets: I. Pseudoscalar mediators". In: *JHEP* 05 (2017), p. 138. DOI: 10.1007/JHEP05(2017)138 (page 47).

[70] The ATLAS collaboration. "Search for an invisibly decaying Higgs boson or dark matter candidates produced in association with a Z boson in pp collisions at $\sqrt{s} = 13$ TeV with the ATLAS detector". In: *Phys. Lett.* B776 (2018), pp. 318–337. DOI: 10.1016/j.physletb.2017.11.049 (pages 47, 107).

[71] Robert H. Sanders and Stacy S. McGaugh. "Modified Newtonian dynamics as an alternative to dark matter". In: *Ann. Rev. Astron. Astrophys.* 40 (2002), pp. 263–317. DOI: 10.1146/annurev.astro.40.060401.093923 (page 48).

[72] Pieter van Dokkum et al. "A Second Galaxy Missing Dark Matter in the NGC 1052 Group". In: *The Astrophysical Journal* 874.1 (Mar. 2019), p. L5. DOI: 10.3847/2041-8213/ab0d92 (page 48).

[73] Douglas Clowe, Anthony Gonzalez, and Maxim Markevitch. "Weak lensing mass reconstruction of the interacting cluster 1E0657-558: Direct evidence for the existence of dark matter". In: *Astrophys. J.* 604 (2004), pp. 596–603. DOI: 10.1086/381970 (page 48).

[74] Farnes, J. S. "A unifying theory of dark energy and dark matter: Negative masses and matter creation within a modified framework". In: *A&A* 620 (2018), A92. DOI: 10.1051/0004-6361/201832898 (page 48).

[75] Andrew Johnson et al. "Searching for Modified Gravity: Scale and Redshift Dependent Constraints from Galaxy Peculiar Velocities". In: *Mon. Not. Roy. Astron. Soc.* 458.3 (2016), pp. 2725–2744. DOI: 10.1093/mnras/stw447 (page 48).

[76] Lyndon R Evans and Philip Bryant. "LHC Machine". In: *JINST* 3 (2008). This report is an abridged version of the LHC Design Report (CERN-2004-003), S08001. 164 p. DOI: 10.1088/1748-0221/3/08/S08001 (pages 49, 54).

[77] *About CERN*. July 29, 2019. URL: https://home.cern/about (page 49).

[78] The ATLAS collaboration. "The ATLAS experiment at the CERN large hadron collider". In: *Journal of Instrumentation* 3.08 (2008), S08003 (pages 50, 56–59, 61–63).

[79] *CMS, the Compact Muon Solenoid : technical proposal*. LHC Tech. Proposal. Cover title : CMS, the Compact Muon Solenoid : technical proposal. Geneva: CERN, 1994 (page 50).

[80] *ALICE: Technical proposal for a Large Ion collider Experiment at the CERN LHC*. LHC Tech. Proposal. Geneva: CERN, 1995 (page 50).

[81] *LHCb : Technical Proposal*. Tech. Proposal. Geneva: CERN, 1998 (page 50).

[82] D. Gamba et al. "The CLEAR user facility at CERN". In: *Nuclear Instruments and Methods in Physics Research Section A: Accelerators, Spectrometers, Detectors and Associated Equipment* 909 (2018). 3rd European Advanced Accelerator Concepts workshop (EAAC2017), pp. 480–483. ISSN: 0168-9002. DOI: https://doi.org/10.1016/j.nima.2017.11.080 (page 51).

[83] Fabienne Marcastel. "CERN's Accelerator Complex. La chaîne des accélérateurs du CERN". In: (Oct. 2013). General Photo (page 51).

[84] *Concept of Luminosity*. CERN. Geneva: CERN, 2006. DOI: 10.5170/CERN-2006-002 (page 52).

[85] *LuminosityPublicResultsRun2*. July 28, 2019. URL: https://twiki.cern.ch/twiki/bin/view/AtlasPublic/LuminosityPublicResultsRun2 (page 53).

[86] Massimiliano Ferro-Luzzi. "Determination of the luminosity at the LHC experiments". In: *PoS* ICHEP2010 (2010), 010. 6 p. DOI: 10.22323/1.120.0010 (page 53).

[87] The ATLAS collaboration. "Luminosity determination in pp collisions at $\sqrt{s} = 8$ TeV using the ATLAS detector at the LHC". In: *The European Physical Journal C* 76.12 (Nov. 28, 2016), p. 653. ISSN: 1434-6052. DOI: 10.1140/epjc/s10052-016-4466-1 (page 54).

[88] Burkhard Schmidt. "The High-Luminosity upgrade of the LHC: Physics and Technology Challenges for the Accelerator and the Experiments". In: *Journal of Physics: Conference Series* 706 (Apr. 2016), p. 022002. DOI: 10.1088/1742-6596/706/2/022002 (page 54).

[89] ATLAS collaboration. "Measurement of the total cross section from elastic scattering in pp collisions at $\sqrt{s} = 8$ TeV with the ATLAS detector". In: *Phys. Lett. B* 761 (2016), pp. 158–178. DOI: 10.1016/j.physletb.2016.08.020 (page 54).

[90] The TOTEM collaboration. "First measurement of elastic, inelastic and total cross-section at $\sqrt{s} = 13$ TeV by TOTEM and overview of cross-section data at LHC energies". In: *Eur. Phys. J. C* 79.2 (2019), p. 103. DOI: 10.1140/epjc/s10052-019-6567-0 (page 54).

[91] G. Duckeck et al. "ATLAS computing: Technical design report". In: (2005) (page 55).

[92] I. Bird et al. "LHC computing Grid. Technical design report". In: (2005) (page 55).

[93] M. Capeans et al. "ATLAS Insertable B-Layer Technical Design Report". In: (2010) (page 58).

[94] Aranzazu Ruiz-Martinez and ATLAS Collaboration. *The Run-2 ATLAS Trigger System*. Tech. rep. ATL-DAQ-PROC-2016-003. Geneva: CERN, Feb. 2016. DOI: 10.1088/1742-6596/762/1/012003 (pages 63, 64).

[95] *Missing Energy Trigger Public Results*. July 7, 2019. URL: https://twiki.cern.ch/twiki/bin/view/AtlasPublic/MissingEtTriggerPublicResults (page 65).

[96] R. Fruhwirth. "Application of Kalman filtering to track and vertex fitting". In: *Nucl. Instrum. Meth.* A262 (1987), pp. 444–450. DOI: 10.1016/0168-9002(87)90887-4 (page 66).

[97] *Performance of the ATLAS Inner Detector Track and Vertex Reconstruction in the High Pile-Up LHC Environment*. Tech. rep. ATLAS-CONF-2012-042. Geneva: CERN, Mar. 2012 (page 66).

[98] *Performance of primary vertex reconstruction in proton-proton collisions at* $\sqrt{s}$ *=7 TeV in the ATLAS experiment*. Tech. rep. ATLAS-CONF-2010-069. Geneva: CERN, July 2010 (page 66).

[99] Gavin P. Salam. "Towards Jetography". In: *Eur. Phys. J. C* 67 (2010), pp. 637–686. DOI: 10.1140/epjc/s10052-010-1314-6 (page 66).

[100] The ATLAS collaboration. "Topological cell clustering in the ATLAS calorimeters and its performance in LHC Run 1". In: *The European Physical Journal C* 77.7 (July 24, 2017), p. 490. ISSN: 1434-6052. DOI: 10.1140/epjc/s10052-017-5004-5 (pages 68–70).

[101] Matteo Cacciari, Gavin P. Salam, and Gregory Soyez. "The Anti-k(t) jet clustering algorithm". In: *JHEP* 04 (2008), p. 063. DOI: 10.1088/1126-6708/2008/04/063 (pages 69, 113).

[102] Matteo Cacciari and Gavin P. Salam. "Dispelling the N3 myth for the kt jet-finder". In: *Physics Letters B* 641.1 (2006), pp. 57–61. ISSN: 0370-2693. DOI: https://doi.org/10.1016/j.physletb.2006.08.037 (page 69).

[103] The ATLAS collaboration. "Jet reconstruction and performance using particle flow with the ATLAS Detector". In: *The European Physical Journal C* 77.7 (July 13, 2017), p. 466. ISSN: 1434-6052. DOI: 10.1140/epjc/s10052-017-5031-2 (pages 70, 72, 99, 102, 103, 146).

[104] *dE/dx measurement in the ATLAS Pixel Detector and its use for particle identification*. Tech. rep. ATLAS-CONF-2011-016. Geneva: CERN, Mar. 2011 (page 70).

[105] *In-situ measurements of the ATLAS large-radius jet response in 13 TeV pp collisions*. Tech. rep. ATLAS-CONF-2017-063. Geneva: CERN, July 2017 (page 72).

[106] Mrinal Dasgupta et al. "Inclusive jet spectrum for small-radius jets". In: *JHEP* 06 (2016), p. 057. DOI: 10.1007/JHEP06(2016)057 (page 72).

[107] *Boosted Object Tagging with Variable-R Jets in the ATLAS Detector*. Tech. rep. ATL-PHYS-PUB-2016-013. Geneva: CERN, July 2016 (page 72).

[108] *Selection of jets produced in 13TeV proton-proton collisions with the ATLAS detector*. Tech. rep. ATLAS-CONF-2015-029. Geneva: CERN, July 2015 (page 73).

[109] *Optimisation of the ATLAS b-tagging performance for the 2016 LHC Run*. Tech. rep. ATL-PHYS-PUB-2016-012. Geneva: CERN, June 2016 (page 73).

[110] *Measurement of the tau lepton reconstruction and identification performance in the ATLAS experiment using pp collisions at* $\sqrt{s} = 13$ TeV. Tech. rep. ATLAS-CONF-2017-029. Geneva: CERN, May 2017 (page 73).

[111] Ulrich Husemann. "Top-Quark Physics: Status and Prospects". In: *Prog. Part. Nucl. Phys.* 95 (2017), pp. 48–97. DOI: 10.1016/j.ppnp.2017.03.002 (page 73).

[112] G Borissov et al. "ATLAS strategy for primary vertex reconstruction during Run-2 of the LHC". In: *Journal of Physics: Conference Series* 664.7 (Dec. 2015), p. 072041. DOI: 10.1088/1742-6596/664/7/072041 (page 73).

[113] *Pile-up subtraction and suppression for jets in ATLAS*. Tech. rep. ATLAS-CONF-2013-083. Geneva: CERN, Aug. 2013 (pages 73, 74, 103).

[114] *Tagging and suppression of pileup jets with the ATLAS detector*. Tech. rep. ATLAS-CONF-2014-018. Geneva: CERN, May 2014 (page 74).

[115] The ATLAS collaboration. "Performance of pile-up mitigation techniques for jets in *pp* collisions at $\sqrt{s} = 8$ TeV using the ATLAS detector". In: *Eur. Phys. J. C* 76.11 (2016), p. 581. DOI: 10.1140/epjc/s10052-016-4395-z (page 74).

[116] *Forward Jet Vertex Tagging: A new technique for the identification and rejection of forward pileup jets*. Tech. rep. ATL-PHYS-PUB-2015-034. Geneva: CERN, Aug. 2015 (pages 74, 103).

[117] The ATLAS collaboration. "Electron reconstruction and identification in the ATLAS experiment using the 2015 and 2016 LHC proton-proton collision data at $\sqrt{s} = 13$ TeV". In: *Eur. Phys. J.* (2019) (pages 74, 129).

[118] *Electron identification measurements in ATLAS using* $\sqrt{s} = 13$ *TeV data with 50 ns bunch spacing*. Tech. rep. ATL-PHYS-PUB-2015-041. Geneva: CERN, Sept. 2015 (page 75).

[119] The ATLAS collaboration. "Electron efficiency measurements with the ATLAS detector using 2012 LHC proton–proton collision data". In: *The European Physical Journal C* 77.3 (Mar. 27, 2017), p. 195. ISSN: 1434-6052. DOI: 10.1140/epjc/s10052-017-4756-2 (page 75).

[120] *Electron efficiency measurements with the ATLAS detector using the 2015 LHC proton-proton collision data*. Tech. rep. ATLAS-CONF-2016-024. Geneva: CERN, June 2016 (page 75).

[121] *Electron and photon energy calibration with the ATLAS detector using data collected in 2015 at* $\sqrt{s} = 13$ TeV. Tech. rep. ATL-PHYS-PUB-2016-015. Geneva: CERN, Aug. 2016 (page 75).

[122] The ATLAS collaboration. "Muon reconstruction performance of the ATLAS detector in proton–proton collision data at $\sqrt{s}$ =13 TeV". In: *Eur. Phys. J. C* 76.5 (2016), p. 292. DOI: 10.1140/epjc/s10052-016-4120-y (pages 75, 76, 129).

[123] *Expected performance of missing transverse momentum reconstruction for the ATLAS detector at* $\sqrt{s} = 13$ *TeV*. Tech. rep. ATL-PHYS-PUB-2015-023. Geneva: CERN, July 2015 (pages 76–78).

[124] *Object-based missing transverse momentum significance in the ATLAS detector*. Tech. rep. ATLAS-CONF-2018-038. Geneva: CERN, July 2018 (page 77).

[125] The ATLAS collaboration. *Expected performance of the ATLAS experiment: detector, trigger and physics*. Geneva: CERN, 2009 (page 78).

[126] Geant 4 collaboration. "GEANT4: A Simulation toolkit". In: *Nucl. Instrum. Meth.* A506 (2003), pp. 250–303. DOI: 10.1016/S0168-9002(03)01368-8 (page 79).

[127] Andy Buckley et al. "General-purpose event generators for LHC physics". In: *Phys. Rept.* 504 (2011), pp. 145–233. DOI: 10.1016/j.physrep.2011.03.005 (page 80).

[128] Stefan Höche. "Introduction to parton-shower event generators". In: *Proceedings, Theoretical Advanced Study Institute in Elementary Particle Physics: Journeys Through the Precision Frontier: Amplitudes for Colliders (TASI 2014): Boulder, Colorado, June 2-27, 2014*. 2015, pp. 235–295. DOI: 10.1142/9789814678766_0005 (page 80).

[129] Frank Krauss. "Matrix Elements and Parton Showers in Hadronic Interactions". In: *Journal of High Energy Physics* 2002.08 (Aug. 2002), pp. 015–015. DOI: 10.1088/1126-6708/2002/08/015 (page 80).

[130] Bo Andersson et al. "Parton Fragmentation and String Dynamics". In: *Phys. Rept.* 97 (1983), pp. 31–145. DOI: 10.1016/0370-1573(83)90080-7 (page 81).

[131] X. Artru and G. Mennessier. "String model and multiproduction". In: *Nucl. Phys.* B70 (1974), pp. 93–115. DOI: 10.1016/0550-3213(74)90360-5 (page 81).

[132] Tanju Gleisberg and Stefan Hoeche. "Comix, a new matrix element generator". In: *JHEP* 12 (2008), p. 039. DOI: 10.1088/1126-6708/2008/12/039 (pages 81, 110).

[133] Ansgar Denner et al. "HAWK 2.0: A Monte Carlo program for Higgs production in vector-boson fusion and Higgs strahlung at hadron colliders". In: *Comput. Phys. Commun.* 195 (2015), pp. 161–171. DOI: 10.1016/j.cpc.2015.04.021 (pages 81, 110, 130).

[134] Stefan Hoeche et al. “QCD matrix elements + parton showers: The NLO case”. In: *JHEP* 04 (2013), p. 027. DOI: 10.1007/JHEP04(2013)027 (pages 81, 110).

[135] Fabio Cascioli, Philipp Maierhofer, and Stefano Pozzorini. “Scattering Amplitudes with Open Loops”. In: *Phys. Rev. Lett.* 108 (2012), p. 111601. DOI: 10.1103/PhysRevLett.108.111601 (pages 81, 110).

[136] Stefano Frixione, Paolo Nason, and Giovanni Ridolfi. “A Positive-weight next-to-leading-order Monte Carlo for heavy flavour hadroproduction”. In: *JHEP* 09 (2007), p. 126. DOI: 10.1088/1126-6708/2007/09/126 (pages 82, 110).

[137] Torbjorn Sjostrand, Stephen Mrenna, and Peter Z. Skands. “A Brief Introduction to PYTHIA 8.1”. In: *Comput. Phys. Commun.* 178 (2008), pp. 852–867. DOI: 10.1016/j.cpc.2008.01.036 (pages 82, 91, 110, 152).

[138] T. Gleisberg et al. “Event generation with SHERPA 1.1”. In: *JHEP* 02 (2009), p. 007. DOI: 10.1088/1126-6708/2009/02/007 (pages 82, 108).

[139] The ATLAS collaboration. “The ATLAS Simulation Infrastructure”. In: *Eur. Phys. J. C* 70 (2010), pp. 823–874. DOI: 10.1140/epjc/s10052-010-1429-9 (pages 82, 108, 152).

[140] The ATLAS collaboration. *The simulation principle and performance of the ATLAS fast calorimeter simulation FastCaloSim*. Tech. rep. ATL-PHYS-PUB-2010-013. Geneva: CERN, Oct. 2010 (pages 82, 108).

[141] The ATLAS Collaboration. “The ATLAS Simulation Infrastructure”. In: *The European Physical Journal C* 70.3 (Dec. 1, 2010), pp. 823–874. ISSN: 1434-6052. DOI: 10.1140/epjc/s10052-010-1429-9 (page 82).

[142] *Monte Carlo Calibration and Combination of In-situ Measurements of Jet Energy Scale, Jet Energy Resolution and Jet Mass in ATLAS*. Tech. rep. ATLAS-CONF-2015-037. Geneva: CERN, Aug. 2015 (pages 84, 85, 149, 150).

[143] The ATLAS Collaboration. “Jet energy scale measurements and their systematic uncertainties in proton-proton collisions at $\sqrt{s} = 13$ TeV with the ATLAS detector”. In: *Phys. Rev. D* 96 (7 Oct. 2017), p. 072002. DOI: 10.1103/PhysRevD.96.072002 (pages 85–88, 94, 101, 149, 167, 168).

[144] Matteo Cacciari and Gavin P. Salam. “Pileup subtraction using jet areas”. In: *Phys. Lett. B* 659 (2008), pp. 119–126. DOI: 10.1016/j.physletb.2007.09.077 (page 85).

[145] *Pile-up subtraction and suppression for jets in ATLAS*. Tech. rep. ATLAS-CONF-2013-083. Geneva: CERN, Aug. 2013 (page 85).

[146] *Data-driven determination of the energy scale and resolution of jets reconstructed in the ATLAS calorimeters using dijet and multijet events at* $\sqrt{s} = 8$ *TeV*. Tech. rep. ATLAS-CONF-2015-017. Geneva: CERN, Apr. 2015 (page 88).

[147] *Determination of the jet energy scale and resolution at ATLAS using* Z/γ*–jet events in data at* $\sqrt{s} = 8$ *TeV*. Tech. rep. ATLAS-CONF-2015-057. Geneva: CERN, Oct. 2015 (page 88).

[148] A. Schwartzman D. Lopez Mateos E.W. Hughes. "A Simple p_T and η-Dependent Monte Carlo-Based Jet Calibration". In: *ATLAS NOTE* ATL-PHYS-INT-2009-077 (2009) (pages 89, 149).

[149] Atlas Collaboration. "Jet energy measurement and its systematic uncertainty in proton–proton collisions at $\sqrt{s} = 7$ TeV with the ATLAS detector". In: *The European Physical Journal C* 75.1 (Jan. 15, 2015), p. 17. ISSN: 1434-6052. DOI: 10.1140/epjc/s10052-014-3190-y (pages 90, 149).

[150] The ATLAS Collaboration. "Jet energy measurement with the ATLAS detector in proton-proton collisions at $\sqrt{s} = 7$ TeV". In: *The European Physical Journal C* 73.3 (Mar. 2, 2013), p. 2304. ISSN: 1434-6052. DOI: 10.1140/epjc/s10052-013-2304-2 (pages 90, 91, 100).

[151] *Jet global sequential corrections with the ATLAS detector in proton-proton collisions at $\sqrt{s} = 8$ TeV*. Tech. rep. ATLAS-CONF-2015-002. Geneva: CERN, Mar. 2015 (pages 90, 91, 95, 100).

[152] *MC Weights and Quality Cuts in 2012*. July 30, 2012. URL: https://twiki.cern.ch/twiki/bin/viewauth/AtlasProtected/JetStudies2012 (pages 91, 154).

[153] The ATLAS collaboration. "Monte Carlo calibration update for electrons and photons using multivariate techniques". In: *ATLAS PUB note* ATL-PHYS-PUB-2016-015 (2016), p. 015 (page 104).

[154] A. Hoecker et al. "TMVA - Toolkit for Multivariate Data Analysis". In: *arXiv e-prints*, physics/0703039 (Mar. 2007), physics/0703039 (page 104).

[155] Ignatios Antoniadis, Marc Tuckmantel, and Fabio Zwirner. "Phenomenology of a leptonic goldstino and invisible Higgs boson decays". In: *Nucl. Phys. B* 707 (2005), pp. 215–232. DOI: 10.1016/j.nuclphysb.2004.11.061 (page 105).

[156] Nima Arkani-Hamed et al. "Neutrino masses from large extra dimensions". In: *Phys. Rev. D* 65 (2001), p. 024032. DOI: 10.1103/PhysRevD.65.024032 (page 105).

[157] Anindya Datta et al. "Invisible Higgs in theories of large extra dimensions". In: *Phys. Rev. D* 70 (2004), p. 075003. DOI: 10.1103/PhysRevD.70.075003 (page 105).

[158] The ATLAS collaboration. "Constraints on new phenomena via Higgs boson couplings and invisible decays with the ATLAS detector". In: *JHEP* 11 (2015), p. 206. DOI: 10.1007/JHEP11(2015)206 (page 105).

[159] *A combination of searches for the invisible decays of the Higgs boson using the CMS detector*. Tech. rep. CMS-PAS-HIG-15-012. Geneva: CERN, 2015 (page 105).

[160] The ATLAS collaboration. "Search for invisible decays of a Higgs boson using vector-boson fusion in pp collisions at $\sqrt{s} = 8$ TeV with the ATLAS detector". In: *Journal of High Energy Physics* 2016.1 (Jan. 28, 2016), p. 172. DOI: 10.1007/JHEP01(2016)172 (page 106).

[161] The ATLAS collaboration. "Constraints on new phenomena via Higgs boson couplings and invisible decays with the ATLAS detector". In: *Journal of High Energy Physics* 2015.11 (Nov. 30, 2015), p. 206. ISSN: 1029-8479. DOI: 10.1007/JHEP11(2015)206 (page 106).

[162] The CMS collaboration. "Search for invisible decays of Higgs bosons in the vector boson fusion and associated ZH production modes". In: *The European Physical Journal C* 74.8 (Aug. 13, 2014), p. 2980. ISSN: 1434-6052. DOI: 10.1140/epjc/s10052-014-2980-6 (page 106).

[163] The CMS collaboration. *Search for invisible decays of the Higgs boson produced through vector boson fusion at* $\sqrt{s} = 13$ TeV. Tech. rep. CMS-PAS-HIG-17-023. Geneva: CERN, 2018 (pages 107, 145).

[164] The CMS collaboration. "Searches for invisible decays of the Higgs boson in pp collisions at $\sqrt{s}$ = 7, 8, and 13 TeV". In: *JHEP* 02 (2017), p. 135. DOI: 10.1007/JHEP02(2017)135 (page 107).

[165] The CMS collaboration. "Search for associated production of dark matter with a Higgs boson decaying to $b\bar{b}$ or $\gamma\gamma$ at $\sqrt{s} = 13$ TeV". In: *JHEP* 10 (2017), p. 180. DOI: 10.1007/JHEP10(2017)180 (page 107).

[166] Steffen Schumann and Frank Krauss. "A Parton shower algorithm based on Catani-Seymour dipole factorisation". In: *JHEP* 03 (2008), p. 038. DOI: 10.1088/1126-6708/2008/03/038 (page 110).

[167] Richard D. Ball et al. "Parton distributions for the LHC Run II". In: *JHEP* 04 (2015), p. 040. DOI: 10.1007/JHEP04(2015)040 (page 110).

[168] Hung-Liang Lai et al. "New parton distributions for collider physics". In: *Phys. Rev. D* 82 (7 Oct. 2010), p. 074024. DOI: 10.1103/PhysRevD.82.074024 (page 110).

[169] Torbjorn Sjostrand, Stephen Mrenna, and Peter Z. Skands. "PYTHIA 6.4 Physics and Manual". In: *JHEP* 05 (2006), p. 026. DOI: 10.1088/1126-6708/2006/05/026 (page 110).

[170] William Buttinger. *Using Event Weights to account for differences in Instantaneous Luminosity and Trigger Prescale in Monte Carlo and Data*. Tech. rep. ATL-COM-SOFT-2015-119. Geneva: CERN, May 2015 (pages 111, 112).

[171] The ATLAS collaboration. "Performance of the ATLAS Trigger System in 2015". In: *Eur. Phys. J. C* 77.5 (2017), p. 317. DOI: 10.1140/epjc/s10052-017-4852-3 (page 112).

[172] Marcus Morgenstern and Mark Owen. *Muon trigger efficiency in early 2018 data taking*. Tech. rep. ATL-COM-DAQ-2018-047. Geneva: CERN, May 2017 (page 112).

[173] Ketevi Assamagan et al. *Search for an invisibly decaying Higgs boson produced via Vector Boson Fusion in pp collisions at* $\sqrt{s} = 13$ *TeV using data collected by the ATLAS Experiment*. Tech. rep. ATL-COM-PHYS-2016-1802. Geneva: CERN, Dec. 2016 (pages 119, 120, 122–126, 131–133, 136–141, 190–194).

[174] The ATLAS collaboration. *Search for new physics in final states with jets and missing transverse momentum using pp collision data collected in 2015 and 2016 by ATLAS*. Tech. rep. ATL-COM-PHYS-2016-1487. Geneva: CERN, Oct. 2016 (page 128).

[175] The ATLAS collaboration. "Measurement of the Inelastic Proton-Proton Cross Section at $\sqrt{s} = 13$ TeV with the ATLAS Detector at the LHC". In: *Phys. Rev. Lett.* 117.18 (2016), p. 182002. DOI: 10.1103/PhysRevLett.117.182002 (page 129).

[176] John M. Campbell, R. Keith Ellis, and Ciaran Williams. "Vector boson pair production at the LHC". In: *JHEP* 07 (2011), p. 018. DOI: 10.1007/JHEP07(2011)018 (page 130).

[177] Iain W. Stewart and Frank J. Tackmann. "Theory Uncertainties for Higgs and Other Searches Using Jet Bins". In: *Phys. Rev. D* 85 (2012), p. 034011. DOI: 10.1103/PhysRevD.85.034011 (page 130).

[178] B. Cooper et al. "Importance of a consistent choice of alpha(s) in the matching of AlpGen and Pythia". In: *Eur. Phys. J. C* 72 (2012), p. 2078. DOI: 10.1140/epjc/s10052-012-2078-y (page 130).

[179] S. Catani et al. "QCD matrix elements + parton showers". In: *JHEP* 11 (2001), p. 063. DOI: 10.1088/1126-6708/2001/11/063 (page 130).

[180] Helmut G. Katzgraber. "Introduction to Monte Carlo Methods". In: *arXiv e-prints*, arXiv:0905.1629 (May 2009), arXiv:0905.1629 (page 135).

[181] Glen Cowan et al. "Asymptotic formulae for likelihood-based tests of new physics". In: *Eur. Phys. J. C* 71 (2011). [Erratum: Eur. Phys. J.C73,2501(2013)], p. 1554. DOI: 10.1140/epjc/s10052-011-1554-0, 10.1140/epjc/s10052-013-2501-z (page 135).

[182] Martin Hoferichter et al. "Improved limits for Higgs-portal dark matter from LHC searches". In: *Phys. Rev. Lett.* 119.18 (2017), p. 181803. DOI: 10.1103/PhysRevLett.119.181803 (page 143).

[183] D. S. Akerib et al. "Results from a search for dark matter in the complete LUX exposure". In: *Phys. Rev. Lett.* 118.2 (2017), p. 021303. DOI: 10.1103/PhysRevLett.118.021303 (page 143).

[184] Xiangyi Cui et al. "Dark Matter Results From 54-Ton-Day Exposure of PandaX-II Experiment". In: *Phys. Rev. Lett.* 119.18 (2017), p. 181302. DOI: 10.1103/PhysRevLett.119.181302 (page 143).

[185] The ATLAS Collaboration. "Combination of Searches for Invisible Higgs Boson Decays with the ATLAS Experiment". In: *Phys. Rev. Lett.* 122 (23 June 2019), p. 231801. DOI: 10.1103/PhysRevLett.122.231801 (page 145).

[186] Thomas Koffas. *ATLAS Higgs Physics Prospects at the High Luminosity LHC*. Tech. rep. ATL-PHYS-PROC-2016-268. Geneva: CERN, Dec. 2016. DOI: 10.22323/1.282.0426 (page 148).

[187] *Prospects for New Physics in Higgs Couplings Studies with the ATLAS Detector at the HL-LHC*. Tech. rep. ATL-PHYS-PUB-2014-017. Geneva: CERN, Oct. 2014 (page 148).

[188] Wolfgang Walkowiak. *ATLAS Plans for the High-Luminosity LHC*. Tech. rep. ATL-PHYS-PROC-2018-048. Geneva: CERN, June 2018. DOI: 10.22323/1.326.0055 (page 148).

[189] Noemi Calace. "Jet Substructure Techniques for the Search of Diboson Resonances at the LHC and Performance Evaluation of the ATLAS Phase-II Inner Tracker Layouts". Presented 20 Jun 2018. May 2018 (page 150).

[190] Peter Berta. "ATLAS jet and missing-ET reconstruction, calibration, and performance". In: *Nuclear and Particle Physics Proceedings* 273-275 (2016). 37th International Conference on High Energy Physics (ICHEP), pp. 1121–1126. ISSN: 2405-6014. DOI: https://doi.org/10.1016/j.nuclphysbps.2015.09.176 (page 150).

[191] Matthias Schröder. "Quality of jet measurements and impact on a search for new physics at CMS". PhD thesis. Hamburg U., 2012 (pages 150, 181).

[192] The DØ collaboration. "High-p_T jets in $\bar{p}p$ collisions at $\sqrt{s} = 630$ GeV and 1800 GeV". In: *Phys. Rev. D* 64 (2001), p. 032003. DOI: 10.1103/PhysRevD.64.032003 (page 151).

[193] The CMS collaboration. "Determination of jet energy calibration and transverse momentum resolution in CMS". In: *JINST* 6 (2011), p. 102. DOI: 10.1088/1748-0221/6/11/P11002 (page 151).

[194] *Jet energy resolution and selection efficiency relative to track jets from in-situ techniques with the ATLAS Detector Using Proton-Proton Collisions at a Center of Mass Energy $\sqrt{s}$ = 7 TeV*. Tech. rep. ATLAS-CONF-2010-054. Geneva: CERN, July 2010 (page 151).

A.5 Acknowledgements

In my four-year Ph.D. journey I had the privilege of working with the greatest experts in their fields, being guided by the wisest counsellors and being supported by the most loyal friends. Below I want to thank some of my companions that were of great help in this special period of my life. Even if I cannot mention all of the people in this long list by name, I want everyone to know that I still remember their contributions dearly. This is not the work of one person but the accomplishment of many.

First of all I want to thank my supervisor at DESY, Krisztian Peters, for being with me every step of the way. He not only taught me the scientific process and advised me in my research, but he was also always there for me as a friend. I grew a lot by following him.

I also want to thank my supervisor at the university of Hamburg, Peter Schleper, for his excellent advice. I got to profit from his experience in order to focus on the most important topics without losing myself in this great challenge.

For each of the projects that constitute this work I had guidance from one of four passionate and knowledgeable experts: Alexander Madsen, Christian Sander, Jonathan Sola and Othmane Rifki. They all were very patient with my many questions even in times of slow progress. I am eternally grateful for their helpful instructions and advice.

The search for invisible decays of the Higgs boson produced in vector-boson fusion was a group effort with input from many scientists. My work on the analysis profited greatly from the feedback from highly motivated colleagues: Andrew White, Ben Carlson, Ketevi Assamagan, Marta Perego, Rui Zou, Tae Min Hong and William Balunas. The list includes the scientists I had the most interaction with, unless they are otherwise mentioned above or below. There are many more contributions to the analysis that are not mentioned here but still worthy of respect.

I also want to thank my proofreaders for fighting their way through the first drafts of this thesis. They did not have to do this, but put in a lot of time and effort out of the kindness of their hearts. My thanks go to Alicia Wongel, Arthur Linss, Chris Pollard, Janik von Ahnen, Jonas Neundorf, Jonathan Burr, Kurt Brendlinger, Nicholas Styles, Pablo Bracho, William Leight, Xuanghong Lou and Yu-Heng Chen.

I will also never forget the DESY ATLAS group that was like a second family for the past four years. Everyone is just happy to offer help at any time despite being a collection of the most busy people I know. With every member of the group working so closely together it feels like every title and degree is another victory for the entire family rather than just the individual. I will not attempt to name all of them because at times we were 100 scientist. I just want to mention David South and Ingrid-Maria Gregor for always finding the time to make my life at work easier, supporting me and giving me the opportunity to join the group. I also want to take this time to remember Jihyun Jeong for I am filled with gratitude for having met her.

This phase of my life was also rough at times. Therefore, I want to thank my therapist, Carsten Dietze, for helping me find my inner strength and evolve into a person that was able to meet the challenge.

I am also grateful to my friends and their everlasting patience. They are too many to name and thankfully their numbers did not dwindle despite me not finding enough time for them this past year. I will make it all up in 2020.

Last but not least my family was an endless source of positive energy. They always believed in me even when I did not. My step-father, Matthias Lipp, deserves praise for teaching me

how fast the speed of light really is. I thank my sister, Felicitas Kitali, for her wisdom, wit and kindness. Whenever I talked to her I always knew where to head next. I am also thankful to my sister-in-law, Aranka Bader. With her humour and resourcefulness she quickly became another sister this past few years and I am just happy to have her around. Finally, I am deeply grateful to my mother, Susanne Lipp, who was always there for me and cheered me on from my lowest lows to my highest highs. Too rarely do I take the time to tell her how much I look up to her. Thank you for being you!

Eidesstattliche Versicherung / Declaration on oath

Hiermit versichere ich an Eides statt, die vorliegende Dissertationsschrift selbst verfasst und keine anderen als die angegebenen Hilfsmittel und Quellen benutzt zu haben.

Die eingereichte schriftliche Fassung entspricht der auf dem elektronischen Speichermedium.

Die Dissertation wurde in der vorgelegten oder in einer ähnlichen Form nicht schon einmal in einem früheren Promotionsverfahren angenommen oder als ungenügend beurteilt.

Vincent Kitali	Ort, Datum